

Effect of Surface State on Water Wetting and Carbon Dioxide Corrosion in  
Oil-water Two-phase Flow

A dissertation presented to  
the faculty of  
the Russ College of Engineering and Technology of Ohio University

In partial fulfillment  
of the requirements for the degree  
Doctor of Philosophy

Xuanping Tang

June 2011

© 2011 Xuanping Tang. All Rights Reserved.

This dissertation titled  
Effect of Surface State on Water Wetting and Carbon Dioxide Corrosion in  
Oil-water Two-phase Flow

by

XUANPING TANG

has been approved for  
the Department of Chemical and Biomolecular Engineering  
and the Russ College of Engineering and Technology by

---

Srdjan Nesic

Professor of Chemical and Biomolecular Engineering

---

Dennis Irwin

Dean, Russ College of Engineering and Technology

**ABSTRACT**

TANG, XUANPING, Ph.D., 2011, Chemical Engineering

Effect of Surface State on Water Wetting and Carbon Dioxide Corrosion in

Oil-water Two-phase Flow (206 pp.)

Director of Dissertation: Srdjan Nestic

Internal corrosion is one of the most common problems within the transportation pipelines of the oil and gas industry. Water wetting is one of the most important issues in the prediction of internal corrosion in mild steel pipelines, and it is affected by water chemistry, flow regime, pipe orientation and water cut. Another possible factor is the nature of the wetted surface itself, such as bare metal surfaces with different degrees of roughness or surfaces covered with iron carbonate film produced by corrosion. The primary objective of this study is to investigate and model the effect of surface state on water wetting and carbon dioxide corrosion in oil-water flow.

Five types of crude oil and one model oil (LVT200) were tested with 1wt% NaCl brine in a 4" I.D. fully inclinable large scale flow loop. Four main techniques were used to determine flow regime: flow pattern visualization, wall conductance probes, wall fluid sampling, and corrosion rate monitoring. Based on the overlapping information from these four techniques, three types of phase wetting regimes (stable water wetting, intermittent wetting and stable oil wetting) were identified. Comprehensive phase wetting maps were constructed based on the results obtained from wall conductance probes, including the transition from intermittent wetting to stable oil wetting.

A goniometer contact angle measurement system was designed and successfully used to investigate the effect of steel surface state on wettability. Contact angle measurements were made for bare steel surfaces with different degrees of roughness, with iron carbonate film, and different pre-wetting scenarios. The results showed that surface roughness and iron carbonate do not affect wettability. However, pre-wetting the steel surface with either water or oil had a great effect on wettability. Pre-wetting the steel surface with crude oil led to a transition of the wettability of the steel surface from hydrophilicity to hydrophobicity. Adding a corrosion inhibitor (“quat”) produced a similar effect.

A new mechanistic phase wetting prediction model was proposed. The new model considers the effect of surface wettability to calculate the maximum water droplet size in oil-water flow. The model significantly improves the prediction of the critical oil phase velocity required for full water entrainment compared to the existing water wetting model incorporated in MULTICORP software. The new model was verified with the experimental results for different crude oils and by using different additive chemicals which alter the wettability.

Approved: \_\_\_\_\_

Srdjan Nestic

Professor of Chemical and Biomolecular Engineering

*To*

*My parents, Tang Qingbo and Wang Dongmei*

*My wife, Yang Yang*

*My brother, Tang Yongping*

*and all other family members*

*For their*

*Love, care and support*

## ACKNOWLEDGMENTS

I am deeply indebted to my esteemed advisor Dr. Srdjan Nesic for his guidance, encouragement and support throughout this work. I am also thankful to Dr. Michael Prudich, Dr. David Ingram, Dr. Khairul Alam and Dr. Hao Chen who served as my dissertation committee members.

I would like to thank Dr. Jiyong Cai, Dr. Khairul Alam and Dr. Sonja Richter for their leadership in this project and their help with my research. I would like to express my sincere appreciation to Mr. Bruce Brown, Mr. Albert Schubert, Mr. John Goettge, Mr. Danny Cain, Mr. Cody Shafer and Mr. Garret Brown for their assistance in the experimental instrumentation. I want to thank all fellow students in the WWJIP, Dr. Chong Li, Dr. Francois Ayello, Mr. Pankaj Ajmera and Ms. Shanshan Yang, for their unselfish help and full cooperation. I thank all fellow students in the Institute for Corrosion and Multiphase Technology for creating such a comfortable environment and atmosphere for research and life.

I gratefully acknowledge the financial support and technical directions from sponsoring companies: BP, ConocoPhillips, Eni, ExxonMobil, Petrobras, Saudi Aramco, Shell and Total.

Finally, I would like to express my sincere appreciation for all of my family members and friends for their encouragement, help and understanding during the long journey toward reaching my academic goal.

## TABLE OF CONTENTS

	Page
ABSTRACT .....	3
ACKNOWLEDGMENTS .....	6
LIST OF TABLES .....	11
LIST OF FIGURES .....	13
CHAPTER 1 : INTRODUCTION .....	19
CHAPTER 2 : RESEARCH OBJECTIVES .....	23
CHAPTER 3 : LITERATURE REVIEW .....	25
3.1 Surface roughness and microtopography .....	25
3.1.1 Surface roughness parameters .....	25
3.1.2 Techniques for surface roughness measurement .....	28
3.2 Wetting phenomena .....	31
3.2.1 Surface tension and interfacial tension .....	31
3.2.2 Wettability and contact angle .....	34
3.3 Oil-water two-phase flow .....	38
3.3.1 Flow pattern identification and classification .....	39
3.3.2 Flow pattern transition prediction .....	43
3.3.3 Water wetting model .....	45
3.4 Carbon dioxide corrosion .....	58
3.4.1 Electrochemistry of CO <sub>2</sub> corrosion .....	59
3.4.2 Key factors influencing CO <sub>2</sub> corrosion .....	61
CHAPTER 4 : EXPERIMENTAL STUDY OF OIL-WATER TWO-PHASE FLOW ...	64

	8
4.1 Experimental setup .....	65
4.1.1 Test facilities .....	65
4.1.2 Test techniques .....	69
4.1.3 Test Matrix .....	72
4.1.4 Properties of the experimental fluids .....	72
4.1.5 Experimental procedure .....	76
4.2 Results and discussion .....	77
4.2.1 Horizontal pipe flow test results .....	77
4.2.2 Transition between stable oil wetting and intermittent wetting .....	101
4.3 Comparison of experimental results with water wetting model prediction in MULTICORP .....	110
4.3.1 Water wetting model in MULTICORP .....	110
4.3.2 Verification of water wetting model in MULTICORP .....	112
4.4 Summary .....	118
CHAPTER 5 : EXPERIMENTAL STUDY OF SURFACE WETTABILITY .....	120
5.1 Effect of the surface state of steel on its wettability .....	120
5.1.1 Experimental setup and procedure .....	120
5.1.2 Experimental results .....	130
5.2 Effect of temperature on surface wettability .....	135
5.2.1 Experimental setup and procedure .....	135
5.2.2 Experimental results .....	137
5.3 Wettability of pre-wetted surface .....	140

5.3.1 Experimental setup.....	140
5.3.2 Test matrix .....	141
5.3.3 Experimental procedure.....	145
5.3.4 Experimental results.....	150
5.4 Summary.....	161
<b>CHAPTER 6 : EFFECT OF DYNAMIC WETTING ON CARBON DIOXIDE</b>	
<b>CORROSION IN A HORIZONTAL ROTATING CYLINDER.....</b>	
6.1 Experimental setup .....	164
6.1.1 Horizontal rotating cylinder (HRC).....	164
6.1.2 Test matrix and experimental procedure.....	165
6.1.3 Methodology of data interpretation.....	167
6.2 Results and discussion .....	169
6.2.1 Verification of HRC.....	169
6.2.2 Results of the low speed test.....	171
6.3 Summary.....	176
<b>CHAPTER 7 : NEW IMPROVED WATER WETTING MODEL.....</b>	
7.1 Water wetting model including surface wettability effect.....	177
7.1.1 Maximum drop diameter.....	177
7.1.2 Critical drop diameter .....	180
7.2 Model verification.....	182
7.2.1 Baseline test results.....	182
7.2.2 Results with crude oils.....	183

	10
7.2.3 Results with corrosion inhibitor .....	186
7.2.4 Results with surface active chemical additive .....	189
7.3 Summary.....	191
CHAPTER 8 : CONCLUSIONS AND RECOMMENDATIONS FOR FUTURE WORK	
.....	193
8.1 Conclusions.....	193
8.2 Recommendations for future work .....	195
REFERENCES .....	197

## LIST OF TABLES

	Page
<i>Table 4-1.</i> Main test parameters for oil-water two-phase flow loop tests. ....	72
<i>Table 4-2.</i> Water concentration in the fluid samples for LVT200 oil in horizontal pipe flow at different mixture velocities and different water cuts. ....	86
<i>Table 4-3.</i> The change in $Fe^{2+}$ concentration under different flow conditions in LVT200 oil and $CO_2$ saturated, 1 wt% NaCl D.I. water horizontal flow. ....	86
<i>Table 4-4.</i> Water concentration in the fluid samples for C1 crude oil in horizontal pipe flow at different mixture velocities and different water cuts. ....	89
<i>Table 4-5.</i> $Fe^{2+}$ concentration changes under water wetting in C1 crude oil-water horizontal flow and the estimate of the corresponding corrosion rate. ....	90
<i>Table 4-6.</i> Water concentration in the fluid samples for C2 crude oil-water in horizontal pipe flow at different oil-water mixture velocities and water cuts. ....	92
<i>Table 4-7.</i> Change in $Fe^{2+}$ concentration under different flow conditions with C2 crude oil and $CO_2$ saturated, 1 wt% NaCl D.I. water in horizontal flow and the corresponding corrosion rate. ....	93
<i>Table 4-8.</i> Water concentration in the fluid samples for C3 crude oil-water in horizontal pipe flow at different oil-water mixture velocities and water cuts. ....	95
<i>Table 4-9.</i> Changes in the $Fe^{2+}$ concentration under different phase wetting conditions with C3 crude oil-water horizontal flow and the corresponding corrosion rate. ....	95
<i>Table 4-10.</i> Water concentration in the fluid samples for C4 crude oil-water in horizontal pipe flow at different oil-water mixture velocities and water cuts. ....	98
<i>Table 4-11.</i> Corrosion rates measured by an ER probe when C4 crude oil and water form emulsion at different oil-water mixture velocities and water cuts in horizontal pipe flow. ....	98
<i>Table 4-12.</i> Water concentration in the fluid samples for C5 crude oil-water in horizontal pipe flow at different oil-water mixture velocities and water cuts. ....	100
<i>Table 4-13.</i> Corrosion rates measured by ER probe when C5 crude oil and water form emulsion at oil-water mixture velocity of 0.9 m/s and different water cuts in horizontal pipe flow. ....	101
<i>Table 5-1.</i> Text matrix of water-in-oil contact angle measurement for different surface conditions at the temperature of 25 °C. ....	123
<i>Table 5-2.</i> Chemical composition of X65 carbon steel. ....	124
<i>Table 5-3.</i> Text matrix of oil-in-water contact angle measurement for different surface conditions at the temperature of 25 °C. ....	124
<i>Table 5-4.</i> Experimental conditions for iron carbonate film formation. ....	126
<i>Table 5-5.</i> Test matrix for water-in-oil contact angle measurement at different temperatures. ....	135
<i>Table 5-6.</i> Test matrix for oil-in-water contact angle measurement at different temperatures. ....	136
<i>Table 5-7.</i> Test matrix for effect of surface state on the wettability of pre-wetted surfaces. ....	141

<i>Table 5-8.</i> Test matrix for mill scale formation.....	142
<i>Table 5-9.</i> Test matrix for testing of the effect of corrosion inhibitor on the wettability of pre-wetted surfaces. ....	144
<i>Table 5-10.</i> Test matrix for testing the effect of crude oils on the wettability of pre-wetted surfaces. ....	144
<i>Table 6-1.</i> Test matrix for HRC test. ....	165
<i>Table 6-2.</i> Chemical composition of carbon steel C1018.....	166
<i>Table 7-1.</i> Comparison of proposed criterion value with experimental value by Bond & Newton (1928). ....	182

## LIST OF FIGURES

	Page
<i>Figure 3-1.</i> Average roughness, $R_a$ (Farshad, Rieke, <i>et al.</i> , 2001).....	27
<i>Figure 3-2.</i> Root mean square roughness, $R_q$ (Farshad, Rieke, <i>et al.</i> , 2001).....	27
<i>Figure 3-3.</i> Mean peak-to-valley height or ten-point height, $R_z$ (Whitehouse, 2003). .....	28
<i>Figure 3-4.</i> Schematic of a stylus instrument for surface roughness measurement (Thomas, 1999).....	29
<i>Figure 3-5.</i> Molecules in the liquid bulk and the interface (de Gennes, Brochard-Wyart, <i>et al.</i> , 2003). .....	32
<i>Figure 3-6.</i> A soap film stretched by a wire slider (Adamson & Gast, 1997).....	33
<i>Figure 3-7.</i> Classification of techniques for interfacial tension measurements (Drelich, Fang, <i>et al.</i> , 2002). .....	34
<i>Figure 3-8.</i> Du Noüy ring method (Drelich, Fang, <i>et al.</i> , 2002). .....	34
<i>Figure 3-9.</i> Sessile drop on a solid surface, surrounded by either another liquid, gas or vapor (Berg, 1993). .....	35
<i>Figure 3-10.</i> Determination of equilibrium contact angle $\theta_E$ from the interfacial forces of gas, liquid and solid. ....	36
<i>Figure 3-11.</i> Schematic of the Whilhelmy plate method (Drelich, Fang, <i>et al.</i> , 2002). ...	37
<i>Figure 3-12.</i> Sketches of flow patterns in horizontal oil-water flow (Trallero, Sarica, <i>et</i> <i>al.</i> ,1997). .....	41
<i>Figure 3-13.</i> Flow patterns in oil-water horizontal flows (Cai, Nestic, & de Waard, 2004) .....	46
<i>Figure 3-14.</i> The forces of axial direction acting on droplets in oil-water dispersed flow. .....	54
<i>Figure 4-1.</i> Schematic of a 4” fully inclinable multiphase flow loop used in the study (Cai, Nestic, Li, <i>et al.</i> ,2005). .....	66
<i>Figure 4-2.</i> Schematic of internal structure of oil-water separator (Courtesy of Jiyong Cai). .....	68
<i>Figure 4-3.</i> Schematic of test section made of carbon steel (Courtesy of Jiyong Cai).....	69
<i>Figure 4-4.</i> Wall conductance probes. (a) wall conductance probes on the test section, (b) 5 rows of staggered configuration of probe holders (Courtesy of Jiyong Cai).....	70
<i>Figure 4-5.</i> HAAKE® Falling Ball Viscometer for viscosity measurement.....	73
<i>Figure 4-6.</i> CSC-DuNouy® Tensiometer for oil-water interfacial tension measurement. 74	74
<i>Figure 4-7.</i> The density of the testing oils at room temperature (25 °C). .....	74
<i>Figure 4-8.</i> The API gravity of the testing oils at room temperature (25 °C). .....	75
<i>Figure 4-9.</i> The dynamic viscosity of the testing oils at room temperature (25 °C). .....	75
<i>Figure 4-10.</i> Oil-water interfacial tension of the testing oils at room temperature (25 °C). .....	76
<i>Figure 4-11.</i> Images of oil-water two-phase flow at superficial oil velocity of 0.5 m/s and different water cuts as follows: (a) 4.9 %,( b) 6.9 %,( c) 10,0 %,( d) 12.9 %,( e) 15.6% and (f) 18.2 % . .....	78

<i>Figure 4-12.</i> Images of oil-water two-phase flow at superficial oil velocity of 1.0 m/s and different water cuts as follows: (a) 1.8 %, (b) 3.6%, (c) 6.9 %, (d) 11.5 %, (e) 12.9% and (f) 16.9 %.	79
<i>Figure 4-13.</i> Images of oil-water two-phase flow at superficial oil velocity of 1.5 m/s and different water cuts as follows: (a) 2.4 %, (b) 6.9%, (c) 10 %, (d) 12.9 %.	80
<i>Figure 4-14.</i> Image of oil-water two-phase flow at superficial oil velocity of 2.5 m/s and water cut of 7.5% showing fully dispersed flow.	81
<i>Figure 4-15.</i> Flow pattern map for LVT200 oil-water flow in 4" horizontal pipe.	81
<i>Figure 4-16.</i> Phase wetting map for LVT200 oil at different oil-water mixture velocities and water cuts in horizontal, 4" pipe flow.	83
<i>Figure 4-17.</i> Phase wetting map for C1 crude oil at different oil-water mixture velocities and water cuts in horizontal, 4" pipe flow.	89
<i>Figure 4-18.</i> Phase wetting map for C2 crude oil at different oil-water mixture velocities and water cuts in horizontal, 4" pipe flow.	91
<i>Figure 4-19.</i> Phase wetting map for C3 crude oil at different oil-water mixture velocities and water cuts in horizontal, 4" pipe flow.	95
<i>Figure 4-20.</i> Phase wetting map for C4 crude oil at different oil-water mixture velocities and water cuts in horizontal, 4" pipe flow.	97
<i>Figure 4-21.</i> Phase wetting map for C5 crude oil at different oil-water mixture velocities and water cuts in horizontal, 4" pipe flow.	100
<i>Figure 4-22.</i> Transition lines from intermittent wetting to stable oil wetting for LVT200 oil and five crude oils (C1 – C5) in horizontal pipe flows.	102
<i>Figure 4-23.</i> Transition lines from intermittent wetting to stable oil wetting for C1 crude oil in oil-water two-phase flow at horizontal and different upward inclination angles.	105
<i>Figure 4-24.</i> Transition lines from intermittent wetting to stable oil wetting for C1 crude oil in oil-water two-phase flow at horizontal and different downward inclination angles.	105
<i>Figure 4-25.</i> Transition lines from intermittent wetting to stable oil wetting for C2 crude oil in oil-water two-phase flow at horizontal and different upward inclination angles.	106
<i>Figure 4-26.</i> Transition lines from intermittent wetting to stable oil wetting for C2 crude oil in oil-water two-phase flow at horizontal and different downward inclination angles.	106
<i>Figure 4-27.</i> Transition lines from intermittent wetting to stable oil wetting for C3 crude oil in oil-water two-phase flow at horizontal and different upward inclination angles.	107
<i>Figure 4-28.</i> Transition lines from intermittent wetting to stable oil wetting for C3 crude oil in oil-water two-phase flow at horizontal and different downward inclination angles.	107
<i>Figure 4-29.</i> Transition lines from intermittent wetting to stable oil wetting for C4 crude oil in oil-water two-phase flow at horizontal and different upward inclination angles.	108
<i>Figure 4-30.</i> Transition lines from intermittent wetting to stable oil wetting for C4 crude oil in oil-water two-phase flow at horizontal and different downward inclination angles.	108
<i>Figure 4-31.</i> Transition lines from intermittent wetting to stable oil wetting for C5 crude oil in oil-water two-phase flow at horizontal and different upward inclination angles.	109

<i>Figure 4-32. Transition lines from intermittent wetting to stable oil wetting for C5 crude oil in oil-water two-phase flow at horizontal and different downward inclination angles.</i>	109
<i>Figure 4-33. Comparison of the experimental phase wetting transition line with model prediction (LVT200 oil in 4" horizontal flow loop).</i>	114
<i>Figure 4-34. Comparison of the experimental phase wetting transition line with model prediction (LVT200 oil with 5 ppm "quat" inhibitor in 4" horizontal flow loop) (Li, 2009).</i>	114
<i>Figure 4-35. Comparison of the experimental phase wetting transition line with model prediction (LVT200 oil with 1% myristic acid in 4" horizontal flow loop) (Ayello, 2010).</i>	115
<i>Figure 4-36. Comparison of the experimental phase wetting transition line with model prediction (C1 crude oil in 4" horizontal flow loop).</i>	115
<i>Figure 4-37. Comparison of the experimental phase wetting transition line with model prediction (C2 oil in 4" horizontal flow loop).</i>	116
<i>Figure 4-38. Comparison of the experimental phase wetting transition line with model prediction (C3 crude oil in 4" horizontal flow loop).</i>	116
<i>Figure 4-39. Comparison of the experimental phase wetting transition line with model prediction (C4 crude oil in 4" horizontal flow loop).</i>	117
<i>Figure 4-40. Comparison of the experimental phase wetting transition line with model prediction (C5 crude oil in 4" horizontal flow loop).</i>	117
<i>Figure 5-1. Sketch of a goniometer with optical imaging camera and backlight.</i>	121
<i>Figure 5-2. Photograph of the goniometer system with goniometer cell, backlight and a camera.</i>	121
<i>Figure 5-3. Teflon mount with a carbon steel test specimen mounted on it.</i>	122
<i>Figure 5-4. Glass cell set up for iron carbonate film formation.</i>	126
<i>Figure 5-5. SEM images of different magnifications for iron carbonate film covered surface.</i>	127
<i>Figure 5-6. Schematic of experimental setup for water-in-oil droplet contact angle with metal surface.</i>	129
<i>Figure 5-7. Schematic of experimental setup for oil-in-water droplet contact angle with metal surface.</i>	129
<i>Figure 5-8. Water-in-oil contact angle on different steel surfaces versus time (600s)...</i>	130
<i>Figure 5-9. Water droplets on the steel surface (surface roughness 1.5 <math>\mu\text{m}</math>) immersed in LVT200 oil at different time.</i>	131
<i>Figure 5-10. Equilibrium water-in-oil contact angles on different steel surfaces.</i>	132
<i>Figure 5-11. Typical images of water droplets on different steel surfaces in LVT200 oil.</i>	132
<i>Figure 5-12. Equilibrium oil-in-water contact angles beneath different steel surfaces for different oils.</i>	133
<i>Figure 5-13. Typical images of different oil droplets beneath 6 <math>\mu\text{m}</math> roughness steel surface in water.</i>	134
<i>Figure 5-14. Typical images of oil droplet (C1 crude oil) beneath different steel surfaces in water.</i>	134

<i>Figure 5-15.</i> Dynamic viscosity of oils at different temperatures.....	136
<i>Figure 5-16.</i> Oil-water interfacial tension of oils at different temperatures.....	136
<i>Figure 5-17.</i> Water-in-oil (LVT200) contact angles at different temperatures for 1.5 $\mu\text{m}$ surface.....	137
<i>Figure 5-18.</i> Water-in-oil (LVT200) contact angles at different temperatures for 6 $\mu\text{m}$ surface.....	138
<i>Figure 5-19.</i> Oil-in-water contact angles at different temperatures (Oil phase: LVT200). .....	139
<i>Figure 5-20.</i> Oil-in-water contact angles at different temperatures (Oil phase: C3 crude oil). .....	140
<i>Figure 5-21.</i> SEM images of mill scale covered steel surface. ....	142
<i>Figure 5-22.</i> SEM images of cross section of a mill scale covered steel surface.....	143
<i>Figure 5-23.</i> General chemical structures of the quaternary ammonium chloride (“quat”), R represents a hydrocarbon chain (Li, 2009). ....	144
<i>Figure 5-24.</i> Visual description of the procedure for water pre-wetted surface preparation for the test of the effect of steel surface. Blue color stands for water phase and green color stands for oil phase.....	148
<i>Figure 5-25.</i> Visual description of the procedure for oil pre-wetted surface preparation for the test of the effect of steel surface. Blue color stands for water phase and green color stands for oil phase.....	149
<i>Figure 5-26.</i> Process of water droplet wetting water pre-wetted surface. ....	150
<i>Figure 5-27.</i> Oil-in-water contact angle with different surfaces pre-wetted by LVT200 oil. ....	152
<i>Figure 5-28.</i> Typical images of oil droplet with different surfaces pre-wetted by LVT200 oil. ....	152
<i>Figure 5-29.</i> Process of the displacement of oil by water on the steel surface.....	153
<i>Figure 5-30.</i> Process of displacement of oil phase (LVT200) by water phase (1wt NaCl brine). ....	155
<i>Figure 5-31.</i> Process of displacement of oil phase (LVT200) by water phase (1wt% NaCl brine with 1 ppm “quat” inhibitor).....	155
<i>Figure 5-32.</i> Process of displacement of oil phase (LVT200) by water phase (1wt% NaCl brine with 5 ppm “quat” inhibitor).....	156
<i>Figure 5-33.</i> Process of displacement of oil phase (LVT200) by water phase (1wt% NaCl brine with 20 ppm “quat” inhibitor).....	156
<i>Figure 5-34.</i> Comparison of equilibrium oil-in-water contact angle of oil droplet underneath the steel surface pre-wetted by oil and the steel surface pre-wetted by water (Li, 2009) in 1wt% NaCl brine with different “quat” inhibitor concentrations.....	157
<i>Figure 5-35.</i> Process of displacement of oil phase (C1) by water phase (1wt% NaCl brine). ....	158
<i>Figure 5-36.</i> Process of displacement of oil phase (C2) by water phase (1wt% NaCl brine). ....	159
<i>Figure 5-37.</i> Images of steel specimen pre-wetted by C3 crude oil in 1wt% NaCl brine. .....	159

<i>Figure 5-38</i> Images of steel specimen pre-wetted by C4 crude oil in 1wt% NaCl brine. .....	160
<i>Figure 5-39.</i> Images of steel specimen pre-wetted by C5 crude oil in 1wt% NaCl brine. .....	160
<i>Figure 5-40.</i> Equilibrium oil-in-water contact angle of different oil droplets underneath the steel surface pre-wetted by different crude oils. ....	161
<i>Figure 6-1.</i> Schematic of horizontal rotating cylinder (HRC). ....	164
<i>Figure 6-2.</i> Schematic of steel surface wetted by water and oil phase. (a): Neutral surface, (b): Hydrophilic surface. ....	168
<i>Figure 6-3.</i> Potentiodynamic sweep showing the velocity effect on limiting current densities in HCl solution at pH 3, 1wt% NaCl, $P_{N_2}=1$ bar, $T=25$ °C and carbon steel C1018. ....	170
<i>Figure 6-4.</i> Comparison to the Eisenberg's correlation for a rotating cylinder for the verification of the validity of the electrochemical measurements using the HRC. ....	171
<i>Figure 6-5.</i> Corrosion rates with increasing velocity at different water fractions for 1.5 $\mu\text{m}$ roughness surface (corrosion rate calculated using whole surface area). ....	172
<i>Figure 6-6.</i> Corrosion rates with increasing velocity at different water fractions for 6.0 $\mu\text{m}$ roughness surface (corrosion rate calculated using whole surface area). ....	172
<i>Figure 6-7.</i> Corrosion rates with increasing velocity at different water fractions for 40 $\mu\text{m}$ roughness surface (corrosion rate calculated using whole surface area). ....	173
<i>Figure 6-8.</i> The value of $A_E/A_N$ at different water fractions for 1.5 $\mu\text{m}$ roughness surface. .....	174
<i>Figure 6-9.</i> The value of $A_E/A_N$ at different water fractions for 6.0 $\mu\text{m}$ roughness surface. .....	175
<i>Figure 6-10.</i> The value of $A_E/A_N$ at different water fractions for 40 $\mu\text{m}$ roughness surface. .....	175
<i>Figure 7-1.</i> Schematic representation of transition from stratified flow to water-in-oil dispersion flow. ....	178
<i>Figure 7-2.</i> Comparison of model prediction results with experimental results (LVT200 oil in 4" horizontal pipe flow, $\theta=73^\circ$ , $C_H=1$ , $C_W=30$ ). ....	183
<i>Figure 7-3.</i> Comparison of model prediction results with experimental results in 4" horizontal flow loop (C1 crude oil, $\theta=142^\circ$ , $C_H=1$ , $C_W=30$ ). ....	184
<i>Figure 7-4.</i> Comparison of model prediction results with experimental results in 4" horizontal flow loop (C2 crude oil, $\theta=157^\circ$ , $C_H=1$ , $C_W=30$ ). ....	184
<i>Figure 7-5.</i> Comparison of model prediction results with experimental results in 4" horizontal flow loop (C3 crude oil, $\theta=180^\circ$ , $C_H=1$ , $C_W=30$ ). ....	185
<i>Figure 7-6.</i> Comparison of model prediction results with experimental results in 4" horizontal flow loop (C4 crude oil, $\theta=180^\circ$ , $C_H=1$ , $C_W=30$ ). ....	185
<i>Figure 7-7.</i> Comparison of model prediction results with experimental results in 4" horizontal flow loop (C5 crude oil, $\theta=180^\circ$ , $C_H=1$ , $C_W=30$ ). ....	186

<i>Figure 7-8.</i> Comparison of model prediction results with experimental results in doughnut cell scaled up to 4” horizontal flow loop (LVT200 oil with 1ppm “quat”, $\theta = 75^\circ$ , $C_H = 1$ , $C_W = 30$ ) (Li, 2009).....	187
<i>Figure 7-9.</i> Comparison of model prediction results with experimental results in doughnut cell scaled up to 4” horizontal flow loop (LVT200 oil with 5ppm “quat”, $\theta = 103^\circ$ , $C_H = 1$ , $C_W = 30$ ) (Li, 2009).....	188
<i>Figure 7-10.</i> Comparison of model prediction results with experimental results in doughnut cell scaled up to 4” horizontal flow loop (LVT200 oil with 20ppm “quat”, $\theta = 143^\circ$ , $C_H = 1$ , $C_W = 30$ ) (Li, 2009).....	188
<i>Figure 7-11.</i> Comparison of model prediction results with experimental results in 4” horizontal flow loop (LVT200 oil with 5ppm “quat”, $\theta = 143^\circ$ , $C_H = 1$ , $C_W = 30$ ) (Li, 2009). .....	189
<i>Figure 7-12.</i> Comparison of model prediction results with experimental results in 4” horizontal flow loop (LVT200 oil with 0.01% myristic acid, $\theta = 180^\circ$ , $C_H = 1$ , $C_W = 30$ ) (Ayello, 2010). .....	190
<i>Figure 7-13.</i> Comparison of model prediction results with experimental results in 4” horizontal flow loop (LVT200 oil with 0.05% myristic acid, $\theta = 180^\circ$ , $C_H = 1$ , $C_W = 30$ ) (Ayello, 2010). .....	191

## CHAPTER 1 : INTRODUCTION

Corrosion is a natural phenomenon commonly defined as “the destructive result of a chemical reaction between a metal or metal alloy and its environment” (Jones,1996). Like natural disasters such as earthquakes, fires, floods, hurricanes etc., corrosion can cause enormous damage to the economy, human life and safety. The U.S. Federal Highway Administration (FHWA) released a study entitled “Corrosion Costs and Preventive Strategies in the United States” (Koch, Brongers, *et al.*, 2002), showing that the total annual economic loss directly caused by corrosion in the USA has been estimated to be \$276 billion, about 3.1% of the USA’s Gross Domestic Product (GDP) in 1998. In this study, corrosion was said to affect the USA economy in five major sector categories, namely infrastructure, production and manufacturing, utilities, transportation, and government, which were further broken down into twenty-six industry sectors. Among them, the direct corrosion cost to the oil and gas industry alone was estimated to be \$1.4 billion annually. Corrosion problems in the oil and gas industry have become a severe and visible concern to the industry, the government and the public. This was highlighted when the state of Alaska experienced an oil spill resulting from a pipeline failure in the Prudhoe Bay oil field, caused by internal corrosion (BBC, 2006). The estimated 267,000 gallon spill resulted in the operational shutdown of Prudhoe Bay oil field for many months.

Corrosion problems occur in every aspect of the oil and gas industry, from production and transportation to storage and refinery operations. One of the most common occurrences of corrosion is that of internal corrosion within transportation

pipelines. In multiphase well streams, there are many different corrosive species, such as untreated drilling mud, hydrogen sulfide ( $H_2S$ ), water and carbon dioxide ( $CO_2$ ) produced or injected for secondary recovery and acid used to reduce formation damage around the well or to remove scale (Brondel, Edwards, *et al.*,1994). Although corrosion-resistant alloys (CRAs) like 13Cr martensitic stainless steel or Alloy 316 stainless steel can be used to avoid or mitigate corrosion problems, they increase the capital cost of construction enormously. Therefore carbon steel is the only economically feasible selection for long-distance, large-diameter pipelines. Nyborg (2003) pointed out that internal corrosion in oil and gas wells and pipelines made from carbon steel is affected by many factors, including water chemistry, flow velocity, temperature,  $CO_2$  and  $H_2S$  content, phase wetting (water wetting or oil wetting) and the compositions and surface condition of the carbon steel itself.

Water plays a key role in the internal corrosion associated with wells and pipelines. In general, the probability of corrosion increases with increasing the fraction of the water phase. Whenever water comes into contact with the internal wall of a pipeline, which is known as “water wetting”, there is a potential for an internal corrosion of the pipeline. On the other hand, if the oil phase is intense enough to entrain all the water phase, the internal wall of the pipeline will be continuously wetted by the oil phase, known as “oil wetting”, and the risk of corrosion is very small.

Because it is almost impossible to prevent corrosion completely, it is very important for corrosion engineers to be able to predict and control the corrosion rate. The involvement of corrosion engineers is vital in corrosion control strategy and estimating

the useful life of the equipment. The subject of water wetting is an indispensable link towards the full understanding of internal corrosion in mild steel pipelines. In the past, no systematic, extensive experimental study has been performed on the relationship between water wetting and internal corrosion in oil-water two-phase flow, which is still a great challenge for researchers and corrosion engineers.

In order to understand and study the relationship between water wetting and carbon dioxide corrosion in oil-water two-phase flow, a comprehensive long-term experimental program sponsored by Saudi Aramco was initiated at the Institute for Corrosion and Multiphase Technology (ICMT) at Ohio University in 2004. Six types of oil: one model oil and five crude oils, were used in conjunction with 1 wt% NaCl brine as working fluids. Five different techniques – visual recording, wall conductance probes, wall sampling, electrical resistance (ER) probe and iron ( $\text{Fe}^{2+}$ ) concentration measurements, were successfully applied during the investigation. Comprehensive phase wetting maps for different oils were built for different flow conditions in oil-water two-phase flow. Based on experimental results, a mechanistic model was created for the prediction of water wetting and entrainment in horizontal and inclined oil-water pipe flows. This model considers the effects of flow velocity, oil and water properties (density, viscosity and interfacial tension), pipe diameter, pipe inclination, and water cut. Good agreement was achieved between experimental results and the predictions only for the model oil. However, the effects of steel surface state, corrosion inhibitive additives and crude oil chemistry were not included in the original model due to lack of understanding and reliable experimental data. To bridge that gap, a new project named the Water Wetting Joint Industry Project (WW JIP) was initiated in 2006, financed by BP, ConocoPhillips, Eni,

ExxonMobil, Petrobras, Saudi Aramco, Shell and Total. The WW JIP included five research topics: effects of steel surface state, corrosion inhibitors, crude oil chemistry, asphaltenes and wax on water wetting and carbon dioxide corrosion in oil-water two-phase flow. These were assigned individually to three PhD students and two master's degree students.

## CHAPTER 2 : RESEARCH OBJECTIVES

The present dissertation focuses on investigating the effects of steel surface state on water wetting and CO<sub>2</sub> corrosion in oil-water two-phase flows. The main research objectives are:

- Experimentally investigate the effects of different surface states (bare metal surfaces with different roughness measures, surfaces with corrosion film and surfaces pre-wetted by oil or water) on surface wettability in oil-water two-phase system in a goniometer system.
- Study the effect of dynamic wetting on CO<sub>2</sub> corrosion in a horizontal rotating cylinder (HRC) system.
- Experimentally investigate flow patterns, phase wetting regimes and CO<sub>2</sub> corrosion in large diameter, horizontal and inclined oil-water two-phase flow using LVT200 model oil and crude oils.
- Modify and update the water wetting model by incorporating the effects of surface conditions, additive inhibitors and chemicals.

It should be noted that the work and the results related to oil-water two-phase flow in large scale flow loop tests were shared between three PhD students: the present author, Dr. Chong Li and Dr. Francois Ayello. All the work related to large scale flow loop tests constitutes the collaborative work of the three students named above and the former project leader, Dr. Jiyong Cai. Portions of the work discussed in the present dissertation have been already been published by the present author in the following conference papers:

- Tang, X., Richter, S., & Nešić, S., “Study of wettability of different mild steel surfaces”, 17th International Corrosion Congress, Paper 3109, Las Vegas, NV, 2009.
- Ayello, F., Li, C., & Tang, X., “Determination of phase wetting in oil-water pipe flows”, NACE CORROSION/08, Paper No. 08566, New Orleans, LA, 2008.
- Tang, X., Li, C., Ayello, F., Cai, J., & Nešić, S., “Effect of oil type on phase wetting transition and corrosion in oil-water flow”, NACE CORROSION/07, Paper No. 07170, Nashville, TN, 2007.
- Li, C., Tang, X., Ayello, F., Cai, J., & Nešić, S., “Experimental Study on Water Wetting and CO<sub>2</sub> Corrosion in Oil-Water Two-Phase Flow”, NACE CORROSION/06, Paper No. 06595, San Diego, CA, 2006.
- Tang, X., Ayello, F., Li, C., Cai, J., & Nešić, S., “Water wetting and corrosion in horizontal and inclined flow of oil - water mixture”, 11<sup>th</sup> Middle East conference, Manama, Bahrain, 2006.

## CHAPTER 3 : LITERATURE REVIEW

The current chapter contains a literature survey that focuses on the following broad research areas which were foundations for the development of the current project: surface roughness and microtopography, wetting phenomena, oil-water two-phase flow and carbon dioxide corrosion.

### 3.1 Surface roughness and microtopography

Surface roughness is the measure of fine irregularities of surface texture; roughness is often the result of processes involved in manufacturing, i.e. cutting, turning, grinding or polishing (Whitehouse, 2003). The importance of characterizing a rough surface has been widely recognized in science and industry (Thomas, 1999). Surface roughness evaluation plays a very important role in applications involving friction, lubrication, wear, heat and electric current conduction. Surface roughness is also a topic of interest in fluid dynamics, since the roughness of a pipeline surface affects the friction factor, which is a very important parameter in calculating head loss or pressure drop in fluid flow.

#### 3.1.1 Surface roughness parameters

Surface parameters can generally be divided into three categories based on their functions: surface roughness or amplitude parameters, spacing parameters or lateral surface parameters and hybrid surface parameters (Gadelmawla, Koura, *et al.*, 2002; Mattsson, 1997). Surface roughness or amplitude parameters measure the surface height variations and are the most important parameters for surface characterization. Spacing

parameters assess the characteristic features of the lateral structure of the surface texture, including the mean spacing of adjacent local peaks,  $S$ , and the mean spacing at the mean line,  $S_m$  (Mattsson, 1997). Hybrid parameters are parameters that combine the information of amplitude and lateral spacing. Gadelmawla, Koura, *et al.* (2002) “illustrated the definitions and mathematical formulae for 59 roughness parameters”. According to the usage of these parameters and their relevance to this dissertation, only amplitude parameters are detailed in the sections that follow.

### 3.1.1.1 $R_a$ – Average roughness

Average roughness,  $R_a$ , is also known as the arithmetic average height parameter, the center line average (CLA) or the arithmetical mean deviation of the profile. It is the most universally recognized roughness parameter in the engineering industry (Gadelmawla, Koura, *et al.*, 2002). The average roughness,  $R_a$ , is defined as the area between the roughness profile and its mean line, or the average absolute deviation of roughness irregularities from the mean line over the evaluation length, as shown in *Figure 3-1*. The mathematical definition of average roughness,  $R_a$ , can be expressed as

$$R_a = \frac{1}{l_m} \int_0^{l_m} |y(x)| dx \quad (3.1)$$

In Equation (3.1),  $l_m$  is the evaluation length and  $y(x)$  is the height deviation of the profile from the mean line.

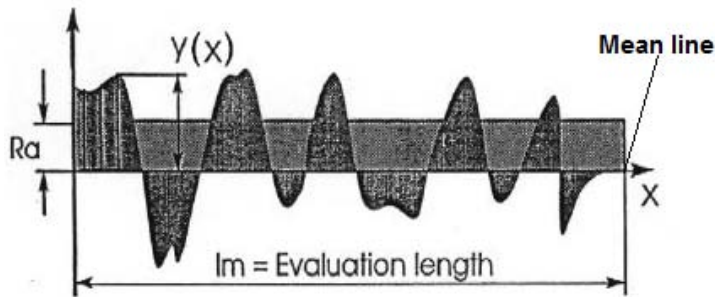


Figure 3-1. Average roughness,  $R_a$  (Farshad, Rieke, *et al.*, 2001).

### 3.1.1.2 $R_q$ – Root mean square roughness

The root mean square (RMS) roughness of a surface is the standard deviation of the surface heights relative to the mean line of the profile, as shown in *Figure 3-2*. It is more sensitive than average roughness,  $R_a$ , to large height deviations (Mattsson, 1997).

The mathematical definition of the RMS roughness,  $R_q$ , can be expressed as

$$R_q = \sqrt{\frac{1}{l_m} \int_0^{l_m} |y^2(x)| dx} \quad (3.2)$$

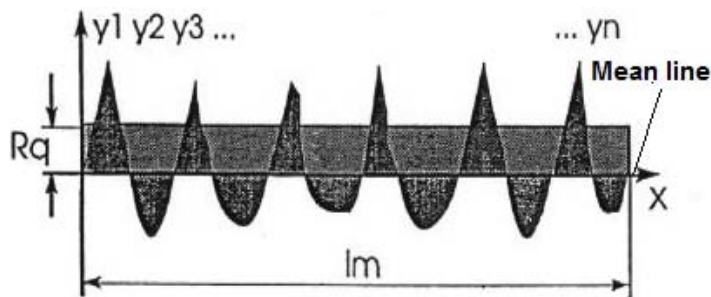
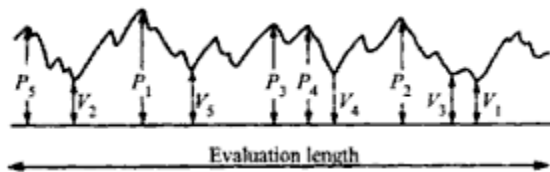


Figure 3-2. Root mean square roughness,  $R_q$  (Farshad, Rieke, *et al.*, 2001).

### 3.1.1.3 $R_z$ – Mean peak-to-valley height or ten-point height

Mean peak-to-valley height or ten-point height,  $R_z$ , is defined as the average of the height difference between the five highest peaks and the five lowest valleys along the evaluation length of the profile, as shown in *Figure 3-3*. The mathematical formula for  $R_z$  is

$$R_z = \frac{\sum_{i=1}^5 P_i - \sum_{i=1}^5 V_i}{5} \quad (3.3)$$



*Figure 3-3.* Mean peak-to-valley height or ten-point height,  $R_z$  (Whitehouse, 2003).

There are many other roughness parameters, such as maximum height of peaks,  $R_p$ , maximum depth of valleys,  $R_v$ , mean height of peaks,  $R_{pm}$ , mean depth of valley,  $R_{vm}$ , mean of maximum peak to valley height,  $R_{im}$ , etc., but these are not employed in the current study.

### *3.1.2 Techniques for surface roughness measurement*

Mattsson (1997) pointed out that the most common technique for surface profiling is a mechanical stylus method, using a pick-up head across the surface in order to detect height variations and convert it to electrical signals. The stylus instrument includes these important components: a pick-up head driven by a gearbox, a stylus traversing across the

surface, a transducer recording the signal, an amplifier and a device for recording the amplified signal. Although the mechanical stylus is the most common standard technique used in measurement rooms at production plants, its accuracy is influenced by several factors: stylus size, stylus road, lateral deflection of the stylus and the possibility of the stylus losing contact with the surface (Thomas, 1999).

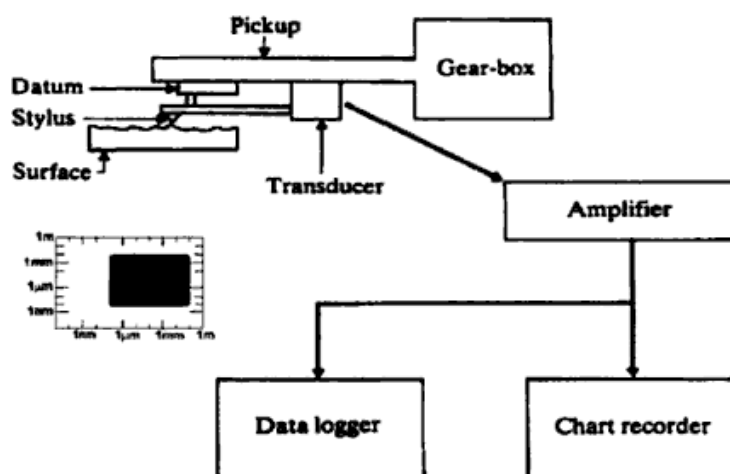


*Figure 3-4.* Schematic of a stylus instrument for surface roughness measurement (Thomas, 1999)

In contrast with conventional measurement instruments like the stylus method, microscope techniques, including optical, electron and scanning probe types, are dominant in research laboratories. As one type of optical microscope, interferometric microscopes record the height variations as fringes in an image plane, similar to the contour lines of equal height in a topographic map (Mattsson, 1997). Another type of optical microscope is “a scanning system with a small depth-of-focus imaging system for determining the height distribution of a surface” (Mattsson, 1997). InfiniteFocus<sup>®</sup>,

manufactured by ALICONA (Alicona Imaging GmbH, Teslastraße 8, 8074 Grambach/Graz, Austria), is an example of this type optical microscope.

As a typical electron probe, the scanning electron microscope (SEM) probes the surface using an electron beam. The back-scattered electrons interact with the sample's atoms, generating signals which can be used to produce the sample's surface topography. There are some drawbacks to using SEM in surface roughness measurement, however. First, while it is practical for rough surfaces with high slope angles, it is not feasible for a smooth surface (Mattsson, 1997). Second, it requires the tested specimen to be conductive.

The scanning tunneling microscope (STM) and the atomic force microscope (AFM) are two members of a growing family of scanning probe microscopes (SPM). The STM uses the tunneling of electrons from a sharp tip, which scans very close to the surface but is not physically in contact with it. The tunneling current of electrons can describe the topography of the surface. The AFM uses a cantilever with a sharp tip to scan the surface without touching it, and this detects the interatomic forces between the tip and the sample. Unlike the STM, the AFM does not require the specimens to be conductive and in high vacuum. There are many other scanning microscopes - laser force microscope (LFM), magnetic force microscope (MFM), electrostatic force microscope (EFM), scanning thermal microscope (SThM), scanning ion conductive microscope (SICM), etc. - which will not be covered in this review.

### 3.2 Wetting phenomena

Wetting, in general, is the interaction of a liquid phase with a solid phase when surrounded by a gas phase or a second liquid phase. The wetting phenomenon is pertinent to numerous industrial areas and to our daily life; examples include the spreading of a liquid over a surface (paints, ink), the penetration of a liquid into a porous medium, or the wetting of the eye. Understanding the wetting phenomenon can help to characterize surfaces and the interaction between liquids and solids.

#### 3.2.1 Surface tension and interfacial tension

The molecules of a liquid attract each other. *Figure 3-5* shows a molecule (noted as molecule A) in the liquid bulk and a molecule (noted as molecule B) in the liquid/gas or liquid/vapor interface. The molecule A in the liquid bulk is attracted by the surrounding molecules in all directions, leading to a zero net force. By contrast, the molecule B in the interface experiences a net attractive force pointing toward the liquid interior, because the attractive force exerted on the upper part of the molecule B by gas or vapor molecules is much smaller than the attractive force exerted on the lower part by liquid molecules. Thus the energy of molecule B must be greater than that of molecule of A.

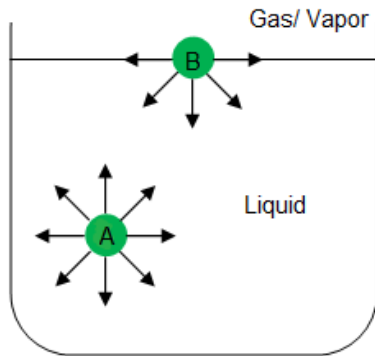


*Figure 3-5.* Molecules in the liquid bulk and the interface (de Gennes, Brochard-Wyart, *et al.*, 2003).

Surface tension is the measure of excess free energy per unit of surface area (de Gennes, Brochard-Wyart, *et al.*, 2003). Surface tension is also thought of as a force per unit length. In order to understand the definition of surface tension, consider a soap film on a C-shape wire with a movable slider (*Figure 3-6*). The work done in making the film bigger (extending the film area by  $dA$ ) is:

$$dW = F \cdot dx = 2\sigma \cdot ldx = 2\sigma \cdot dA \quad (3.4)$$

where the factor 2 reflects the presence of two interfaces on both sides of the soap film and  $\sigma$  is the surface tension, expressed as a force per unit length, with common units being mN/m and dyne/cm, which have the same numerical value.

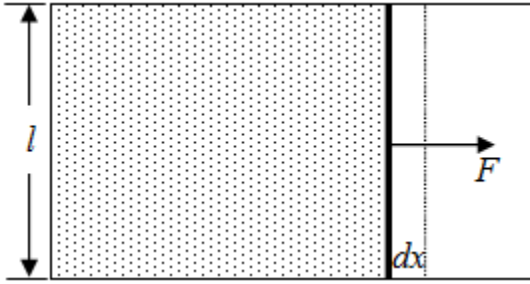


Figure 3-6. A soap film stretched by a wire slider (Adamson & Gast, 1997).

Miller & Neogi (1985) pointed out that surface tension is a term typically used when the liquid surface is in contact with gas or vapor. If the interface is between two liquids or one liquid and one solid, it is called “interfacial tension”. There are many techniques available for measuring surface tension or interfacial tension, and these are described in the book of Adamson & Gast (1997). Drelich, Fang, *et al.* (2002) reviewed the most common techniques used to measure the interfacial tension in fluid-fluid systems, as shown in *Figure 3-7*. Only the du Noüy ring method and the Wilhelmy plate technique will be discussed in detail in this dissertation. The du Noüy ring method uses a microbalance to measure the force required to pull a wire ring or loop of wire off of the interface, as illustrated in *Figure 3-8*. The measured force  $F$  can be used to calculate the interfacial tension with the following equation (Adamson & Gast, 1997):

$$\sigma = \frac{F - G_{ring}}{p \cos \theta} C \quad (3.5)$$

In Equation (3.5),  $p$  is the perimeter of the three-phase contact line and equals twice the circumference of the ring.  $\theta$  is the contact angle and  $G_{ring}$  is the gravity of the ring.  $C$  is a

correction factor that depends on the dimension of the ring, with the meniscus volume detached. In order to eliminate the effect of contact angle  $\theta$ , platinum is often used as the material for the ring, since it has a high surface energy and is wettable by all usual liquids ( $\theta \approx 0^\circ$ ) (de Gennes, Brochard-Wyart, *et al.*, 2003). The Wilhelmy plate technique can be used to measure both interfacial tension and contact angle, and will be discussed in the following section.

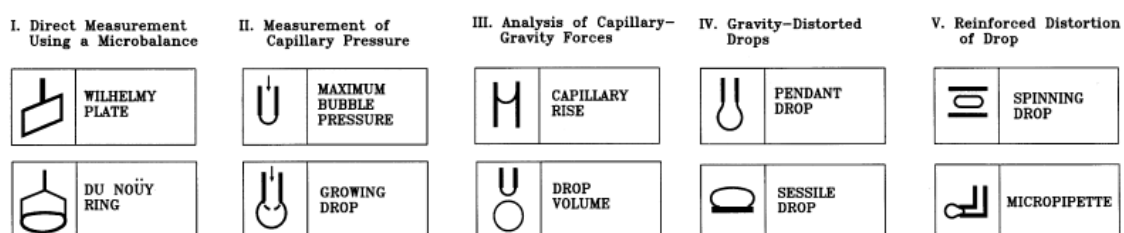


Figure 3-7. Classification of techniques for interfacial tension measurements (Drelich, Fang, *et al.*, 2002).

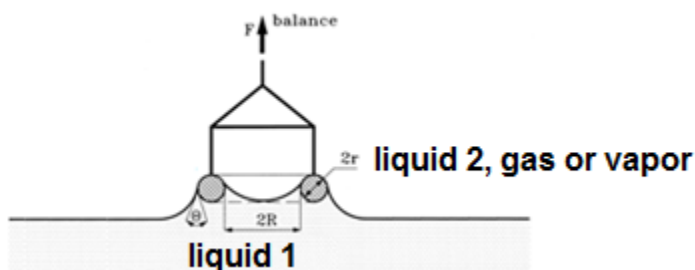


Figure 3-8. Du Noüy ring method (Drelich, Fang, *et al.*, 2002).

### 3.2.2 Wettability and contact angle

Wettability is most often described by the geometry of a sessile or resting drop (Figure 3-9). Contact angle ( $\theta$ ) can be used to measure wettability. When water is one of

the liquids, a low contact angle indicates hydrophilia and a high contact angle indicates hydrophobia.

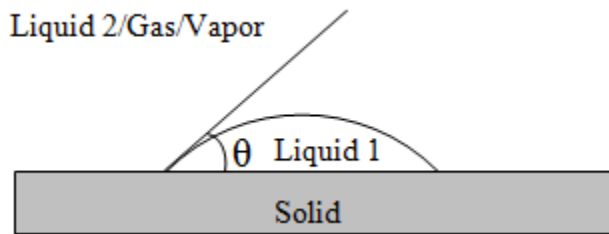


Figure 3-9. Sessile drop on a solid surface, surrounded by either another liquid, gas or vapor (Berg, 1993).

The contact angle between two phases is determined by the molecular attractive forces between the phases. At the interface, the molecules of different phases attract each other, resulting in adhesive forces. Meanwhile, inside the same phase the action of like molecules results in cohesive forces. The result of the competition of adhesive forces and cohesive forces is the interfacial tension, or interfacial energy  $\sigma_{ij}$ , which can be defined thermodynamically (Berg, 1993):

$$\sigma_{ij} = \left( \frac{\partial G}{\partial A_{ij}} \right)_{T,P,n} \quad (3.6)$$

where  $\sigma_{ij}$  is interfacial energy at the interface between the phase  $i$  and  $j$ ,  $G$  the Gibbs free energy of the  $i/j$  interface,  $A_{ij}$  the surface area between phases  $i$  and  $j$ ,  $T$  absolute temperature,  $P$  the pressure and  $n$  the number of surface excess moles.

The different interfacial tensions reach equilibrium when the free energy of the system is at a minimum. This produces the shape of the liquid interface, which is primarily defined by the contact angle (Schmitt & Stradmann, 1998). Young (1805) first related the contact angle to the surface energy of the three interfaces meeting at the contact line, (*Figure 3-10*) using Equation (3.7).

$$\sigma_{sg} - \sigma_{sl} = \sigma_{gl} \cos \theta_E \quad (3.7)$$

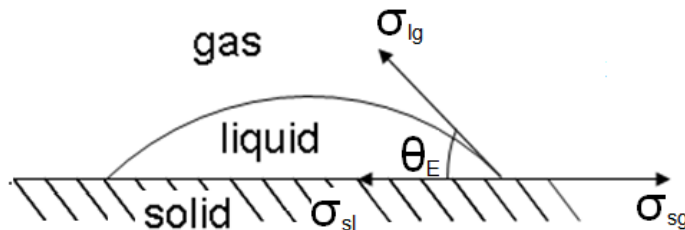


*Figure 3-10.* Determination of equilibrium contact angle  $\theta_E$  from the interfacial forces of gas, liquid and solid.

However, non-ideal conditions due to environmental, chemical heterogeneity and surface roughness effects lead to deviations from this relationship, which is called contact angle hysteresis. Static contact angle is the contact angle when “the speed of the contact line in the direction of its outward normal and along the substrate surface is zero in the frame of reference of the solid” (Berg, 1993). On the other hand, a dynamic contact angle is measured when the three-phase contact line is in motion.

The static contact angle can be measured using the sessile drop method, which is an optical contact angle technique used to determine the wettability of a liquid phase on a solid surface. The angle between the substrate surface and the tangent at the

interface between the droplet and other liquid or vapor phase (*Figure 3-10*) is measured. Either a microscope with a goniometer is used to observe and measure the contact angle, or a camera is used to capture the image of the droplet contacting the solid surface. Specific software is then used to analyze the image and calculate the contact angle.

The dynamic contact angles can be either advancing contact angle or receding contact angle. The advancing angle is the angle measured when liquid is added to the droplet just as the contact line starts to move. Conversely, the receding angle is the angle measured when liquid is removed from the droplet just as the contact line starts to move (Berg, 1993). Berg (1993) stated that “the difference between the advancing and receding contact angles is called contact angle hysteresis”. A common technique to measure dynamic contact angles is the Wilhelmy plate technique.

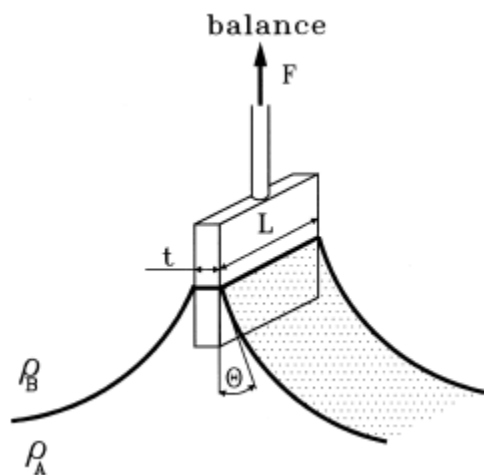


*Figure 3-11*. Schematic of the Wilhelmy plate method (Drelich, Fang, *et al.*, 2002).

In the Wilhelmy technique, a vertical thin plate is immersed into and then withdrawn from the liquid phase. The force ( $F$ ), vertically acting on the plate by the

liquid meniscus, is measured with a microbalance, as shown in *Figure 3-11*. The dynamic contact angles can be calculated using Equation (3.8):

$$P \cdot \sigma \cos \theta = F + G - \text{boyancy} \quad (3.8)$$

where  $P=2L+2t$  is the perimeter of the three-phase contact line,  $L$  is the length of the plate,  $t$  is the thickness of the plate,  $G$  is the weight of probe and  $\sigma$  is the liquid surface tension. As mentioned in the previous section, the Wilhelmy plate technique can also be used to measure surface tension when eliminating the contact angle  $\theta$  in Equation (3.8), which can be achieved by using platinum as the plate material. The high surface energy of platinum renders it perfectly wetted ( $\theta \approx 0^\circ$ ) by most liquids.

### 3.3 Oil-water two-phase flow

Oil-water two-phase flow is a very common occurrence in the oil and gas industry, and can be seen everywhere from the wellbores to the final stage of separation. Indigenous water often found in the reservoir is termed produced water and can be mixed with water injected into the reservoir to enhance oil recovery. The water may be difficult to separate from the oil, especially when the densities of oil and water approach each other. Corrosive species such as carbon dioxide ( $\text{CO}_2$ ) and hydrogen sulfide ( $\text{H}_2\text{S}$ ) dissolved in the water phase can cause serious internal corrosion problems within the carbon steel pipelines. All of these problems result in a loss of production efficiency due to higher capital and operational expenditures. Therefore, it is very important to

understand the behavior and characteristics of oil-water two-phase flow when designing and operating wells, production facilities and transportation pipelines.

In the past decades, a number of research initiatives have focused on oil-water two-phase flow identifying and predicting different flow patterns. The following sections will review some of the main research achievements in field of oil-water two-phase flow.

### *3.3.1 Flow pattern identification and classification*

Flow pattern or flow regime is a term that refers to the geometric distribution or topology of the components within multiphase flow (Brennen, 2005). For oil-water two-phase flow, a substantial number of investigations have been conducted to determine the dependence of different flow patterns on flow rates, water volume fraction (water cut) and fluid properties such as density, viscosity, and surface tension. The results are typically displayed as a flow pattern map, which indicates different flow patterns depending on fluid flow rates (Brennen, 2005).

Russell, Hodgson, *et al.* (1959) examined oil-water two-phase flow in a horizontal, smooth 2 cm I.D. pipe with white mineral oil (834 kg/m<sup>3</sup> of density and 18 cP of viscosity at 25 °C), water over a range of water cut from 9% to 90% and superficial water velocity from 0.04 m/s to 1.08 m/s. Three different flow patterns were observed: bubbles, stratified and mixed flow.

Charles, Govier, *et al.* (1961) conducted experiments using the same density oil-water mixtures with oils of three different viscosities in a 1” horizontal pipe. Four different flow patterns were observed and defined as: water droplets in oil, concentric water in oil flow in the core, oil slugs in water and oil bubbles in water.

Cox (1985) conducted oil-water flow experiments with a 2" I.D. transparent plastic pipe at different inclination angles ( $0^\circ$ ,  $-15^\circ$  and  $-30^\circ$  to horizontal) using a wide range of oil and water flow rates. Different flow patterns were observed and defined for different angles of inclinations. Stratified smooth (SS) flow only occurred in horizontal flow. Stratified wavy with churning (SWC) flow was observed in downhill flow at  $-15^\circ$  and  $-30^\circ$  inclination. Stratified wavy (SW), stratified bubble (SB) and massive bubble (MB) flow occurred in all pipe inclinations.

Valle & Kvandal (1995) studied stratified oil-water flow experimentally in a 37.5 mm I.D. glass pipe using a crude oil with  $794 \text{ kg/m}^3$  density and 2.30 cP viscosity and 1wt% NaCl brine as working fluids. Five flow patterns were identified visually and grouped as follows: stratified smooth (SS), stratified wavy (SW), stratified wavy with entrained droplets (SWE), stratified wavy flow with highly dispersed water zone and moderate dispersed oil zone (SWWD) and stratified wavy flow with highly dispersed oil zone and moderate dispersed water zone (SWOD).

Trallero, Sarica, *et al.* (1997) experimentally and theoretically studied oil-water flow pattern transitions in a 15.54 m long, 5.013 cm I.D. horizontal pipe. Mineral oil with a density of  $884 \pm 3 \text{ kg/m}^3$  and viscosity of  $28.8 \pm 5.2 \text{ cP}$  and water were the working fluids. Six flow patterns were identified and classified as shown in *Figure 3-12*. Stratified flow (ST) and stratified flow with mixing at the interface (ST & MI) were categorized into segregated flow. For dispersed flow when the water phase was dominant, dispersion of oil in water and water (Do/w & w) and oil in water emulsion occurred. On the other hand,

when oil phase was dominant, dispersion of water in oil and oil in water (Dw/o & Do/w) and water in oil emulsion (w/o) existed.

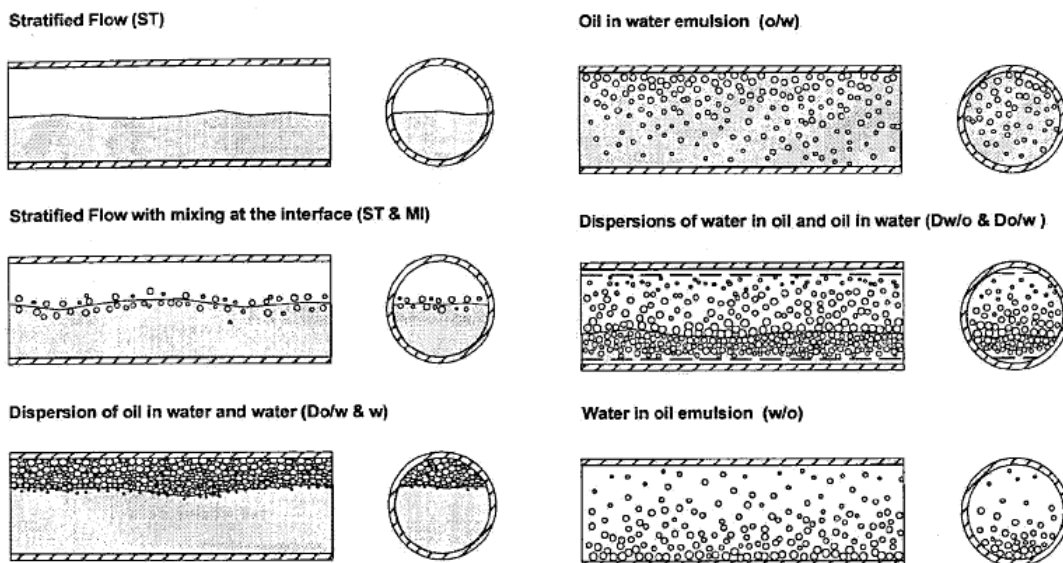


Figure 3-12. Sketches of flow patterns in horizontal oil-water flow (Trallero, Sarica, *et al.*,1997).

Vedapuri, Bessette, *et al.* (1997) studied the influence of inclination, oil viscosity and mixture velocity on the flow pattern and holdup of water in oil-water flow in an 18 m long, 10 cm diameter plexiglass pipeline with oil (viscosity 2 cP and 90 cP) and ASTM standard seawater as working fluids. Three different flow patterns - semi-segregated, semi-mixed and semi-dispersed flow - were observed.

Angeli & Hewitt (1998, 2000) investigated the pressure gradient and the flow structure of the concurrent flow of oil (1.6 cP viscosity and 801 kg/m<sup>3</sup> density) and water in two 1" nominal bore horizontal test sections made from stainless steel and acrylic resin, respectively. Two techniques, high speed video recording and high frequency

impedance probe, were deployed to determine the flow patterns. Four different flow patterns, including stratified wavy flow pattern (SW), three layer flow pattern (3L), stratified mixed flow pattern (SM) and fully dispersed or mixed flow pattern (M), were identified over a range of conditions with mixture velocity ranging from 0.2 to 3.9 m/s and input water volume fractions from 6% to 86%. The authors reported that pressure gradients were higher in the steel pipe than in the acrylic tube for the same operational conditions. Furthermore, the flow pattern and phase distribution between the acrylic and the stainless steel tubes were substantially different. The authors speculated that the difference was attributed to the effect of the properties (roughness and wettability) of the different pipe walls.

Fairuzov, Arenas-Medina, *et al.* (2000) conducted an investigation of flow pattern transitions in a 16" I.D. schedule 80 pipeline conveying light crude oil and fresh water. The transversal water fraction profile was measured using a multi-point sampling probe (MPSP). Based on the analysis of measured water volume fraction profiles, two major categories of flow patterns - stratified flow and dispersed flow - were identified.

Oddie, Shi, *et al.* (2003) conducted water-gas(nitrogen), oil(kerosene)-water and oil(kerosene)-water-gas(nitrogen) multiphase flows experiments in steady state and transient state in a transparent 11 m long, 15 cm I.D inclinable pipe. Different flow patterns maps were constructed for different flow conditions. For oil-water two-phase flow, six flow patterns (segregated, semi-segregated, semi-mixed, mixed, dispersed, and homogeneous flow), identified according the definition of Oglesby (1979), were observed.

Rodriguez & Oliemans (2006) studied oil-water flow in a 15 m long, 8.28 cm I.D., inclinable steel pipe. Flow patterns of flowing mineral oil (7.5 cP viscosity and 830 kg/m<sup>3</sup> density) and brine (0.8 cP viscosity and 1060 kg/m<sup>3</sup> density) were identified via observation of video recordings. The flow patterns observed were in agreement with the flow pattern classification proposed by Trallero, Sarica, *et al.* (1997), with the exception of the stratified wavy (SW) flow pattern newly found in downward and upward flow.

The studies reviewed above were conducted with different test liquids, different pipe diameters ranging from 0.8 inch to 16 inches, different pipe materials (steel, perspex, plexiglass, acrylic, PVC etc.) and different measurement techniques (visual observation, differential pressure transducer, conductance probes, impedance probes, etc.). Although diverse flow pattern names were reported by different authors, the flow patterns observed can be classified into two basic types: stratified flow with either smooth or wavy interface, and dispersed flow.

### 3.3.2 Flow pattern transition prediction

Although experimental investigations for oil-water two-phase flow have been extensively conducted by many researchers as reviewed in the above section, the modeling of the flow pattern transition attempts are much fewer. However, there are some correlations for predicting pressure gradient and water holdup, (Charles & Lilleleht, 1966; Arirachakaran, Oglesby, *et al.*, 1989; Vedapuri, Bessette, *et al.*, 1997; Shi, 2001; Al-Wahaibi & Angeli, 2009), and water layer thickness (Kurban, Angeli, *et al.*, 1995;

Vedapuri, Bessette, *et al.*, 1997) in the oil-water flow. The details of these correlations are beyond the topic of this dissertation and will not be expatiated in the review.

In oil-water flow, the density differential between two fluids is relatively low compared to gas-liquid two-phase flow. Therefore, the effect of gravity on flow pattern in oil-water system is not as important as it is in gas-liquid system. Due to these differences, the gas-liquid flow pattern prediction models (Taitel & Dukler, 1976; Dvora Barnea, 1987; Chen, Cai, *et al.*, 1997) cannot be readily employed in oil-water two-phase flow.

Brauner & Moalem Maron (1992a) first modeled the flow pattern transitions in two-phase liquid-liquid flow in horizontal pipes. The transitional criterion of the departure from a steady stratified flow was developed from “a linear stability analysis and well-posedness on the transient formulation of the two-fluid model” (Brauner & Moalem Maron, 1992b). The authors pointed out that the departure from a stratified pattern cannot be predicted by “a single stability criterion, but rather in terms of a “buffer” transitional zone”, which is formed between “two transition lines, namely the zero neutral stability (ZNS) line and the zero real characteristics (ZRC) line” (Brauner & Moalem Maron, 1992b). As for the model of the transition to fully dispersed flow, a mechanistic model was used and will be detailed in the next section of this review. The data available to the authors at that time limited any further extension and validation of the proposed models.

Trallero, Sarica, *et al.* (1997) presented a model of the oil-water flow pattern transition using a two-fluid model based on the Kelvin-Helmholtz stability analysis of the interface for oil-water flow and a force balance between gravity and turbulent

fluctuations normal to the main flow direction. The model performed very well when compared with published experimental data.

Fairuzov (2000) proposed a two-fluid model in oil-water two-phase system in pipeline “based on two transient continuity equations and a combined momentum equation in a quasi-steady form”. The transition criterion from segregated flow to dispersed flow was based on the well-posedness analysis by Brauner & Moalem Maron (1992b). The model has been successfully used to simulate the transport of corrosion inhibitor in oil-water pipeline flow.

Al-Wahaibi and Angeli (2007) developed a model to predict the transition from stable stratified flow to unstable stratified flow. When the superficial oil and water velocities are low, stratified flow prevails. At increased flow rates, interfacial waves appear and become more disturbed. The model uses Kelvin-Helmholtz instability analysis theoretically to predict the critical amplitude for the onset of instability of the wave in stratified flow at a certain wavelength. In order to predict the transition to dispersed flow, Al-Wahaibi, Smith, *et al.* (2007) proposed a drop formation model based on the force balance on the wave. It is assumed that the wave will break to form drops when the drag force originating from the relative movement between the oil and water phases exceeds the counteracting surface tension force.

### *3.3.3 Water wetting model*

In oil-water two-phase flow in pipeline systems, water and oil are transported simultaneously. Different flow regimes, which involve different distributions of water

and oil phases in the cross-section of the pipeline, can be found at different flow rates, as shown in *Figure 3-13*. At very low flow rates, the complete separation of water and oil phases occurs. The oil phase flows on the top and water on the bottom of the pipeline with an undisturbed oil-water interface between them. The water and oil phases are fully stratified in this flow regime. With increasing flow rate, the undisturbed oil-water interface is altered and waves are formed between the continuous water and oil phases. Some water droplets migrate to the oil phase and some oil droplets migrate to the water phase. The amplitude of the waves and the amount of water droplets and oil droplets depend on the flow rate as well as the ratio between the water phase and the oil phase. In special cases involving low water cut and oil-water flow rate, the water phase will be lifted up and entrained by the oil phase to form a water-in-oil dispersion flow. In this case, no water contacts the pipe wall and a zero corrosion rate can be expected. On the other hand, at higher water cut and sufficiently high flow rate, the oil phase will be broken into oil droplets and entrained by the water phase to form an oil-in-water dispersion flow.

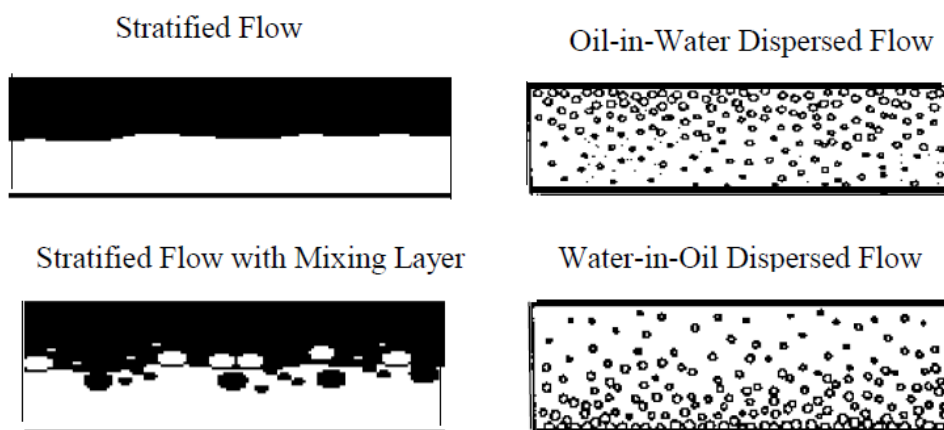


*Figure 3-13*. Flow patterns in oil-water horizontal flows (Cai, Nestic, & de Waard, 2004)

In order to properly predict the corrosion rate in pipelines, it is very important to know which liquid phase (water or oil) is in contact with the pipe wall and at what point all water phase will be entrained by the oil phase so as to get a zero corrosion rate within the pipeline. Nestic, Wang, *et al.* (2004) and Cai, Nestic, & de Waard (2004) proposed a new approach for predicting water-in-oil fully dispersed flow on the basis of the extension and modification of the work by Brauner (2001) and Barnea (1987). The effects of flow velocity, oil and water properties (density, viscosity and interfacial tension), pipe diameter, pipe inclination, and water cut on the critical oil velocity required for full water entrainment are considered in the model (Nestic, Wang, *et al.*, 2004 and Cai, Nestic, & de Waard, 2004). This model is incorporated as a water wetting model or module in the mechanistic CO<sub>2</sub> corrosion prediction software package MULTICORP, released by the Institute for the Corrosion and Multiphase Technology at Ohio University.

In the original Brauner (2001) model, a unified approach was proposed for the prediction of dispersed flow pattern in gas-liquid and liquid-liquid systems. A criterion for transition to dispersed flow based on a revised and extended Hinze (1955) model was developed. Two physical properties: maximum drop diameter ( $d_{max}$ ), related to droplet breakup and coalescence and critical drop diameter ( $d_{crit}$ ), related to drop migration and deformation, were calculated and compared in order to determine whether the transition to dispersed flow pattern takes place.

### 3.3.3.1 Maximum drop diameter $d_{max}$

Hinze (1955) analyzed the controlling forces for the splitting or breakup of a droplet in turbulent flow. The author stipulated that three forces: dynamic pressures, viscous shear and surface tension force, control the breakup of the droplet. Hinze (1955) pointed out that for not too small values of Reynolds number, the spatial regions of viscous flow are too small compared with the size of the largest drops. The first requisite for breakup of drops by viscous shear is that drops must be smaller than the local regions of viscous flow. He logically assumed that in turbulent flow, the size of the largest drops would be determined by the dynamic pressure forces of the turbulent motions. A dimensionless group called Weber number ( $N_{We}$ ), “which represents the ratio between the external force that tends to deform the drop and the counteracting surface tension force” (Brauner, 2001), was introduced:

$$N_{We} = \frac{\rho_c u'^2 d}{\sigma} \quad (3.9)$$

where  $\rho_c$  is the density of the continuous phase,  $u'^2$  is the mean square of the velocity fluctuations over a distance equal to the droplet diameter  $d$ , and  $\sigma$  is the interfacial tension between oil and water. The greater the value of  $N_{We}$ , the greater the external force compared to the counteracting interfacial tension force, and the easier it is to break up the water droplet. At a critical value ( $N_{We})_{crit}$ , breakup of the water droplet occurs.

The critical Weber number  $(N_{We})_{crit}$  is associated with the maximum drop diameter  $d_{max}$  as follows:

$$(N_{We})_{crit} = \frac{\rho_c u'^2 d_{max}}{\sigma} \quad (3.10)$$

Rewriting Equation (3.10) can get:

$$C_1 \rho_c u'^2 = \frac{\sigma}{d_{max}} \quad (3.11)$$

where  $C_1$  in Equation (3.11) is a constant that represents the portion of the turbulent kinetic energy used to counteract the surface energy to break up the droplet. For an isotropic homogenous turbulence, the turbulent kinetic energy has relationship with the energy dissipation rate  $e$  (the energy input per unit mass per unit time) as follows:

$$e = \frac{[energy\ input]}{[mass] \cdot [time]} = \frac{C_2 m_c u'^2}{m_c \cdot (d_{max} / u')} = C_2 \frac{u'^3}{d_{max}} \quad (3.12)$$

Rearranging Equation (3.12), one can arrive at the following relation:

$$u'^2 = C_2^{2/3} (e d_{max})^{2/3} \quad (3.13)$$

According to the work done by Batchelor (1951), the constant  $C_2^{2/3}$  in Equation (3.13) was 2. Substituting Equation (3.13) into Equation (3.11), the following relation was derived by Hinze (1955).

$$d_{\max} \left( \frac{\rho_c}{\sigma} \right)^{3/5} e^{2/5} = C \quad (3.14)$$

Hinze (1955) applied his model to the results obtained by Clay (1940) and found that constant  $C$  in Equation (3.14) was equal to 0.725, and the corresponding critical Weber number  $(N_{We})_{crit} = 1.17$ . In pipe flow, the energy dissipation rate  $e$  can be related to the frictional pressure drop  $\Delta p$  as follows (Brauner, 2001):

$$e = \frac{[\text{energy input}]}{[\text{mass}] \cdot [\text{time}]} = \frac{[\text{pressure drop}] \cdot [\text{volume}]}{[\text{mass}] \cdot [\text{time}]} = \frac{\Delta p \cdot \frac{1}{4} \pi D^2 L}{\frac{1}{4} \pi D^2 L \varepsilon_c \rho_c \cdot \frac{L}{U_c}} = \frac{\Delta p U_c}{\varepsilon_c \rho_c L} \quad (3.15)$$

In Equation (3.15),  $L$  is the pipe length,  $D$  is the pipe diameter,  $\varepsilon_c$  is volume percentage of continuous phase,  $\rho_c$  is continuous phase density and  $U_c$  is continuous phase velocity. For the pipe flow in the pipeline with the diameter of  $D$  and the length of  $L$ , the pressure drop  $\Delta p$  can be related as follows:

$$\Delta P \cdot \frac{1}{4} \pi D^2 = \tau \cdot \pi D L \quad (3.16)$$

$$\Delta P = \frac{4\tau L}{D} \quad (3.17)$$

$$\tau = \frac{1}{2} f \rho_m U_c^2 \quad (3.18)$$

The mixture velocity  $\rho_m$  is determined by following equation:

$$\rho_m = \varepsilon_c \rho_c + \varepsilon_d \rho_d \quad (3.19)$$

where  $\varepsilon_d$  and  $\rho_d$  are the volume percentage of dispersed flow and the density of dispersed flow, respectively. Substituting Equation (3.17) and Equation (3.18) into Equation (3.15), the energy dissipation rate  $e$  is expressed in terms of friction factor,  $f$ :

$$e = \frac{2f\rho_m U_c^3}{D\varepsilon_c \rho_c} \quad (3.20)$$

Combining Equation (3.14) and Equation (3.20), the maximum drop diameter can be calculated as in the following equation:

$$d_{\max} = 0.725 \left( \frac{\rho_c}{\sigma} \right)^{-0.6} \left( \frac{2f\rho_m U_c^3}{D\rho_c \varepsilon_c} \right)^{-0.4} \quad (3.21)$$

Brauner (2001) pointed out that the Hinze model, Equation (3.21), only considers the stability of a single droplet in a turbulent field. Equation (3.21) is only valid for so-called dilute dispersion, where the volume of dispersed phase (water) is much smaller than the volume of continuous phase (oil), and there is no interaction between drops.

Therefore we can conclude that, so far, we have only the expression for the maximum drop diameter  $d_{\max}^{dilute}$  in dilute dispersion:

$$d_{\max}^{dilute} = 0.725 \left( \frac{\rho_c}{\sigma} \right)^{-0.6} \left( \frac{2f\rho_m U_c^3}{D\rho_c \varepsilon_c} \right)^{-0.4} \quad (3.22)$$

Since the Hinze model is only applicable for dilute dispersions, Brauner (2001) extended it to the so-called “dense dispersions”. In dense dispersions, where droplet interaction including coalescence is predominant, turbulent kinetic energy flux in the continuous phase needs to be sufficient to generate new surface energy for newly formed droplets and disrupt the droplet coalescence of the dispersed phase. The total surface energy of the dispersed phase, which flows at a rate of  $Q_d$ , can be estimated by Equation (3.23). The total surface energy  $E_s$  of the dispersed phase is proportional to the turbulent kinetic energy supplied by the continuous phase (Brauner, 2001), as shown in Equation (3.24), where  $C_H$  is a adjustable constant, which was set to 1 by Nestic, Wang, *et al.*(2004) and Cai, Nestic & de Waard (2004) in their water wetting prediction model. Inserting Equation (3.13) and Equation (3.20) into Equation (3.24) yields the maximum drop diameter calculated in Equation (3.25) for dense phase.

$$E_s = \frac{Q_d}{\pi d_{\max}^3 / 6} \cdot \pi d_{\max}^2 \sigma = \frac{6\sigma}{d_{\max}} Q_d \quad (3.23)$$

$$\frac{\rho_c u'^2}{2} Q_c = C_H \frac{6\sigma}{d_{\max}} Q_d \quad (3.24)$$

$$d_{\max}^{dense} = 2.22D \left( \frac{\rho_c D U_c^2}{\sigma} \right)^{-0.6} \left( \frac{\varepsilon_d}{1 - \varepsilon_d} \right)^{0.6} \left[ \frac{\rho_m}{\rho_c (1 - \varepsilon_d)} f \right]^{-0.4} \quad (3.25)$$

Brauner (2001) suggested taking the larger of the two drop diameters calculated in Equation (3.22) and (3.25), respectively, as the maximum drop diameter in a given two-phase flow system and operational conditions, as in Equation (3.26):

$$d_{\max} = \text{Max}(d_{\max}^{dilute}, d_{\max}^{dense}) \quad (3.26)$$

### 3.3.3.2 Criterion for stable water-in-oil dispersion

In stable water-in-oil dispersion, water is the dispersed phase and oil is the continuous phase. In order to make oil-water stratified flow transit to stable water-in-oil dispersion, the oil phase turbulence should be intense enough to break the water phase into droplets smaller than a critical drop diameter  $d_{crit}$ . Then, the criterion for stable water-in-oil dispersion is as suggested by Brauner (2001) in Equation (3.27). Brauner (2001) adopted the method from Barnea (1987) for calculating the critical drop diameter  $d_{crit}$  (3.27) in Equation to oil-water two-phase system.

$$d_{\max} \leq d_{crit} \quad (3.27)$$

### 3.3.3.3 Critical drop diameter $d_{crit}$

The critical drop diameter in oil-water two phase flow can be calculated following the work done for gas-liquid system by Barnea (1986). Above the critical drop diameter, the dispersed water droplets will migrate toward the bottom of pipe and separate out from

the oil phase to form stratified flow due to gravity. Taitel & Dukler (1976) suggested that for horizontal and slightly inclined gas-liquid flow, the transition to dispersed bubble flow occurs when the turbulent fluctuations can counteract buoyant forces. So for oil-water flow, it can be suggested that the transition to dispersed water-in-oil flow occurs if the turbulent fluctuations are sufficiently strong to counteract the gravity force that drags the water drops toward the pipe wall. Let us consider a water-in-oil dispersed flow in an inclined pipe (*Figure 3-14*). The gravity force component in radial direction  $F_g$  is calculated by Equation (3.28). The force due to turbulent fluctuations  $F_T$  is calculated according to Levich (1962) by Equation (3.29), where the radial velocity fluctuations  $v'$  is estimated to be approximately equal to the friction velocity,  $U_*$  (Equation (3.30)). When  $F_g = F_T$ , the critical drop diameter  $d_{cg}$  can be calculated by using Equation (3.31).

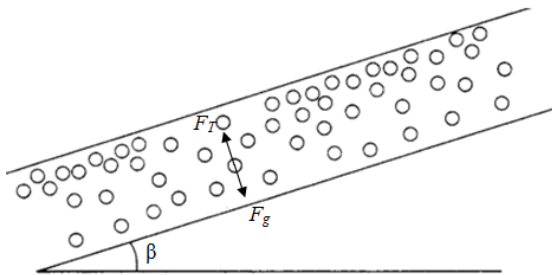


*Figure 3-14.* The forces of axial direction acting on droplets in oil-water dispersed flow.

$$F_g = \frac{\pi d_{cg}^3}{6} |\rho_d - \rho_c| g \cos \beta \quad (3.28)$$

$$F_T = \frac{\pi d_{cg}^2}{4} \cdot \frac{1}{2} \rho_c v'^2 \quad (3.29)$$

$$v' = U_* = U_o \left( \frac{f}{2} \right)^{0.5} \quad (3.30)$$

$$d_{cg} = \frac{3}{8} \frac{\rho_c U_o^2 f}{|\rho_d - \rho_c| g \cos \beta} \quad (3.31)$$

Another way to arrive at the critical drop diameter,  $d_{c\sigma}$  in oil-water system is to look at the maximum drop diameter above which the droplet will be deformed or cannot sustain its spherical shape. Based on the dimensional arguments of Bond & Newton (1928), Brodkey (1967) developed a rough criterion to determine whether a drop will deviate from solid-like behavior or be deformed. Brodkey (1967) obtained the following correlation (Equation (3.32)) for the critical drop diameter by fitting the experimental data into carbon tetrachloride and water liquid-liquid system. Barnea, Shoham, *et al.* (1982) claimed that, based on experimental data, bubbles maintain their spherical shape up to the size about twice the value given by Equation (3.32). So, Barnea (1986, 1987) used the following correlation (Equation (3.33)) to calculate  $d_{c\sigma}$ :

$$d_{c\sigma} = \sqrt{\frac{0.4\sigma}{|\rho_d - \rho_c| g}} \quad (3.32)$$

$$d_{c\sigma} = 2 \sqrt{\frac{0.4\sigma}{|\rho_d - \rho_c| g}} \quad (3.33)$$

Brauner (2001) extended Brodkey's (1967) work by adding the effect of inclination angle of the pipeline, as shown in Equation (3.34), where  $\beta$  is the inclination angle of the pipeline to the horizontal level. Brauner (2001) claimed that “the inclusion of  $(\cos \beta')^{1/2}$  in  $d_{c\sigma}$  is not critical since its effect is of the order of uncertainty in the value of the constant parameter 0.4 in Equation (3.34)”:

$$d_{c\sigma} = \sqrt{\frac{0.4\sigma}{|\rho_d - \rho_c|g \cos \beta'}}, \quad \beta' = \begin{cases} |\beta|, & |\beta| < 45^\circ \\ 90^\circ - |\beta|, & |\beta| > 45^\circ \end{cases} \quad (3.34)$$

Finally, Barnea (1987) suggested that the critical drop diameter,  $d_{crit}$ , in Equation (3.27) can be estimated using Equation (3.35).

$$d_{crit} = \text{Min}(d_{c\sigma}, d_{cb}) \quad (3.35)$$

#### 3.3.3.4 Friction factor $f$

Friction Factor used in all above equations is also called Fanning friction factor  $f$ , which is one-fourth of Darcy friction factor  $f_D$  or Moody friction factor  $f_M$ . So attention must be paid to note what the “friction factor” really means when referring the friction factor correlations by other authors. The Darcy or Moody friction factor is calculated as described below (Moody, 1944). In Equation (3.36),  $h_f$  is the energy loss due to friction undergone by a Newtonian liquid flowing in a pipe with the diameter of  $D$  and the length of  $L$ .

$$f_D = f_M = \frac{D}{L} \frac{gh_f}{\frac{1}{2}u^2} = \frac{D}{L} \frac{\Delta P}{\frac{1}{2}\rho u^2} = 4f \quad (3.36)$$

There are many equations for calculating the friction factor proposed by several authors since Blasius first used experimental data to obtain a correlation (Equation (3.37)) of friction factor for a smooth pipe (Hager, 2003). Nesic, Wang, *et al.* (2004) and Cai, Nesic, & de Waard (2004) used a Blasius type equation (Equation (3.38)) for the calculation of friction factor in a smooth pipe in their water wetting prediction model. Prandtl and von-Karman derived a better correlation (Equation (3.39)) from experimental data on smooth pipe (Colebrook, 1939). Equation (3.39) is valid for  $Re > 4000$ . Based on the work of Prandtl and von-Karman, Colebrook (1939) proposed an implicit equation (Equation (3.40)) for turbulent flow considering the effect of pipe roughness on the friction factor. Equation (3.40) is called the Colebrook-White equation, which is valid for Reynolds number ( $Re$ ) ranging from 4000 to  $10^8$  and values of relative roughness ( $\lambda/D$ ) ranging from 0 to 0.05. Moody (1947) plotted the Colebrook-White equation into what is known as the Moody chart, which avoids the complexity of solving the implicit equation for friction factor, and is widely used today. Moody (1947) proposed an approximate formula (Equation (3.41)) for pipe friction factors. The author claimed the equation to be valid for Reynolds number ( $Re$ ) ranging from 4000 to  $10^8$  and relative roughness ranging from 0 to 0.01. Churchill (1973) and Haaland (1983) developed explicit expressions for friction factor as shown in Equation (3.42) and (3.43), respectively.

$$f_D = \frac{0.3164}{\text{Re}^{0.25}}, \quad (3 \times 10^3 \leq \text{Re} \leq 2 \times 10^5) \quad (3.37)$$

$$f = \frac{0.046}{\text{Re}_c^{0.2}}, \quad \text{Re}_c = \frac{\rho_c D U_c}{\mu_c} \quad (3.38)$$

$$\frac{1}{\sqrt{f_D}} = 2 \log(\text{Re} \sqrt{f_D}) - 0.8 = 2 \log\left(\frac{\text{Re} \sqrt{f_D}}{2.51}\right) \quad (3.39)$$

$$\frac{1}{\sqrt{f_D}} = -2 \log\left(\frac{2.51}{\text{Re} \sqrt{f_D}} + \frac{\lambda}{3.70D}\right) \quad (3.40)$$

$$f_D = 0.0055 \left( 1 + \left( 2 \times 10^4 \frac{\lambda}{D} + \frac{10^6}{\text{Re}} \right)^{1/3} \right) \quad (3.41)$$

$$\frac{1}{\sqrt{f_D}} = -2 \log\left( \left( \frac{7}{\text{Re}} \right)^{0.9} + \frac{\lambda}{3.70D} \right) \quad (3.42)$$

$$\frac{1}{\sqrt{f_D}} = -1.8 \log\left( \frac{6.9}{\text{Re}} + \left( \frac{\lambda}{3.70D} \right)^{1.11} \right) \quad (3.43)$$

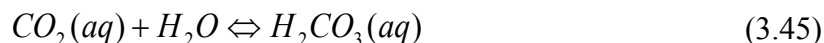
### 3.4 Carbon dioxide corrosion

In the oil and gas industry, corrosion is a major impediment to successful hydrocarbon production, economical design of facilities, and their safe and optimum operations. Carbon dioxide (CO<sub>2</sub>) corrosion or “sweet corrosion” is regarded as the most prevalent type of attack in “upstream” operations in the oil and gas industry (Kermani & Morshed, 2003). CO<sub>2</sub>, usually present in produced fluids, can be dissolved in the aqueous phase to create a corrosive environment for carbon steel and low alloy steels, which are widely used in the construction of oil and gas industry facilities. Therefore, the understanding of CO<sub>2</sub> corrosion has received great attention from industry and research

institutions. Various mechanisms of CO<sub>2</sub> corrosion have been proposed by some authors since the 1970s (de Waard & Milliams, 1975a; Hurlen, Gunvaldsen, *et al.*, 1984; Gray, Anderson, *et al.*, 1989; Netic & Postlethwaite, 1996a; etc.). The most comprehensive reviews on CO<sub>2</sub> corrosion have been published by Kermani & Morshed (2003) and Netic (2007).

### 3.4.1 Electrochemistry of CO<sub>2</sub> corrosion

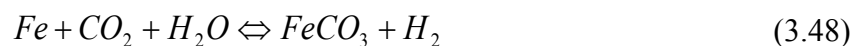
In aqueous phase, CO<sub>2</sub> is dissolved to form a weak acid-carbonic acid as shown in Equation (3.44) and (3.45).



The carbonic acid (H<sub>2</sub>CO<sub>3</sub>) has two hydrogen atoms, which may dissociate from the parent molecule to form a bicarbonate ion (HCO<sub>3</sub><sup>-</sup>) and a carbonate ion (CO<sub>3</sub><sup>2-</sup>).



The overall reaction for aqueous CO<sub>2</sub> corrosion of carbon steel is



The corrosion of iron is an electrochemical process which includes both the anodic dissolution (oxidation) of iron and the cathodic evolution (reduction) of hydrogen. The corrosion product iron carbonate (FeCO<sub>3</sub>) will precipitate on the steel surface to form

solid iron carbonate film according to Equation (3.49) when the concentrations of  $Fe^{2+}$  and  $CO_3^{2-}$  exceed the solubility limit.



Supersaturation is a very important parameter indicating the precipitation tendency of the solid corrosion layer, which is defined as

$$SS = \frac{c_{Fe^{2+}} c_{CO_3^{2-}}}{K_{sp}} \quad (3.50)$$

where  $K_{sp}$  is the solubility limit of iron carbonate,  $c_{Fe^{2+}}$  and  $c_{CO_3^{2-}}$  represent the equilibrium concentrations of ferrous ion and carbonate ion.

Therefore in aqueous  $CO_2$  corrosion of carbon steel, the anodic reaction is the iron dissolution (Equation (3.51) ) to supply ferrous ions.



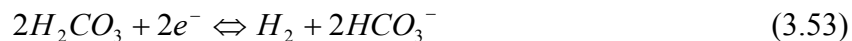
The mechanisms of iron dissolution have been widely studied by a number of authors during the last five decades (Bockris, Drazic, *et al.*, 1961; de Waard. C. & Milliams, 1975b; Hurlen, Gunvaldsen, *et al.*, 1984; Nescic, Thevenot, *et al.*, 1996b).

In an acid solution, the reduction of  $H^+$



is the most important cathodic reaction. In strong acids such as hydrochloric acid (HCl) and sulfuric acid ( $H_2SO_4$ ), the rate of hydrogen evolution is controlled by the mass transfer rate of  $H^+$  from the bulk solution to the iron surface. Nescic & Postlethwaite

(1996a) pointed out that in CO<sub>2</sub> systems at low pH (<4), the H<sup>+</sup> reduction is the dominant cathodic reaction. In CO<sub>2</sub> systems at pH>4, de Waard & Milliams (1975a, 1975b) found aqueous CO<sub>2</sub> solutions to be more corrosive than a completely dissociated acid at the same pH. They explained this using the addition of the direct reduction of H<sub>2</sub>CO<sub>3</sub> (Equation (3.53)) except for the H<sup>+</sup> reduction in the solution:



Nesic & Postlethwaite (1996a) suggested that at currents beyond the limiting current, and with pH>5 and very low partial pressures of CO<sub>2</sub>, direct reduction of H<sub>2</sub>O becomes important.



### 3.4.2 Key factors influencing CO<sub>2</sub> corrosion

CO<sub>2</sub> corrosion can be influenced by many parameters including water chemistry, operating conditions (i.e. pH, temperature, CO<sub>2</sub> partial pressure), fluid dynamics, water wetting, steel surface characteristics, steel chemistry, corrosion inhibitors, etc. (Nesic & Postlethwaite, 1996a.; Kermani & Morshed, 2003). The effects of these parameters on CO<sub>2</sub> corrosion have been widely investigated by many authors. In accordance with the scope of this dissertation, the effect of water chemistry and water wetting on CO<sub>2</sub> corrosion will be briefly reviewed.

#### 3.4.2.1 Effect of water chemistry

Water chemistry is among the most influential factors affecting CO<sub>2</sub> corrosion. Understanding the water chemistry of CO<sub>2</sub> systems plays a vital role in predicting CO<sub>2</sub> corrosion rate. Nesic & Postlethwaite (1996a) pointed out that concentrations of different species in the solution can be calculated by solving chemical equilibrium equations with the electroneutrality equation. Nesic (2007) summarized typical dissolved species found in oil field brines and typical chemical reactions for oil/gas brines. Knowing partial pressure of CO<sub>2</sub>, solution pH and the concentrations of dissolved species at a given temperature, supersaturation *SS* can be determined. Higher supersaturation leads to the precipitation of corrosion scales, which can mitigate the corrosion process by providing a diffusion layer for the corrosive species and decreasing the steel surface exposed to the corrosive bulk solution.

#### 3.4.2.2 Effect of water wetting

In a multiphase flow systems, such as oil-water two-phase flow or oil-water-gas three-phase system, corrosion occurs when the water phase wets the pipeline surface. The intensity of the corrosion will increase with the water cut and the amount of surface area wetted by the water phase. Therefore it is very important to know the flow pattern and phase wetting regimes under given operating conditions. As recently pointed out by Nesic, Cai, *et al.* (2005), only a handful of studies are available on this topic (Wicks & Fraser, 1975; de Waard & Lotz, 1993; Wu, 1995; de Waard, Smith, *et al.*, 2001), although water wetting has long been known to be an issue in CO<sub>2</sub> corrosion. In the well-known corrosion prediction model proposed by de Waard & Lotz (1993), the authors

included a simple water wetting factor based on water cut and mixture velocity, but pointed out that the effects of a number of other parameters such as protective corrosion products, pH, flow pattern, and flow rate should be accounted for in the future. de Waard, Smith, *et al.* (2001) proposed a new empirical model by linking the API gravity to water-in-oil-emulsion stability and considered the effects of the water cut, fluid velocity, and angle of deviation of the tubing. Although this model corresponds well with specific sets of field data, it neglects the effects of pipe diameter, oil properties, and surface state on the critical oil velocity for full water entrainment. A comprehensive hydrodynamic water wetting model was proposed by Cai, Nesic, & de Waard (2004), where the effects of many key parameters such as flow rates, water cut, pipe diameter, pipe inclination, oil density, oil viscosity and surface tension were all considered. However, the model did not account for the effect of steel surface state or chemicals in the water phase that affect the corrosion rate, such as corrosion and scale inhibitors and various compounds present in the crude oil.

## CHAPTER 4 : EXPERIMENTAL STUDY OF OIL-WATER TWO-PHASE FLOW

In order to validate and improve the water wetting model (see Chapter 3), a comprehensive experimental program was initiated at Ohio University in 2004 to explore the key factors related to water wetting in oil-water two-phase flow. The work and the results presented in this chapter were shared between three PhD students: the present author, Dr. Chong Li and Dr. Francois Ayello. All the work constitutes the collaborative work of the three students named above and the former project leader, Dr. Jiyong Cai. Portions of the work discussed in this chapter have been already been published by the present author and his fellow students in the following conference papers:

- Ayello, F., Li, C., & Tang, X., “Determination of phase wetting in oil-water pipe flows”, NACE CORROSION/08, Paper No. 08566, New Orleans, LA, 2008.
- Tang, X., Li, C., Ayello, F., Cai, J., & Nešić, S., “Effect of oil type on phase wetting transition and corrosion in oil-water flow”, NACE CORROSION/07, Paper No. 07170, Nashville, TN, 2007.
- Li, C., Tang, X., Ayello, F., Cai, J., & Nešić, S., “Experimental Study on Water Wetting and CO<sub>2</sub> Corrosion in Oil-Water Two-Phase Flow”, NACE CORROSION/06, Paper No. 06595, San Diego, CA, 2006.
- Tang, X., Ayello, F., Li, C., Cai, J., & Nešić, S., “Water wetting and corrosion in horizontal and inclined flow of oil - water mixture”, 11<sup>th</sup> Middle East conference, Manama, Bahrain, 2006.

## 4.1 Experimental setup

### 4.1.1 Test facilities\*

The large scale oil-water two-phase flow experiments were carried out in a 50 m long, 4" I.D. fully inclinable multiphase flow loop, which is specially designed to investigate corrosion and multiphase flow under realistic flow conditions similar to those found in the field (*Figure 4-1*). Two 1.2 m<sup>3</sup> stainless steel storage tank were used to store the oil and D.I. water with 1 wt% NaCl, respectively. A Moyno<sup>®</sup> positive displacement pump equipped with a variable speed motor was used to pump the oil through the system. A range of 0.5 to 3 m/s for the oil flow rate was controlled using variable motor speeds and a bypass system. Two Moyno<sup>®</sup> positive displacement pumps with low and high flow rates were used to pump water through the system from the water storage tank. For the flow with a water cut higher than 20%, the pump with high flow rate was used. Otherwise the pump with low flow rate was used.

---

\* The content in the denoted section (Section 4.1.1) is adapted from the co-authored paper (Li, C., Tang, X., Ayello, F., Cai, J., and Nešić, S., "Experimental Study on Water Wetting and CO<sub>2</sub> Corrosion in Oil-Water Two-Phase Flow", NACE CORROSION/06, Paper No. 06595, San Diego, CA, 2006.)

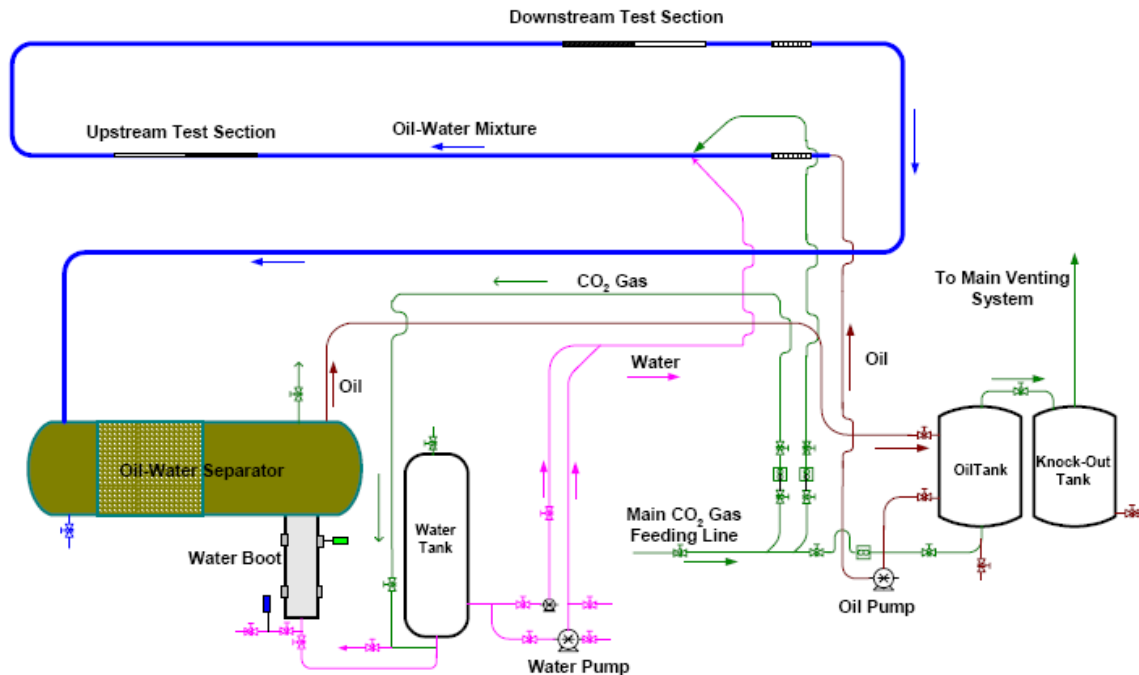


Figure 4-1. Schematic of a 4" fully inclinable multiphase flow loop used in the study (Cai, Nestic, Li, *et al.*,2005).

Oil flowed through a 3 m long, 4" I.D. flexible hose which allowed the rig to be inclined at any angle, from 0° (horizontal) to 90° (vertical), and mixed with water in a T-shape section. The oil-water mixture then entered a 4" I.D., 14 m long stainless steel section, where the phases settled into a stable flow pattern before entering the 2 m long "upstream" mild steel test section, where the measurements were carried out. A 2 m long transparent pipe section immediately followed the mild steel section and was used to view the flow pattern. The oil-water mixture then flowed through a 180° C-shape bend, and into another 14 m long stainless steel pipe section followed by a 2 m long "downstream" mild steel test section and a 2 m long transparent section. The oil-water mixture then flowed through a 20 m long PVC pipe to an oil-water separator (Figure 4-2). The water accumulated in the water boot at the bottom of the separator, and flowed

back into the water storage tank. The separated oil phase flowed up through the oil outlet at the top of the separator and back to the oil storage tank for further circulation.

The oil-water separator (*Figure 4-2*) played a key role in the successful execution of the oil-water two-phase testing by enabling the oil-water mixture to separate and prevented emulsions forming and circulating in the system. Inside the separator, three main components were installed to enhance the oil-water separation efficiency. The liquid distributor near the oil-water mixture inlet distributed the mixture uniformly over the cross section of the separator. Following the liquid distributor was a droplet coalescer made from two materials with very different surface free energy - stainless steel and plastic - with four sets of enhanced plate separators, which could greatly enhance the rate of coalescence of the dispersed droplets. Two sampling ports, one for water and one for oil, were installed on the water boot and oil outline line, respectively, in order to collect water and oil samples and determine the separation efficiency. The internal wall of the separator, made from carbon steel, was coated with corrosion resistance epoxy to eliminate potential corrosion problems.

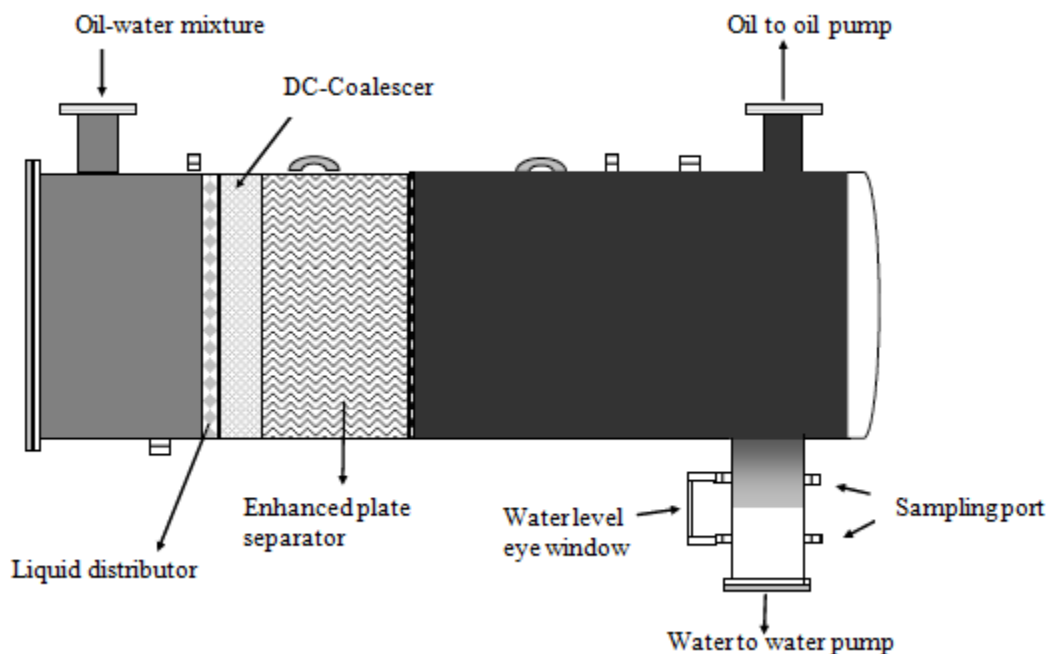


Figure 4-2. Schematic of internal structure of oil-water separator (Courtesy of Jiyong Cai).

A schematic of a mild steel test section used in the study is shown in *Figure 4-3*. During the experiments, the test section was allowed to corrode, leading to an increase in ferrous ion ( $\text{Fe}^{2+}$ ) concentration in the water phase, which could then be measured. Five rows of wall conductance probes with a staggered row arrangement, a wall sampling port and an electrical resistance (ER) probe holder were installed and located at the downstream test section. The test sections were connected to the flow loop with special flanges, which allowed the test sections to be rotated. For the purpose of minimizing the effect of oxygen on the corrosion process, carbon dioxide ( $\text{CO}_2$ ) was used to de-oxygenate the system before experiments began. The oxygen concentration in the system was measured using an Oxygen CHEMets<sup>®</sup> test kit, and was typically below 25 ppb.

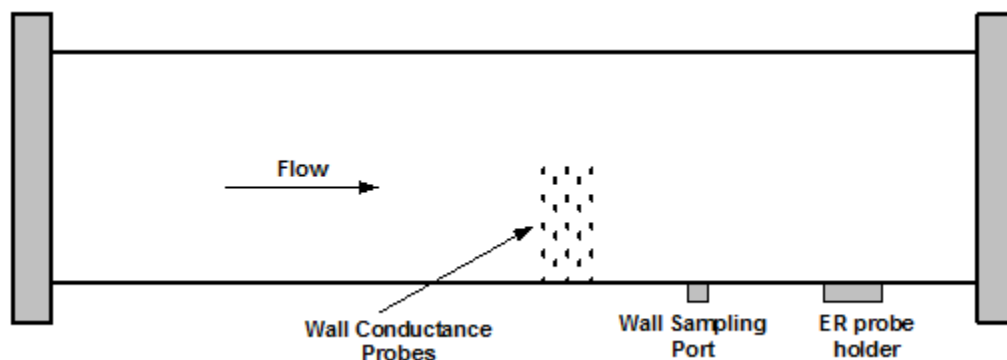


Figure 4-3. Schematic of test section made of carbon steel (Courtesy of Jiyong Cai).

#### 4.1.2 Test techniques\*

Four main techniques were used to determine the water wetting regime on the internal pipe wall at different superficial oil and water velocities in oil-water flow: flow pattern visualization, wall conductance probes, wall fluid sampling and corrosion rate monitoring.

Visual recordings were made at the transparent test section just downstream from the mild steel test section. Artificial red coloring of the water was used to enhance the contrast between the oil and the water phases. This visual technique worked very well with clear model oils, but was not suitable with crude oils, since no visual distinction could be inferred.

The flush mounted wall conductance probes (*Figure 4-4 (a)*) were used to detect the nature of the fluid in contact with the surface of the pipe internal wall, i.e. whether it was conductive (water) or not (oil). The probes were epoxy-coated stainless steel pins

---

\* The content in the denoted section (Section 4.1.2) is adapted from the co-authored paper (Li, C., Tang, X., Ayello, F., Cai, J., and Nešić, S., “Experimental Study on Water Wetting and CO<sub>2</sub> Corrosion in Oil-Water Two-Phase Flow”, NACE CORROSION/06, Paper No. 06595, San Diego, CA, 2006.)

with 0.45 mm O.D. threaded through a 0.5 mm I.D. hole in the pipe. On the downstream test section, five staggered rows of 18 probes (a total of 90 probes) were flush-mounted on the bottom half of the pipe wall covering 180° of the internal circumference. On the upstream test section, five staggered rows of 32 probes (a total of 160 probes) were flush-mounted on the whole internal circumference of the pipe wall, covering 360°. *Figure 4-4* (b) shows the staggered configuration of wall conductance probes. The use of a large number of spatially distributed probes minimized errors due to the effect of the water phase deviating or “snaking” around individual probes. This redundant configuration was also useful for characterizing intermittent wetting and for eliminating outliers.

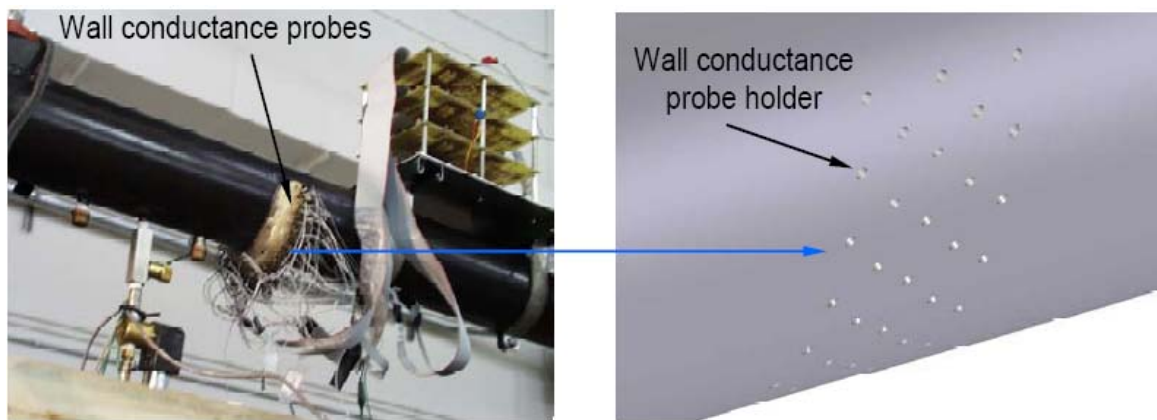


*Figure 4-4.* Wall conductance probes. (a) wall conductance probes on the test section, (b) 5 rows of staggered configuration of probe holders (Courtesy of Jiyong Cai).

A wall fluid sampling method was used to measure the water/oil content very close to the surface of the inner wall by extracting the fluid from the bottom of pipe. The combination of a very precisely controlled needle valve and a solenoid valve was used to

extract the fluid very close the wall surface through the wall sampling port shown in *Figure 4-3*.

Because a CO<sub>2</sub> saturated water/oil mixture was circulated through the flow loop, the mild steel test section was subject to corrosion. The corrosion process enabled an alternative method for determining water wetting. If water wetting was present, the mild steel section corroded, manifested as a rise in the concentration of dissolved ferrous ion (Fe<sup>2+</sup>) in the water phase, which could be measured by sampling the water and employing a standard colorimetric technique with a Turner SP-870 spectrophotometer. This increase in ferrous ion concentration over time was used to calculate the average corrosion rate, because only the two mild steel test sections corroded during the test. An ER probe mounted in the test section was also used to monitor the corrosion rate and indirectly determine the water wetting; however, the specific values obtained with this probe were not considered accurate and only the trends were used.

Each of these four very different techniques for the detection of water wetting (flow pattern visualization, wall conductance probes, wall fluid sampling, and corrosion rate monitoring) has its strengths and weaknesses. For example, the visual technique works very well with clear model oils, but it is not suitable for the tests with crude oils. Fluid sampling at the wall can easily lead to errors if the applied suction is too intense and draws liquid from the upper layers of the fluid; if it is too weak, on the other hand, it allows for escape of the oil from the sample tube. The intention was therefore to use the overlapping information from the four techniques to corroborate the various pieces of evidence and to strengthen confidence in the conclusions.

#### 4.1.3 Test Matrix

The experiments were carried out with one model oil (LVT200), and 5 different crude oils (named C1-C5 provided by a sponsor company) at different flow conditions. The key test matrices for the oil-water two-phase flow loop tests are shown in *Table 4-1*.

*Table 4-1*. Main test parameters for oil-water two-phase flow loop tests.

Oil phase	LVT200, C1, C2, C3, C4, C5
Water phase	1 wt% NaCl D.I. water
Superficial oil velocity	0.5 - 2.5m/s
Superficial water velocity	0 - 0.22 m/s
Water cut	0 - 20%
Pipe inclination	Horizontal, $\pm 2^\circ$ , $\pm 5^\circ$ , $\pm 45^\circ$ and $\pm 90^\circ$
Pipe diameter	4"
System temperature	25 °C
System pressure	0.1013 MPa

#### 4.1.4 Properties of the experimental fluids

The varying physical properties of the different oils at room temperature, such as density, American Petroleum Institute (API) gravity, viscosity, oil-water interfacial tension, are shown in *Figure 4-7* to *Figure 4-10*. The density was measured and calculated by weighing 50 milliliters of the testing oil in a volumetric flask. The API gravities were calculated using the following equation.

$$API = \frac{141.5\rho_{H_2O}}{\rho_{oil}} - 131.5 \quad (4.1)$$

The dynamic viscosity was measured with a HAAKE® Falling Ball Viscometer (Model B), per ASTM D445 standard, and the oil-water interfacial tension was measured with a

CSC-DuNouy<sup>®</sup> Tensiometer (Model 70735), per ASTM D971 standard. *Figure 4-5* and *Figure 4-6* show the picture of HAAKE<sup>®</sup> Falling Ball Viscometer and CSC-DuNouy<sup>®</sup> Tensiometer, respectively.



*Figure 4-5.* HAAKE<sup>®</sup> Falling Ball Viscometer for viscosity measurement.



Figure 4-6. CSC-DuNouy® Tensiometer for oil-water interfacial tension measurement.

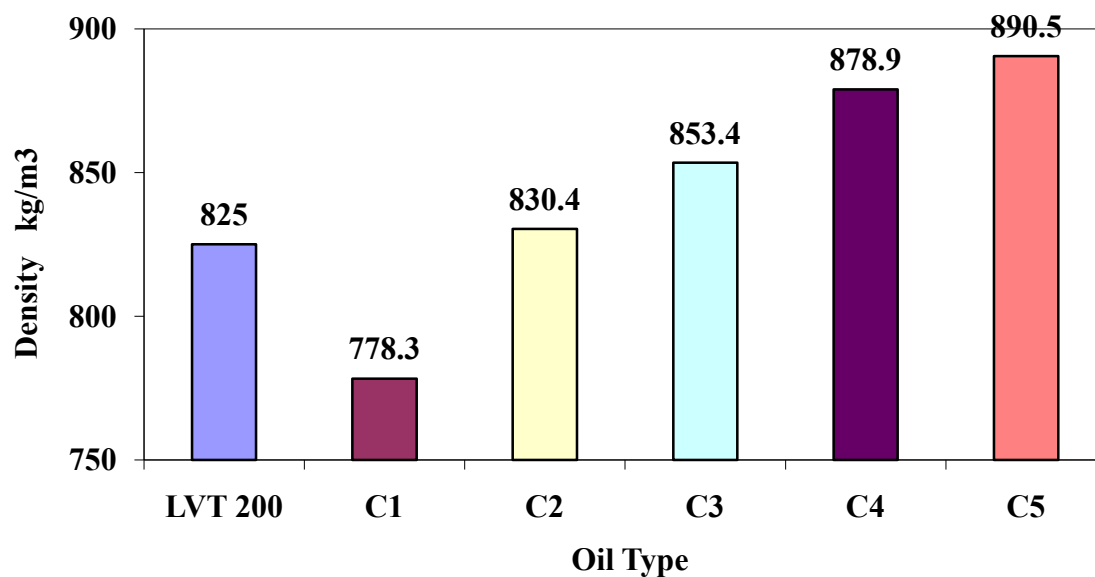


Figure 4-7. The density of the testing oils at room temperature (25 °C).

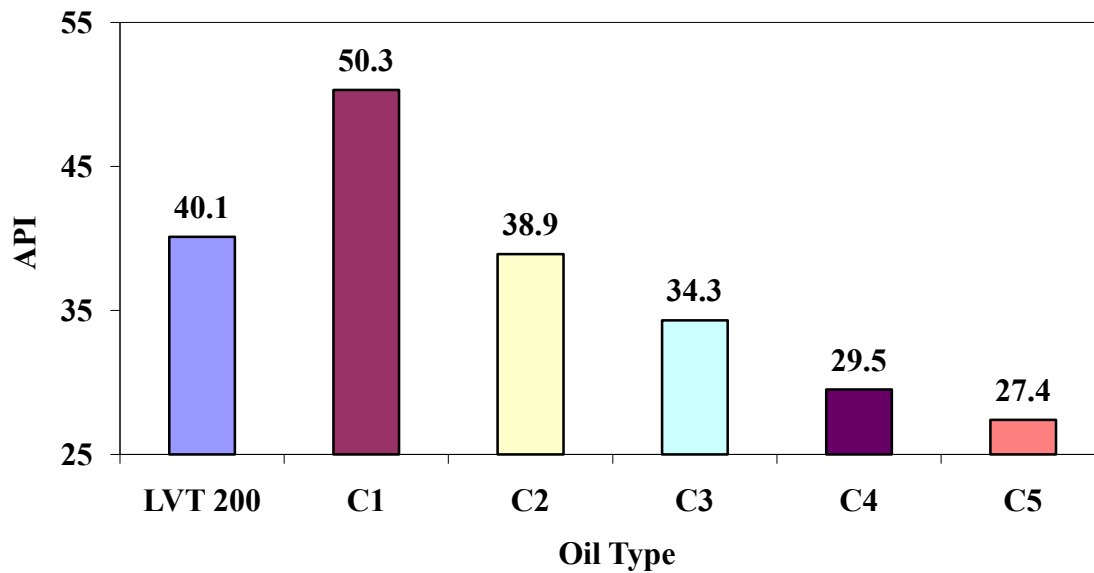


Figure 4-8. The API gravity of the testing oils at room temperature (25 °C).

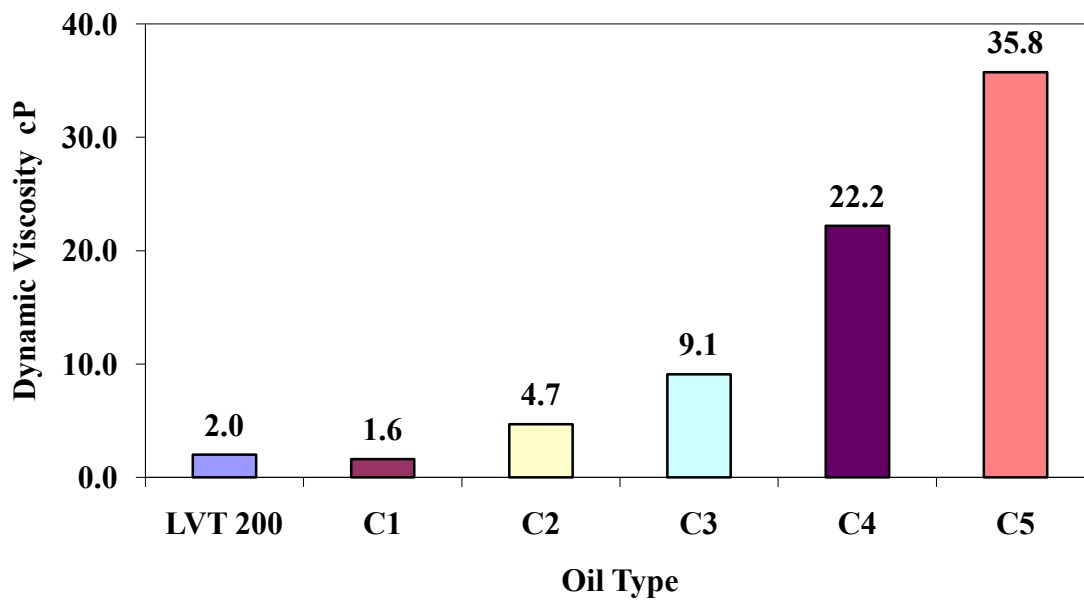


Figure 4-9. The dynamic viscosity of the testing oils at room temperature (25 °C).

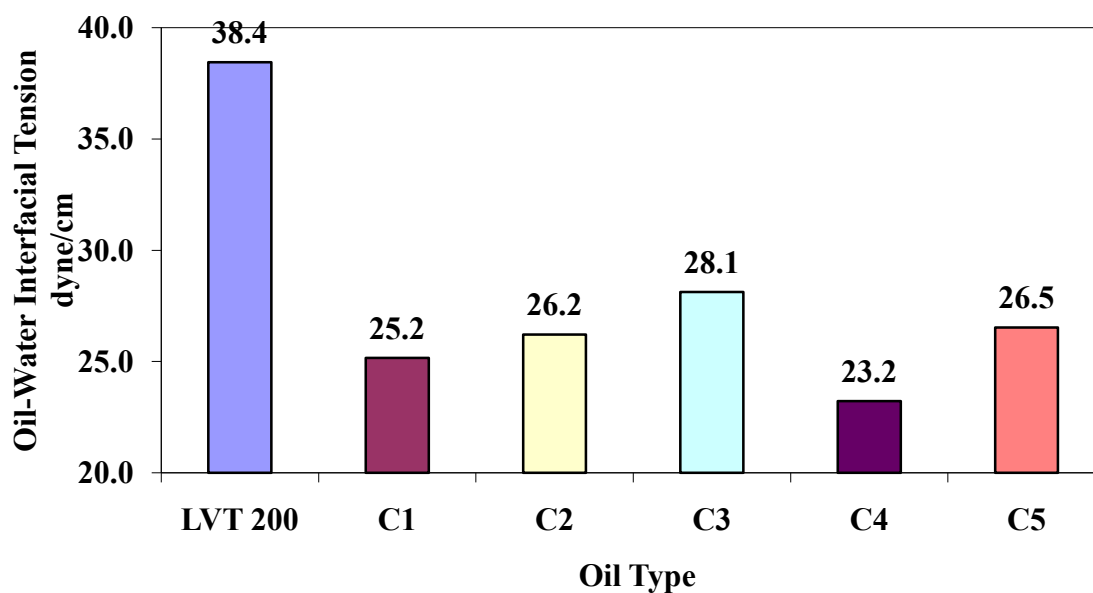


Figure 4-10. Oil-water interfacial tension of the testing oils at room temperature (25 °C).

#### 4.1.5 Experimental procedure

Each series of experiments followed the experimental procedure below.

1. 16 barrels of oil and 400 gallons de-ionized water were loaded into the flow loop.
2. The system was deoxygenated by purging it with CO<sub>2</sub> gas until the final oxygen concentration was below 25 ppb.
3. The test was started at the lowest superficial oil velocity (0.5 m/s) and water cut (1-2%).
4. The water cut was gradually increased to 20% at a constant superficial oil velocity. Meanwhile the measurements of wall conductance probes, wall sampling and ferrous ion concentration were taken.

5. The superficial oil velocity was gradually increased to 2 m/s and step 4 was repeated for each superficial oil velocity.
6. After the tests at one angle of inclination were completed, steps 3-5 were repeated for another angle of inclination.

## **4.2 Results and discussion**

### *4.2.1 Horizontal pipe flow test results*

#### 4.2.1.1 LVT200 oil

Because LVT200 oil is a transparent oil, flow pattern visualization could be used in the LVT200 oil test. Based on the results from video images, five different flow patterns were observed: stratified flow with globules, smooth stratified flow, stratified flow with mixing layer, semi-dispersed flow and dispersed flow.

*Superficial oil velocity of 0.5 m/s.* It can be seen in *Figure 4-11* that at lower water cuts (5%-7%) the water phase mainly flowed as clusters of water droplets on the bottom of the pipeline, although thinner water layer was observed from time to time. Stratified flow with globules formed at the bottom of the pipe. By increasing the water cut to 10%, a stable water layer appeared on the bottom of the transparent section and smooth stratified flow formed. As the water cut was increased to 15%, a mixing layer (droplets of water in oil and oil in water) was formed at the oil-water interface. With further increase of the water cut, this layer thickened and a three-layer flow pattern was identified: stratified flow with mixing layer.

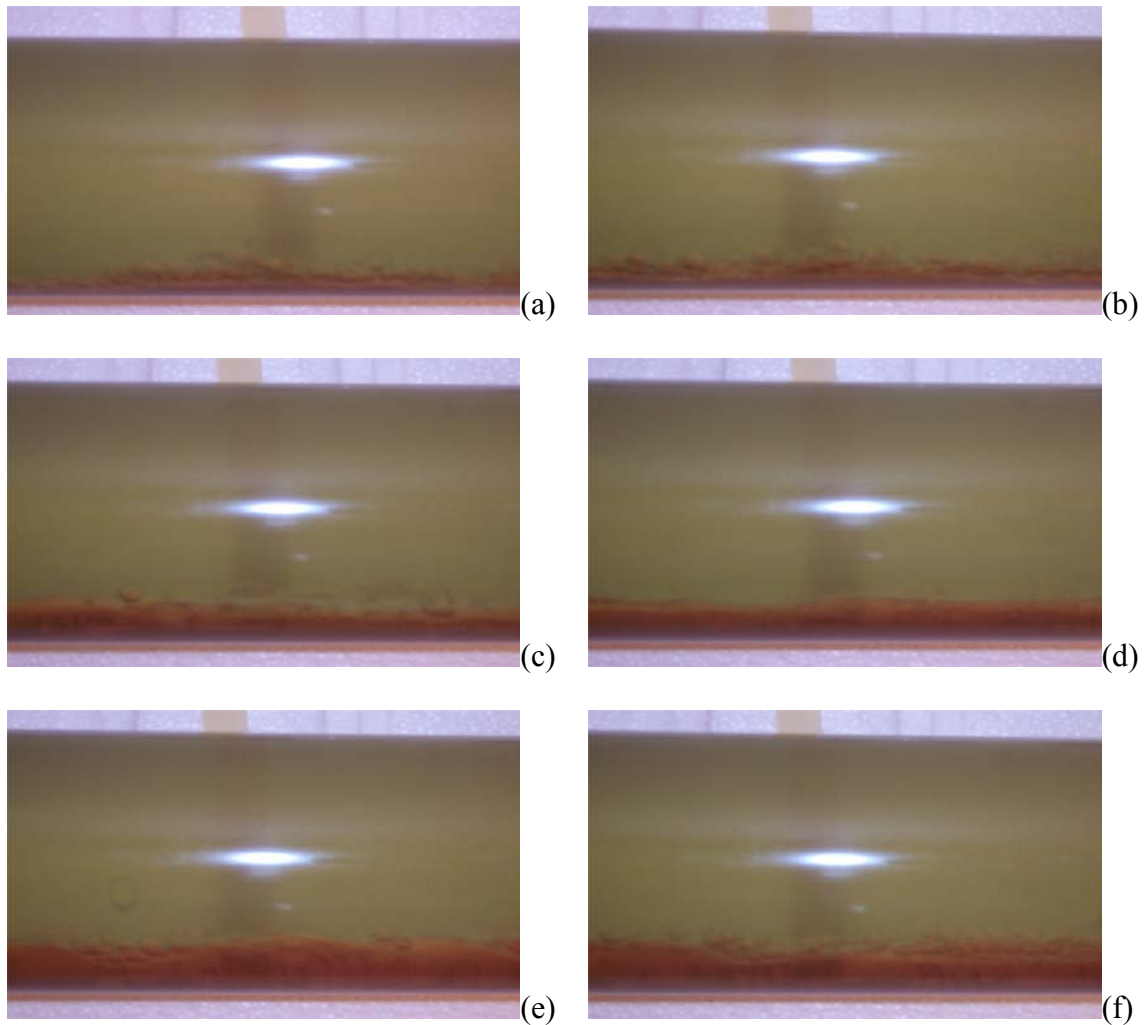


*Figure 4-11.* Images of oil-water two-phase flow at superficial oil velocity of 0.5 m/s and different water cuts as follows: (a) 4.9 %, (b) 6.9 %, (c) 10,0 %, (d) 12.9 %, (e) 15.6% and (f) 18.2 %.

*Superficial oil velocity of 1.0 m/s.* As seen in *Figure 4-12*, three different flow patterns were recorded for a superficial oil velocity of 1.0 m/s: stratified flow with globules, smooth stratified flow and stratified flow with mixing layer. At very low water cut (1.8%), no clear water layer was seen and the water flowed as smaller water droplets in the oil phase with larger water droplets toward the bottom of the pipeline. With

increasing water cut, a stable water layer gradually formed and smooth stratified flow occurred. At water cut higher than 12.9%, fully stratified flow with mixing layer formed.

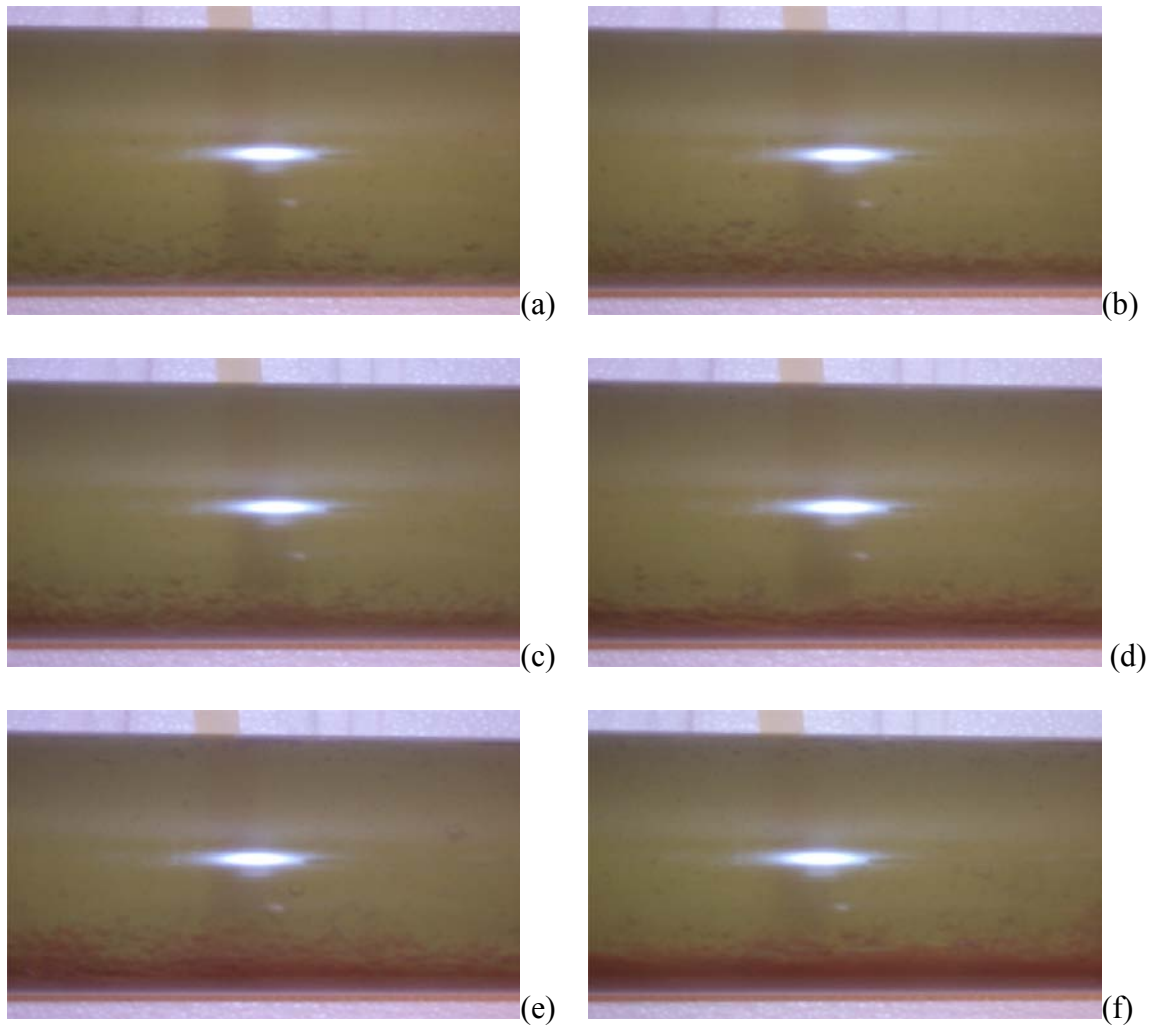


*Figure 4-12.* Images of oil-water two-phase flow at superficial oil velocity of 1.0 m/s and different water cuts as follows: (a) 1.8 %, (b) 3.6%, (c) 6.9 %, (d) 11.5 %, (e) 12.9% and (f) 16.9 %.

*Superficial oil velocity of 1.5 m/s.* At this velocity, no stable water layer formed even at water cut up to 13%, whereas dispersed flow and semi-dispersed flow prevailed (*Figure 4-13*). At very low water cut (2.4%), the intense turbulence caused by higher

superficial oil velocity broke the water phase into small droplets and fully dispersed flow occurred. With increasing water cut to above 6.9%, the distribution of the water droplets was much denser in the bottom part of the pipe than at the top, and semi-dispersed flow formed.

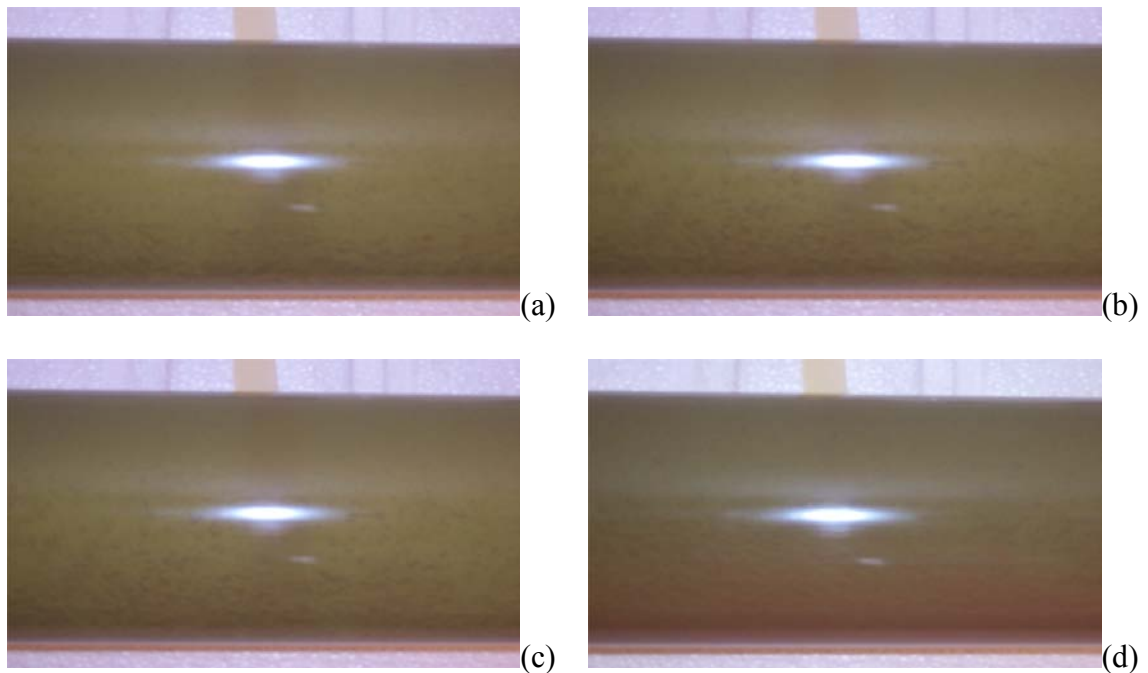


*Figure 4-13.* Images of oil-water two-phase flow at superficial oil velocity of 1.5 m/s and different water cuts as follows: (a) 2.4 %, (b) 6.9%, (c) 10 %, (d) 12.9 %.

*Superficial oil velocity of 2.5 m/s.* By increasing the superficial oil velocity to 2.5 m/s, the intense turbulence broke the water phase into very small droplets not even visible in *Figure 4-14* . The water droplets were distributed uniformly in the cross section of the pipe, and a fully dispersed flow occurred.

By summarizing the flow pattern visualization results discussed above for different flow conditions, a flow pattern map can be created as shown in *Figure 4-15*.



Figure 4-14. Image of oil-water two-phase flow at superficial oil velocity of 2.5 m/s and water cut of 7.5% showing fully dispersed flow.

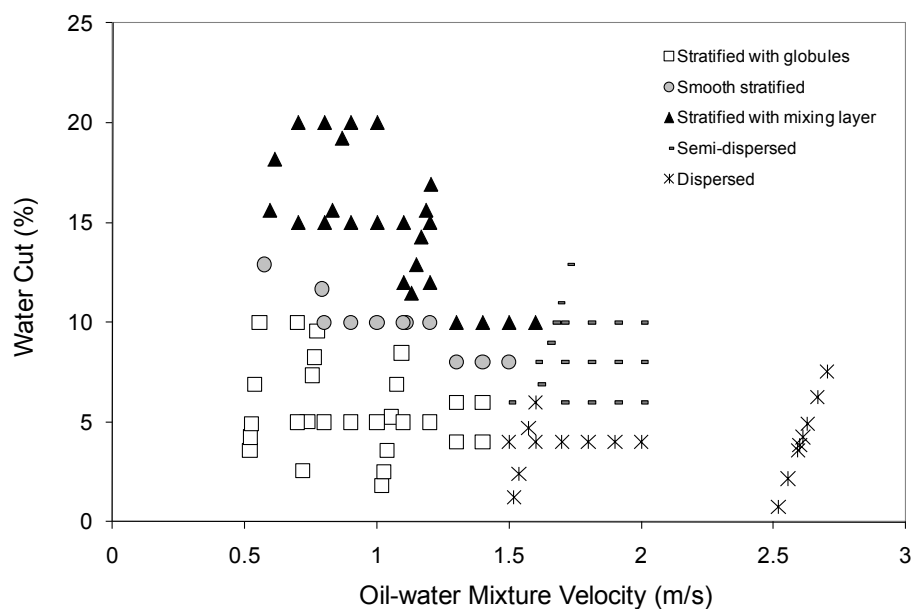


Figure 4-15. Flow pattern map for LVT200 oil-water flow in 4'' horizontal pipe.

After cross-validation of test results using the various techniques, the wall conductance probe data was pulled together in the form of a phase wetting map as shown in Figure 4-16. Three different phase wetting scenarios were identified: water wetting,

where the water phase continuously wetted the pipe surface; oil wetting, where the oil phase continuously wetted the pipe surface; and intermittent wetting, where the oil and water phases wetted the pipe surface intermittently. It can be seen in *Figure 4-16* that intermittent wetting was dominant at oil-water mixture velocities lower than 1.5 m/s and at water cuts less than 10%. Water separation occurred when the water cut was higher than 10%. It is speculated that for a constant oil-water mixture velocity, increasing water cut leads to increased coalescence of water droplets and the oil phase does not carry sufficient turbulent energy to disperse the water phase. Stable stratified flow existed at low velocities, although there was still some mixing at the oil-water interface. Full water entrainment occurred when the oil-water mixture velocity was higher than 1.5 m/s and when water cut was lower than 10%. In this case, all the water phase flowed as water droplets dispersed in the oil phase. Within this oil-water mixture velocity range, increasing the water cut led to the possibility of intermittent phase wetting and corrosion.

It should be stressed that the phase wetting map shown in *Figure 4-16* is valid only for the particular oil (LVT200) in horizontal flow with no chemical additives and for clean steel surface conditions. Results generated subsequently show that the map can change substantially as some of the conditions change. However, from the phase wetting map shown in *Figure 4-16* it is clear that the commonly used rule of thumb stating that water entrainment occurs at oil velocity higher than 1 m/s at water cut less than 30% (Smith, 1987; Adams, Garber, *et al.*, 1993) is not generally valid. With reference to a

phase wetting map, one can predict the phase wetting scenario in the oil pipeline at specific operating conditions\*.

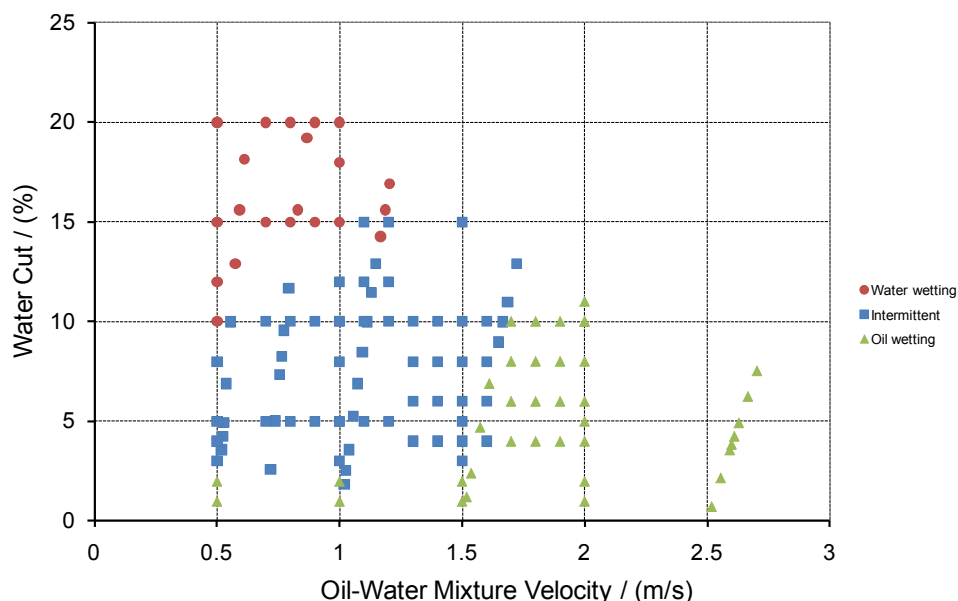


Figure 4-16. Phase wetting map for LVT200 oil at different oil-water mixture velocities and water cuts in horizontal, 4" pipe flow.

The results shown in the above phase wetting map (Figure 4-16) can also be validated with fluid sampling. Table 4-2 shows the fluid sampling results for LVT200 oil in horizontal pipe flow at different mixture velocities and different water cuts. At mixture velocity from 0.5 to 0.6 m/s and water cuts lower than 10%, the concentration of water in the liquid sampling was around 99%, which indicates that the pipe surface is mainly wetted by the water phase and occasionally wetted by oil. This is consistent with

\* The content in the denoted paragraph is adapted from the co-authored paper (Li, C., Tang, X., Ayello, F., Cai, J., and Nešić, S., "Experimental Study on Water Wetting and CO<sub>2</sub> Corrosion in Oil-Water Two-Phase Flow", NACE CORROSION/06, Paper No. 06595, San Diego, CA, 2006.)

the occurrence of intermittent wetting determined by wall conductance probes shown in *Figure 4-16*. By increasing the water cut to above 13%, there was only water in the sample - which further validates the existence of a stable water layer at the bottom of pipe - and water wetting occurred. For mixture velocity of around 1 m/s, at low water cuts (1.9%-5.3%), less water (50%-90%) was found in the liquid sample than at mixture velocity around 0.5 m/s. This is because more water was entrained by oil flow and more oil wetted the bottom of the pipe. By increasing the water cut to above 13%, however, almost 100% water could be seen in the sample. In this case, the intensity of the oil flow was not enough to entrain the water phase, and water wetting occurred. When the oil-water mixture velocity was higher than 1.5 m/s, oil and water formed dispersion flow. It took around 2 minutes for the oil phase and the water phase in the sampling fluid to separate completely. When the water concentration in the sample was lower than 20%, the dispersion formed was water-in-oil dispersion, in which oil is the continuous phase and water is the dispersed phase. However, when the water concentration in the sample was 40% or higher, the dispersion formed in the pipe changed from water-in-oil dispersion to oil-in-water dispersion, which is in agreement with the phase inversion point for LVT200 oil found by Shi (2001). The bottom of the pipe was intermittently wetted by oil and water phase. Only 2-5% water was found in the liquid samples when the mixture velocity was higher than 2.5 m/s. This implies that under these conditions, almost all the water was entrained by the highly turbulent oil flow, and the oil phase continuously wetted the pipe surface, as indicated by the wall conductance probe results shown in *Figure 4-16*.

$\text{Fe}^{2+}$  concentration monitoring was also applied to corroborate the results obtained through other techniques. Water samples were acquired from the sampling port at the water boot of the oil-water separator every 30 minutes during a 2.5 hour test, while the flow conditions were kept constant. *Table 4-3* shows the results of  $\text{Fe}^{2+}$  concentration changes under different phase wettings in LVT200 oil-water horizontal flow. It can be seen that under water wetting and intermittent wetting conditions, the  $\text{Fe}^{2+}$  concentration increased, which indicates the occurrence of corrosion. However, there was no change of the  $\text{Fe}^{2+}$  concentration under oil wetting conditions, which means no corrosion occurred. This validates the conclusion that the pipe was continuously wetted by the flowing oil phase.

Table 4-2. Water concentration in the fluid samples for LVT200 oil in horizontal pipe flow at different mixture velocities and different water cuts.

Oil-water mixture velocity (m/s)	Water cut (%)	Water concentration in the fluid sample (%)	Phase Wetting From Wall Conductance Probes
0.519	3.7	99	Intermittent wetting
0.522	4.2	99	Intermittent wetting
0.556	10.1	99	Water wetting
0.574	12.9	100	Water wetting
0.593	15.7	100	Water wetting
1.019	1.9	50	Intermittent wetting
1.037	3.6	75	Intermittent wetting
1.056	5.3	90	Intermittent wetting
1.15	13.0	99	Water wetting
1.17	14.5	100	Water wetting
1.19	16.0	100	Water wetting
1.2	16.7	100	Water wetting
1.574	4.7	10	Oil wetting
1.61	6.8	20	Intermittent wetting
1.65	9.1	40	Intermittent wetting
1.69	11.2	60	Intermittent wetting
1.72	12.8	60	Intermittent wetting
2.519	0.7	5	Oil wetting
2.556	2.2	5	Oil wetting
2.593	3.6	4	Oil wetting
2.6	3.9	2	Oil wetting
2.67	6.4	2	Oil wetting
2.7	7.4	2	Oil wetting

Table 4-3. The change in  $Fe^{2+}$  concentration under different flow conditions in LVT200 oil and  $CO_2$  saturated, 1 wt% NaCl D.I. water horizontal flow.

Oil-water mixture velocity (m/s)	Water cut (%)	Testing time (Min.)	$Fe^{2+}$ Change (ppm)	Phase wetting	Corrosion rate (mm/yr)
0.6	16	30	1.32	Water wetting	1.7
0.8	14	30	0.57	Intermittent wetting	0.9
1.6	7	30	0	Oil wetting	0

#### 4.2.1.2 C1 crude oil

In comparison with the LVT200 model oil, the C1 crude oil is lighter (see *Figure 4-7*), slightly less viscous (see *Figure 4-9*) and has a significantly lower interfacial tension (see *Figure 4-10*). On one hand, the lower density of this oil would suggest a higher propensity for separation from water; on the other hand, the lower surface tension points to the opposite effect, i.e. that this oil would be easier to “mix” with water.

The phase wetting map for C1 crude oil and 1 wt% NaCl water at different mixture velocities and water cuts in a 4” horizontal pipe flow is shown in *Figure 4-17*, as obtained by the wall conductance probes. From this plot, for very low water cuts (<3%), complete water entrainment already happened readily at 0.8 m/s mixture velocity. However, the entrainment velocity rapidly increased between water cuts of 5 – 10%, a different trend from that which was observed with the LVT200 model oil. At water cuts of 10% and beyond, C1 oil could not completely entrain the water even at 2 m/s mixture velocity. Water wetting prevailed when the water cut was higher than 10% and oil-water mixture velocity was lower than 1.3 m/s.

The result from the wall fluid sampling for C1 crude oil in the horizontal pipe flow shown in *Table 4-4* was roughly consistent with the result simultaneously obtained from the wall conductance probes. At an oil-water mixture velocity of 0.8 m/s and water cuts of 1% and 4%, the water concentrations in the fluid samplings were 60% and 80%, respectively; under these conditions, the wall conductance probes showed intermittent wetting. By increasing the water cuts to 5% and 10% at the same mixture velocity of 0.8 m/s, water concentrations in the fluid samplings increased to 90% and 99%, which

indicates that stable water wetting occurred and a pure water layer was formed at the bottom of the pipe. When the results for a water cut of 10% were compared for mixture velocities of 0.8 m/s and 1.3 m/s, the water concentration in the fluid sample decreased from 99% to 70%, which indicates that more water was entrained in the oil phase at the higher mixture velocity, since higher oil flow rate leads to higher turbulence and higher entrainment. From the results of the wall conductance probes (*Figure 4-17*), it can be seen that the phase wetting changed from stable water wetting to intermittent wetting. However, in many instances where stable oil wetting was detected, some water was seen in the samples. This shows that, while the fluid sampling technique results showed trends that were consistent with the wall conductivity measurements, they alone could not provide sufficient information to identify which fluid was wetting the wall.

*Table 4-5* shows the average corrosion rate results obtained with  $\text{Fe}^{2+}$  monitoring for C1 crude oil at oil-water mixture velocity of 0.7 m/s and a water cut of 15%. These conditions were expected to produce water wetting according to the phase wetting map of C1 crude oil in the horizontal pipe flow (*Figure 4-17*). The increase in  $\text{Fe}^{2+}$  concentration during flow loop tests was consistent with the water wetting results obtained from the wall conductance probes.

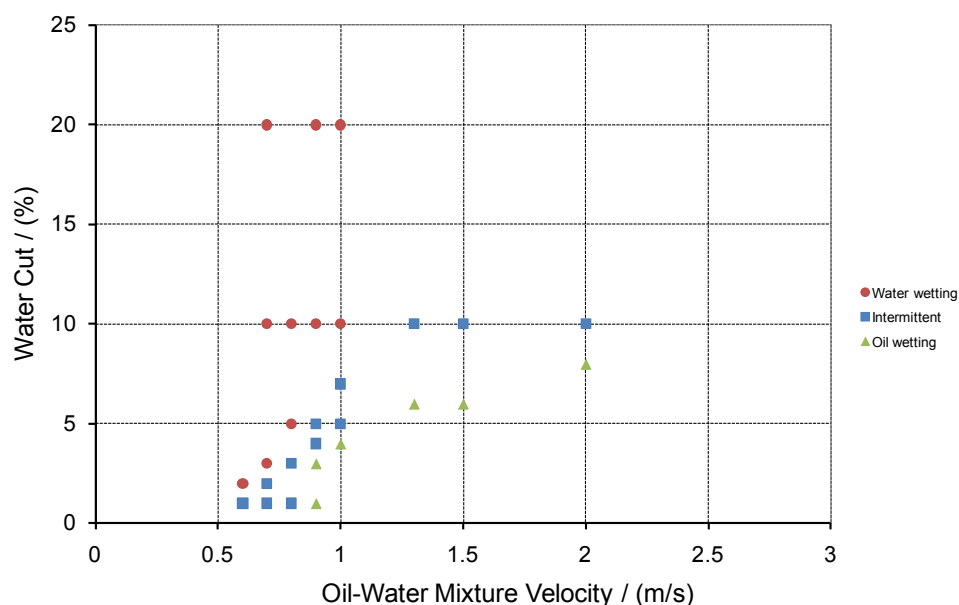


Figure 4-17. Phase wetting map for C1 crude oil at different oil-water mixture velocities and water cuts in horizontal, 4" pipe flow.

Table 4-4. Water concentration in the fluid samples for C1 crude oil in horizontal pipe flow at different mixture velocities and different water cuts.

Oil-Water Mixture Velocity m/s	Input Water Cut %	Water Concentration by Volume %	Phase Wetting From Wall Conductance Probes
0.8	1	60	Intermittent Wetting
0.8	4	80	Intermittent Wetting
0.8	10	99	Water Wetting
0.9	3	10	Oil Wetting
0.9	5	80	Intermittent Wetting
0.9	10	99	Water Wetting
1.0	4	5	Oil Wetting
1.0	7	80	Intermittent Wetting
1.0	10	95	Water Wetting
1.3	6	5	Oil Wetting
1.3	10	70	Intermittent Wetting
1.5	6	5	Oil Wetting
1.5	10	70	Intermittent Wetting
2.0	8	5	Oil Wetting
2.0	10	50	Intermittent Wetting

Table 4-5. Fe<sup>2+</sup> concentration changes under water wetting in C1 crude oil-water horizontal flow and the estimate of the corresponding corrosion rate.

Oil-water mixture velocity (m/s)	Water cut (%)	Testing time (Min.)	Fe <sup>2+</sup> Change (ppm)	Phase wetting	Average corrosion rate (mm/yr)
0.7	15	30	1.9	Water wetting	2.3
0.7	15	30	2.4	Water wetting	

#### 4.2.1.3 C2 crude oil<sup>\*</sup>

The C2 crude oil is similar to the LVT200 model oil in terms of density (see *Figure 4-7*); however it is more viscous than the LVT200 or the C1 crude oil (see *Figure 4-9*), suggesting that it may be more effective in entraining water. Like the C1 crude oil, the C2 oil exhibits rather low oil-water interfacial tension (see *Figure 4-10*), reinforcing the same expectation of increased water entrainment.

*Figure 4-18* shows the phase wetting map for C2 crude oil at different oil-water mixture velocities in horizontal pipe flow based on the wall conductance probe data. It was found that for the lower water cuts (<5%), C2 crude oil was able to entrain the water at 0.7 m/s mixture velocity. However, as more water was added, the entrainment velocity increased to 1 m/s at 10% water cut and 1.3 m/s at 15% water cut. The minimum water cut for forming stable water wetting ranged from 6% to 11% at oil-water mixture velocity ranging from 0.6 to 0.9 m/s. However it jumped to 20% when the mixture velocity increased to 1 m/s. This is because when oil-mixture velocity was higher than 1 m/s, stable oil-water emulsion formed and both the oil-water separation and the coalescence of water droplets became more difficult.

<sup>\*</sup> The content in the denoted section (Section 4.2.1.3) is adapted from the co-authored paper (Li, C., Tang, X., Ayello, F., Cai, J., and Nešić, S., "Experimental Study on Water Wetting and CO<sub>2</sub> Corrosion in Oil-Water Two-Phase Flow", NACE CORROSION/06, Paper No. 06595, San Diego, CA, 2006.)

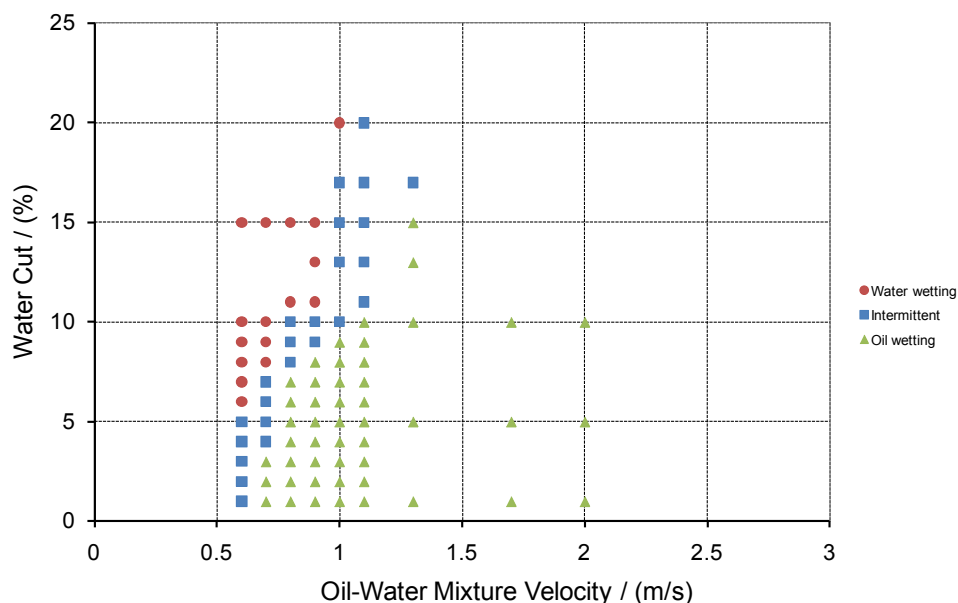


Figure 4-18. Phase wetting map for C2 crude oil at different oil-water mixture velocities and water cuts in horizontal, 4" pipe flow.

In order to confirm the accuracy of results obtained from the wall conductance probes, fluid sampling at the wall is displayed in *Table 4-6*. At mixture velocity of 0.6 m/s and water cut of 5%, liquid sampling recovered about 90% water and 10% oil. This is consistent with the occurrence of intermittent wetting determined by wall conductance probes. When the input water cut was between 8% and 10%, liquid samples were about 99% water and 1% oil. When the input water cut was 15%, the fluid sample contained only water. This denotes that a pure water layer was formed at the bottom of the pipe. At a mixture velocity of 1.0 m/s and a 3% water cut - conditions with stable oil wetting according to the phase wetting map (*Figure 4-18*) - the water concentration in the sample

Table 4-6. Water concentration in the fluid samples for C2 crude oil-water in horizontal pipe flow at different oil-water mixture velocities and water cuts.

Oil-Water Mixture Velocity m/s	Input Water Cut %	Water Concentration by Volume %	Phase Wetting From Wall Conductance Probes
0.6	5	90	Intermittent Wetting
0.6	8	99	Water Wetting
0.6	10	99	Water Wetting
0.6	15	100	Water Wetting
0.7	3	5	Oil Wetting
0.7	5	90	Intermittent Wetting
0.7	8	99	Water Wetting
0.7	10	99	Water Wetting
0.7	15	100	Water Wetting
0.8	3	5	Oil Wetting
0.8	5	5	Oil Wetting
0.8	8	90	Intermittent Wetting
0.8	10	90	Intermittent Wetting
0.8	15	99	Water Wetting
0.9	3	10	Oil Wetting
0.9	5	10	Oil Wetting
0.9	8	10	Oil Wetting
0.9	10	90	Intermittent Wetting
0.9	15	99	Water Wetting
1	3	10	Oil Wetting
1	5	10	Oil Wetting
1	8	10	Oil Wetting
1	10	80	Intermittent Wetting
1	15	80	Intermittent Wetting
1	20	99	Water Wetting
1.1	3	8	Oil Wetting
1.1	5	8	Oil Wetting
1.1	8	8	Oil Wetting
1.1	10	7	Oil Wetting
1.1	15	80	Intermittent Wetting
1.1	20	80	Intermittent Wetting
1.3	5	5	Oil Wetting
1.3	10	8	Oil Wetting
1.3	15	8	Oil Wetting
1.3	17	80	Intermittent Wetting
1.7	5	5	Oil Wetting
1.7	10	5	Oil Wetting
2	5	5	Oil Wetting

was still 10%. Even at a mixture velocity of 2 m/s and low water cuts, the water concentration in the fluid sample was still measurable at about 5%. This suggests that the oil-water mixture close to the bottom of the pipe wall was not a pure oil layer, but can be characterized as water-in-oil suspension with oil wetting the pipe wall.

*Table 4-7* shows the corrosion rate results obtained with the  $\text{Fe}^{2+}$  concentration monitoring for C2 crude oil and  $\text{CO}_2$  saturated 1 wt% NaCl D.I. water in horizontal pipe flow. At a mixture velocity of 0.9 m/s and water cut of 4%, where oil wetting was seen, no corrosion was detected (i.e., the  $\text{Fe}^{2+}$  concentration did not increase with time). If the water cut was increased to 8% at the same mixture velocity, which was identified as intermittent wetting, corrosion did occur, and a corrosion rate of 1.8 mm/yr was measured. When even more water was present (water cut of 12%), leading to stable water wetting, the corrosion rate increased to 3.9 mm/yr. The corrosion rate under stable water wetting was thus almost double that under intermittent wetting conditions.

*Table 4-7.* Change in  $\text{Fe}^{2+}$  concentration under different flow conditions with C2 crude oil and  $\text{CO}_2$  saturated, 1 wt% NaCl D.I. water in horizontal flow and the corresponding corrosion rate.

Oil-water mixture velocity (m/s)	Water cut (%)	Testing time (Min.)	$\text{Fe}^{2+}$ change (ppm)	Phase wetting	Corrosion rate (mm/yr)
0.9	4	10	0	Oil wetting	0
0.9	8	10	0.2	Intermittent wetting	1.8
0.9	12	10	0.4	Water wetting	3.9

#### 4.2.1.4 C3 crude oil

The C3 crude oil is a medium heavy oil (see *Figure 4-7*), and is more viscous than the C1 and C2 crude oils (see *Figure 4-9*), which suggests that it should be more

effective in entraining water. The C3 has slightly higher oil-water interfacial tension than the C1 and C2 crude oils (*Figure 4-10*).

*Figure 4-19* shows the phase wetting map for C3 crude oil at different oil-water mixture velocities and water cuts in horizontal pipe flow. While data for the very low water cuts is not available, it can nevertheless be seen that this oil was more effective in entraining water at lower water cuts. For instance, at 7% water cut, all of the water was already entrained beyond a mixture velocity of 0.5 m/s. Even for very high water cuts the entrainment velocity was just over 1 m/s.

*Table 4-8* shows the fluid sampling results for C3 crude oil and 1 wt% NaCl water in horizontal pipe flow. A similar trend was seen as in the C1 and C2 oils, where water was present in the samples even under conditions where stable oil wetting was measured.

*Table 4-9* shows the corrosion rate obtained with  $\text{Fe}^{2+}$  concentration monitoring for C3 crude oil and 1 wt% NaCl, D.I water in horizontal pipe flow. When oil wetting was detected by the conductance probes, no corrosion could be measured. In intermittent wetting conditions, the corrosion rate was measured to be 1.3 mm/yr, while under stable water wetting it increased to 2.8 mm/yr. The corrosion rate under stable water wetting was almost double the rate under intermittent wetting condition.

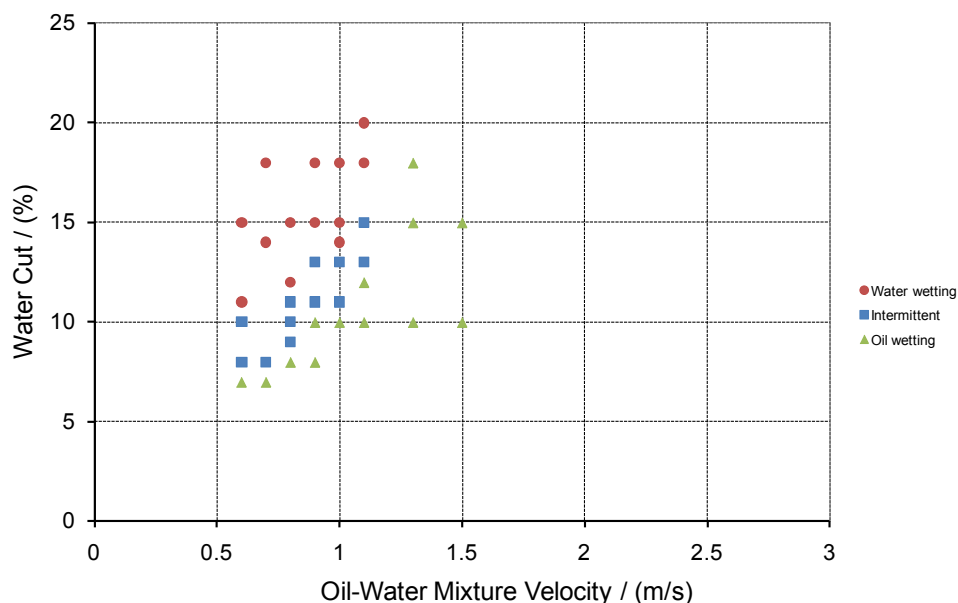


Figure 4-19. Phase wetting map for C3 crude oil at different oil-water mixture velocities and water cuts in horizontal, 4" pipe flow.

Table 4-8. Water concentration in the fluid samples for C3 crude oil-water in horizontal pipe flow at different oil-water mixture velocities and water cuts.

Oil-Water Mixture Velocity m/s	Input Water Cut %	Water Concentration by Volume %	Phase Wetting From Wall Conductance Probes
0.6	7	5	Oil Wetting
0.6	10	70	Intermittent Wetting
0.6	15	99	Water Wetting
1.0	10	5	Oil Wetting
1.0	13	80	Intermittent Wetting
1.0	15	95	Water Wetting

Table 4-9. Changes in the  $Fe^{2+}$  concentration under different phase wetting conditions with C3 crude oil-water horizontal flow and the corresponding corrosion rate.

Oil-water mixture velocity (m/s)	Water cut (%)	Testing time (Min.)	$Fe^{2+}$ change (ppm)	Phase wetting	Corrosion rate (mm/yr)
0.6	5	30	0	Oil wetting	0
0.6	8	30	0.18	Intermittent wetting	1.3
0.6	15	30	0.44	Water wetting	2.8

#### 4.2.1.5 C4 crude oil

C4 crude oil is the second-heaviest of all the oils tested (see *Figure 4-7*). It is considerably more viscous than crude oils C1 through C3 (see *Figure 4-9*). C4 has the smallest oil-water interfacial tension of all the tested oils. These features of C4 indicate a large propensity to form emulsion when it flows with water in the pipeline.

*Figure 4-20* shows the phase wetting map for C4 crude oil at different oil-water mixture velocities and water cuts in horizontal pipe flow. When the mixture velocity was between 0.6 m/s and 1 m/s and the water cut was higher than 10%, water wetting prevailed. The water cut leading to the transition from intermittent wetting to stable water wetting increased from 8% to 15% when the oil-water mixture velocity increased from 0.6 m/s to 1 m/s. When the oil-water mixture velocity was higher than 1m/s, oil wetting prevailed even at a high water cut (up to 25%) and stable water-in-oil emulsion formed, which was confirmed by the water samples taken from the test section.

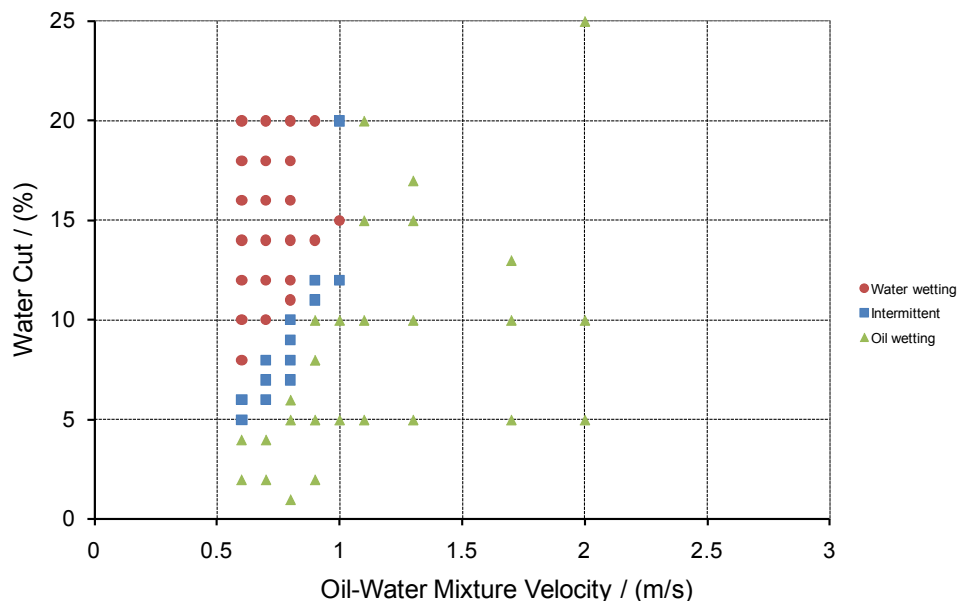


Figure 4-20. Phase wetting map for C4 crude oil at different oil-water mixture velocities and water cuts in horizontal, 4" pipe flow.

The results shown in the phase wetting map are validated by the fluid sampling and  $\text{Fe}^{2+}$  concentration monitoring results. Table 4-10 shows the fluid sampling results at different oil-water mixture velocities and water cuts. Under flow conditions where oil wetting occurred, the water volume recovered from the fluid sampling was less than 5%. While at the flow conditions water wetting happened, the water volume was more than 95%. The wall sampling results validate the results obtained from wall conductance probes. When the mixture velocity was higher than 1 m/s, oil-water emulsion formed. In this case, the fluid samples required a few days to allow the oil and water to separate completely. The measured water concentration was less than 5%, which indicates the occurrence of stable oil wetting.

In order to confirm the results from the wall conductance probes and wall sampling method, ER probe corrosion monitoring was used when oil and water formed a stable emulsion. It can be seen from the results shown in *Table 4-11* that corrosion was negligible, even with water present up to 40%, once the emulsion formed. When the water cut increased from 50% to 55%, the corrosion rate increased abruptly, indicating that the phase wetting transitioned from oil wetting to intermittent wetting.

*Table 4-10.* Water concentration in the fluid samples for C4 crude oil-water in horizontal pipe flow at different oil-water mixture velocities and water cuts.

Oil-Water Mixture Velocity m/s	Input Water Cut %	Water Concentration by Volume %	Phase Wetting From Wall Conductance Probes
0.6	2	1	Oil wetting
0.6	5	50	Intermittent wetting
0.6	15	99	Water wetting
0.9	10	5	Oil wetting
0.9	12	60	Intermittent wetting
0.9	15	95	Water wetting
1	10	60	Intermittent wetting
1	15	70	Intermittent wetting
1.3	15	5	Oil wetting

*Table 4-11.* Corrosion rates measured by an ER probe when C4 crude oil and water form emulsion at different oil-water mixture velocities and water cuts in horizontal pipe flow.

Oil-water mixture velocity (m/s)	Water cut (%)	Corrosion rate (mm/yr)
1	10	0.02
1	15	0
1	40	0
1	50	0.08
1	55	0.34
1	60	0.36
2	10	0.02
2	15	0

#### 4.2.1.6 C5 crude oil

C5 crude oil is the heaviest and the most viscous of all the oils tested (see *Figure 4-7* and *Figure 4-9*). C5 crude oil was expected to form emulsion much more easily than other oils when flowing with water in the pipe.

*Figure 4-21* shows the phase wetting map for C5 crude oil at different oil-water mixture velocities and water cuts in horizontal pipe flow. It is clear that at a mixture velocity of 0.6 m/s, the oil phase fully entrained up to 5% water. By increasing the mixture velocity to 0.9 m/s, at least 20% of the water was entrained, reaching the upper limit of the tested water cuts. A stable water wetting regime could only be obtained at very low velocity (0.6-0.7 m/s) and very high water cut (15-20%).

*Table 4-12* shows wall sampling results for C5 crude oil, which agree with the results obtained from wall conductance probes. Under flow conditions where oil wetting occurred, the water volume recovered from the water sampling was less than 10%; in the case of water wetting, however, the water volume was greater than 90%,

*Table 4-13* shows corrosion rate results given by ER probe monitoring at 0.9 m/s oil-water mixture velocity and water cuts from 20%-70%. There was a near absence of corrosion with water cut up to 60%.

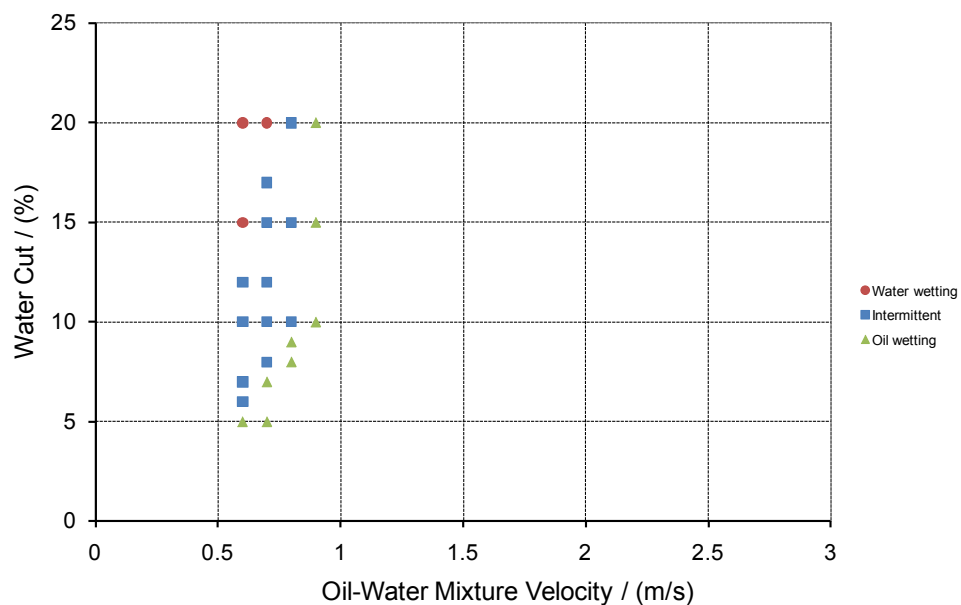


Figure 4-21. Phase wetting map for C5 crude oil at different oil-water mixture velocities and water cuts in horizontal, 4" pipe flow.

Table 4-12. Water concentration in the fluid samples for C5 crude oil-water in horizontal pipe flow at different oil-water mixture velocities and water cuts.

Oil-Water Mixture Velocity m/s	Input Water Cut %	Water Concentration by Volume %	Phase Wetting From Wall Conductance Probes
0.6	5	10	Oil Wetting
0.6	10	70	Intermittent Wetting
0.6	15	95	Water Wetting
0.8	9	5	Oil Wetting
0.8	15	80	Intermittent Wetting
0.9	15	Emulsion	Oil Wetting

*Table 4-13.* Corrosion rates measured by ER probe when C5 crude oil and water form emulsion at oil-water mixture velocity of 0.9 m/s and different water cuts in horizontal pipe flow.

Oil-water mixture velocity (m/s)	Water cut (%)	Corrosion rate (mm/yr)
0.9	20	0
0.9	40	0.01
0.9	50	0.02
0.9	60	0.05
0.9	70	0.1

#### *4.2.2 Transition between stable oil wetting and intermittent wetting*

Based on the experimental results, it can be concluded that corrosion is eliminated when oil wetting occurs. Therefore, from a corrosion protection perspective, it is very important to determine the flow conditions that lead to a transition from intermittent wetting to stable oil wetting, represented by a transition line that is the boundary between the oil wetting region and the adjacent intermittent wetting region. The effects of oil type and pipe inclination on this transition line are discussed in the following sections.

##### 4.2.2.1 Effect of oil type

*Figure 4-22* shows the transition lines from intermittent wetting to stable oil wetting for LVT200 oil and the five crude oils in horizontal pipe flow. It appears that the transition line between stable oil wetting and intermittent wetting, which is really the demarcation line of corrosion/non-corrosion conditions, is different for all the oils tested. The differences in the physical properties of the oils provide some clues as to why various water wetting outcomes appear.

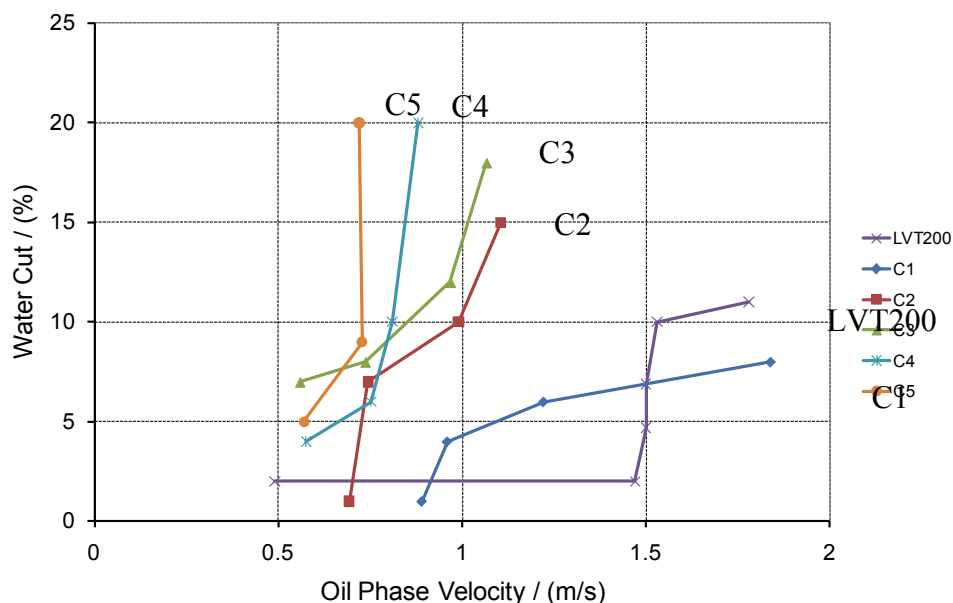


Figure 4-22. Transition lines from intermittent wetting to stable oil wetting for LVT200 oil and five crude oils (C1 – C5) in horizontal pipe flows.

As can be seen from the transition lines in *Figure 4-22*, stable oil wetting occurs at much lower oil phase velocity for all crude oils except C1, compared to LVT200 model oil. This can be explained by the effect of their differences in oil-water interfacial tension. As shown in the water wetting model described in Chapter 3 (Equation (3.24)), the smaller the oil-water interfacial tension, the more water can be entrained by the same turbulence energy, i.e. lower oil phase velocity is needed to entrain the same amount of water. It can be seen in *Figure 4-10* that crude oils have much lower oil-water interfacial tension (23.2-28.1 dyne/cm) than LVT200 oil (38.4 dyne/cm).

The effect of the oil viscosity on the transition line from intermittent wetting to stable oil wetting can also be explained through analysis of the water wetting model described in Chapter 3. From Equations (3.25) to (3.38), it can be concluded that the

greater the oil viscosity, the smaller the water droplet that will be produced, i.e. the easier it will be for the higher viscosity oil phase to entrain the water phase. Comparing the viscosity of different oils in *Figure 4-9*, it can be seen that C5 has the greatest viscosity, and its transition line lies farthest to the left in *Figure 4-22*, meaning that C5 is the most efficient in entraining water.

The oil density also plays a role in the performance of different oils in entraining water. From Equation (3.28), the higher the oil density (which is closer to density of water), the smaller the gravity force  $F_g$ , which pulls the water droplet to the pipe wall. Therefore, higher density of oil is more favorable for water entrainment. *Figure 4-22* shows the transition lines for C1 to C5 laid from right to left, which is in accordance with the density of C1 to C5 shown in *Figure 4-7*. It is also interesting to note that C1 crude oil entrains less water than LVT200 model oil in high oil phase region (1.5 m/s). This can be explained by the fact that C1 crude oil is a very light oil, even lighter and less viscous than LVT200.

#### 4.2.2.1 Effect of pipe inclination on phase wetting transition

Series of experiments with different crude oils in horizontal and inclined pipe flows were carried out in order to investigate the effect of pipe inclination on phase wetting. *Figure 4-23* to *Figure 4-32* show the transition lines from intermittent wetting to stable oil wetting in horizontal and various inclined pipe flows for different crude oils (C1-C5). A positive inclination angle stands for the results obtained from the upstream test section, and a negative inclination angle stands for the results from the downstream test section. For all the crude oils tested in both upstream and downstream pipe flow, the

pipe inclination had an effect on the transition from intermittent wetting to stable oil wetting, depending on how much the inclination deviated from the horizontal direction. It can be seen that for near-horizontal pipe flow (inclination lower than  $5^\circ$ ), either upstream or downstream, the change of inclination had a very minor effect on the phase wetting transition. However, for crude oils C1-C3, when the inclination increased to  $45^\circ$  angle, the effect was very significant, and the phase wetting transition line shifted to a higher water cut at a given oil-water mixture velocity. In horizontal flow, gravity force tends to separate oil and water because of the density difference. In inclined pipe flow, however, the gravity force tends to pull the fluid back or forth, which accelerates the mixing of oil and water and makes the water more easily entrained by the flowing oil. For crude oils C4-C5, a very tight water-in-oil dispersion was formed under all test conditions when the inclination of the pipeline was increased to  $45^\circ$  or  $90^\circ$ . Once water-in-oil dispersion formed, wall conductance probes indicated that oil wetting prevailed.

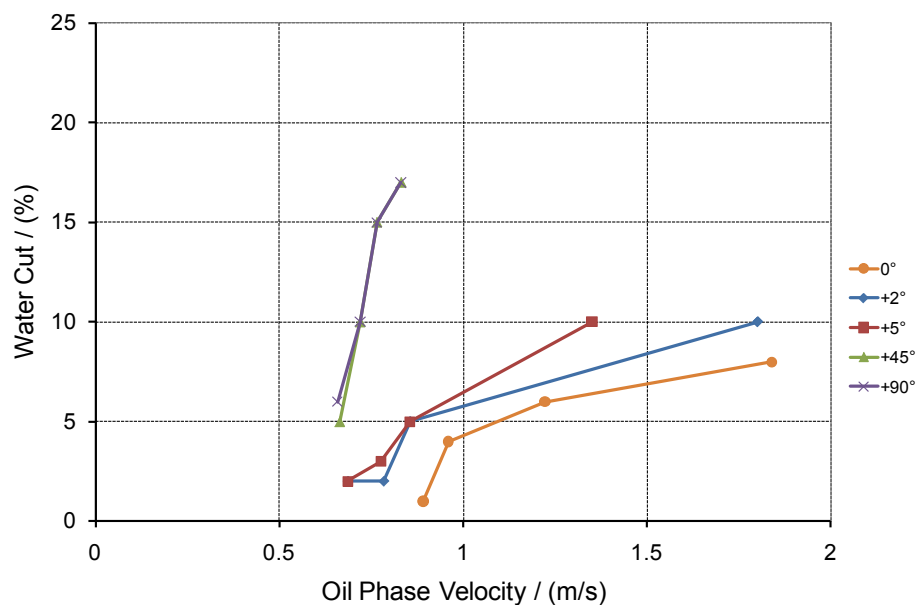


Figure 4-23. Transition lines from intermittent wetting to stable oil wetting for C1 crude oil in oil-water two-phase flow at horizontal and different upward inclination angles.

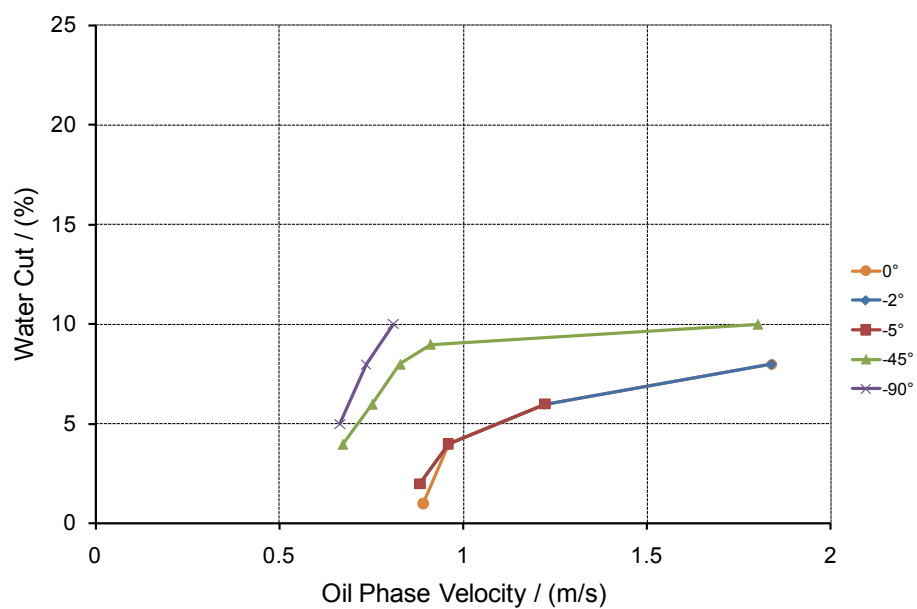


Figure 4-24. Transition lines from intermittent wetting to stable oil wetting for C1 crude oil in oil-water two-phase flow at horizontal and different downward inclination angles.

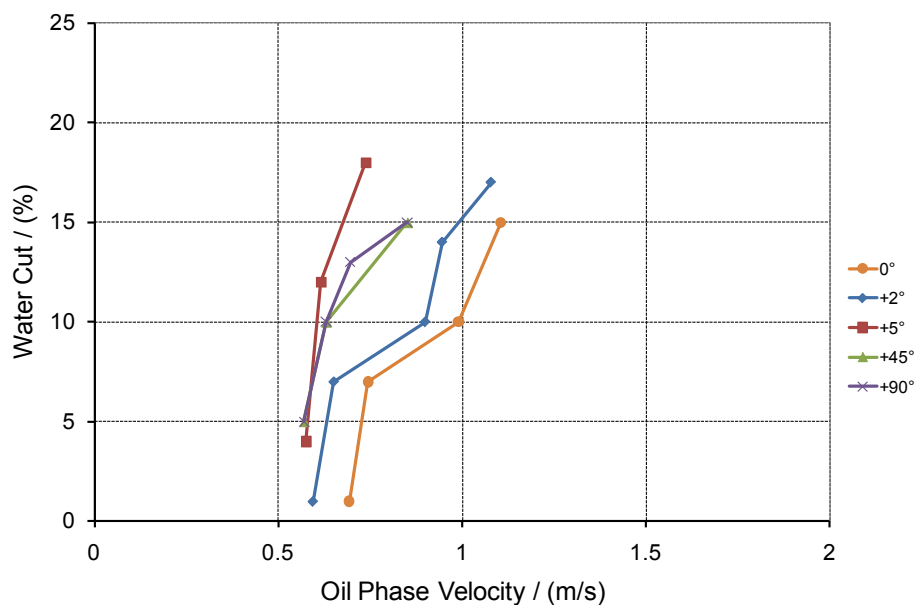


Figure 4-25. Transition lines from intermittent wetting to stable oil wetting for C2 crude oil in oil-water two-phase flow at horizontal and different upward inclination angles.

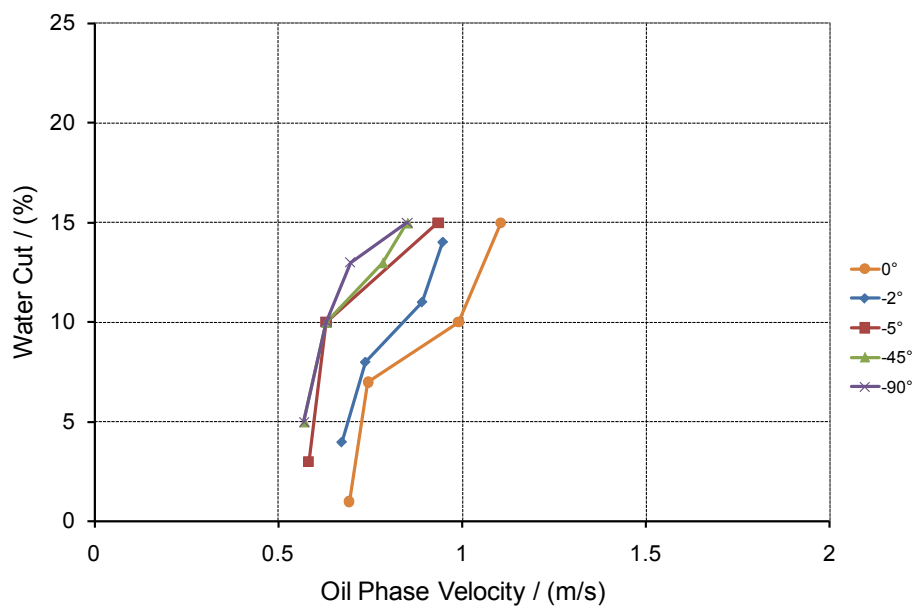


Figure 4-26. Transition lines from intermittent wetting to stable oil wetting for C2 crude oil in oil-water two-phase flow at horizontal and different downward inclination angles.

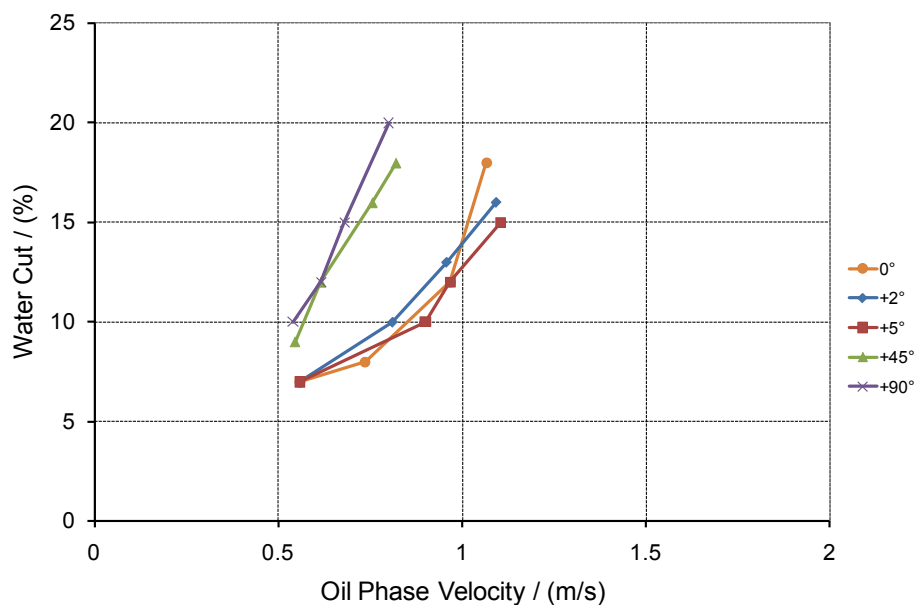


Figure 4-27. Transition lines from intermittent wetting to stable oil wetting for C3 crude oil in oil-water two-phase flow at horizontal and different upward inclination angles.

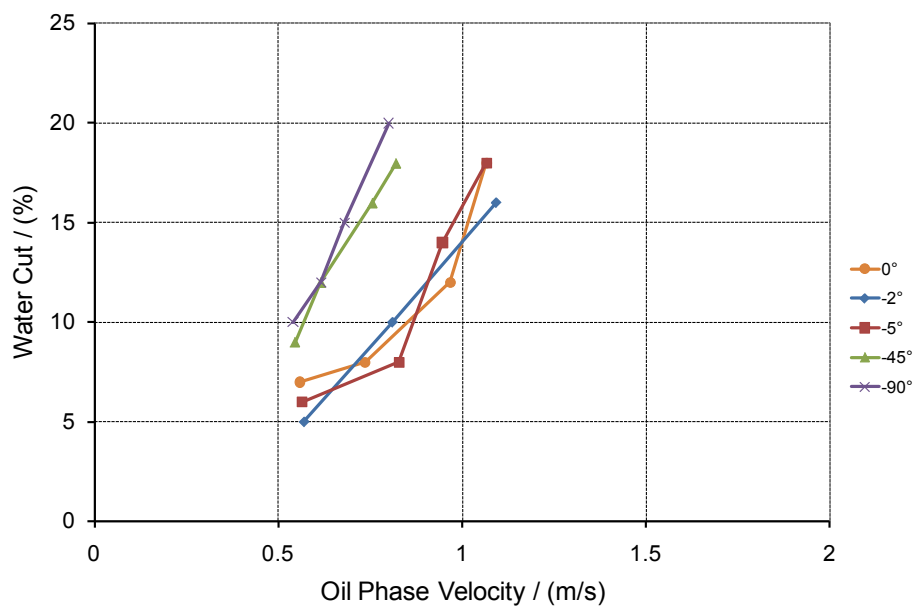


Figure 4-28. Transition lines from intermittent wetting to stable oil wetting for C3 crude oil in oil-water two-phase flow at horizontal and different downward inclination angles.

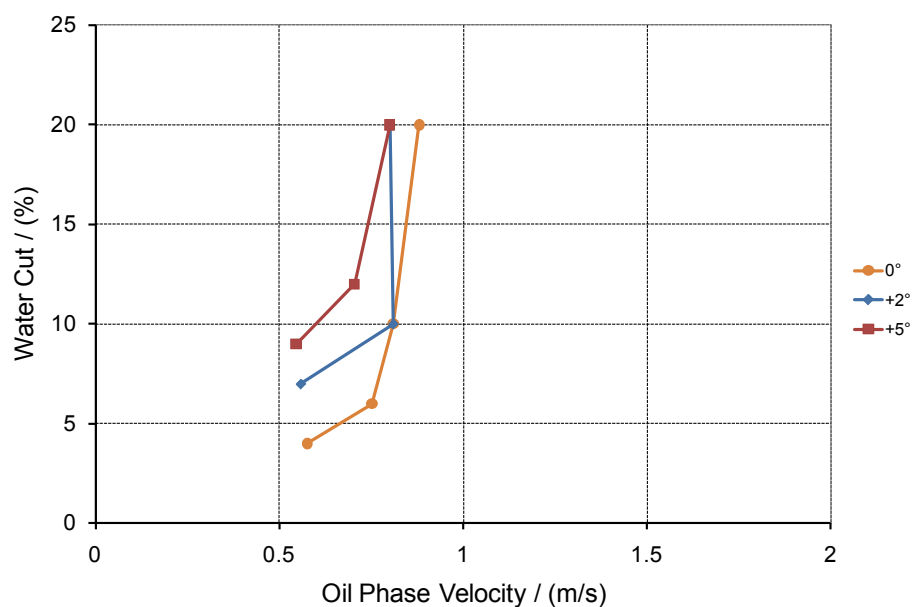


Figure 4-29. Transition lines from intermittent wetting to stable oil wetting for C4 crude oil in oil-water two-phase flow at horizontal and different upward inclination angles.

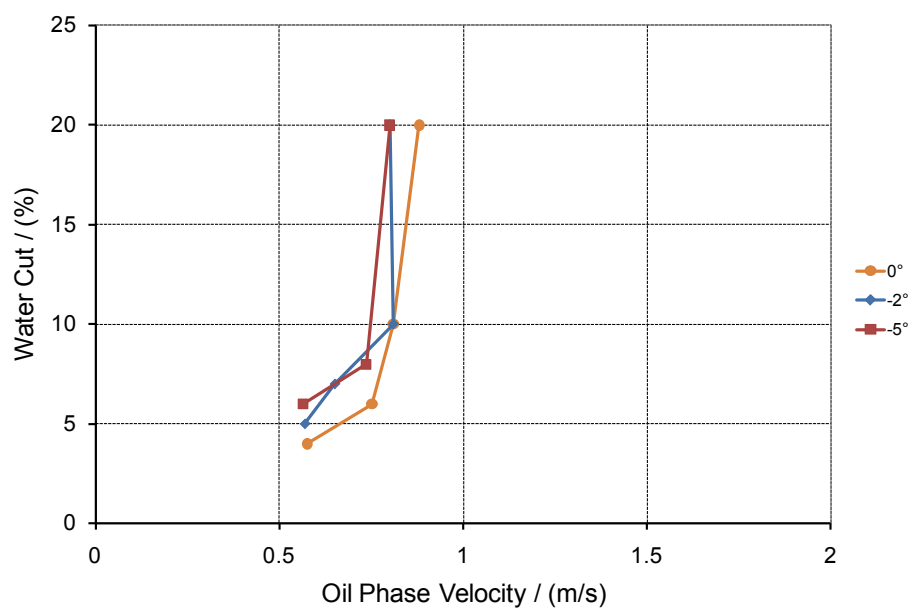


Figure 4-30. Transition lines from intermittent wetting to stable oil wetting for C4 crude oil in oil-water two-phase flow at horizontal and different downward inclination angles.

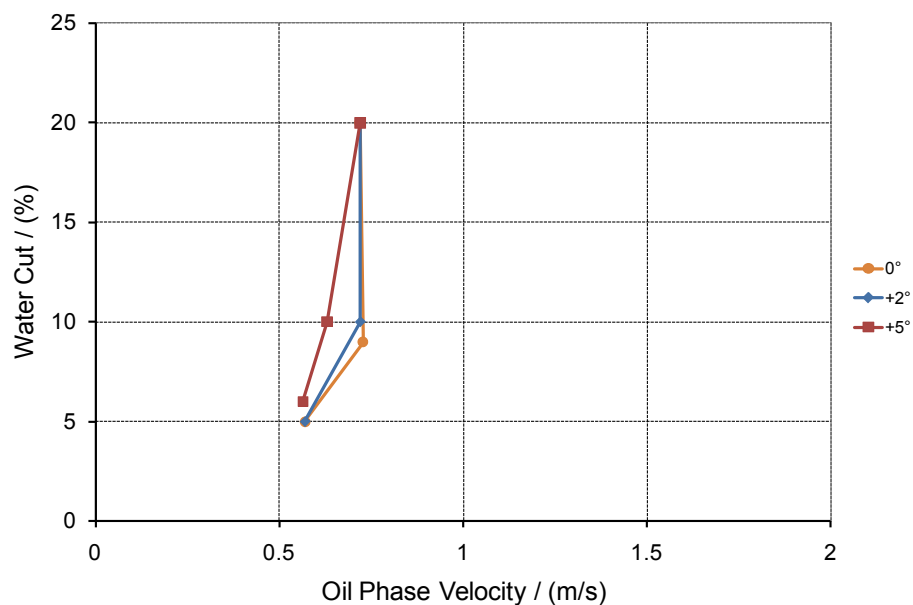


Figure 4-31. Transition lines from intermittent wetting to stable oil wetting for C5 crude oil in oil-water two-phase flow at horizontal and different upward inclination angles.

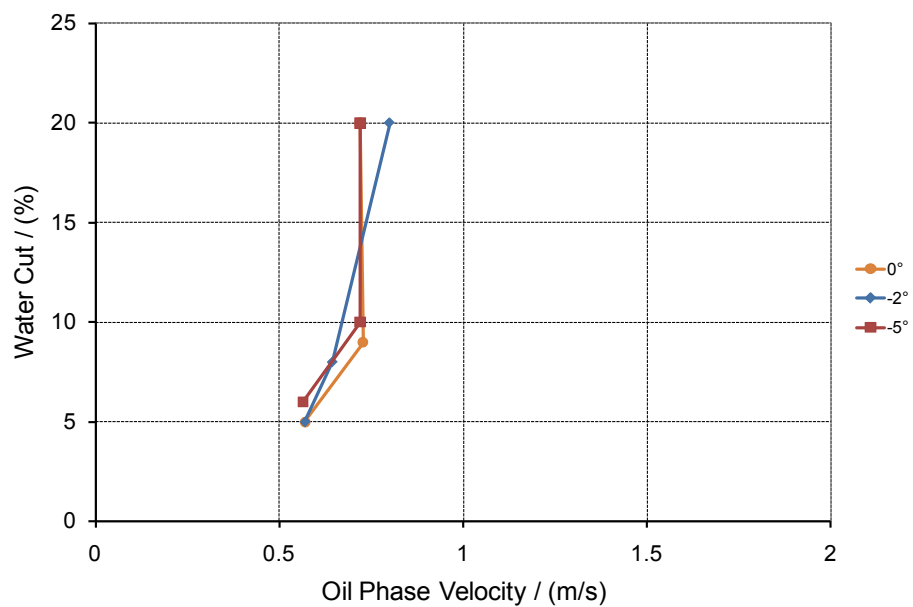


Figure 4-32. Transition lines from intermittent wetting to stable oil wetting for C5 crude oil in oil-water two-phase flow at horizontal and different downward inclination angles.

### 4.3 Comparison of experimental results with water wetting model prediction in MULTICORP

#### 4.3.1 Water wetting model in MULTICORP

MULTICORP is a transient mechanistic CO<sub>2</sub> corrosion prediction software package released by the Institute for Corrosion and Multiphase Technology (ICMT) at Ohio University. The latest release, MULTICORP V4, seamlessly integrates a corrosion model with a multiphase flow model, enabling successful prediction of the multiphase flow effects on water wetting and corrosion. The multiphase flow model in MULTICORP V4, and intrinsically the water wetting model incorporated within it, is based on the theory of transition from stratified flow to dispersed flow developed by Brauner (2001). In Brauner's (2001) model, as explained in Chapter 3, two maximal drop diameters were calculated for dilute dispersion and dense dispersion, respectively. It should be pointed out that Equation (3.22) for the calculation of the maximal drop diameter  $d_{\max}^{dilute}$  only considers one single droplet; hence an assumption that  $\rho_c(1 - \varepsilon_d) / \rho_m \approx 1$ , where  $\rho_c$  is the density of the continuous phase (oil),  $\varepsilon_d$  is the hold up of the dispersed phase (water) and  $\rho_m$  is the density of the oil-water mixture, was made (Brauner, 2001). For oil-water flow system, where  $\rho_c \approx \rho_d$ , this assumption is only valid for  $\varepsilon_d$  very close to 0. This is not practical for oil-water flow under real oil and gas industry conditions. Based on the analysis above, it is reasonable to consider only the maximum drop diameter for dense dispersion (Equation (3.25)). Therefore, the water wetting model for oil-water two-phase flow currently can be summarized as follows.

$$\left\{ \begin{array}{l}
 d_{\max} = 2.22D \left( \frac{\rho_c D U_c^2}{\sigma} \right)^{-0.6} \left( \frac{\varepsilon_d}{1 - \varepsilon_d} \right)^{0.6} \left[ \frac{\rho_m}{\rho_c (1 - \varepsilon_d)} f \right]^{-0.4} \quad (a) \\
 d_{crit} = \text{Min} \left( d_{cg} = \frac{3}{8} \frac{\rho_c U_o^2 f}{|\rho_d - \rho_c| g \cos \beta}, d_{c\sigma} = \sqrt{\frac{0.4\sigma}{|\rho_d - \rho_c| g \cos \beta'}} \right) \quad (b) \quad (4.2) \\
 d_{\max} < d_{crit} \quad (c)
 \end{array} \right.$$

For oil-water two-phase flow system, if the operational parameters are known, the relationship for the maximum drop diameter  $d_{\max}$  and the critical drop diameter  $d_{crit}$  can be determined. These parameters include the superficial oil velocity  $u_c$  and water cut  $\varepsilon_d$  (or alternatively, the superficial water velocity), the pipe diameter  $D$ , the inclination  $\beta$ , the water density  $\rho_d$ , the oil density  $\rho_c$ , the viscosities of water and oil phases and the oil-water interfacial tension  $\sigma$ . If  $d_{\max} < d_{crit}$ , the water phase is entrained by the continuous oil phase. This means that the whole circumference of the pipeline is wetted by the oil phase. In this scenario, there is no corrosion threat to the steel pipeline. Otherwise, if  $d_{\max} > d_{crit}$ , the bottom of the pipeline is wetted by water either continuously or intermittently. Under these circumstances, the steel pipeline may be corroded by stratified water. With the water wetting prediction model, the critical water entrainment velocities for various water cuts can be predicted. This allows corrosion engineers to optimize the operation conditions and to identify when possible corrosion problems could occur and to mitigate corrosion problems.

### 4.3.2 Verification of water wetting model in MULTICORP

The water wetting model (Equation (4.2)) can be verified by experimental results of oil-water two-phase flow in large scale flow loop. The *Figure 4-22* shows the transition lines from intermittent wetting to stable oil wetting for LVT200 oil and the five crude oils in horizontal pipe flows. The transition lines shown in *Figure 4-22* and the water wetting model prediction transition lines for different oils can be compared as follows.

*Figure 4-33* shows the comparison of the experimental phase wetting transition line with the model prediction for LVT200 model oil in a 4" large scale flow loop. In the Figure, the model prediction line is denoted as the "old model", which is distinguished from the new model, whose development is discussed in Chapter 7. It can be seen that the model predictions agreed with the experimental results except at water cuts lower than 2%, whereas, when surface-active substances such as corrosion inhibitors or chemicals were added into the oil-water flow, the model prediction line significantly deviated from the experimental transition line (Li, 2009; Ayello, 2010). *Figure 4-34* shows that the model prediction overestimated the critical entrainment velocity at about 10% when even only 5 ppm "quat" inhibitor was added to the LVT200 oil in the 4" flow loop. When the chemicals such as myristic acid were added to the LVT200 oil, the deviation of the model prediction from the experimental transition line was even greater. *Figure 4-35* shows that the model overestimated the critical entrainment velocity about 20% when as little as 1% myristic acid was added to the LVT200 oil in the 4" flow loop. As for the performance of the old model with regard to crude oils, it always over-predicted the critical oil phase

velocity for full water entrainment, i.e. oil wetting. *Figure 4-36* to *Figure 4-40* show the comparison of the model predictions with the experimental transition lines for C1 to C5 crude oils in a 4" horizontal flow loop, respectively. It can be seen that the model overestimated the critical oil velocity for full water entrainment about 10% to 40% for the different crude oils.

The deviation of the model prediction from the experimental transition line can be caused by the effect of surface wettability changes, which occur due to adsorption of surface active compounds from the oil phase or water phase, not considered in the old water wetting model, where only hydrodynamics are considered. In order to investigate the effect of surface wettability on water wetting, a project named the Water Wetting Joint Industry Project (WW JIP) was initiated in 2006, financed by BP, ConocoPhillips, Eni, ExxonMobil, Petrobras, Saudi Aramco, Shell and Total. Three research topics were proposed and assigned to three PhD students: effect of corrosion inhibitors (Li, 2009), effect of crude oil chemistry (Ayello, 2010) and effect of steels surface state: present work. Based on the experimental results a new, improved water wetting model was formulated and presented in Chapter 7.

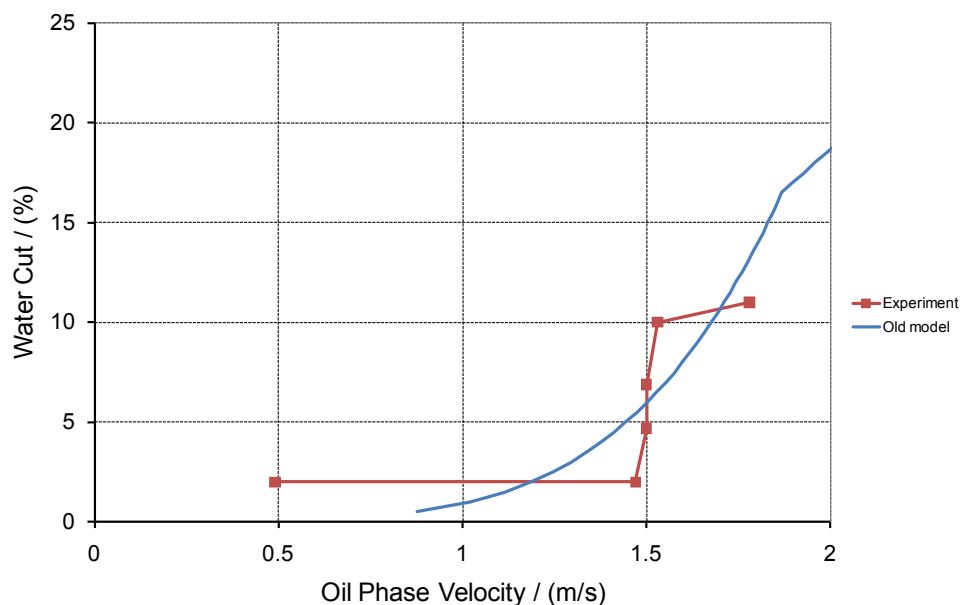


Figure 4-33. Comparison of the experimental phase wetting transition line with model prediction (LVT200 oil in 4" horizontal flow loop).

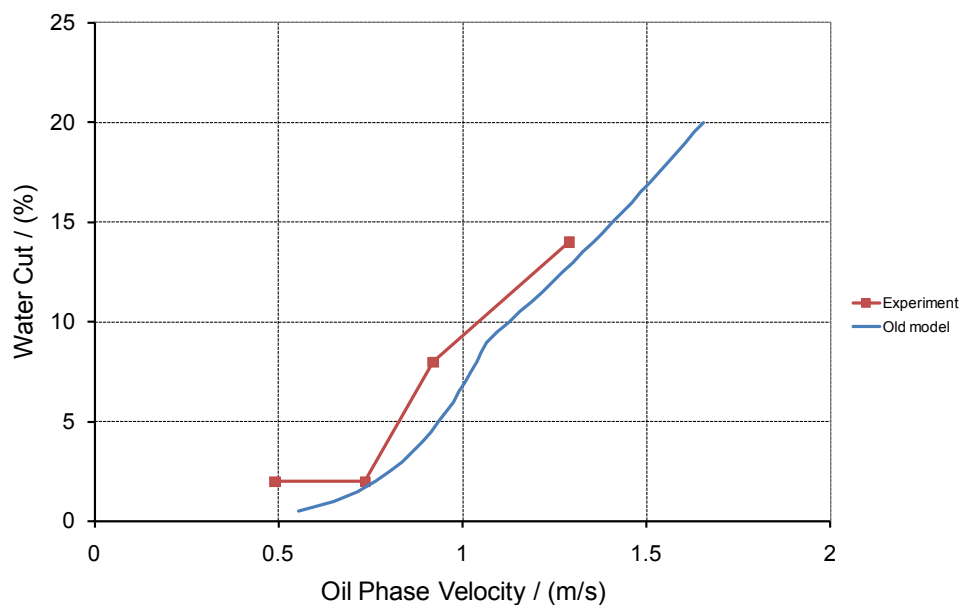


Figure 4-34. Comparison of the experimental phase wetting transition line with model prediction (LVT200 oil with 5 ppm "quat" inhibitor in 4" horizontal flow loop) (Li, 2009).

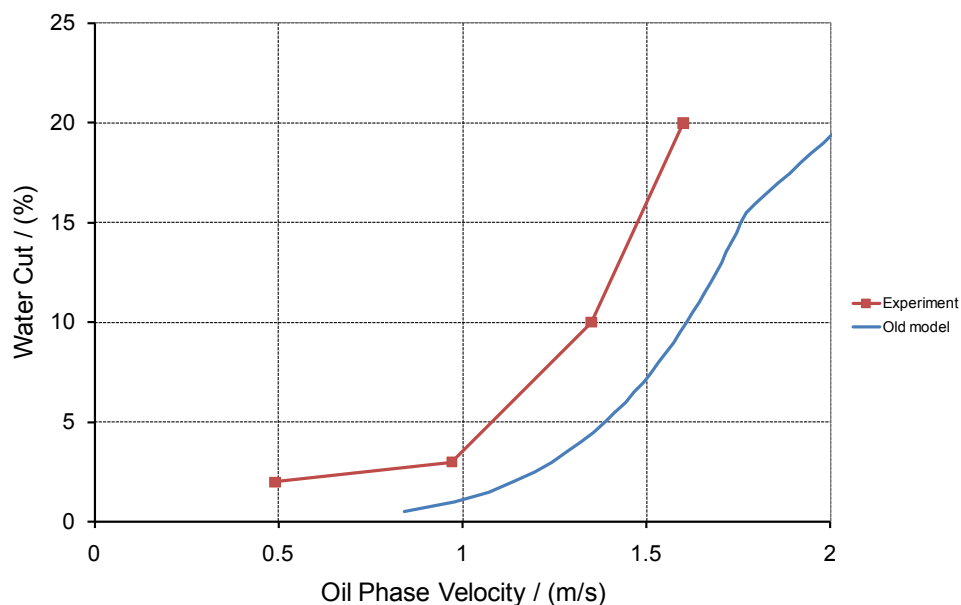


Figure 4-35. Comparison of the experimental phase wetting transition line with model prediction (LVT200 oil with 1% myristic acid in 4" horizontal flow loop) (Ayello, 2010).

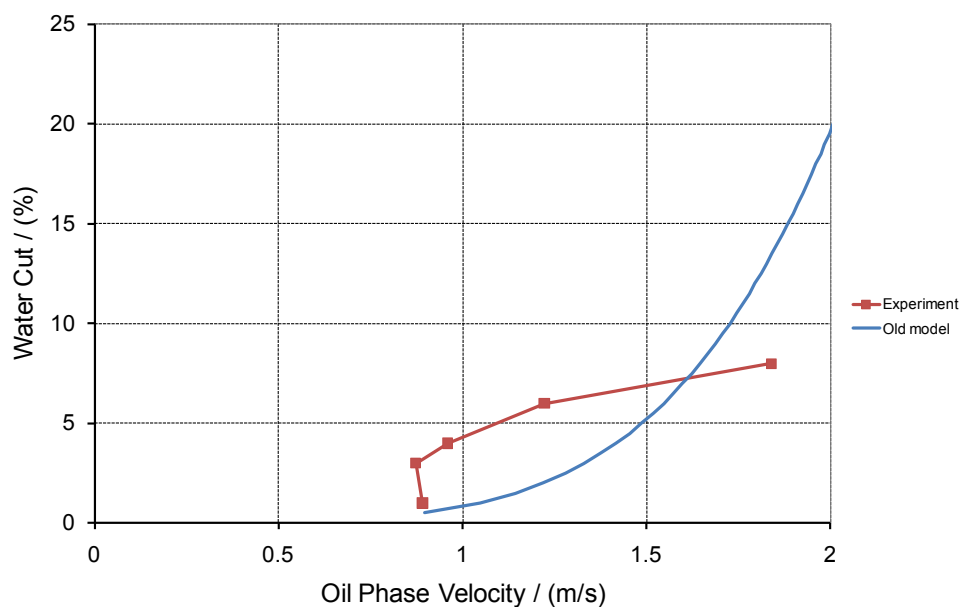


Figure 4-36. Comparison of the experimental phase wetting transition line with model prediction (C1 crude oil in 4" horizontal flow loop).

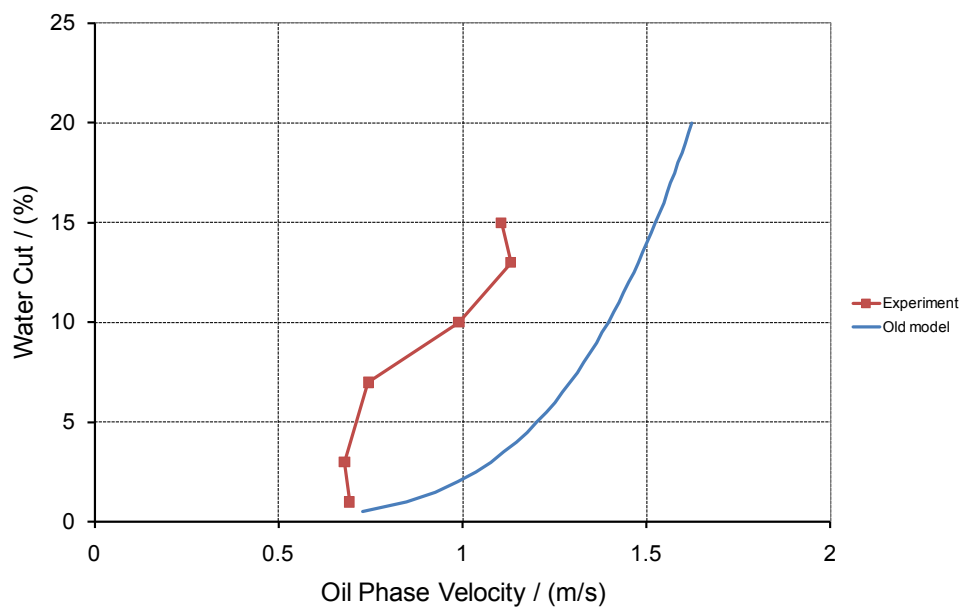


Figure 4-37. Comparison of the experimental phase wetting transition line with model prediction (C2 oil in 4" horizontal flow loop).

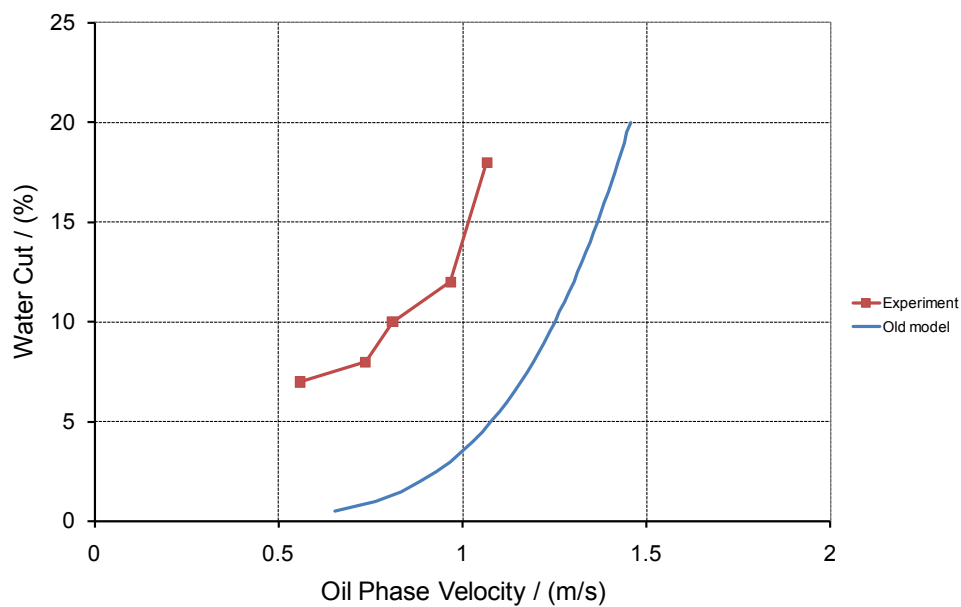


Figure 4-38. Comparison of the experimental phase wetting transition line with model prediction (C3 crude oil in 4" horizontal flow loop).

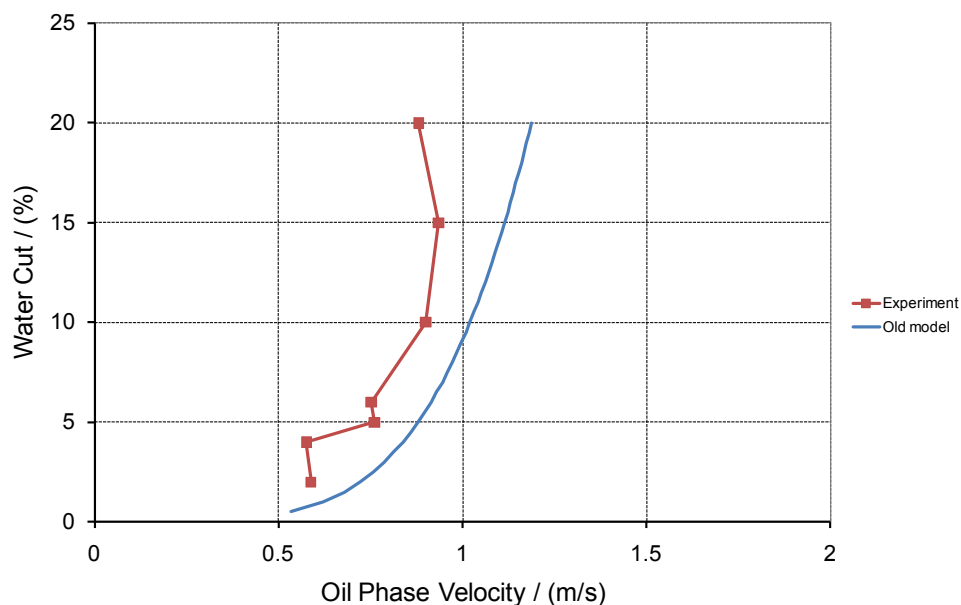


Figure 4-39. Comparison of the experimental phase wetting transition line with model prediction (C4 crude oil in 4" horizontal flow loop).

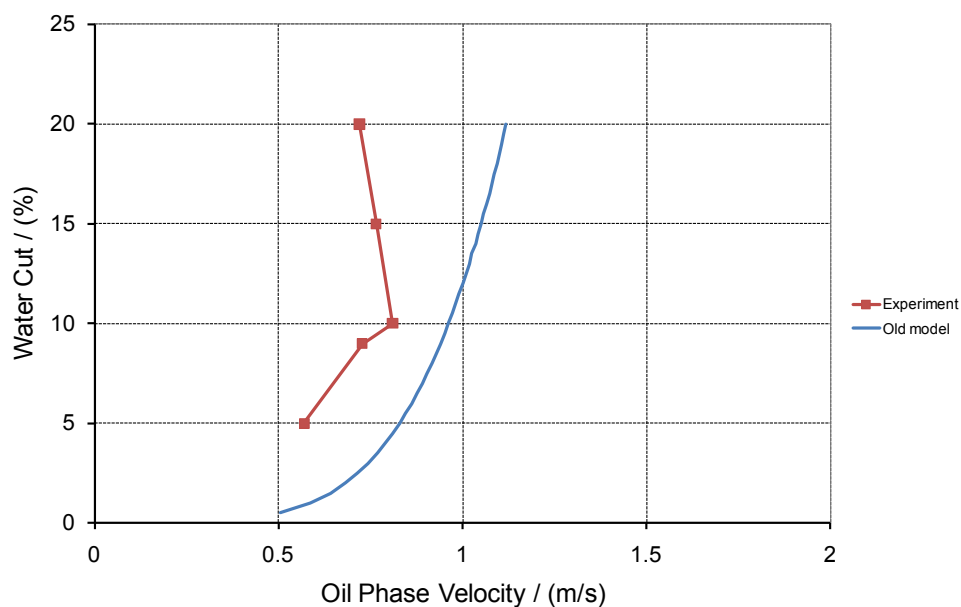


Figure 4-40. Comparison of the experimental phase wetting transition line with model prediction (C5 crude oil in 4" horizontal flow loop).

#### 4.4 Summary

A comprehensive experimental campaign was carried out using six types of oil, one model oil and five crude oils, and 1 wt% NaCl brine as working fluids in a large scale, 4” I.D., fully inclinable flow loop. Flow pattern visualization, wall conductance probes, corrosion monitoring and wall fluid sampling were successfully applied. Based on the overlapping information from these four techniques, three types of phase wetting regimes were identified and verified: stable water wetting, intermittent wetting and stable oil wetting. Comprehensive phase wetting maps, which show the dependence of the phase wetting regimes on water cut and oil phase velocity, were constructed based on the results obtained from the wall conductance probes; these in turn agreed with results from the other experimental techniques.

The transition from intermittent wetting to stable oil wetting was given special attention due to its significance for corrosion management. Oil type was found to have a significant effect on the phase wetting transition, and much of this influence can be ascribed to the physical properties of the oil: density, viscosity and oil-water interfacial tension. The heavier and more viscous the crude oil, the more easily it entrains water at a given oil velocity. In addition, the pipe inclination appears to have a significant effect on this transition, especially when the inclination is 45° or higher.

Based on the results of  $\text{Fe}^{2+}$  concentration monitoring, no corrosion was detected in the stable oil wetting regime, while the corrosion rate in the full water wetting regime was typically twice of that for the intermittent wetting.

A comparison was made between the results of the critical oil phase velocity for full water entrainment obtained experimentally and those predicted using the water wetting

model incorporated in MULTICORP V4. It was found that the model tends to over-predict the critical oil phase velocity for full water entrainment, which may be related to the effect of surface wettability change, which was not considered in the model.

## CHAPTER 5 : EXPERIMENTAL STUDY OF SURFACE WETTABILITY

In order to investigate the surface wettability of carbon steel in oil-water two-phase system, a series of experiments was conducted in a goniometer system designed and built by the present author (*Figure 5-1*). The wettability of the steel surface is characterized either by a water-in-oil contact angle (a water droplet on the steel surface immersed in the oil phase) or by an oil-in-water contact angle (an oil droplet on the steel surface immersed in the water phase). The experiments had three areas of focus: effect of steel surface state on wettability, effect of temperature on wettability and wettability of pre-wetted steel surfaces. The details of these three experiments will be expanded on in the following sections.

### 5.1 Effect of the surface state of steel on its wettability

#### 5.1.1 *Experimental setup and procedure*

##### 5.1.1.1 Instrumentation

The experiments on the effect of steel surface state on its wettability were conducted in a goniometer system used to measure the contact angles, which was designed and built by the present author. The goniometer consists of two main parts, the test cell and the image capture system shown in *Figure 5-1*. *Figure 5-2* shows the photograph of the goniometer. The test cell is a 4" O.D., 3 3/4" I.D. and 6" height stainless steel tube. There are two 2" circular openings on opposite sides of the tube wall to accommodate flat glass windows, which help to avoid the distortion of the droplet image. The water or oil droplet is meant to be deposited on a carbon steel test specimen, which is mounted on a Teflon mount inside the cell (*Figure 5-3*). There are two entry

ports on the cell wall for injecting a water droplet (in an oil environment) on top of the test specimen or an oil droplet (in a water environment) beneath the metal test specimen. On the bottom of the cell wall are two access ports for liquid drainage and infusion.

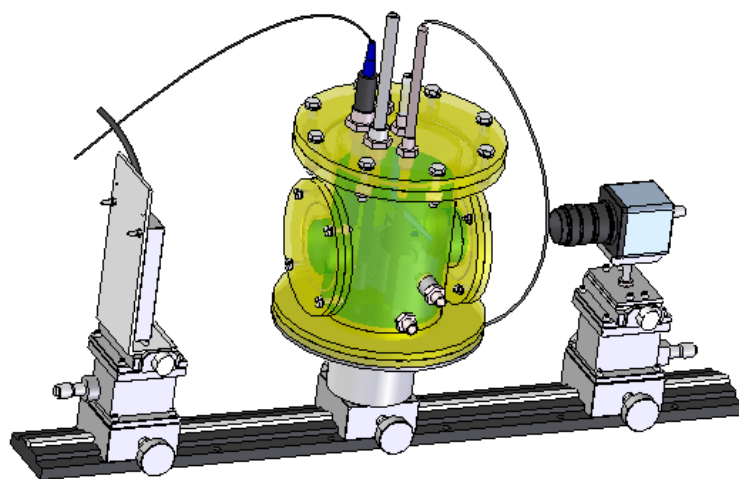


*Figure 5-1.* Sketch of a goniometer with optical imaging camera and backlight.

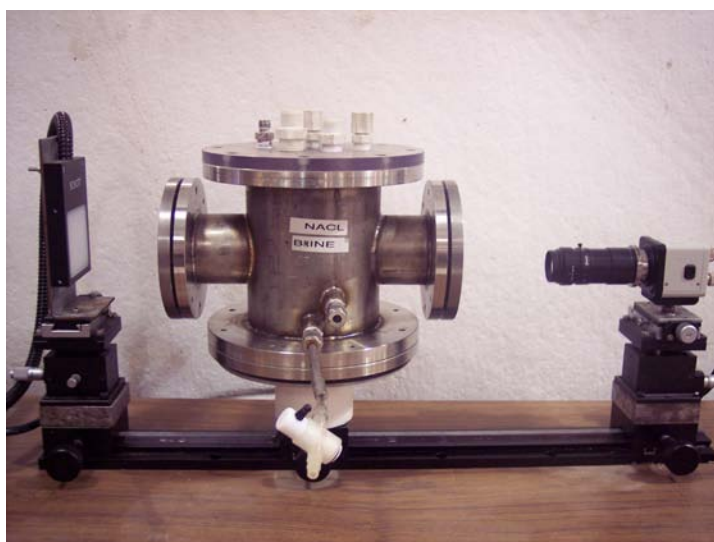


*Figure 5-2.* Photograph of the goniometer system with goniometer cell, backlight and a camera.

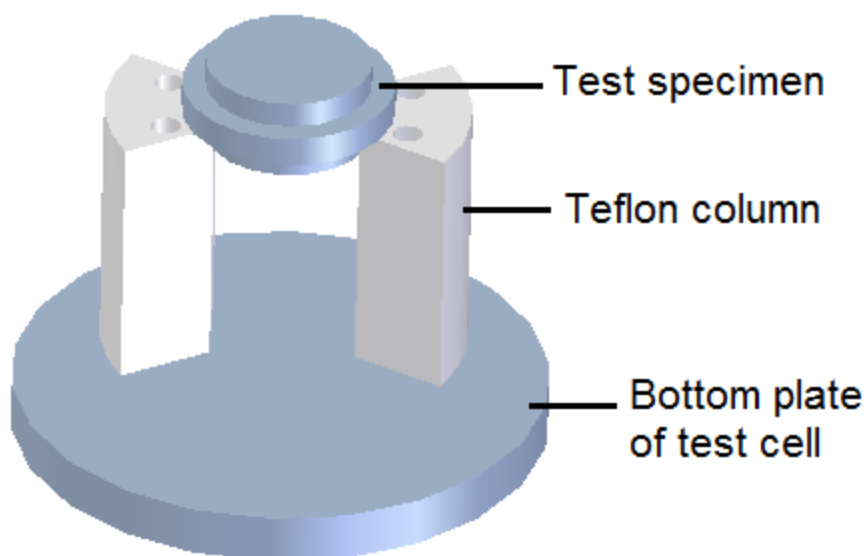


*Figure 5-3.* Teflon mount with a carbon steel test specimen mounted on it.

The image capture system is composed of a camera, a backlight, a PCI card and image analysis software. The camera used is IMAGING PLANET<sup>®</sup> model 221-XS monochrome CCD camera with 768 x 494 pixel array and 570 horizontal lines of resolution. The PCI card installed in the computer connects to the camera to capture the image of a droplet displayed on the computer screen using Snagit<sup>®</sup> software. Using the RINCON<sup>®</sup> image analysis software, one can calculate contact angles from the captured images.

#### 5.1.1.2 Test matrix

The test matrix of the water-in-oil contact angle measurement is shown in *Table 5-1*. The measurement was conducted at 25 °C with 1 wt% NaCl CO<sub>2</sub> saturated brine used to make a water droplet on the steel surface in LVT200 model oil. Bare metal

surface of carbon steel X65 with three different measures of surface roughness (1.5  $\mu\text{m}$ , 6.0  $\mu\text{m}$  and 40  $\mu\text{m}$ ) and iron carbonate film covered surface were used in the test. The composition of carbon steel X65 can be found in *Table 5-2*.

The test matrix for the oil-in-water contact angle measurements (*Table 5-3*) was similar to that for water-in-oil contact angle measurement except that 6 different oils were used to create oil droplets. The main properties for the oils at 25 °C: density, dynamic viscosity and oil-water interfacial tension, are shown in *Figure 4-7*, *Figure 4-9* and *Figure 4-10* respectively.

*Table 5-1*. Text matrix of water-in-oil contact angle measurement for different surface conditions at the temperature of 25 °C.

Steel type	Carbon steel X65
Surface conditions	Bare metal surface: <ul style="list-style-type: none"> <li>• 1.5 <math>\mu\text{m}</math> ( #400 sand paper)</li> <li>• 6 <math>\mu\text{m}</math> (#36 sand paper)</li> <li>• 40 <math>\mu\text{m}</math> ( machined)</li> </ul> Steel surface with iron carbonate film: <ul style="list-style-type: none"> <li>• 20 <math>\mu\text{m}</math></li> </ul>
Temperature	25 °C
Oil phase	LVT200
Water phase	1 wt% NaCl brine
pH	4.0
CO <sub>2</sub> partial pressure	0.96 bar
Deoxygenation time	Half an hour for oil phase in cell, more than one hour for water phase

Table 5-2. Chemical composition of X65 carbon steel.

Element	Composition (%)	Element	Composition (%)
Al	0.032	P	0.009
As	0.008	Pb	<0.001
B	0.001	S	0.009
C	0.13	Sb	0.009
Ca	0.002	Si	0.26
Co	0.007	Sn	0.07
Cr	0.14	Ta	<0.001
Mn	1.16	Ti	<0.001
Mo	0.16	V	0.047
Nb	0.017	Zr	<0.001
Ni	0.36	Fe	Balance

Table 5-3. Text matrix of oil-in-water contact angle measurement for different surface conditions at the temperature of 25 °C.

Steel type	Carbon steel X65
Surface conditions	Bare metal surface: <ul style="list-style-type: none"> <li>• 1.5 <math>\mu\text{m}</math> ( #400 sand paper)</li> <li>• 6 <math>\mu\text{m}</math> (#36 sand paper)</li> <li>• 40 <math>\mu\text{m}</math> ( machined)</li> </ul> iron carbonate film covered surface: <ul style="list-style-type: none"> <li>• 20 <math>\mu\text{m}</math></li> </ul>
Temperature	25 °C
Oil phase	LVT200, C1, C2, C3, C4, C5
Water phase	1 wt% NaCl brine
pH	4.0
CO <sub>2</sub> partial pressure	0.96 bar
Deoxygenation time	Half an hour for oil phase in cell, more than one hour for water phase

### 5.1.1.3 Surface preparation and characterization

The preparation of a clean and characteristic steel surface is very important for contact angle measurement. 1.5  $\mu\text{m}$  and 6  $\mu\text{m}$  roughness bare metal surfaces were achieved using 400 and 36 grit SiC paper, respectively. The 40  $\mu\text{m}$  roughness surface was

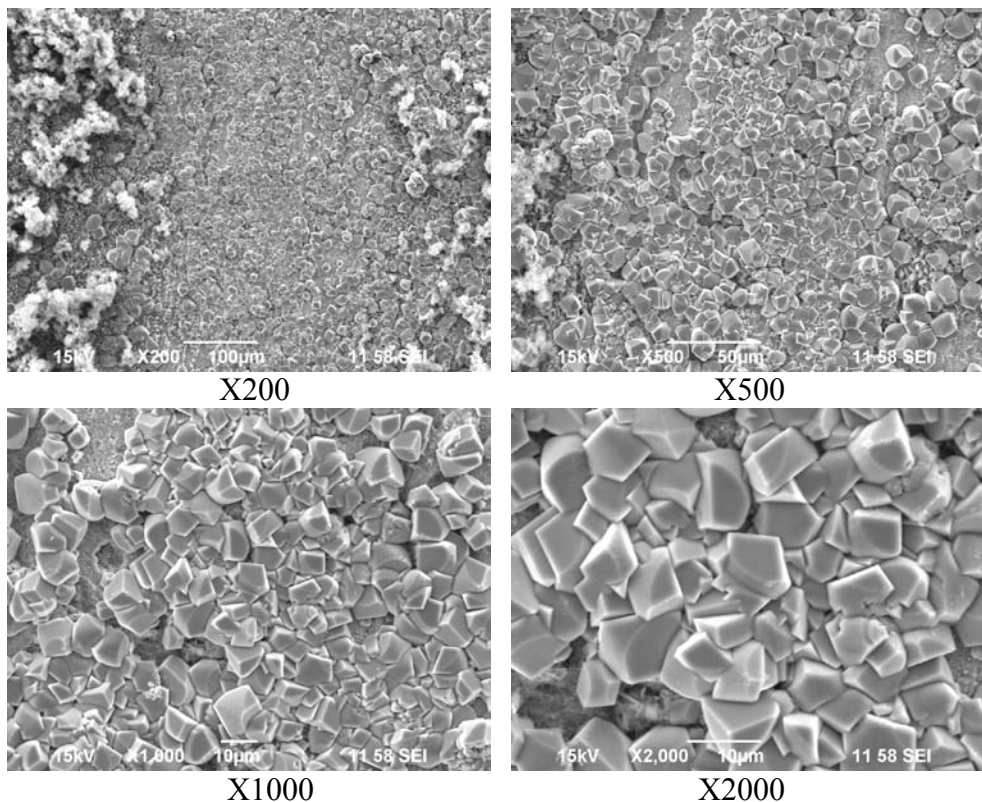
created by machining. All bare metal steel surfaces were first ultrasonicated in an ultrasonic isopropanol bath and then rinsed with isopropanol before being put into the goniometer test cell. The iron carbonate film covered surface was produced in 1 wt% NaCl brine within a glass cell in an environment of pH of 6.6 (adjusted by adding sodium bicarbonate solution) and temperature of 80 °C, in keeping with the conditions shown in *Table 5-4*. The setup of the glass cell is shown in *Figure 5-4*. A bare metal surface with 40 µm roughness was hung in the cell and exposed to these conditions for 24 hours. Scanning electron microscopy (SEM) was used to verify the formation of iron carbonate film. The SEM images for the iron carbonate film-covered surface are shown in *Figure 5-5*, showing a dense layer of iron carbonate film formed on the carbon steel substrate. The surface roughness of all four of these surfaces is the average roughness,  $R_a$ , obtained using an optical 3D measurement device, InfiniteFocus<sup>®</sup> microscopy (IFM), manufactured by ALICONA (Alicona Imaging GmbH, Teslastraße 8, 8074 Grambach/Graz, Austria).

Table 5-4. Experimental conditions for iron carbonate film formation.

Steel type	Carbon steel X65
Original surface conditions	Machined surface with 40 $\mu\text{m}$ roughness
Temperature	80 $^{\circ}\text{C}$
CO <sub>2</sub> partial pressure	0.52 bar
pH	6.6
Time	24 hrs
Temperature	80 $^{\circ}\text{C}$



Figure 5-4. Glass cell set up for iron carbonate film formation.



*Figure 5-5.* SEM images of different magnifications for iron carbonate film covered surface.

#### 5.1.1.4 Experimental procedure

The setup of the test cell for introducing water droplets on the metal surface surrounded by oil is shown in *Figure 5-6*. A microliter syringe allowed a drop of liquid to be positioned on the surface of the metal plate, for instance a water droplet in the oil phase (i.e., sessile droplet). A droplet of oil could likewise be released from a microliter syringe into the water phase as shown in *Figure 5-7*, and the drop then floated to a position underneath the steel test specimen.

The following test procedure for a sessile droplet was used:

Water droplet in oil for water-in-oil contact angle measurement:

1. Put the prepared test specimen in the holder and LVT200 into the cell.
2. Purge the test cell with CO<sub>2</sub> and deoxygenate for more than half an hour.
3. Inject a droplet of deoxygenated 1 wt% NaCl brine on top of the carbon steel test specimen through the injection port.
4. Capture the image of the droplet on the surface of the test specimen using Snagit<sup>®</sup> software.
5. Take multiple measurements by injecting a new droplet on a new position of the test specimen surface.
6. Measure the contact angle between the droplet of water and the surface of the test specimen using RINCON<sup>®</sup> image analysis software.

Oil droplet in water for oil-in-water contact angle measurement:

1. Put the test specimen in the holder and 1 wt% NaCl brine into the cell.
2. Purge the test cell with CO<sub>2</sub> and deoxygenate the cell for more than half an hour.
3. Inject a droplet of test oil into the cell using the oil syringe through the injection port; the droplet will rise and rest against the test specimen surface.
4. Capture the image of the droplet under the surface of the test specimen using Snagit<sup>®</sup> software.
5. Take multiple measurements by injecting a new droplet in a new position under the test specimen surface.
6. Measure the contact angle between the droplet of oil and the surface of the test specimen using RINCON<sup>®</sup> image analysis software.

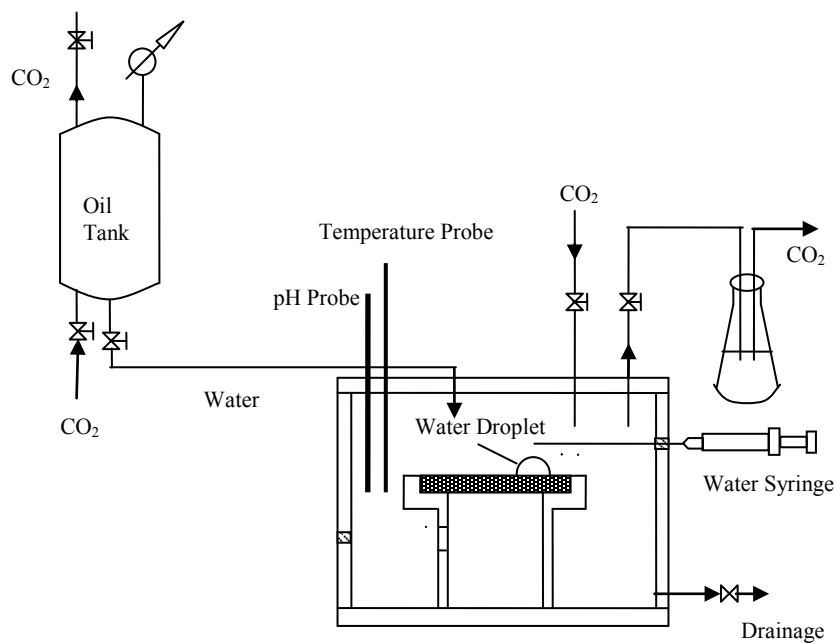


Figure 5-6. Schematic of experimental setup for water-in-oil droplet contact angle with metal surface.

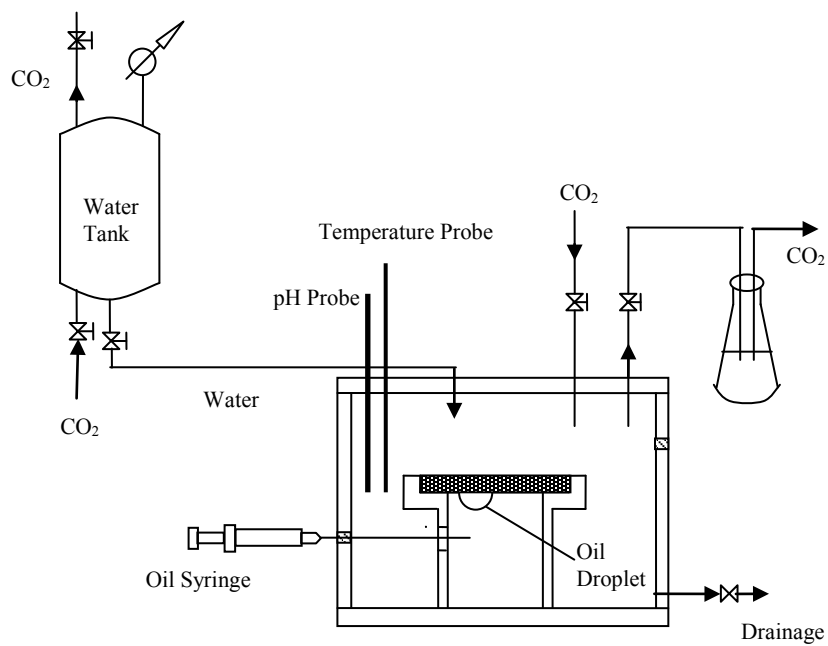
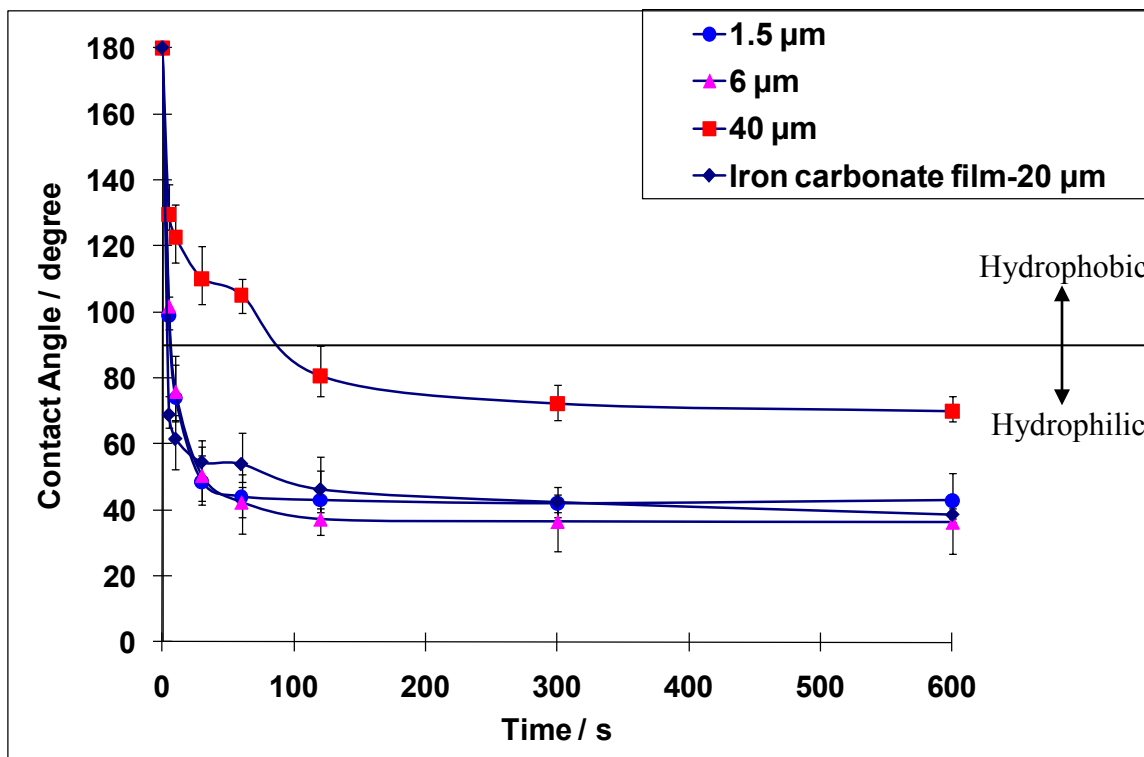


Figure 5-7. Schematic of experimental setup for oil-in-water droplet contact angle with metal surface.

### 5.1.2 Experimental results

#### 5.1.2.1 Water-in-oil contact angle

Contact between the water droplet and the steel surface is a dynamic process. It takes time for the contact angle to reach equilibrium. The effect of time on the contact angles for different surface conditions can be seen in *Figure 5-8*. In the first 5 seconds, the contact angle decreased from the initial  $180^\circ$  to  $130^\circ$ ,  $100^\circ$ ,  $100^\circ$  and  $70^\circ$  for  $40\ \mu\text{m}$ ,  $1.5\ \mu\text{m}$ ,  $6\ \mu\text{m}$  roughness and iron carbonate covered surface, respectively. The contact angles reached an equilibrium after about 120 seconds. *Figure 5-9* shows the water droplets on the  $1.5\ \mu\text{m}$  roughness steel surface at different time.



*Figure 5-8*. Water-in-oil contact angle on different steel surfaces versus time (600s).

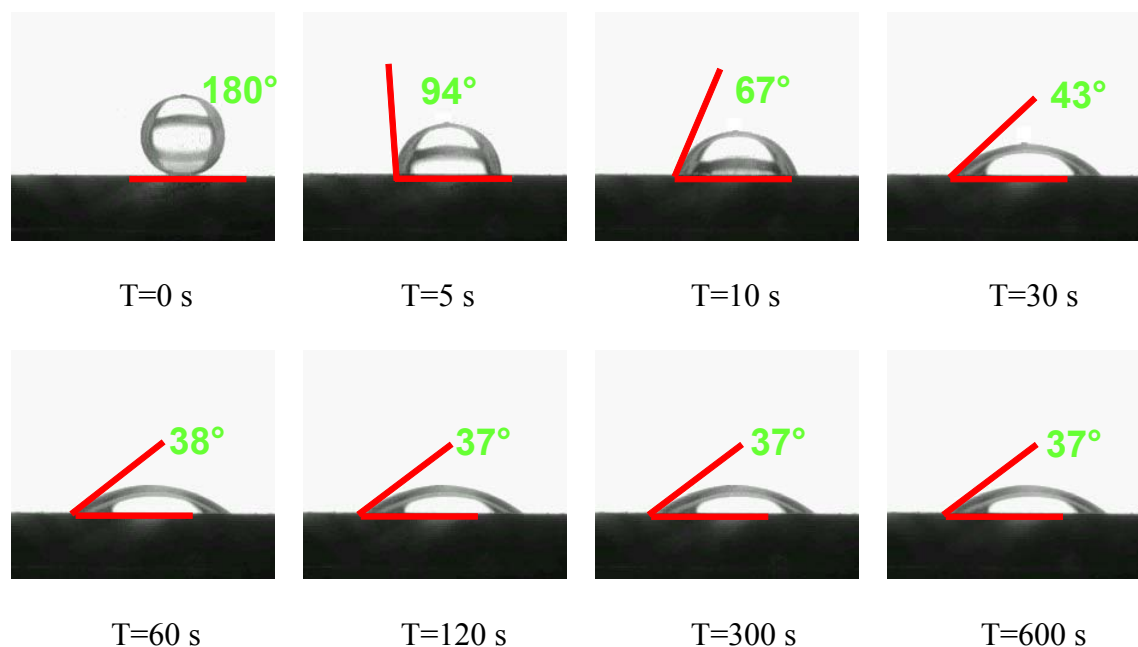


*Figure 5-9.* Water droplets on the steel surface (surface roughness  $1.5 \mu\text{m}$ ) immersed in LVT200 oil at different time.

*Figure 5-10* shows the equilibrium water-in-oil contact angles on different steel surfaces, from which the effect of surface roughness on the contact angle can be deduced. The contact angles for  $1.5 \mu\text{m}$ ,  $6 \mu\text{m}$  roughness and iron carbonate covered surfaces were all around  $40^\circ$ , which is smaller than the contact angle of  $70^\circ$  measured for the  $40 \mu\text{m}$  roughness surface. That means that  $1.5 \mu\text{m}$ ,  $6 \mu\text{m}$  roughness and iron carbonate covered surfaces were more hydrophilic than the  $40 \mu\text{m}$  roughness surface. *Figure 5-11* shows typical images of water droplets on different steel surfaces in LVT200 oil. It can be concluded that for the relatively smooth bare metal surfaces, the surface roughness had no major effect on the contact angle, which was much smaller than the contact angle of the roughest surface. Iron carbonate film made the steel surface more hydrophilic.

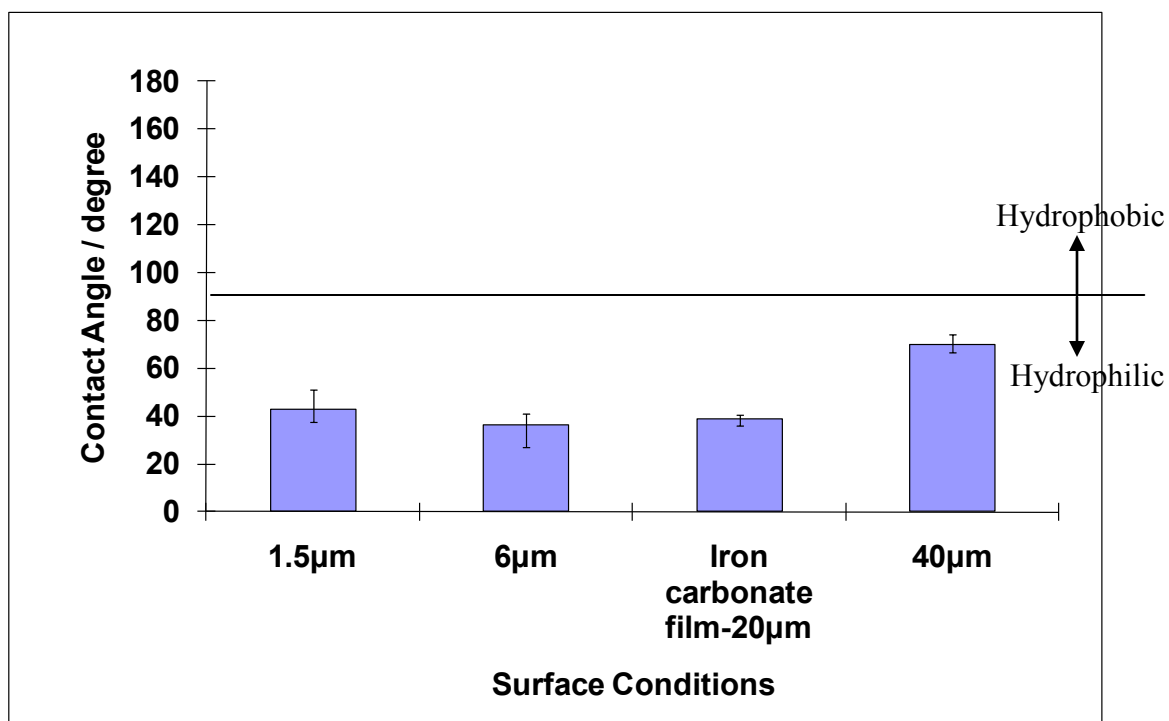


Figure 5-10. Equilibrium water-in-oil contact angles on different steel surfaces.

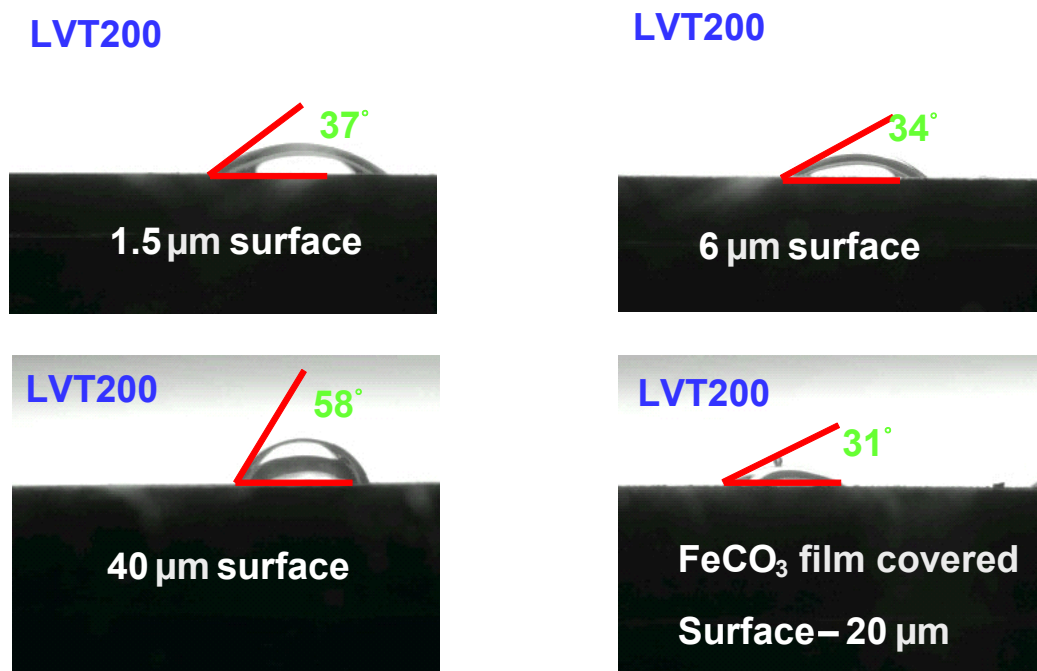
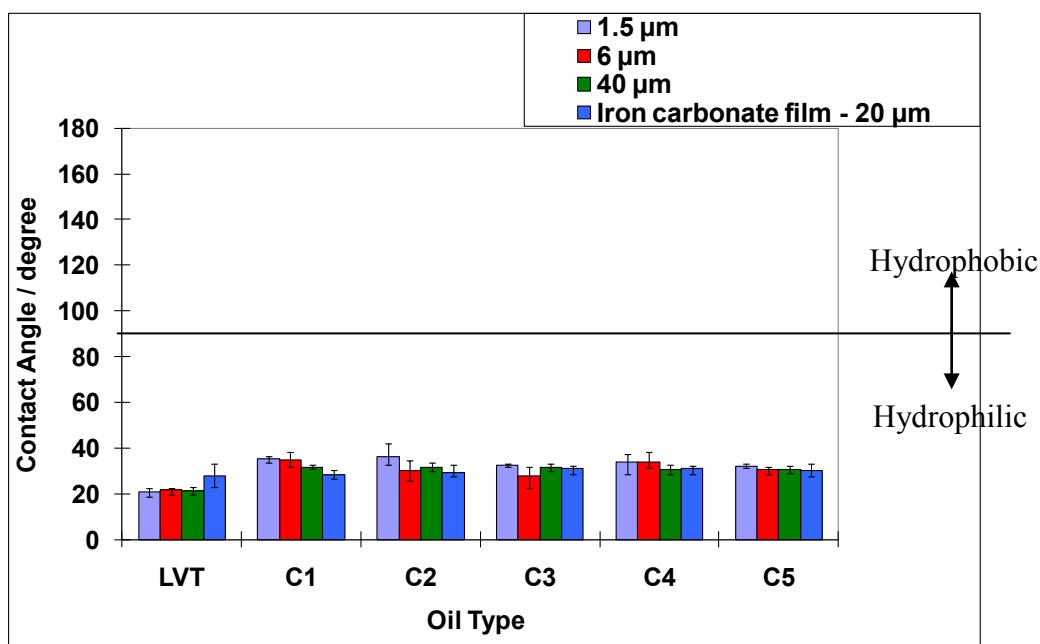


Figure 5-11. Typical images of water droplets on different steel surfaces in LVT200 oil.

### 5.1.2.2 Oil-in-water contact angle

The contact angles of different oil droplets beneath steel surfaces exposed to 1 wt% NaCl brine were measured, and the results are shown in *Figure 5-12*. The contact angles for different oil phases were approximately the same, all around 30°, which indicates that the steel surface was hydrophilic. *Figure 5-13* shows the typical images of different oil droplets on the 6 μm roughness steel surface. The crude oil type did not affect the oil-in-water contact angle. Moreover, in *Figure 5-12* it can be seen that the contact angles for each kind of oil droplet on different surfaces were approximately the same. *Figure 5-14* shows typical images of oil droplets (C1 crude oil) beneath different steel surfaces in water. The surface roughness or state did not affect the contact angle. The steel surfaces of different roughness were all hydrophilic.



*Figure 5-12.* Equilibrium oil-in-water contact angles beneath different steel surfaces for different oils.

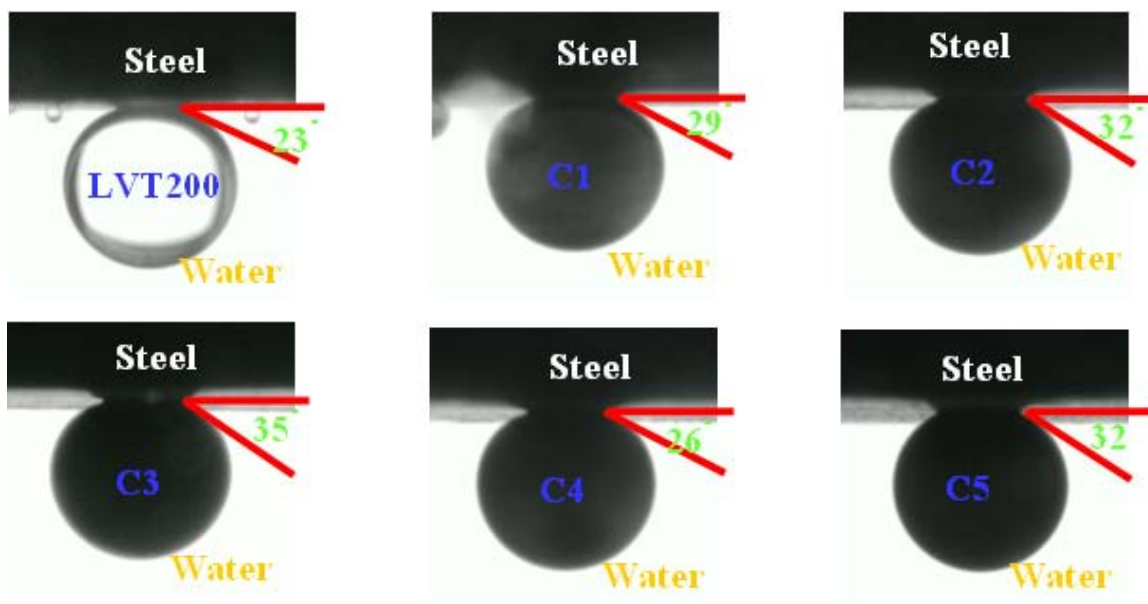


Figure 5-13. Typical images of different oil droplets beneath 6 μm roughness steel surface in water.

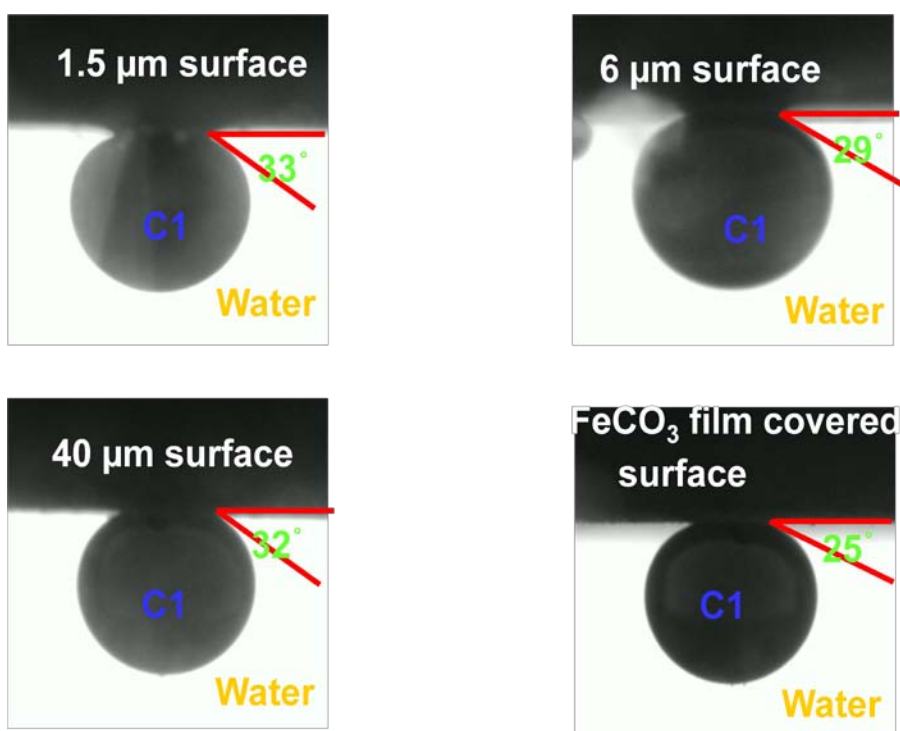


Figure 5-14. Typical images of oil droplet (C1 crude oil) beneath different steel surfaces in water.

## 5.2 Effect of temperature on surface wettability

### 5.2.1 Experimental setup and procedure

The experimental setup and procedure for the study of the effect of temperature on steel surface wettability was similar to that used in previous experiments except that a heater controlled by digital thermostat was used maintain a certain temperature. *Table 5-5* and *Table 5-6* show the test matrix for water-in-oil and oil-in-water contact angle measurements at different temperatures, respectively. For water-in-oil contact angle measurements at different temperatures, 1.5  $\mu\text{m}$  and 6  $\mu\text{m}$  roughness bare metal steel surfaces were tested at 25, 50, and 80  $^{\circ}\text{C}$  with LVT200 oil and 1 wt% NaCl brine as test liquids. However, only the 1.5  $\mu\text{m}$  roughness bare metal steel surface was tested for oil-in-water contact angle measurement, and LVT200 oil and C3 crude oil were used to create oil droplets. The main properties at different temperatures for the LVT200 and C3 oil, such as dynamic viscosity, interfacial tension, are shown in *Figure 5-15* and *Figure 5-16*.

*Table 5-5.* Test matrix for water-in-oil contact angle measurement at different temperatures.

Steel type	Carbon steel X65
Surface conditions	Bare metal surface: <ul style="list-style-type: none"> <li>• 1.5 <math>\mu\text{m}</math> ( #400 sand paper)</li> <li>• 6 <math>\mu\text{m}</math> (#36 sand paper)</li> </ul>
Temperature	25, 50, and 80 $^{\circ}\text{C}$
Oil phase	LVT200
Water phase	1 wt% NaCl brine

Table 5-6. Test matrix for oil-in-water contact angle measurement at different temperatures.

Steel type	Carbon steel X65
Surface conditions	Bare metal surface: • 1.5 $\mu\text{m}$ (#400 sand paper)
Temperature	25, 50 and 80 $^{\circ}\text{C}$
Oil phase	LVT200, C3 crude oil
Water phase	1 wt% NaCl brine

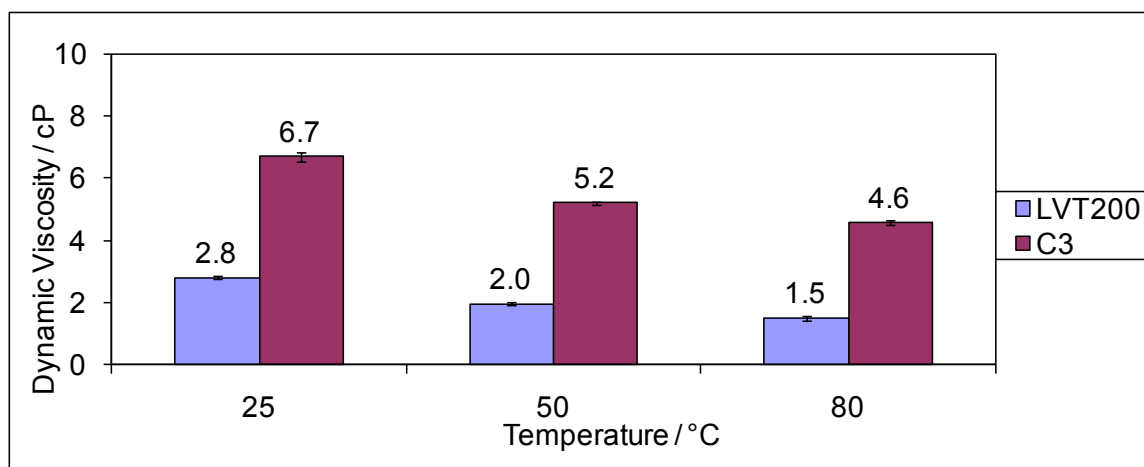


Figure 5-15. Dynamic viscosity of oils at different temperatures.

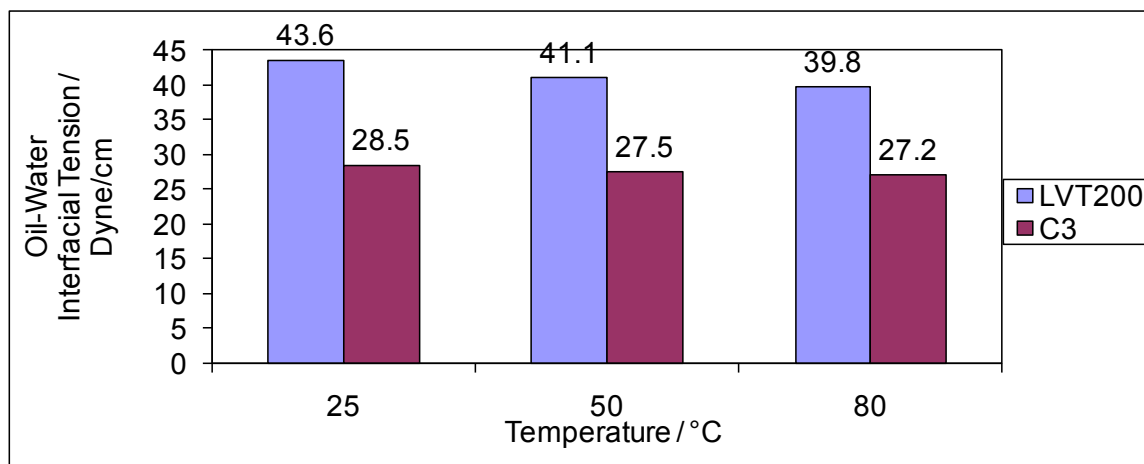


Figure 5-16. Oil-water interfacial tension of oils at different temperatures.

### 5.2.2 Experimental results

Figure 5-17 and Figure 5-18 show the effect of temperature on water-in-oil contact angle for LVT200 on the 1.5  $\mu\text{m}$  roughness surface and the 6  $\mu\text{m}$  roughness surface, respectively. Contact between the water droplet and the steel surface is a dynamic process, and it reached an equilibrium state after about 120 seconds. The equilibrium water-in-oil contact angle slightly increased with temperature and the steel surface became less hydrophilic.

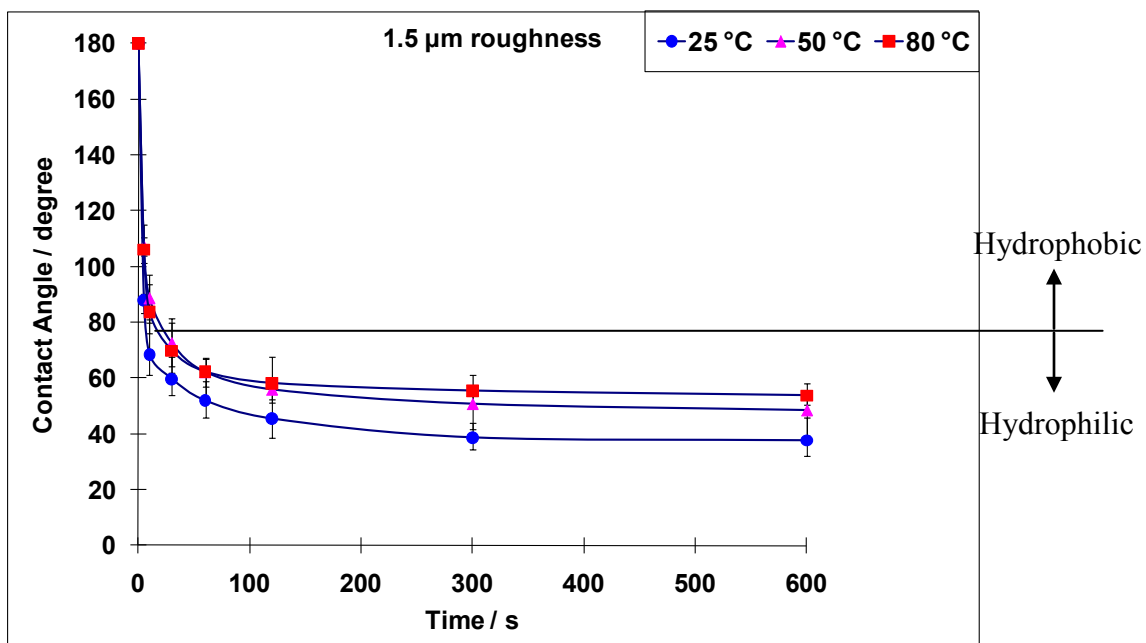


Figure 5-17. Water-in-oil (LVT200) contact angles at different temperatures for 1.5  $\mu\text{m}$  surface.

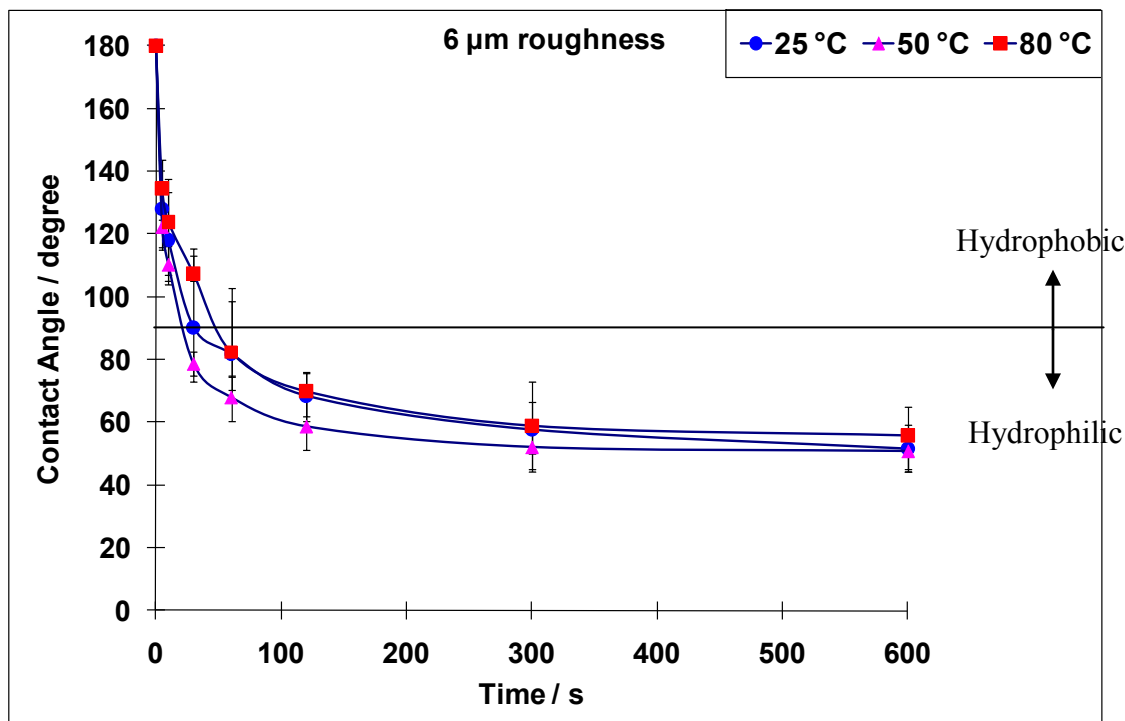


Figure 5-18. Water-in-oil (LVT200) contact angles at different temperatures for 6  $\mu\text{m}$  surface.

The oil-in-water contact angles were measured with LVT200 model oil and C3 crude oil as droplets in 1 wt% NaCl brine at three different temperatures. From *Figure 5-19*, it can be seen that there was no effect of temperature on oil-in-water contact angle for LVT200 oil, which means that the steel surface wettability did not change with temperature variations in the presence of LVT200 oil. *Figure 5-20* shows the oil-in-water contact angle of C3 crude oil at different temperatures. The higher the temperature, the longer it took to reach the equilibrium state for the contact between the oil droplet and steel surface. The equilibrium oil-in-water contact angle increased slightly with temperature, and the steel surface became less hydrophilic. Normally, the oil-in-water contact angle does not change much with time, i.e. at 25 °C. When the droplet touched

the surface, it immediately acquired the shape determined by the equilibrium of surface free energy of oil, steel surface and water. That was not valid in the case of higher temperatures; at higher temperatures the contact angle increased with time. This was more pronounced at 80 °C and resulted in a less hydrophilic surface.

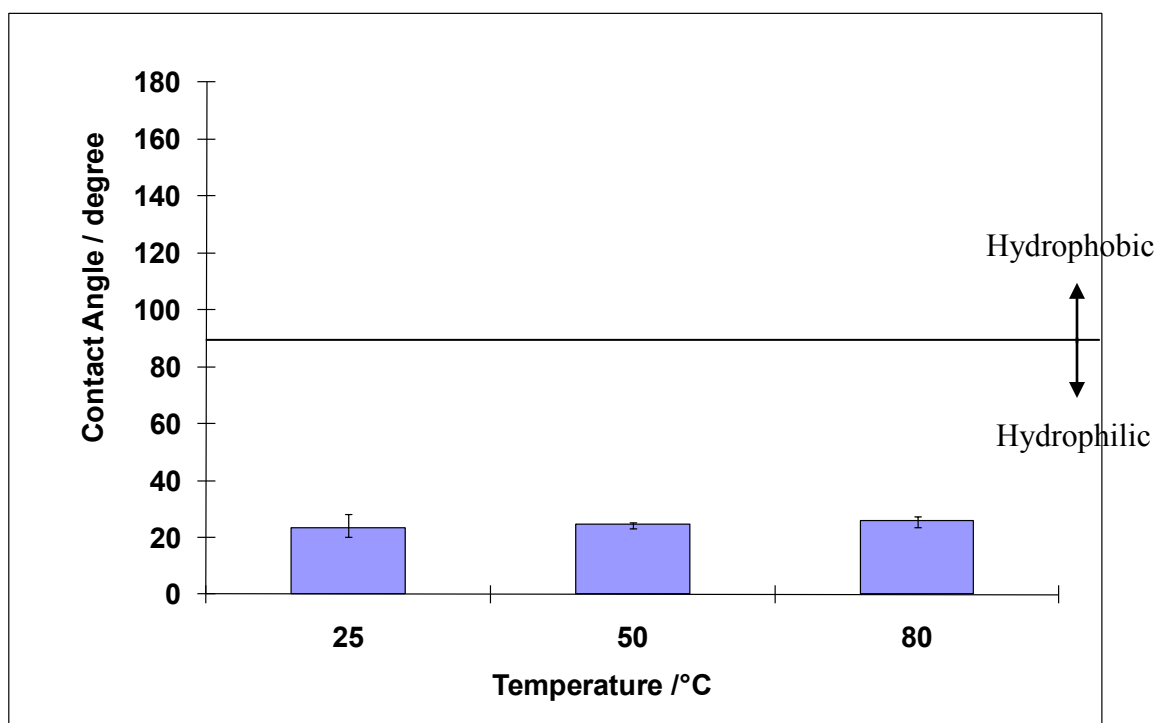


Figure 5-19. Oil-in-water contact angles at different temperatures (Oil phase: LVT200).

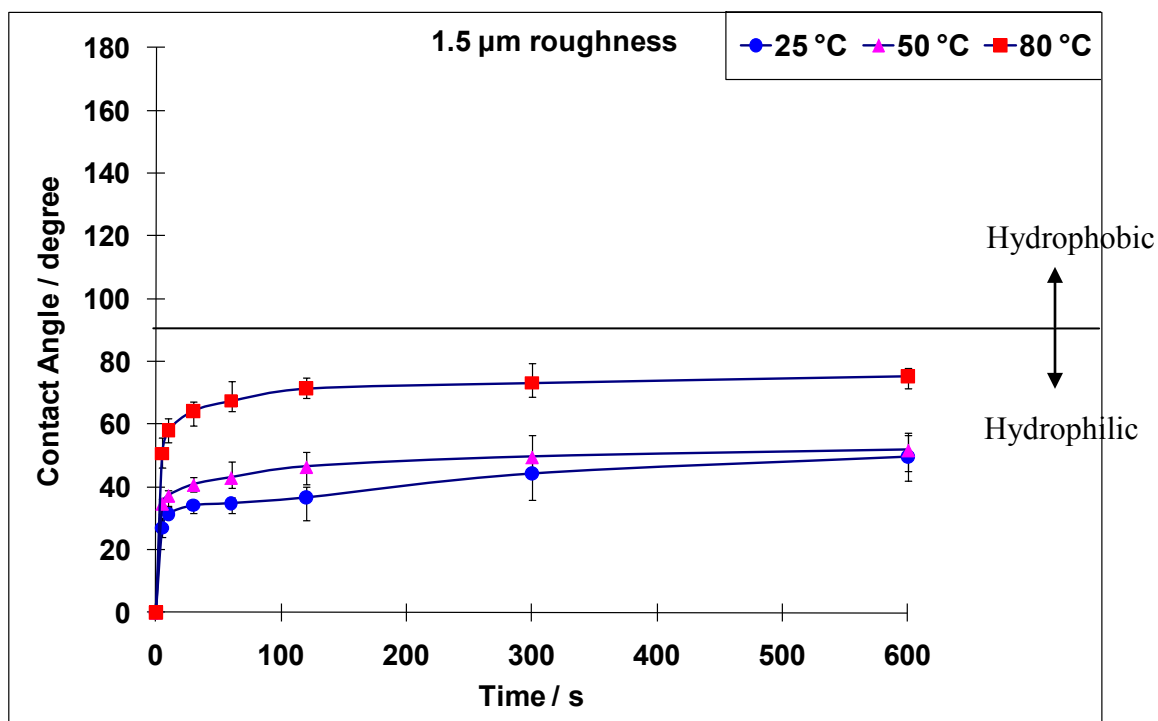


Figure 5-20. Oil-in-water contact angles at different temperatures (Oil phase: C3 crude oil).

### 5.3 Wettability of pre-wetted surface

#### 5.3.1 Experimental setup

Three series of tests were conducted to study the wettability of pre-wetted surfaces:

1. The effect of steel surface state on the wettability of pre-wetted surfaces.
2. The effect of corrosion inhibitor on the wettability of pre-wetted surfaces.
3. The effect of crude oils on the wettability of pre-wetted surfaces.

All three test series were carried out in the goniometer system described in section 5.1.1.2. The test matrices for the test series for pre-wetted steel surfaces are listed below.

### 5.3.2 Test matrix

The test matrix used to test the effect of steel surface state on the wettability of pre-wetted surfaces is shown in *Table 5-7*. Bare metal surfaces with three different surface roughness measures were used in the test, as well as iron carbonate covered surface and mill scale covered surface pre-wetted by either oil or water. The test liquids were LVT200 model oil and 1 wt% NaCl brine.

*Table 5-7.* Test matrix for effect of surface state on the wettability of pre-wetted surfaces.

Steel type	Carbon steel X65
Surface conditions	Bare metal surface: <ul style="list-style-type: none"> <li>• 1.5 <math>\mu\text{m}</math> roughness ( #400 sand paper)</li> <li>• 6 <math>\mu\text{m}</math> roughness (#36 sand paper)</li> <li>• 40 <math>\mu\text{m}</math> roughness ( machined)</li> </ul> Iron carbonate film covered surface: <ul style="list-style-type: none"> <li>• 15 <math>\mu\text{m}</math> roughness</li> </ul> Mill scale covered surface: <ul style="list-style-type: none"> <li>• 15 <math>\mu\text{m}</math> roughness</li> </ul>
Temperature	25 °C
Oil phase	LVT200
Water phase	1 wt% NaCl brine

1.5  $\mu\text{m}$  and 6  $\mu\text{m}$  roughness bare metal surfaces were achieved using 400 and 36 grit SiC paper, respectively. The 40  $\mu\text{m}$  roughness surface was created by machining of a bare metal surface with 1.5  $\mu\text{m}$  roughness. The iron carbonate film covered surface was produced in 1 wt% NaCl brine in a glass cell (*Figure 5-4*) in an environment of pH of 6.6 and temperature of 80 °C. A bare metal surface with roughness of 6  $\mu\text{m}$  was hung in the cell and exposed to these conditions for 24 hours. The mill scale covered surface was produced in an oven at 550 °C air temperature for 24 hours, in accordance with the

conditions shown in *Table 5-8*. The SEM images of the mill scale covered surface and its cross section are shown in *Figure 5-21* and *Figure 5-22*, respectively, showing a mill scale thickness of about 10  $\mu\text{m}$ . Energy dispersive X-ray spectroscopy (EDS) was used to verify the formation of iron carbonate and mill scale. InfiniteFocus<sup>®</sup> microscopy (IFM) was used for surface roughness characterization. The roughness of iron carbonate and mill scale covered surfaces was 15 $\mu\text{m}$  in both cases.

*Table 5-8*. Test matrix for mill scale formation.

Steel type	Carbon steel X65
Original surface conditions	6 $\mu\text{m}$ roughness bare metal surface
Furnace temperature	550 °C in air
Time	24 hrs

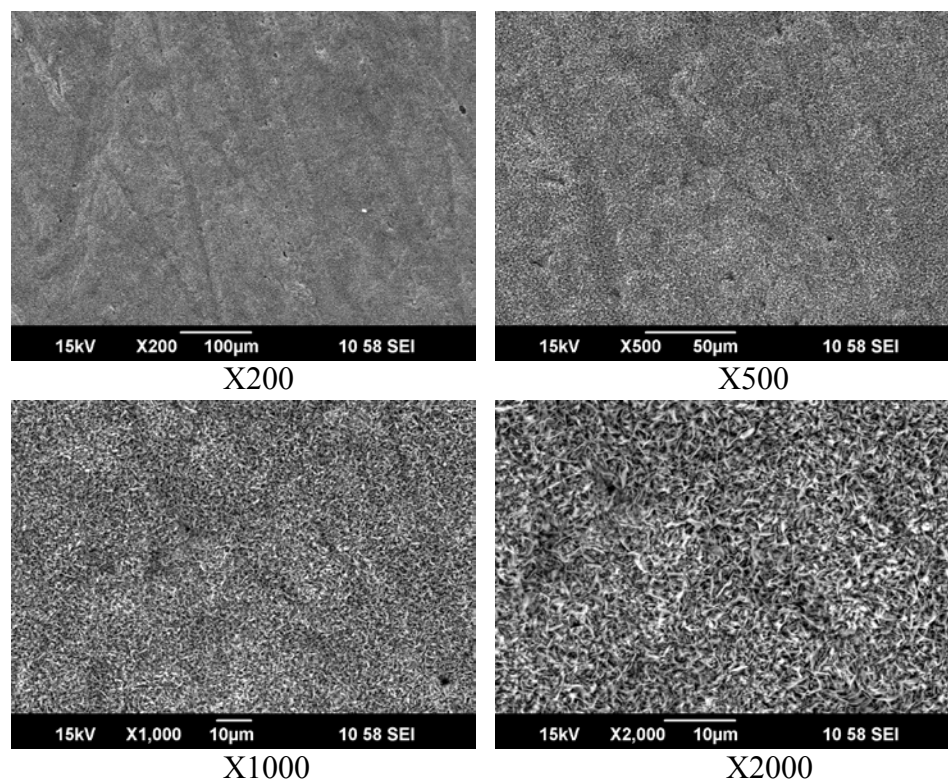


*Figure 5-21*. SEM images of mill scale covered steel surface.

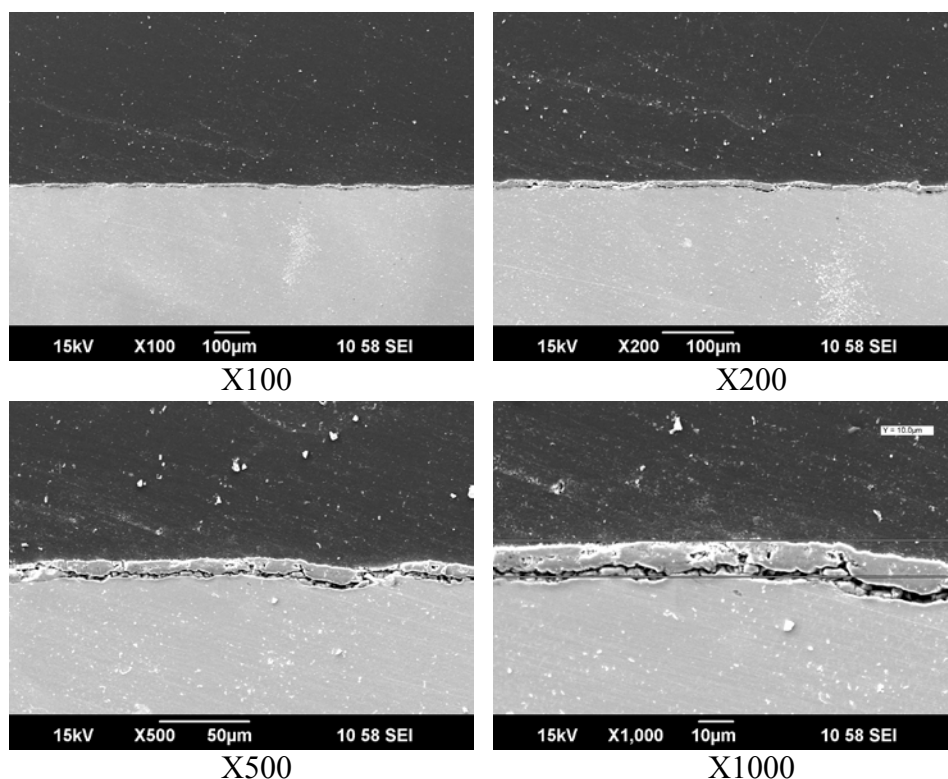


*Figure 5-22.* SEM images of cross section of a mill scale covered steel surface.

*Table 5-9* shows the matrix for testing the effect of pre-wetting with corrosion inhibitor on the wettability of a carbon steel surface. A 1.5 μm roughness bare metal steel surface was used as the test specimen; the test liquids were LVT200 oil and 1 wt% NaCl brine. A water soluble generic inhibitor package provided by Champion Technologies was used, with the main active component being quaternary ammonium chloride ("quat"), whose structure is shown in *Figure 5-23*.

Table 5-9. Test matrix for testing of the effect of corrosion inhibitor on the wettability of pre-wetted surfaces.

Steel type	Carbon steel X65
Surface conditions	Bare metal surface: <ul style="list-style-type: none"> <li>• 1.5 μm roughness ( #400 sand paper)</li> </ul>
Temperature	25 °C
System pressure	0.1013 MPa
Oil phase	LVT200
Water phase	1 wt% NaCl brine
Inhibitor (Quat) concentration (water soluble inhibitor)	0, 1, 5, 20 ppm

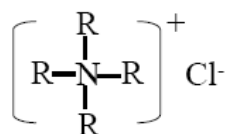


Figure 5-23. General chemical structures of the quaternary ammonium chloride (“quat”), R represents a hydrocarbon chain (Li, 2009).

Table 5-10 shows the test matrix for the pre-wetting of a carbon steel by crude oils. Five different crude oils (C1-C5) were tested. The properties of these five crude oils are shown in Figure 4-7 to Figure 4-10.

Table 5-10. Test matrix for testing the effect of crude oils on the wettability of pre-wetted surfaces.

Steel type	Carbon steel X65
Surface conditions	Bare metal surface: <ul style="list-style-type: none"> <li>• 1.5 μm roughness ( #400 sand paper)</li> </ul>
Temperature	25 °C
System pressure	0.1013 MPa
Oil phase	C1, C2, C3, C4, C5
Water phase	1 wt% NaCl brine

### 5.3.3 Experimental procedure

To test the effect of pre-wetting on the wettability of steel surfaces, a water pre-wetted surface and an oil pre-wetted surface were used to conduct water-in-oil contact angle and oil-in-water contact angle measurements, respectively. The following procedures were used to prepare the water pre-wetted surface and oil pre-wetted surface:

Water-in-oil contact angle measurement for water pre-wetted surface:

1. Put water into the goniometer cell and deoxygenate with CO<sub>2</sub> for 30 minutes (*Figure 5-24.1*).
2. Put the test specimen vertically on the test specimen holder and let the water phase soak the test specimen for 30 minutes (*Figure 5-24.2*).
3. Infuse deoxygenated oil phase into the cell and, at the same time, drain the water phase until the entire test specimen is covered by the oil phase (*Figure 5-24.3* and *Figure 5-24.4*). The oil phase replaces the water phase without exposing the specimen to air.
4. After 15 minutes, place the test specimen on the holder horizontally (*Figure 5-24.5*).
5. After 30 minutes, inject a water droplet into the oil phase so it will deposit on top of the test specimen in order to conduct water-in-oil contact angle measurements (*Figure 5-24.6*).

Oil-in-water contact angle measurement for oil pre-wetted surface:

1. Put oil phase into the goniometer cell and deoxygenate with CO<sub>2</sub> for 30 minutes (*Figure 5-25.1*).

2. Put the test specimen vertically on the test specimen holder and let the oil phase soak the test specimen for 30 minutes (*Figure 5-25.2*).
3. Infuse deoxygenated water phase into the cell and, at the same time, drain the oil phase until the entire test specimen is covered by the water phase (*Figure 5-25.3* and *Figure 5-25.4*). The water phase replaces the oil phase without exposing the specimen to air.
4. After 15 minutes, place the test specimen on the holder horizontally (*Figure 5-25.5*).
5. After 30 minutes, inject an oil droplet in the water phase so it will deposit beneath the test specimen in order to conduct oil-in-water contact angle measurements (*Figure 5-25.6*).

The following procedure was used to prepare the oil pre-wetted surface and conduct oil-in-water contact angle measurements to test the effect of pre-wetting by corrosion inhibitor and crude oils on the wettability of steel surfaces:

1. Polish the steel specimen with 400 grit SiC paper and first ultrasoniate the specimen in an ultrasonic isopropanol bath and then rinse using isopropanol.
2. Put the polished steel specimen into a beaker containing the oil phase. Let the entire specimen be immersed in the oil for 10 minutes.
3. Carefully transfer the steel specimen to the carbon dioxide saturated water phase in the goniometer.

4. Start recording the video of the steel specimen in the goniometer and observe the oil film that remains on the steel specimen and observe whether it contracts to form a droplet underneath the specimen or stays adhered to the steel's surface.
5. Stop recording when the shape of the contract oil phase no longer changes.

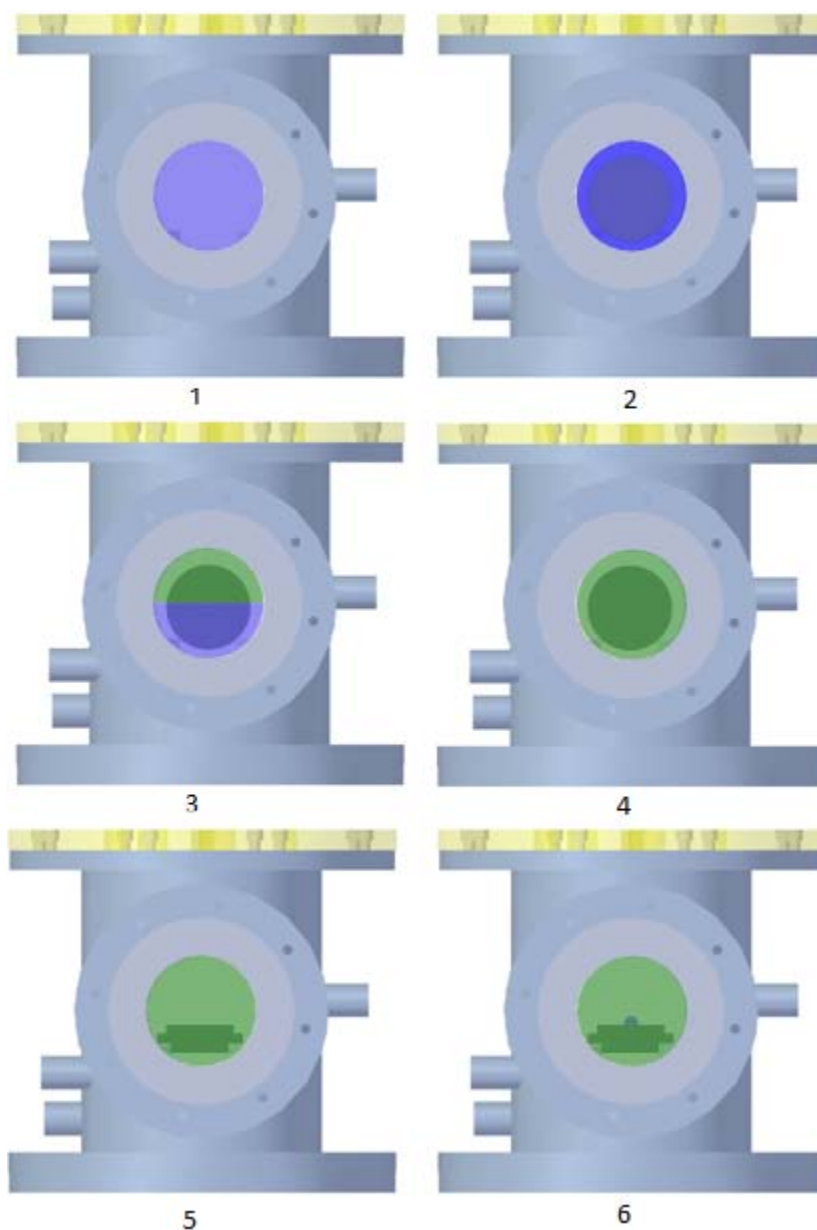


*Figure 5-24.* Visual description of the procedure for water pre-wetted surface preparation for the test of the effect of steel surface. Blue color stands for water phase and green color stands for oil phase.

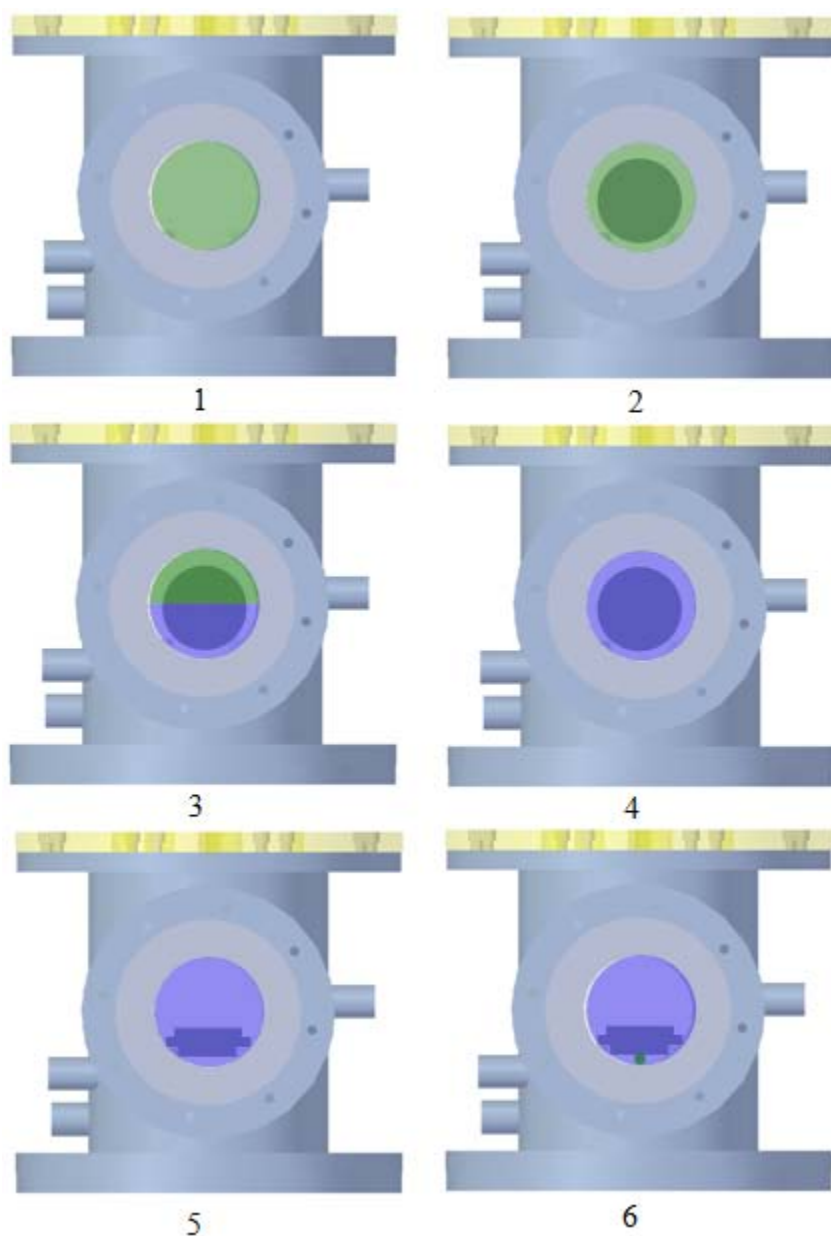


*Figure 5-25.* Visual description of the procedure for oil pre-wetted surface preparation for the test of the effect of steel surface. Blue color stands for water phase and green color stands for oil phase.

### 5.3.4 Experimental results

#### 5.3.4.1 Wettability of pre-wetted steel surface

During the water-in-oil contact angle tests for a water pre-wetted surface, the researcher observed that the water droplets collapsed onto the water pre-wetted steel surface instantaneously. *Figure 5-26.1* shows the water droplet at the time just before it was released onto the water pre-wetted surface. *Figure 5-26.2* shows that the droplet wetted the surface completely to form a very thin water layer after it was released. The whole wetting process took less than 0.07 seconds. For all five different surface conditions shown in *Table 5-7*, the water-in-oil contact angles were practically  $0^\circ$ , which indicates that the steel surface became completely hydrophilic after being pre-wetted by water. By comparing the water-in-oil contact angle results for the surface not pre-wetted by water (shown in *Figure 5-10*) with the water-in-oil contact angle results for the surface pre-wetted by water, it can be concluded that water pre-wetting the surface greatly enhanced the wettability of the surface.

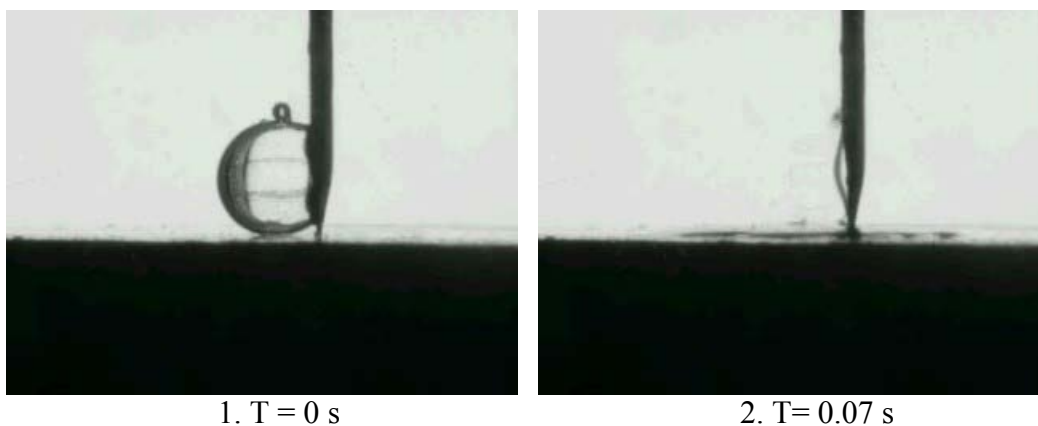


*Figure 5-26.* Process of water droplet wetting water pre-wetted surface.

The results for oil-in-water contact angle measurements for different steel surfaces pre-wetted by LVT200 oil are shown in *Figure 5-27*. The results show that the contact angles for different steel surface conditions ranged from 30 to 60°, which demonstrates that the steel surface was still hydrophilic even when pre-wetted by oil. This means that there was no uniform continuous oil layer formed on the steel substrate. The water phase displaced the oil phase on the steel substrate after the oil pre-wetted steel surface was entirely covered by water. *Figure 5-28* shows typical images of oil droplets beneath different steel surfaces pre-wetted by oil. During the test, a very interesting phenomenon was observed: there were many patches of oil film remaining on the steel surface even after the oil pre-wetted surface was entirely covered by water. One patch of oil film gradually curled up to form an oil droplet, and the oil-in-water contact angle became smaller and smaller. This indicates that the water phase gradually displaced the oil phase and wetted the oil pre-wetted surface. *Figure 5-29* shows the process of displacement of the oil phase by the water phase.

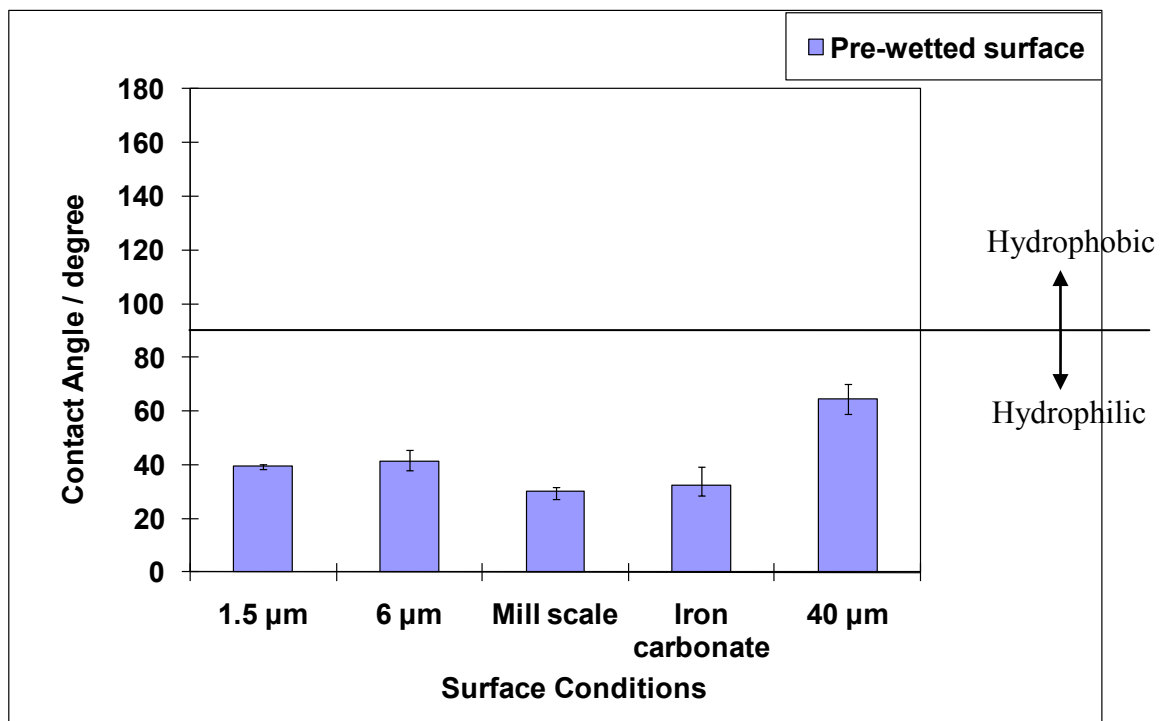


Figure 5-27. Oil-in-water contact angle with different surfaces pre-wetted by LVT200 oil.

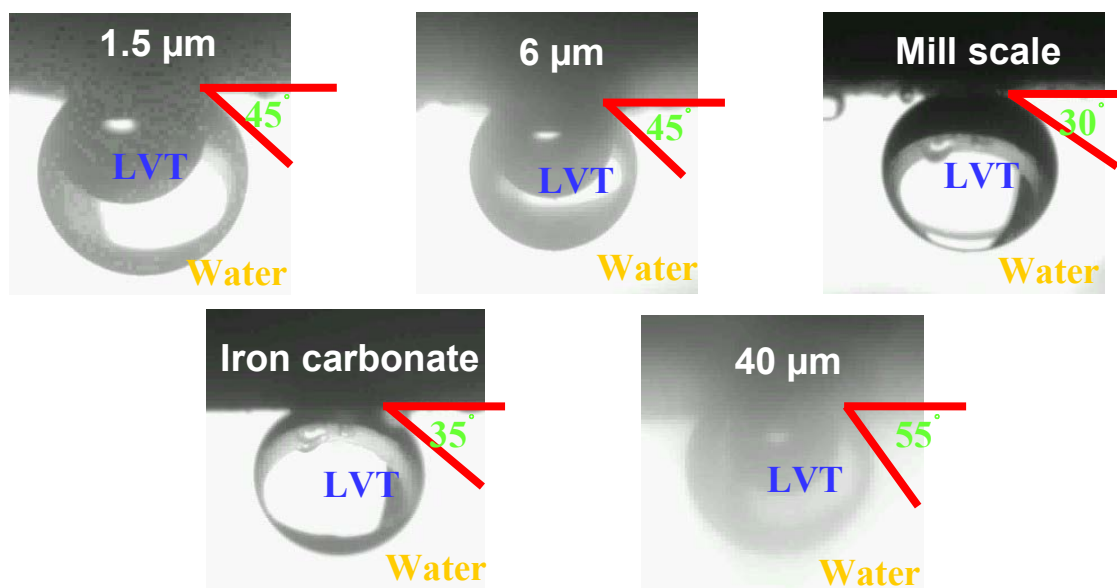


Figure 5-28. Typical images of oil droplet with different surfaces pre-wetted by LVT200 oil.

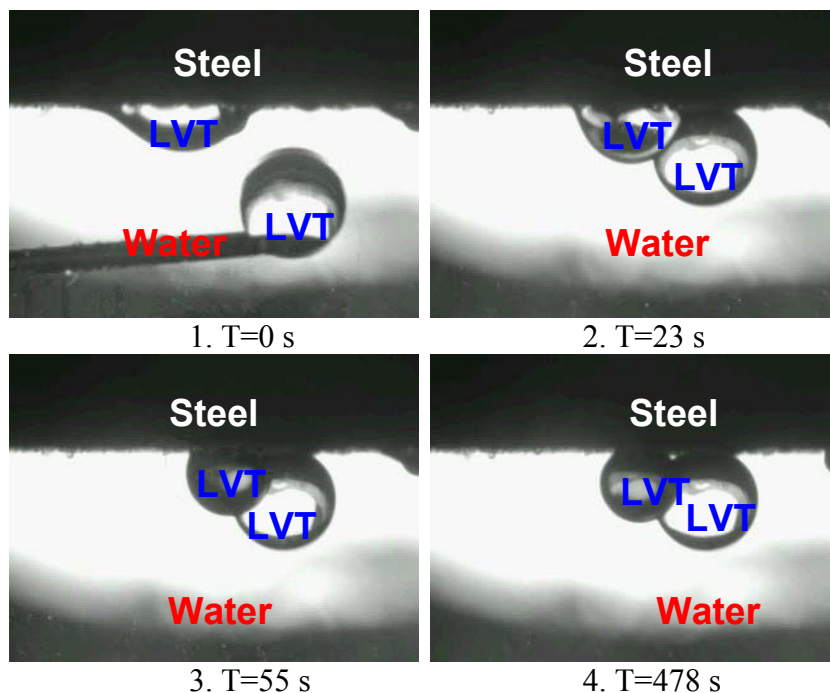


Figure 5-29. Process of the displacement of oil by water on the steel surface.

#### 5.3.4.2 Effect of corrosion inhibitor on the wettability of pre-wetted surface

Figure 5-30 to Figure 5-33 show the images of LVT200 oil droplet or oil film underneath the steel surface in 1wt% NaCl brine with different “quat” inhibitor concentrations (0, 1 5 and 20 ppm), respectively. The oil-water interfacial tensions for 0, 1, 5 and 20 ppm “quat” inhibitor concentrations are 40, 26.4, 5.3 and 3.6 dyne/cm, respectively (Li, 2009). It can be seen that after the oil pre-wetted steel specimen was put into the goniometer, the oil layer on the steel surface was gradually displaced by the water phase. The contact area of the oil to the steel surface became smaller and smaller, and the oil layer slowly contracted to form a droplet hanging beneath the steel surface. After about 8 minutes, the displacement of water phase to oil phase reached an equilibrium state with a stable oil droplet underneath the steel surface, and an equilibrium

contact angle was obtained. *Figure 5-34* shows the comparison of the results of the equilibrium contact angle of oil droplets formed underneath the oil pre-wetted steel surface and the water pre-wetted steel surface (Li, 2009) in 1wt% NaCl brine with different “quat” inhibitor concentrations. It can be seen that for oil pre-wetted steel surfaces, the addition of 1 ppm “quat” inhibitor did not affect the contact angle at all (it remained 73°). The addition of 5 ppm “quat” inhibitor was already enough to reverse the wettability of the steel surface from hydrophilic to hydrophobic, as the contact angle changed to 103°, whereas contact angles above 90° denote a hydrophobic surface. Addition of 20 ppm “quat” inhibitor made the steel surface even more hydrophobic, and the resulting contact angle was 151°. Compared to the contact angle of water pre-wetted steel surfaces obtained by Li (2009), the contact angle of oil pre-wetted steel surface was larger (*Figure 5-34*), which indicates that oil pre-wetting increased the hydrophobicity of the steel surface.

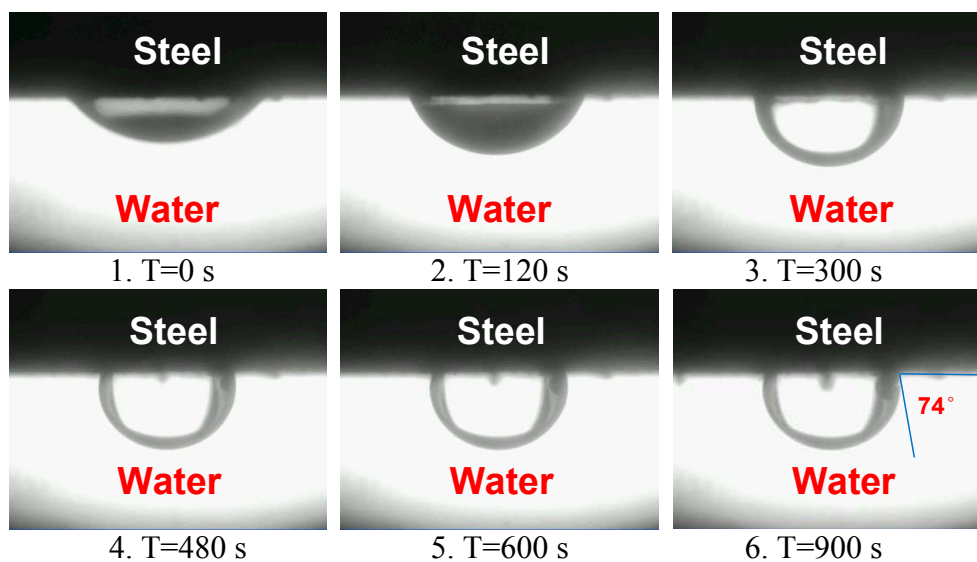


Figure 5-30. Process of displacement of oil phase (LVT200) by water phase (1wt NaCl brine).

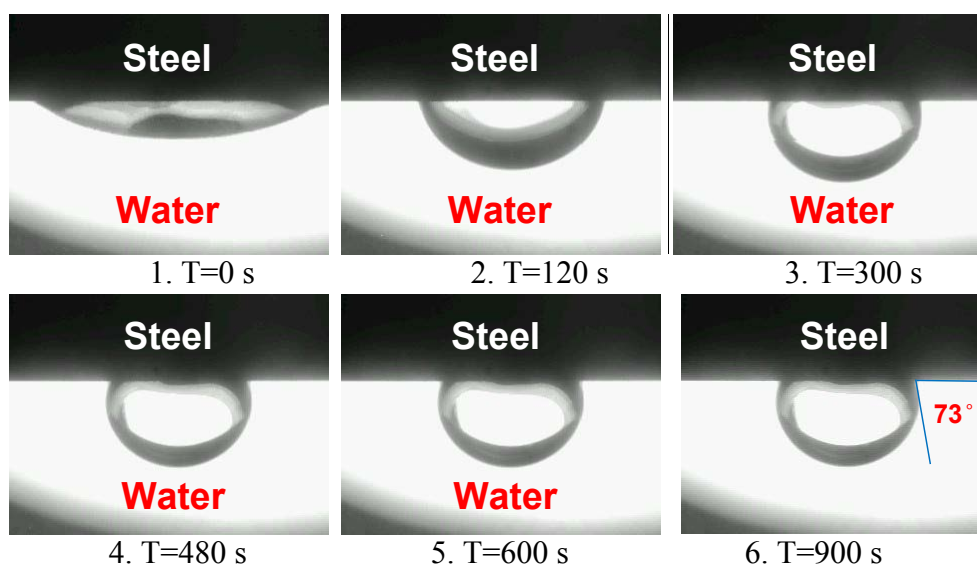


Figure 5-31. Process of displacement of oil phase (LVT200) by water phase (1wt% NaCl brine with 1 ppm "quat" inhibitor).

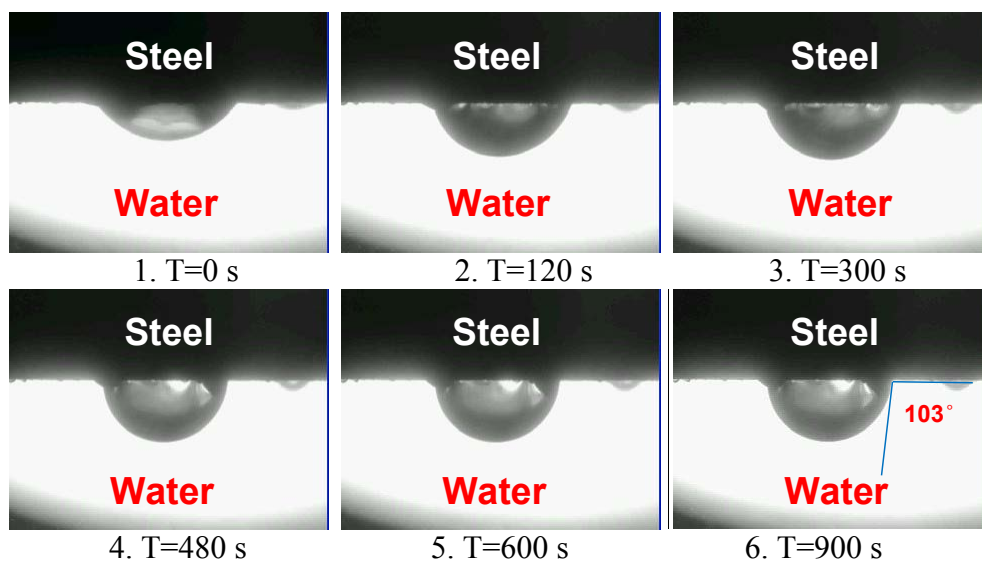


Figure 5-32. Process of displacement of oil phase (LVT200) by water phase (1 wt% NaCl brine with 5 ppm “quat” inhibitor).

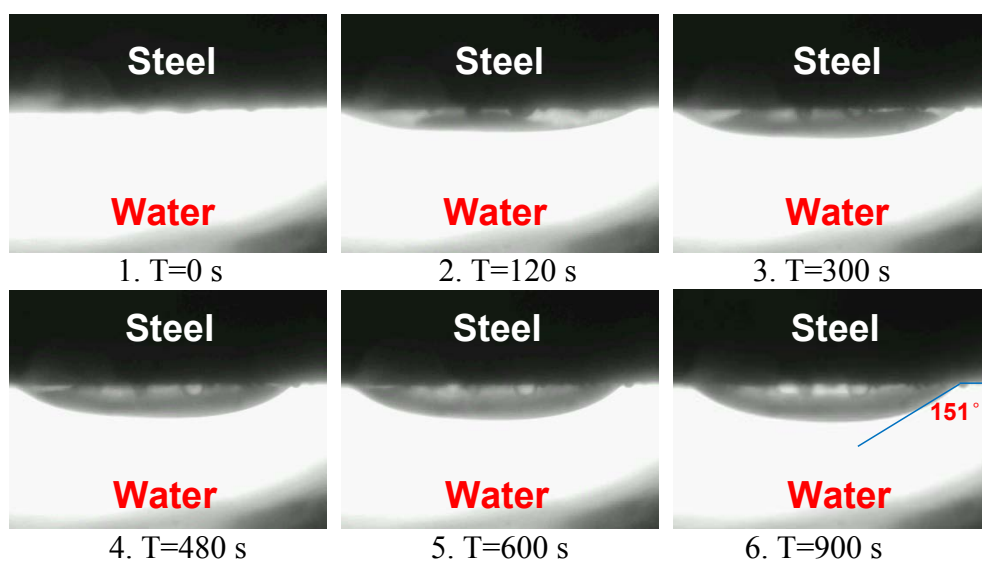


Figure 5-33. Process of displacement of oil phase (LVT200) by water phase (1 wt% NaCl brine with 20 ppm “quat” inhibitor).

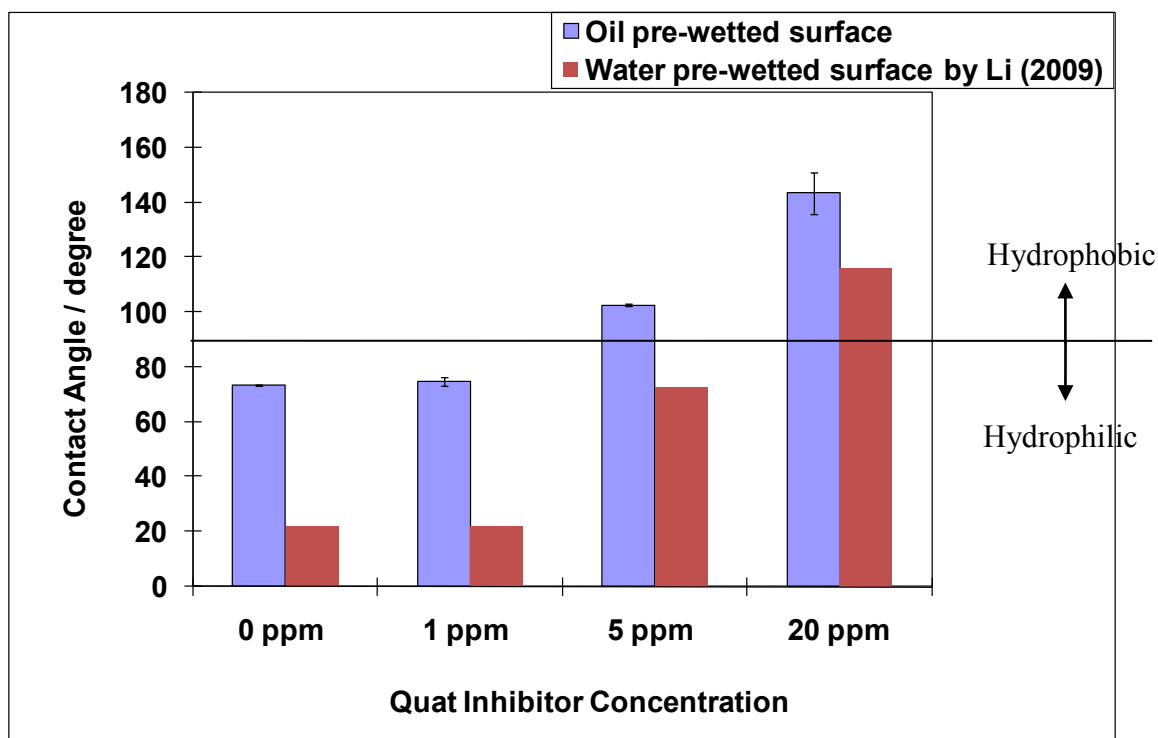
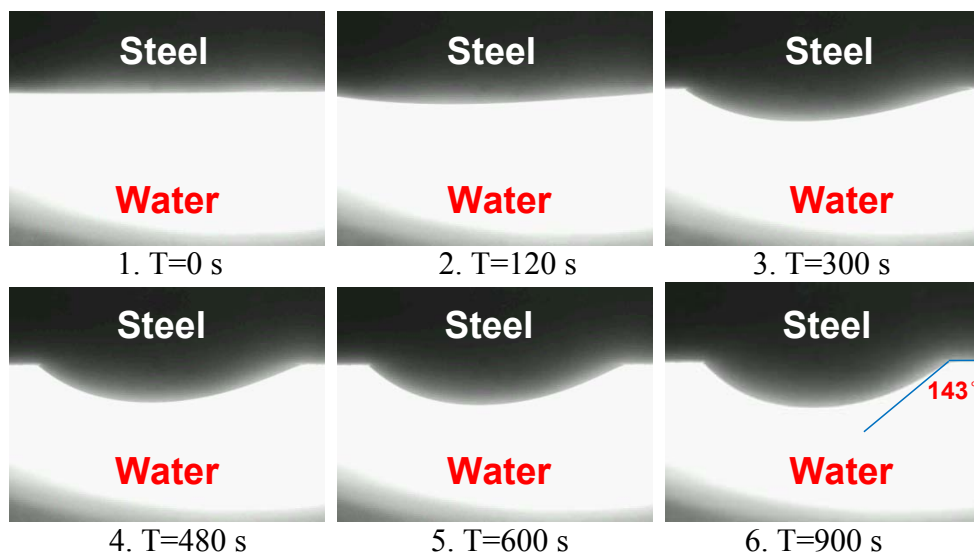


Figure 5-34. Comparison of equilibrium oil-in-water contact angle of oil droplet underneath the steel surface pre-wetted by oil and the steel surface pre-wetted by water (Li, 2009) in 1wt% NaCl brine with different “quat” inhibitor concentrations.

#### 5.3.4.3 Effect of crude oils on the wettability of pre-wetted surface

Figure 5-35 to Figure 5-36 show an oil film consisting of crude oils C1 and C2 contracting to form a droplet underneath the steel surface in 1wt% NaCl brine, respectively. It can be seen that for crude oils C1 and C2, the oil layer on the steel surface was gradually displaced by the water phase. It slowly contracted to form an oil droplet hanging underneath the steel surface, resulting in contact angles of  $143^\circ$  and  $157^\circ$  for crude oils C1 and C2, respectively. However, for heavier and more viscous crude oils (C3, C4 and C5), the oil layer on the steel surface could not be displaced by the water phase at all (Figure 5-37 to Figure 5-39), and the contact angle was concluded to be  $180^\circ$ .

Even after 8 minutes of being immersed in 1wt% NaCl brine, the oil layer for crude oils C3, C4 and C5 kept its original surface coverage and did not contract. *Figure 5-40* shows the equilibrium oil-in-water contact angles of oil droplets underneath the steel surfaces pre-wetted by different crude oils. It can be seen that the contact angle for every crude oil was bigger than  $90^\circ$ , which indicates the crude oil pre-wetted surface to be hydrophobic, especially for the steel surface pre-wetted by C3, C4 and C5 oil. By comparing the results shown in *Figure 5-40* with the oil-in-water contact angle results for water pre-wetted steel surfaces shown in *Figure 5-12*, it can be concluded that crude oil pre-wetting can reverse the wettability of steel surfaces from hydrophilicity to hydrophobicity and significantly affect the wettability of the surface.



*Figure 5-35.* Process of displacement of oil phase (C1) by water phase (1wt% NaCl brine).

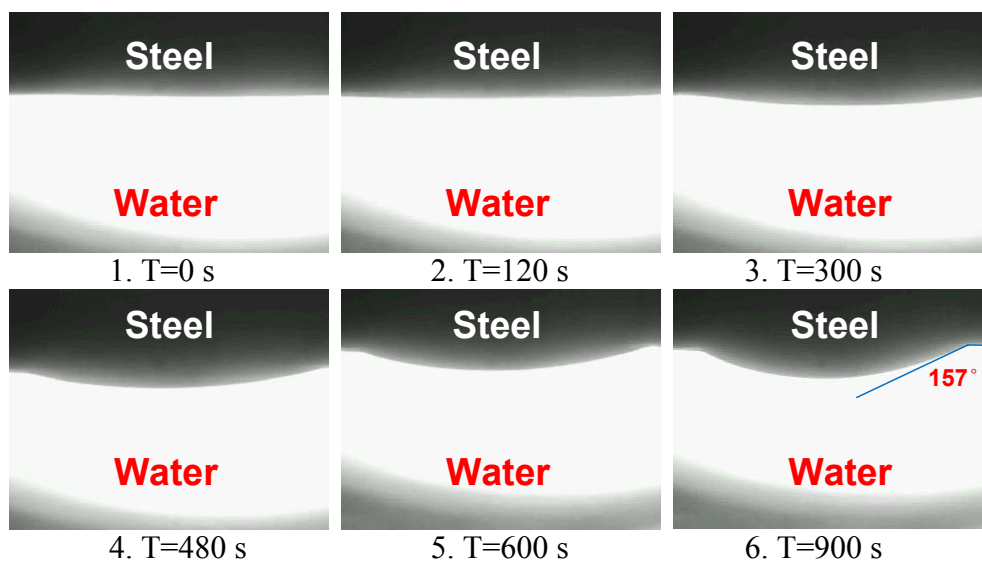


Figure 5-36. Process of displacement of oil phase (C2) by water phase (1wt% NaCl brine).

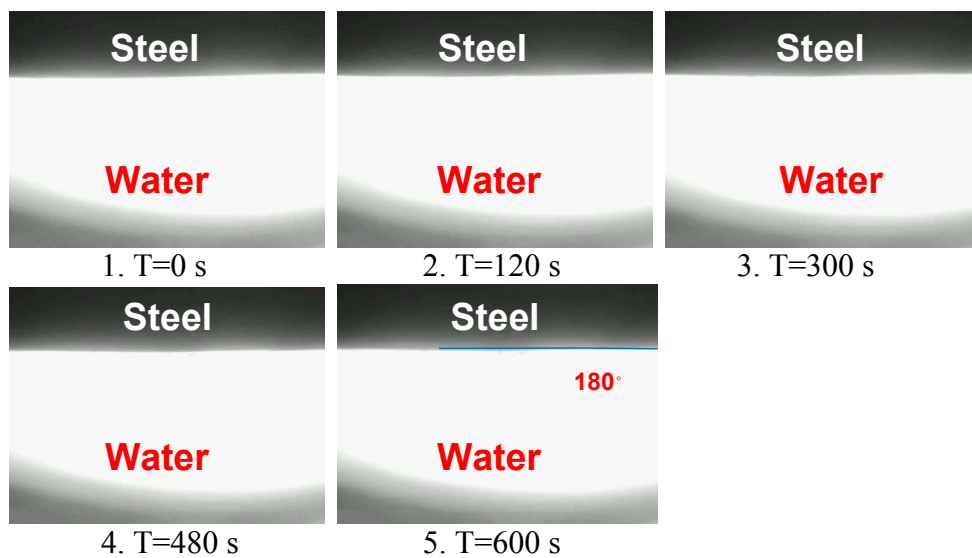


Figure 5-37. Images of steel specimen pre-wetted by C3 crude oil in 1wt% NaCl brine.

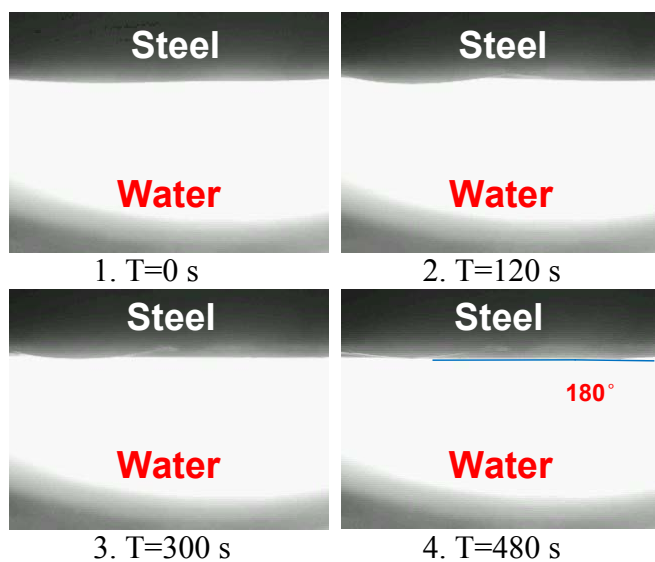


Figure 5-38 Images of steel specimen pre-wetted by C4 crude oil in 1wt% NaCl brine.

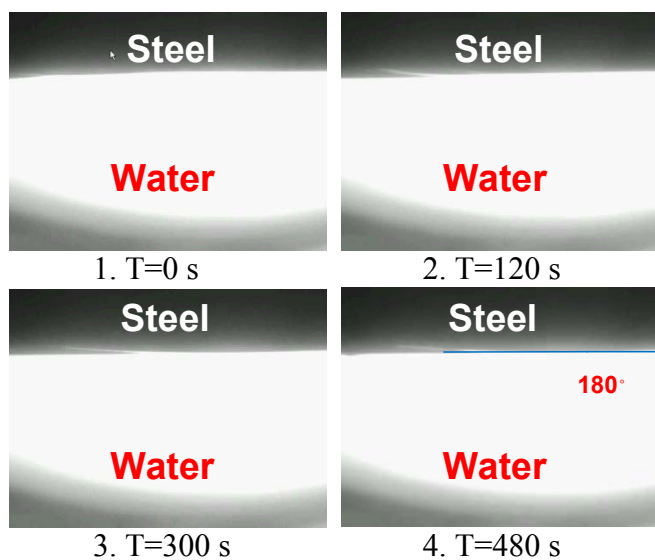


Figure 5-39. Images of steel specimen pre-wetted by C5 crude oil in 1wt% NaCl brine.

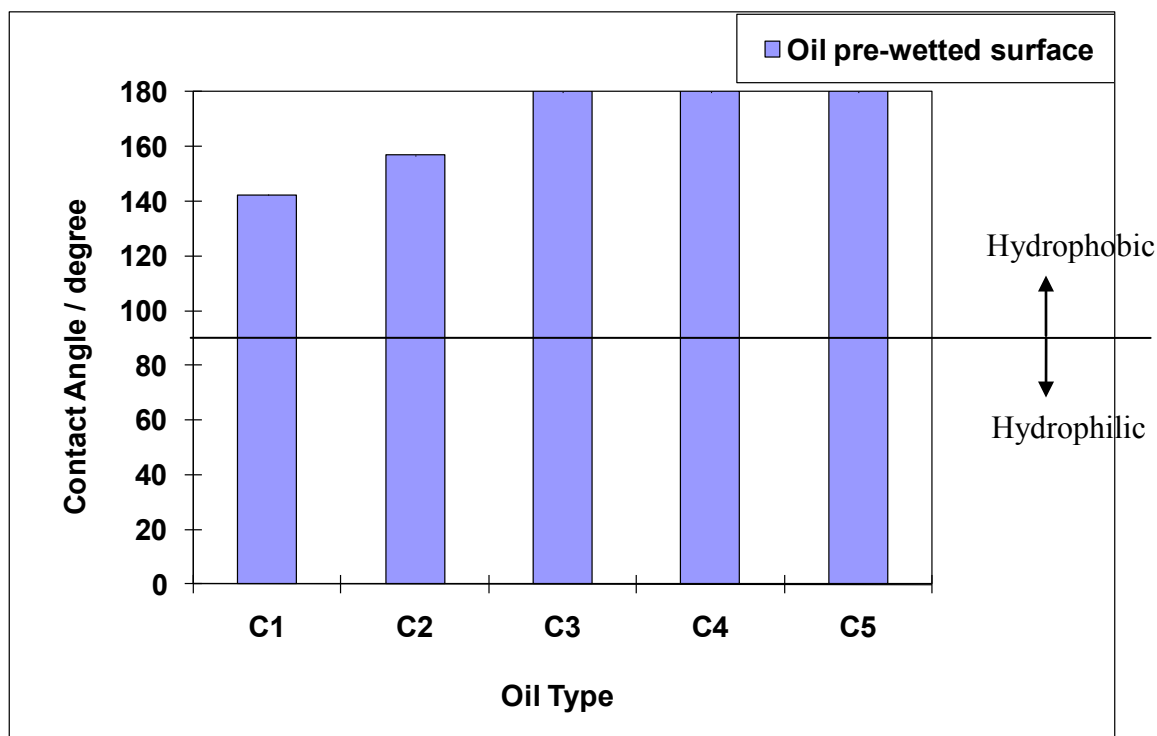


Figure 5-40. Equilibrium oil-in-water contact angle of different oil droplets underneath the steel surface pre-wetted by different crude oils.

#### 5.4 Summary

A comprehensive experimental research program was carried out to investigate the effect of steel surface state on its wettability. It was found that contact angle changed with time before the contact between liquid droplet and solid surface reached equilibrium, especially for water-in-oil contact angles. Surface roughness or surface state (whether iron carbonate covered or not) did not affect wettability, although very rough surfaces had a higher water-in-oil contact angle, which may be due to the hysteresis caused by high surface roughness. Furthermore, the crude oil type did not affect the oil-in-water contact angle for steel surfaces not pre-wetted by oil. As for the effect of

temperature, both water-in-oil and oil-in-water contact angle measurement results show that increasing the temperature made the steel surface less hydrophilic.

The results of the contact angle measurements depended strongly on experimental procedure. For instance, pre-wetting of the steel surface with either water or oil had a great effect on wettability. Crude oil pre-wetting of the steel surface and the addition of “quat” inhibitor (above 5 ppm) both led to a transition of the wettability of steel surface from hydrophilicity to hydrophobicity.

## CHAPTER 6 : EFFECT OF DYNAMIC WETTING ON CARBON DIOXIDE CORROSION IN A HORIZONTAL ROTATING CYLINDER

In order to investigate the effect of steel surface state on water wetting, a series of experiments were conducted on a goniometer system to measure the stationary contact angles in oil-water two-phase system. The experimental results from the goniometer system have been discussed in the previous chapter. Although the results of contact angle measurements in goniometer system are valuable, there are some important points to keep in mind. First, only a stagnant contact angle can be measured in a goniometer system, while the oil-water two-phase flow is a dynamic system. Second, the test procedure affects the contact angle measurement significantly, including whether the surface is pre-wetted with oil or water.

Teeters, Wilson, *et al.*, 1988 pointed out the difference between the static contact angles and the dynamic contact angles present in multiphase flow system. Nestic & Carroll (2003) stated that there were arguments that, at higher flow rates, the hydrodynamic parameters (Blake, 1988; Blake & Ruschak, 1997) played a more important role on the wettability than the surface properties, which almost have no effect on it. Nestic & Carroll (2003) deployed a horizontal rotating cylinder (HRC) to study the effect of water wetting on CO<sub>2</sub> corrosion of mild steel in oil-water two-phase system.

The present study is based on Nestic & Carroll's (2003) work and extends the test parameters to various degrees of steel surface roughness and lower rotating speeds. A novel benchtop apparatus, the horizontal rotating cylinder (HRC), was used to investigate the effects of dynamic water wetting on CO<sub>2</sub> corrosion of mild steel in oil-water flow.

## 6.1 Experimental setup

### 6.1.1 Horizontal rotating cylinder (HRC)

Figure 6-1 shows the schematic of the horizontal rotating cylinder. A 2" O.D. cylindrical mild steel test specimen (working electrode) was mounted on a horizontal stainless steel shaft (covered with Teflon) rotated by a variable-speed 24 V motor. The transparent acrylic cylindrical cell was horizontally mounted on a mobile benchtop. Fittings on the end of the cell were provided for counter electrode and reference electrode (for electrochemical measurements), a gas bubbler, a pH probe and an outlet for filling and emptying the cell. This benchtop apparatus is similar to a standard rotating cylinder, in a three-electrode glass cell setup, except that the direction of the electrode is horizontal and the working electrode is alternatively wetted by the two phases, water and oil during electrochemical measurements. The ratio of time wetted by each phase for the test specimen (working electrode) is related to the level of the oil-water interface.

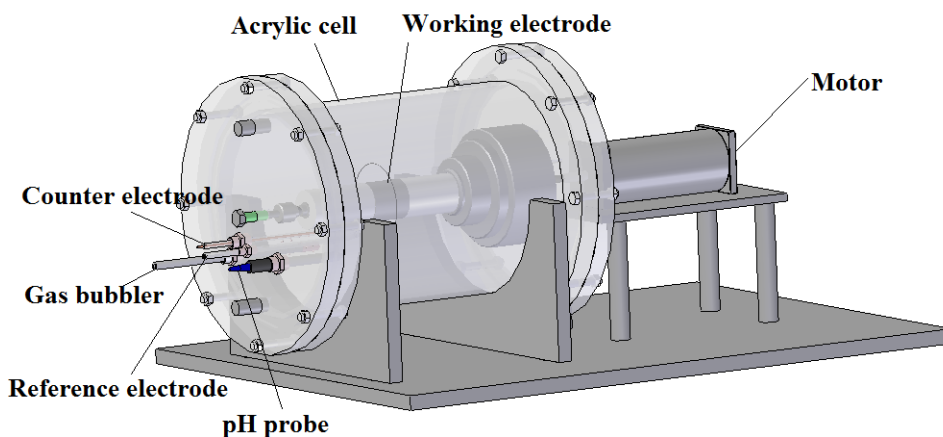


Figure 6-1. Schematic of horizontal rotating cylinder (HRC).

### 6.1.2 Test matrix and experimental procedure

The test matrix is shown in *Table 6-1*. A 2" O.D. and 2" length carbon steel C1018 cylinder with an exposed surface area of 81 cm<sup>2</sup>, was used as the working electrode. The chemical composition of C1018 carbon steel is shown in *Table 6-2*. 1 wt% NaCl brine was used as the water phase. Prior to being added to the cell, this solution was purged with CO<sub>2</sub> more than 1 hour. The temperature was ambient temperature and the pH was not adjusted during the experiments and was measured at pH3.9±0.1 at this temperature. LVT200 model oil was used as the oil phase, and it was saturated with CO<sub>2</sub> before being added to the cell.

*Table 6-1*. Test matrix for HRC test.

Steel type	Carbon steel 1018
Surface conditions	Bare metal surface: <ul style="list-style-type: none"> <li>• 1.5 μm roughness ( #400 sand paper)</li> <li>• 6.0 μm roughness (#36 sand paper)</li> <li>• 40 μm roughness (machined)</li> </ul>
Temperature	25 °C
Pressure	1 bar CO <sub>2</sub>
pH	3.9±0.1
Oil phase	LVT200
Water phase	1 wt% NaCl brine
Water fraction (The fraction of the steel surface area wetted by water)	30%, 50%, 80%, 100%
Rotating speed (rpm)	0 , 3, 10, 20, 30
Tangential velocity (m/s)	0 ~ 0.078

*Table 6-2. Chemical composition of carbon steel C1018.*

Element	Composition (%)	Element	Composition (%)
Al	0.022	S	0.012
As	0.006	Sb	0.011
C	0.20	Si	0.25
Co	0.003	Sn	0.007
Cr	0.10	Ta	0.029
Cu	0.083	Ti	0.001
Mn	0.87	V	0.003
Mo	0.024	W	0.020
Nb	0.001	Zn	0.002
Ni	0.071	Zr	0.003
P	0.009	Fe	Balance

Three bare metal surfaces with different surface roughness measures were tested during the experiments: 1.5  $\mu\text{m}$ , 6  $\mu\text{m}$  and 40  $\mu\text{m}$ . The 1.5  $\mu\text{m}$  and 6  $\mu\text{m}$  roughness bare metal surfaces were achieved by polishing the steel test specimens with 400 and 36 grit SiC paper, respectively. During and after polishing, the test specimens were rinsed with isopropanol to minimize the oxidation on the surfaces. The 40  $\mu\text{m}$  roughness surface was created using machining. The test specimen was mounted on the stainless shaft, and a cover plate with different fittings was promptly fastened on the acrylic cell.  $\text{CO}_2$  was purged into the cell to discharge the air out of the cell. The pre-carbonated NaCl brine solution was infused into the cell at the desired level, and LVT200 oil was added to the top of the steel piece.

Oil-water two phase experiments were carried out at three different water fractions, 30%, 50% and 80%. Water fraction is defined as the fraction of the area of the steel piece that sits below the oil-water interface line. 100% water fraction or single phase water experiments were performed as a baseline test. At each water fraction, a series of

linear polarization resistance (LPR) measurements was conducted to calculate corrosion rate at different rotating speeds varying from 0 rpm to 30 rpm (0.078 m/s) using a Gamry<sup>®</sup> Potentiostat. The electrode was polarized from the open-circuit potential,  $\pm 20$  mV, scanning at a rate of 0.5 mV/s. The polarization resistance  $R_p$  measured by LPR technique was compensated with the solution resistance  $R_s$  measured by the electrochemical impedance spectroscopy (EIS) technique.

### 6.1.3 Methodology of data interpretation

In order to appropriately interpret the results data, two new concepts, nominal water wetted area  $A_N$  and effective water wetted area  $A_E$ , are explained as follows. Nominal water wetted area  $A_N$  is the area fraction of the steel piece below the horizontal oil-water interface line, which is directly related to the water fraction mentioned above in the test matrix. Effective water wetted area  $A_E$  is the area fraction of the steel piece below the oil-water-steel three-phase contact line. If the steel surface is neutral, as shown in *Figure 6-2-(a)*, the nominal water wetted area  $A_N$  is equal to the effective water wetted area  $A_E$ . If the steel surface is hydrophilic, as shown in *Figure 6-2-(b)*, the effective water wetted area  $A_E$  should be greater than the nominal water wetted area  $A_N$ . The corrosion rate  $CR$  (mm/yr), based on effective water wetted area, can be calculated as:

$$CR = \frac{1.16B}{R_p \cdot A_E} \quad (6.1)$$

$$B = \frac{\beta_a \beta_c}{2.3(\beta_a + \beta_c)} \quad (6.2)$$

In Equation (6.2), the Tafel constant  $\beta_a=110$  mV and  $\beta_c=120$  mV. Assuming that the corrosion rate based on effective water wetted area does not change, the following correlation can be claimed:

$$R_{pE} \cdot A_E = R_{P100\%} \cdot A_{100\%} \quad (6.3)$$

$$A_E = \frac{R_{P100\%} \cdot A_{100\%}}{R_{pE}} \quad (6.4)$$

If  $A_E/A_N > 1$ , the steel surface is preferentially water-wetted or hydrophilic. If  $A_E/A_N < 1$ , the steel surface is preferentially oil-wetted or hydrophobic.

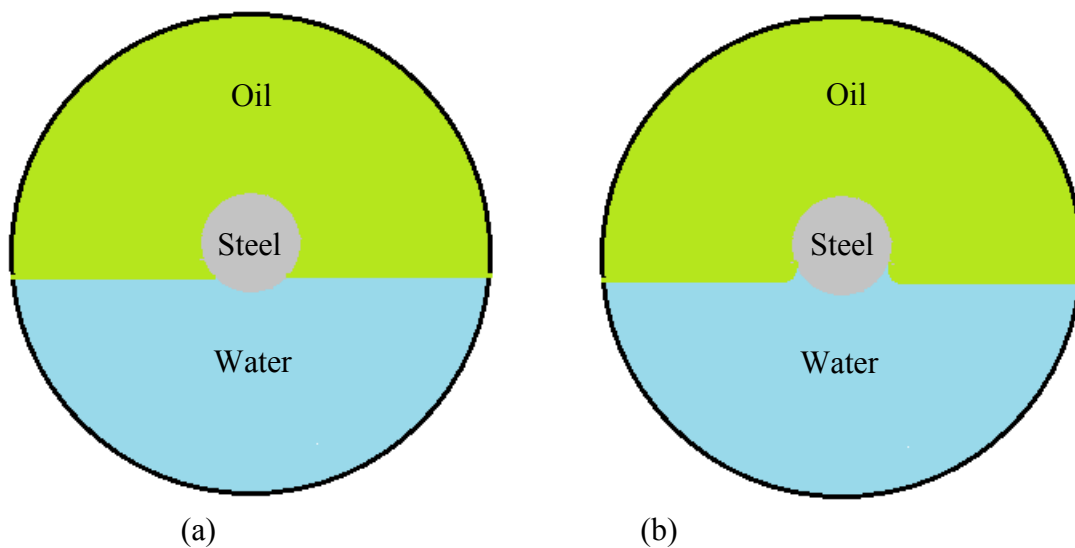


Figure 6-2. Schematic of steel surface wetted by water and oil phase. (a): Neutral surface, (b): Hydrophilic surface.

## 6.2 Results and discussion

### 6.2.1 Verification of HRC

The HRC apparatus had to be verified before being used to perform formal electrochemical measurement. The verification test was performed in 1 wt % NaCl brine at pH 3 (adjusted by HCl solution), 1 bar CO<sub>2</sub> partial pressure and 25 °C temperature. The limiting current correlated with a mass transfer coefficient was determined by the potentiodynamic sweep technique. The potentiodynamic sweep started at 600 mV to 1200 mV below the free corrosion potential and finished 200 mV over the free corrosion potential. The scanning rate was 0.2 mV/s. *Figure 6-3* shows the potentiodynamic sweeps for different rotational speeds. It can be seen that the main cathodic reaction was the reduction of H<sup>+</sup> ions, which was under mass transfer control.

Early work reported by Eisenberg, Tobias, *et al.* (1954) provides a commonly accepted description for rotating cylinder electrode mass transport. The mass transfer coefficient,  $k_m$  (m/s), for a rotating cylinder is derived using the following relationship:

$$k_m = D \cdot Sh / l = 0.0791 Re^{0.7} Sc^{0.356} D / l \quad (6.5)$$

$$Re = \rho u l / \mu \quad (6.6)$$

$$Sc = \mu / \rho D \quad (6.7)$$

where  $Sh$ ,  $Re$  and  $Sc$  are the dimensionless Sherwood, Reynolds and Schmidt numbers, respectively,  $D$  (m<sup>2</sup>/s) is the diffusion coefficient for H<sup>+</sup>,  $l$  (m) is the cylinder electrode diameter,  $\rho$  (kg/m<sup>3</sup>) is the density of the fluid,  $u$  (m/s) is the tangential velocity of the

cylinder electrode, and  $\mu$  (kg/m·s) is the dynamic viscosity of the fluid. Converting the limiting current densities (*Figure 6-3*) to the mass transfer coefficient and comparing them with both Eisenberg's mass transfer correlation and Nesic & Postlethwaite's (1996a) experimental results (as shown in *Figure 6-4*), the present results are within 10% of the proposed correlation, which indicates that the current HRC performed very well.

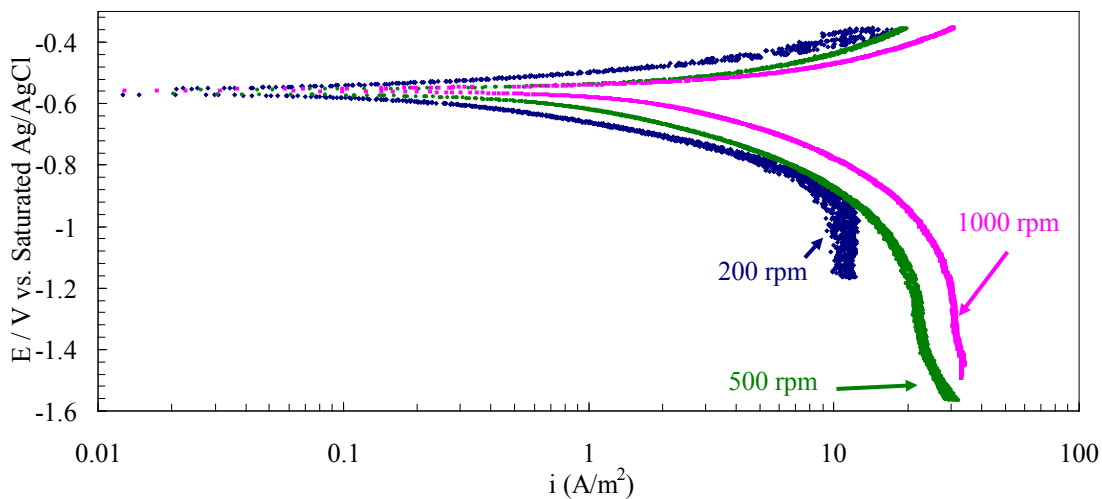


*Figure 6-3.* Potentiodynamic sweep showing the velocity effect on limiting current densities in HCl solution at pH 3, 1wt% NaCl,  $P_{N_2}=1$  bar,  $T=25$  °C and carbon steel C1018.

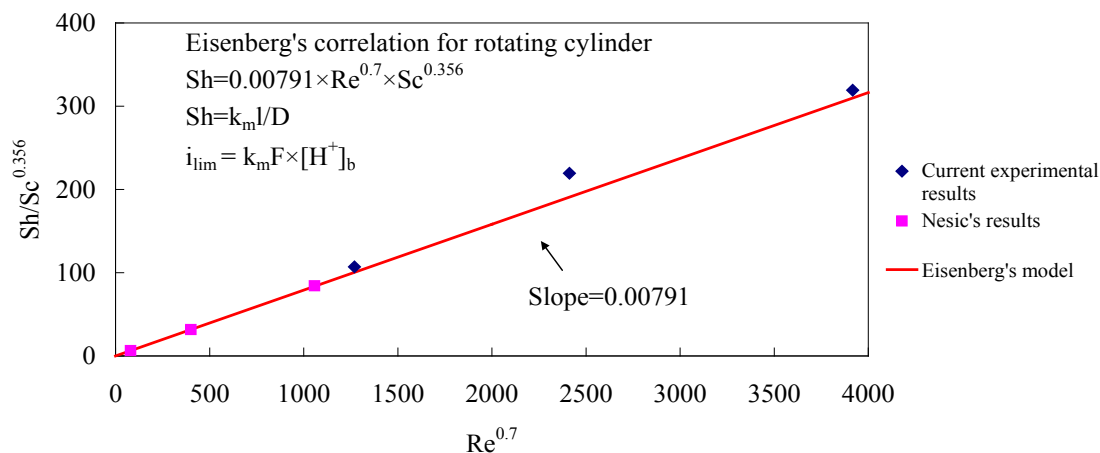


Figure 6-4. Comparison to the Eisenberg's correlation for a rotating cylinder for the verification of the validity of the electrochemical measurements using the HRC.

### 6.2.2 Results of the low speed test

Linear polarization resistance measurements were taken for each test. The corrosion rate trends for increasing rotating speed for different water fractions (nominal water wetted area  $A_N$ ) are shown in Figure 6-5 to Figure 6-7 for 1.5  $\mu\text{m}$ , 6.0  $\mu\text{m}$  and 40  $\mu\text{m}$  roughness steel surfaces, respectively. The corrosion rate was calculated using the entire surface area. It can be seen that, within the rotating speeds tested (0~30 rpm), the corrosion rates for different steel surfaces fully wetted by water (100% water fraction) did not change significantly as rotating speed increased. This indicates that the mass transfer effect on the corrosion rate was very slight and can be neglected. It also can be seen that, within the rotating speeds tested (0~30rpm), the corrosion rate for other water fractions did not change significantly as rotating speed increased. The dynamic wetting had no obvious effect on the  $\text{CO}_2$  corrosion of the carbon steel.

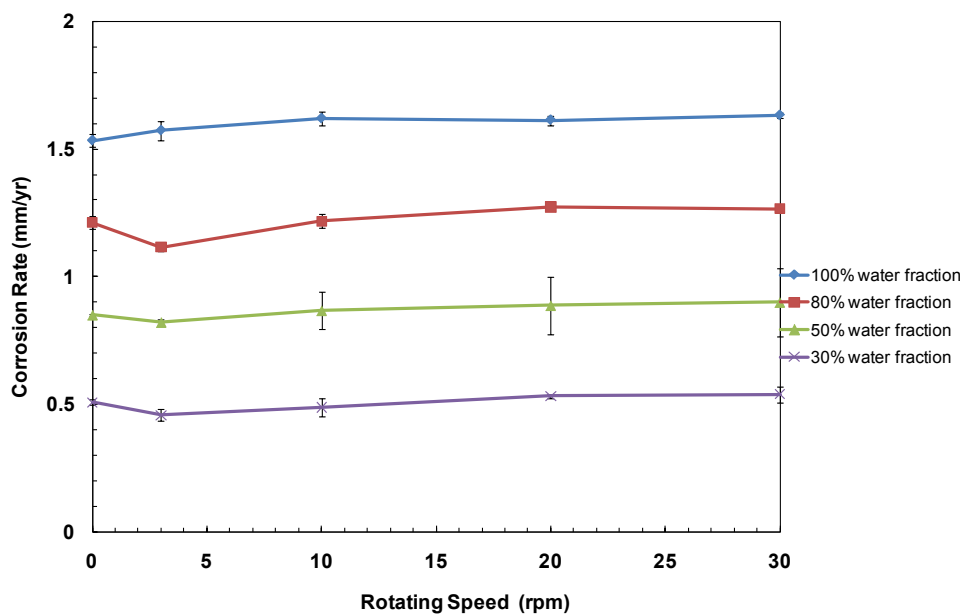


Figure 6-5. Corrosion rates with increasing velocity at different water fractions for 1.5  $\mu\text{m}$  roughness surface (corrosion rate calculated using whole surface area).

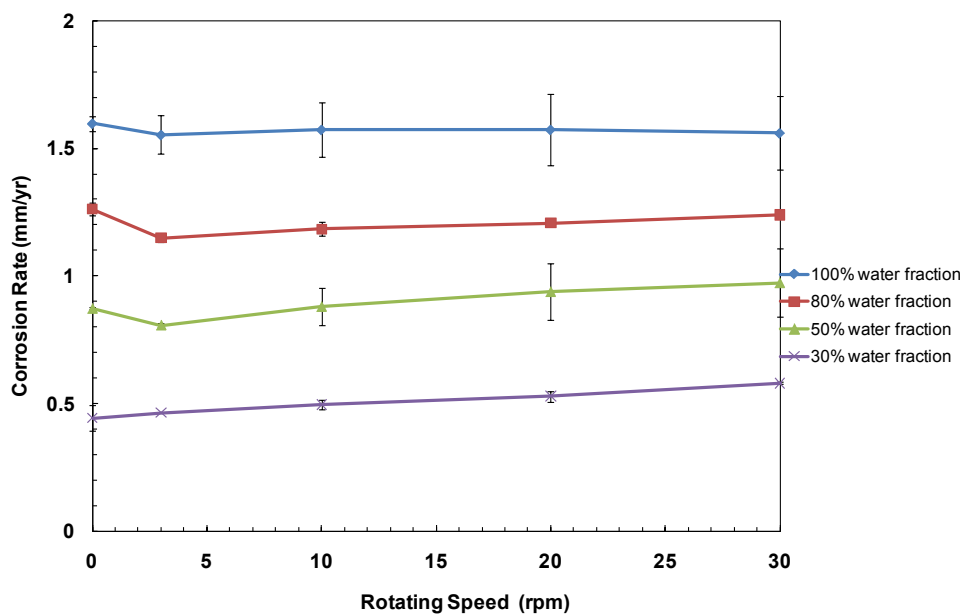


Figure 6-6. Corrosion rates with increasing velocity at different water fractions for 6.0  $\mu\text{m}$  roughness surface (corrosion rate calculated using whole surface area).

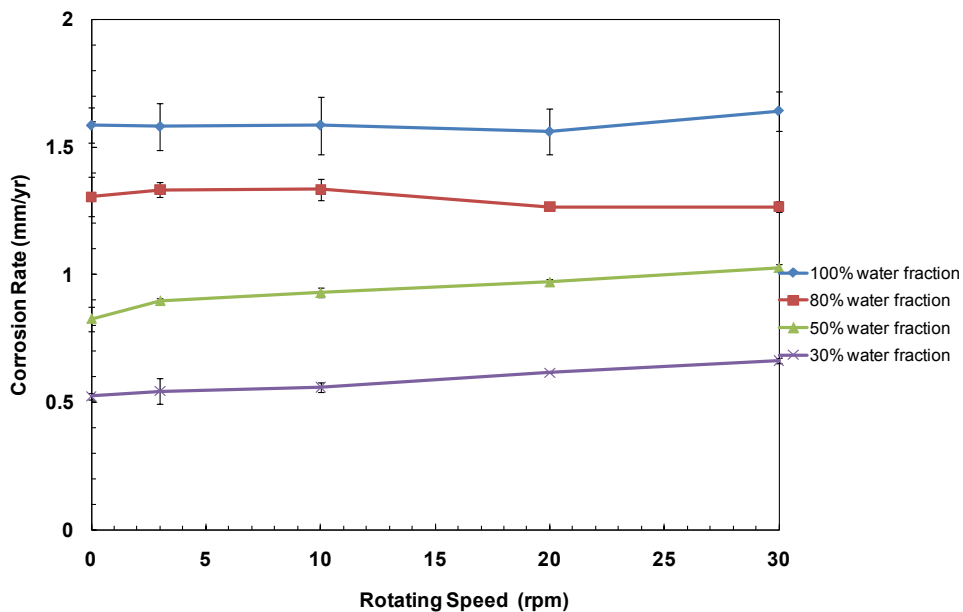


Figure 6-7. Corrosion rates with increasing velocity at different water fractions for 40  $\mu\text{m}$  roughness surface (corrosion rate calculated using whole surface area).

Figure 6-8 to Figure 6-10 show the ratio of  $A_E$  to  $A_N$  for 1.5 $\mu\text{m}$ , 6.0 $\mu\text{m}$  and 40 $\mu\text{m}$  roughness steel surfaces, respectively. As shown in Figure 6-8 and Figure 6-9, the value of  $A_E/A_N$  is greater than 1 at lower water cuts (30% and 50%). The results indicate that the steel surface is somewhat preferentially wetted by the water phase, which is not obvious at higher water cuts. That is because at higher water cuts, the difference in the surface area effectively wetted by water is very small compared to the nominal water-wetted surface area. For rougher surfaces, such as 40 $\mu\text{m}$  roughness steel surface shown in Figure 6-10, the value of  $A_E/A_N$  is greater than 1 even at a higher water cut (80%), which indicates that the rough steel surface shows obvious preferential water wetting behavior under dynamic conditions. However, static contact angle measurement results from the previous chapter indicate that a rougher surface is less hydrophilic than a

smoother surface. So it is important to keep in mind that the static contact angle results of rough surfaces should be interpreted and used very carefully, as they may not reflect the real wettability of the surface due to the hysteresis caused by high surface roughness.

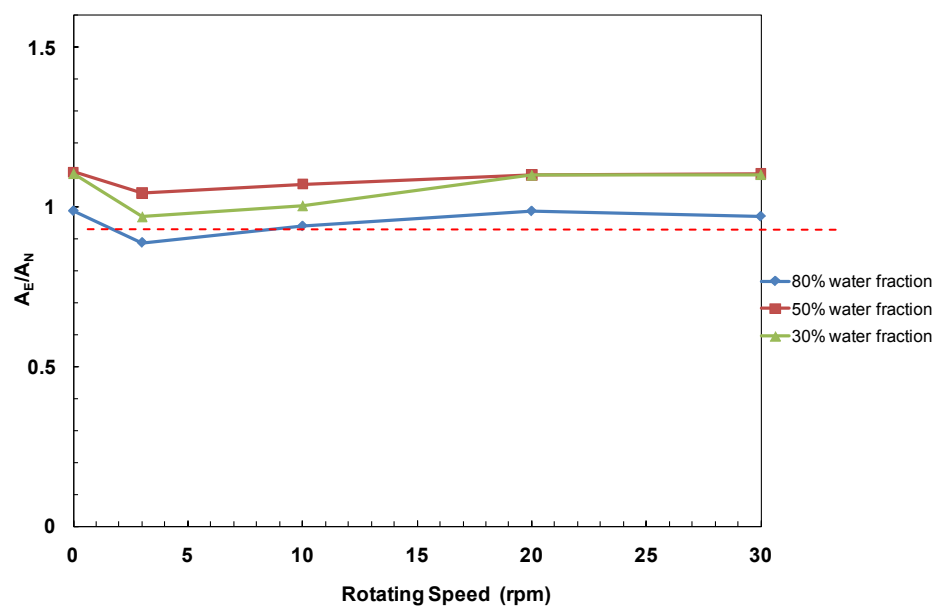


Figure 6-8. The value of  $A_E/A_N$  at different water fractions for 1.5  $\mu\text{m}$  roughness surface.

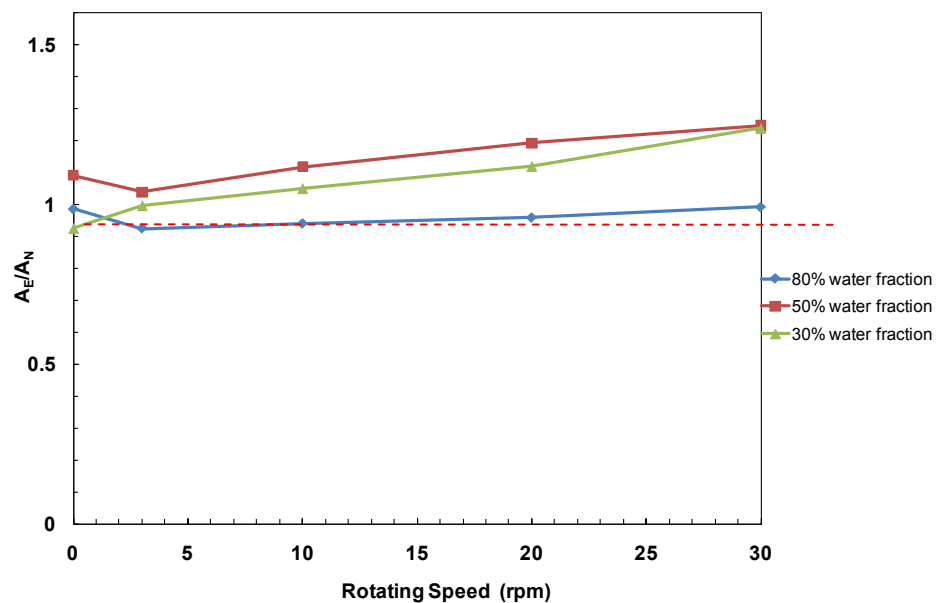


Figure 6-9. The value of  $A_E/A_N$  at different water fractions for 6.0 $\mu$ m roughness surface.

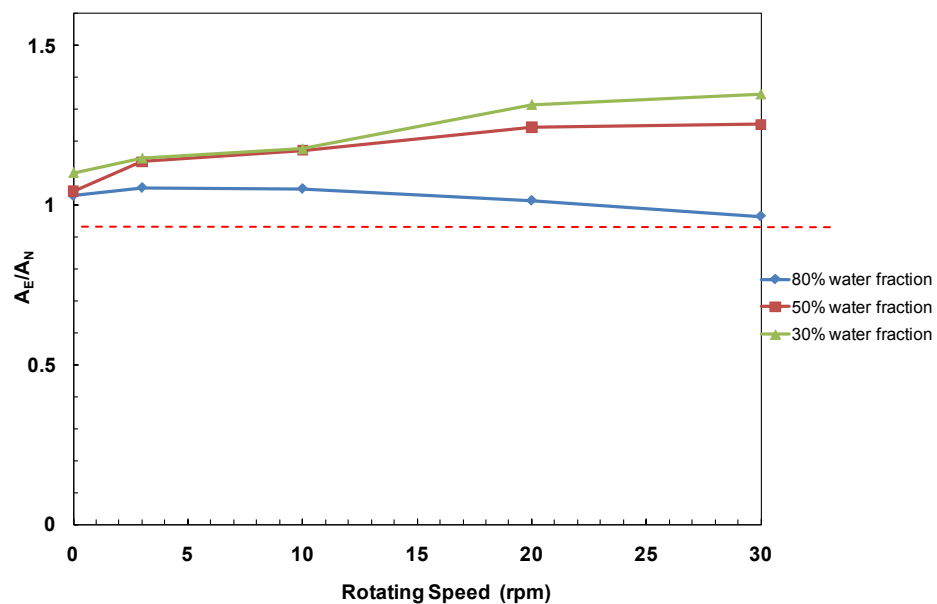


Figure 6-10. The value of  $A_E/A_N$  at different water fractions for 40 $\mu$ m roughness surface.

### 6.3 Summary

A horizontal rotating cylinder was used to investigate the effect of dynamic wetting on CO<sub>2</sub> corrosion of mild steel. According to the experimental results and discussion above, the following major points can be concluded.

- The dynamic wetting did not show any obvious effect on the CO<sub>2</sub> corrosion of carbon steel.
- For a water/LVT oil system, steel surfaces (especially rough surfaces) showed preferential water wetting behavior under dynamic conditions, which is in agreement with the static contact angle measurements results discussed in previous chapter.
- The static contact angle results for rough surface should be interpreted and used very carefully. They may not reflect the real wettability of the surface due to the hysteresis caused by high surface roughness.

## CHAPTER 7 : NEW IMPROVED WATER WETTING MODEL

In order to improve the prediction of the critical entrainment velocity when surface active substances such as corrosion inhibitors or other naturally occurring chemicals are present in the oil-water flow, a new water wetting model that considers the effect of surface wettability is proposed. The new model is based on the old water wetting model (Chapter 4, Section 4.3), with some important modifications.

### 7.1 Water wetting model including surface wettability effect

#### 7.1.1 Maximum drop diameter

In the old water wetting model, as described in Chapter 4, Section 4.3, the assumption is made that the turbulent kinetic energy flux in the continuous phase is used to disrupt the droplet coalescence of the dispersed phase and form separate droplets, i.e. the kinetic energy of the turbulent phase is converted to surface energy of the newly formed droplets. There is an inherent assumption that the water phase has already been lifted from the pipe surface and has been dispersed. However, this assumption neglects the interaction between the water layer and the pipeline surface. The old model considers the change in oil-water surface energy but overlooks the change in oil-steel and water-steel surface energy. Considering the oil-steel and water-steel surface energy changes, a new assumption can be made that the kinetic energy of the oil phase is used to create new surfaces of any kind. The new surfaces now include: new oil-water interfaces in the bulk phase and new oil-steel interfaces. For example, *Figure 7-1* shows a schematic of the transition from stratified flow to water-in-oil dispersed flow.

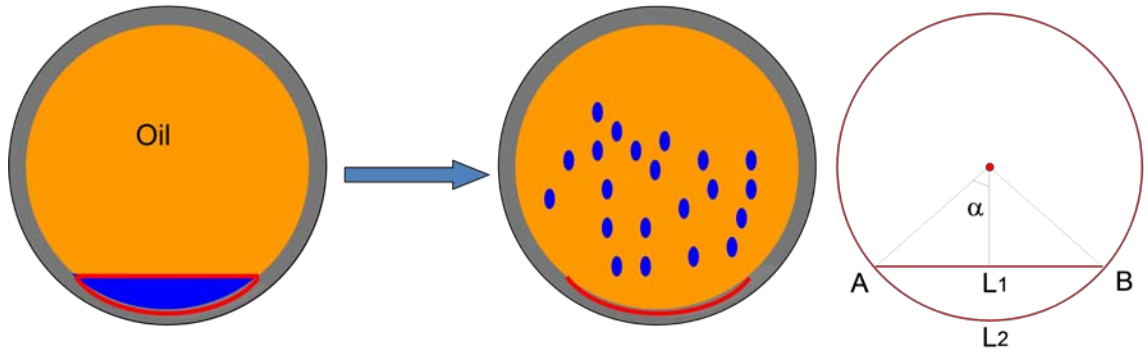


Figure 7-1. Schematic representation of transition from stratified flow to water-in-oil dispersion flow.

During this flow regime transition, the surface energy changes occur in four parts as follows:

1. Surface energy gained from the newly formed oil-water interface:

$$E_{S1} = \frac{Q_w}{\pi d_{\max}^3 / 6} \cdot \pi d_{\max}^2 \cdot \sigma = \frac{6\sigma}{d_{\max}} Q_w \quad (7.1)$$

2. Surface energy lost from the eliminated oil-water interface:

$$E_{S2} = -\frac{Q_w}{\varepsilon_w (\pi D^2 / 4)} \cdot L_1 \cdot \sigma = -\frac{L_1 Q_w}{\varepsilon_w (\pi D^2 / 4)} \sigma \quad (7.2)$$

3. Surface energy gained from the newly formed oil-steel interface:

$$E_{S3} = \frac{Q_w}{\varepsilon_w (\pi D^2 / 4)} \cdot L_2 \cdot \sigma_{os} = \frac{L_2 Q_w}{\varepsilon_w (\pi D^2 / 4)} \sigma_{os} \quad (7.3)$$

4. Surface energy lost from the eliminated water-steel interface:

$$E_{S4} = -\frac{Q_w}{\varepsilon_w (\pi D^2 / 4)} \cdot L_2 \cdot \sigma_{ws} = -\frac{L_2 Q_w}{\varepsilon_w (\pi D^2 / 4)} \sigma_{ws} \quad (7.4)$$

The total surface energy change is proportional to the kinetic energy supplied by the continuous oil phase, and this relationship can be expressed by Equation (7.5):

$$\frac{1}{2} \rho_o u'^2 Q_o \propto \frac{6\sigma}{d_{\max}} Q_w - \frac{L_1 Q_w}{\varepsilon_w (\pi D^2 / 4)} \sigma + \frac{L_2 Q_w}{\varepsilon_w (\pi D^2 / 4)} \sigma_{os} - \frac{L_2 Q_w}{\varepsilon_w (\pi D^2 / 4)} \sigma_{ws} \quad (7.5)$$

or

$$\frac{1}{2} \rho_o u'^2 Q_o = C_H Q_w \left( \frac{6\sigma}{d_{\max}} - \frac{4L_1}{\varepsilon_w \pi D^2} \sigma \right) + C_W Q_w \frac{4L_2}{\varepsilon_w \pi D^2} (\sigma_{os} - \sigma_{ws}) \quad (7.6)$$

From Equation (7.6), it can be seen that the kinetic energy is used to make water droplets and remove the water layer from the steel surface i.e. to create new oil-steel interfaces.

The constant  $C_H$  is set to 1, which is the same as what was used in the original model of Brauner (2001). The new constant  $C_W$  is related to the fraction of the kinetic energy of turbulence consumed for creating the new oil-steel interfaces. The value of  $C_W$  can be estimated using experimental data involving experiments with oils containing surface active substances, such as corrosion inhibitors and other naturally occurring chemicals. In Equation (7.6), the  $\sigma$ ,  $\sigma_{os}$  and  $\sigma_{ws}$  represent oil-water interfacial tension, oil-steel interfacial tension and water-steel interfacial tension, respectively. The parameters  $L_1$  and  $L_2$  are the length of chord AB and arc AB in *Figure 7-1*, respectively, which are directly related to water cut  $\varepsilon_w$  and pipe diameter  $D$  and can be expressed as follows:

$$L_1 = D \sin \alpha \quad (7.7)$$

$$L_2 = D\alpha \quad (7.8)$$

$$\varepsilon_w = \frac{2\alpha - \sin 2\alpha}{2\pi} \quad (7.9)$$

According to Young's equation (Equation (7.10)) (Young, 1805) and Equations (3.13) and (3.20), one can get the maximum drop diameter  $d_{\max}$  (Equation (7.11)). The  $\theta$  is the oil-in-water contact angle on the oil pre-wetted steel surface, whose measurement is discussed in Chapter 5, Section 5.3.

$$\sigma_{os} - \sigma_{ws} = \sigma \cos \theta \quad (7.10)$$

$$\left( \frac{d_{\max}}{D} \cdot 2U_o^3 f \frac{\rho_m}{\rho_o(1-\varepsilon_w)} \right)^{\frac{2}{3}} = \frac{C_H Q_w}{\rho_o Q_o} \left( \frac{6\sigma}{d_{\max}} - \frac{4L_1}{\varepsilon_w \pi D^2} \sigma \right) + \frac{C_W Q_w}{\rho_o Q_o} \frac{4L_2}{\varepsilon_w \pi D^2} \sigma \cos \theta \quad (7.11)$$

### 7.1.2 Critical drop diameter

In a stable water-in-oil dispersion, water is the dispersed phase and oil is the continuous phase. In order to make oil-water stratified flow transit to stable water-in-oil dispersion, the oil phase turbulence should be intense enough to break the water phase into droplets smaller than a critical drop diameter  $d_{crit}$ . Brauner (2001) extended Brodkey's (1967) work by adding the effect of the pipeline inclination to calculate the critical drop diameter  $d_{cs}$ . Brodkey's work was originally based on work done by Bond & Newton (1928), who proposed a rough criterion (Equation (7.12)) using dimensional analysis to determine the critical radius of a bubble or droplet for the deviation from spherical shape, where  $R_{crit}$  is the critical radius of the bubble or droplet. By comparing the proposed criterion value with the experimental value from Bond & Newton (1928)

shown in *Table 7-1*, it can be seen that the proposed criterion for the experimental data in water-castor oil system works quite well. Therefore the critical drop diameter  $d_{c\sigma}$  can be calculated using Bond's criterion with consideration of the effect of pipeline inclination  $\beta$  (Equation (7.13)). As for the calculation of the critical drop diameter  $d_{cg}$ , the equation (Equation (3.31)) proposed by Brauner (2001) can be used; therefore the water wetting model with surface wettability effect (the so-called "new, improved model") can be expressed by Equation (7.14).

With the newly proposed water wetting model and available experimental data, the value of  $C_W$  that makes the model results fit most of the experimental results is estimated to be  $C_W=30$ .

$$R_{crit} = \sqrt{\frac{\sigma}{|\rho' - \rho| g}} \quad (7.12)$$

$$d_{c\sigma} = \sqrt{\frac{4\sigma}{|\rho_w - \rho_o| g \cos \beta}} \quad (7.13)$$

$$\left\{ \begin{array}{l} \left( \frac{d_{max}}{D} \cdot 2U_o^3 f \frac{\rho_m}{\rho_o(1-\varepsilon_w)} \right)^{\frac{2}{3}} = \frac{C_H Q_w}{\rho_o Q_o} \left( \frac{6\sigma}{d_{max}} - \frac{4L_1}{\varepsilon_w \pi D^2} \sigma \right) + \frac{C_W Q_w}{\rho_o Q_o} \frac{4L_2}{\varepsilon_w \pi D^2} \sigma \cos \theta \quad (a) \\ d_{crit} = \text{Min} \left( d_{cg} = \frac{3}{8} \frac{\rho_o U_o^2 f}{|\rho_w - \rho_o| g \cos \beta}, d_{c\sigma} = \sqrt{\frac{4\sigma}{|\rho_w - \rho_o| g \cos \beta}} \right) \quad (b) \\ d_{max} < d_{crit} \quad (c) \end{array} \right. \quad (7.14)$$

*Table 7-1.* Comparison of proposed criterion value with experimental value by Bond & Newton (1928).

Experiment Case	$R_{crit}$	Observed Radius (cm)
Air in water	0.25	0.10
Air in golden syrup	0.25	0.11
Mercury in golden syrup	0.15	0.12
Water in castor oil	0.70	0.77

## 7.2 Model verification

### 7.2.1 Baseline test results

For the baseline test, LVT200 model oil, without any corrosion inhibitors or chemicals, was used as the oil phase in 4" horizontal pipe flow. The oil-in-water contact angle for LVT200 oil underneath the steel surface pre-wetted by LVT200 oil in 1wt% NaCl (shown in *Figure 5-34*) is 73°. The transition lines to oil wetting predicted by the new model and the old model are compared with the empirical transition line in *Figure 7-2*. It can be seen that both models perform very well for the baseline test results.

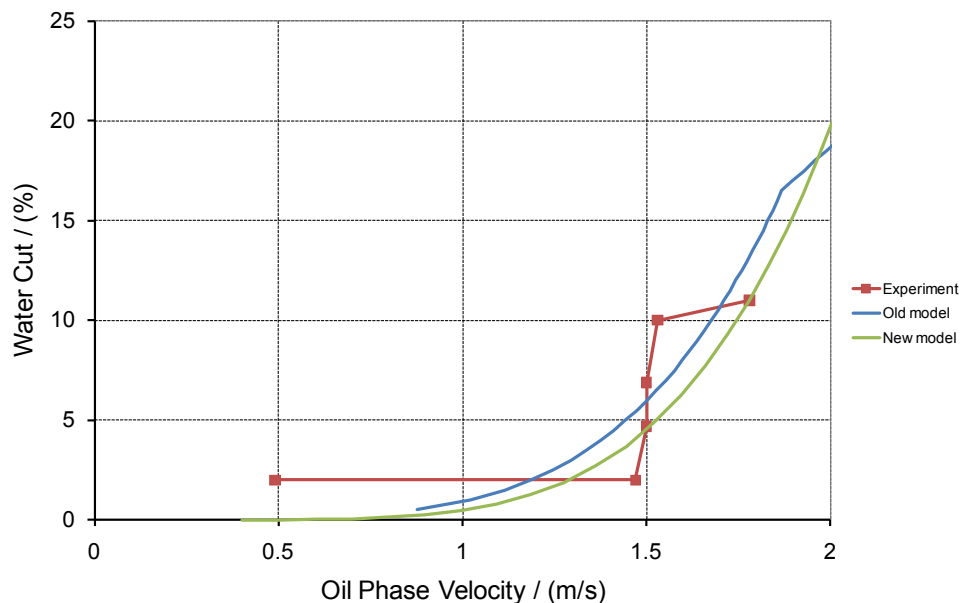


Figure 7-2. Comparison of model prediction results with experimental results (LVT200 oil in 4" horizontal pipe flow,  $\theta=73^\circ$ ,  $C_H=1$ ,  $C_W=30$ ).

### 7.2.2 Results with crude oils

The old model over-predicts the critical oil phase velocity for full water entrainment for different crude oils (see Chapter 4, Section 4.3.2). By considering the effect of surface wettability, the new model significantly improves the accuracy of the prediction of the critical oil phase velocity for full water entrainment, using the value of 30 for  $C_W$ . Figure 7-3 to Figure 7-7 show the comparison of model prediction results with experimental results in a 4" horizontal flow loop for C1, C2, C3, C4 and C5 crude oil, respectively. It can be seen that the new model results agree well with the empirical results.

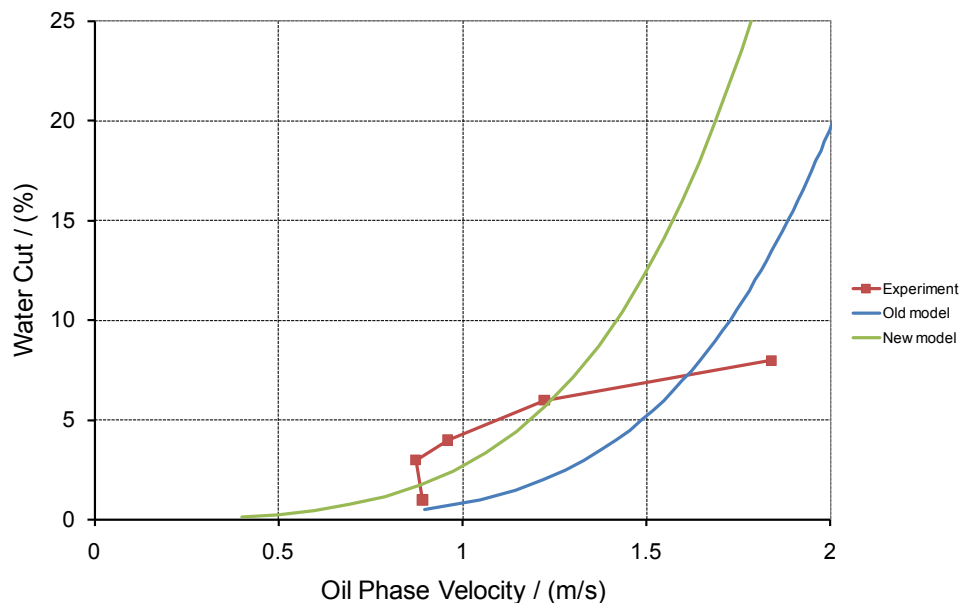


Figure 7-3. Comparison of model prediction results with experimental results in 4'' horizontal flow loop (C1 crude oil,  $\theta=142^\circ$ ,  $C_H=1$ ,  $C_W=30$ ).

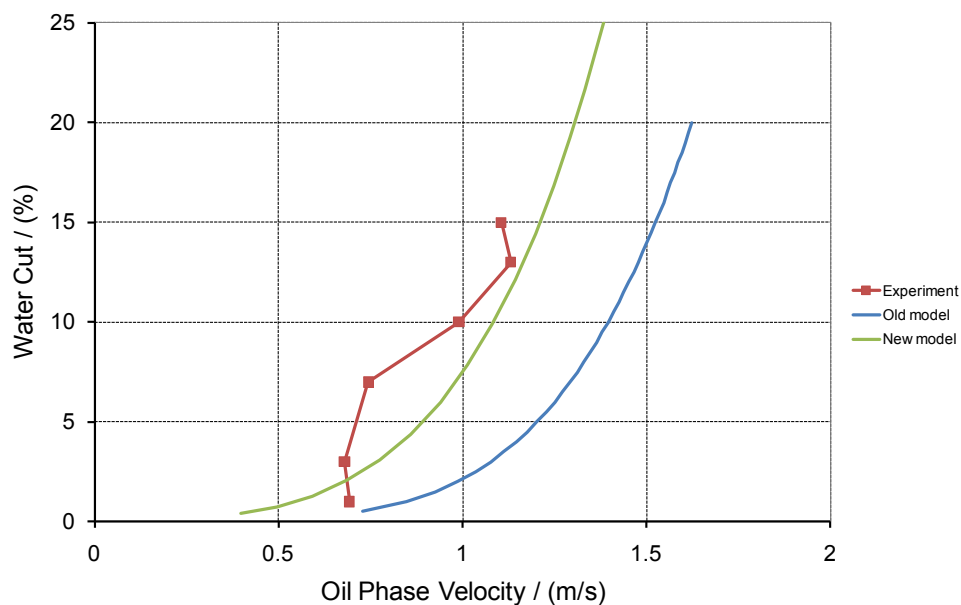


Figure 7-4. Comparison of model prediction results with experimental results in 4'' horizontal flow loop (C2 crude oil,  $\theta=157^\circ$ ,  $C_H=1$ ,  $C_W=30$ ).

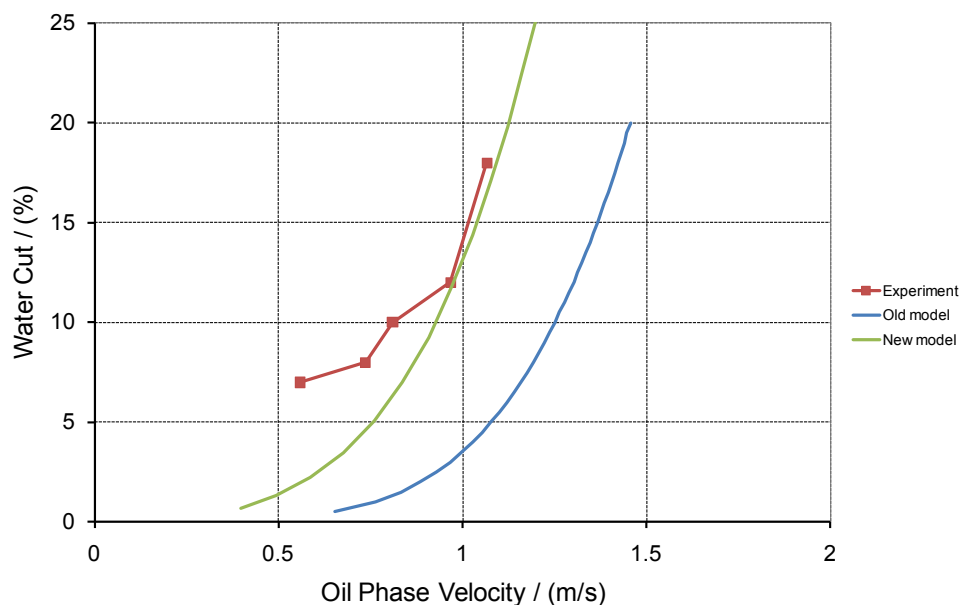


Figure 7-5. Comparison of model prediction results with experimental results in 4'' horizontal flow loop (C3 crude oil,  $\theta=180^\circ$ ,  $C_H=1$ ,  $C_W=30$ ).

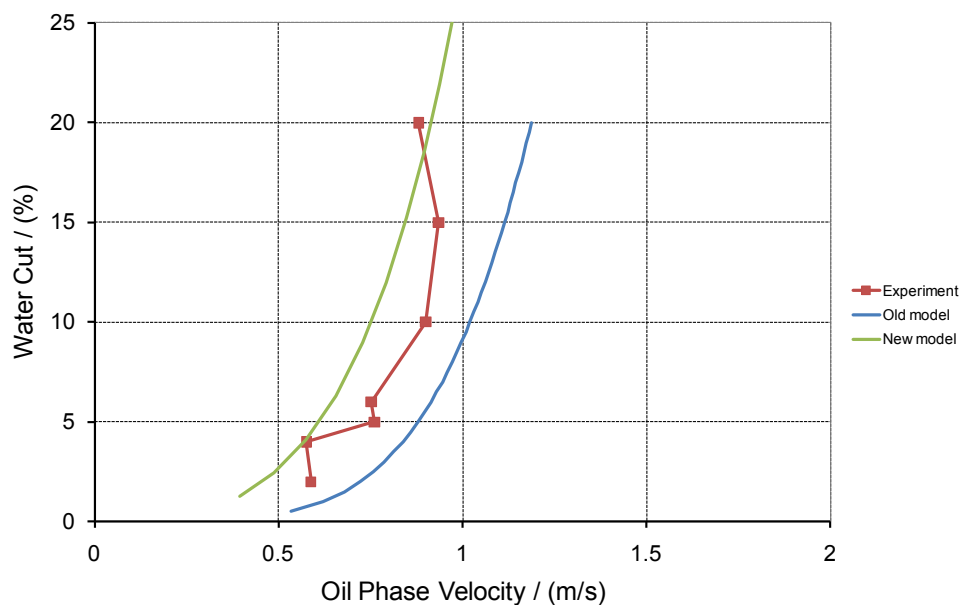


Figure 7-6. Comparison of model prediction results with experimental results in 4'' horizontal flow loop (C4 crude oil,  $\theta=180^\circ$ ,  $C_H=1$ ,  $C_W=30$ ).

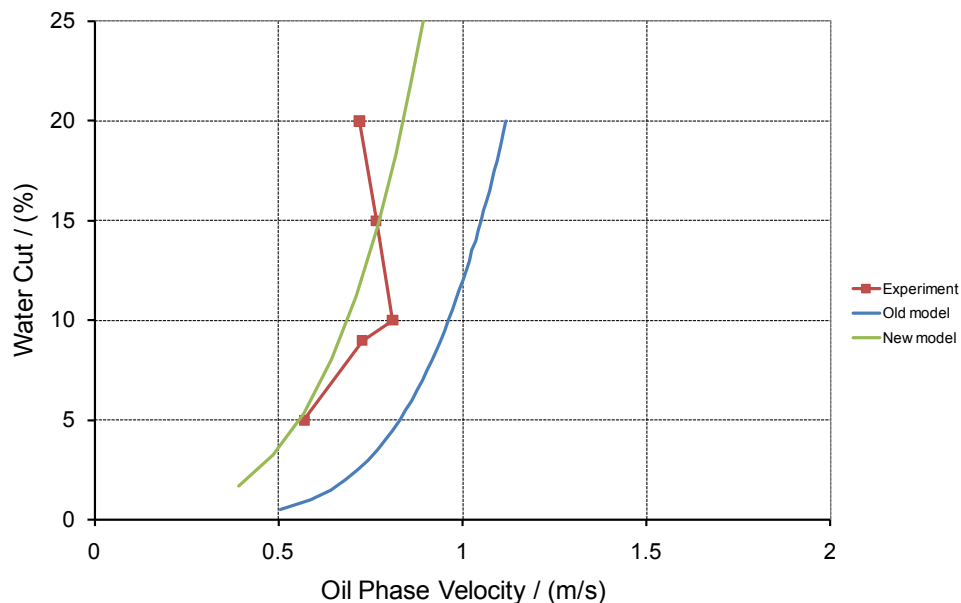
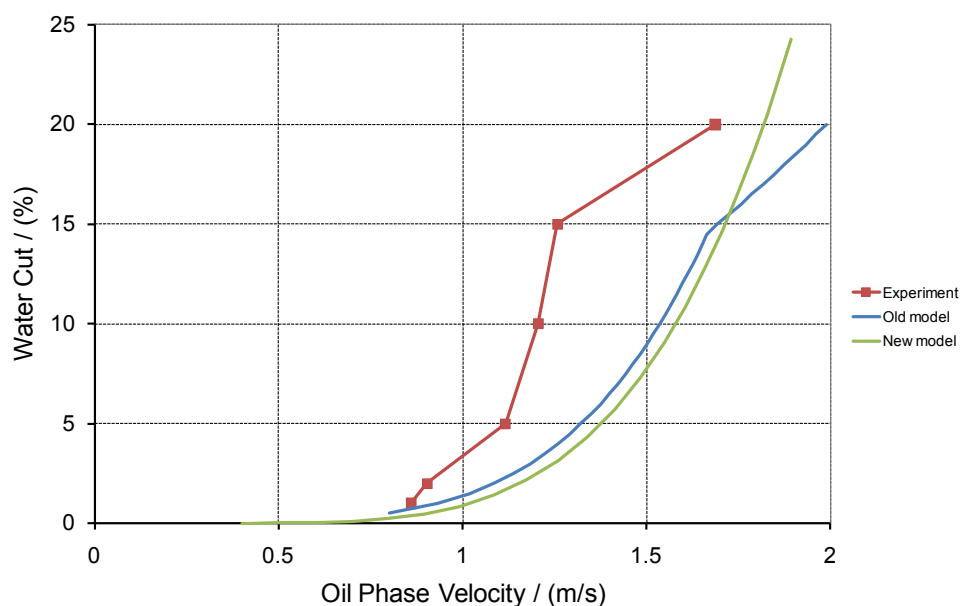


Figure 7-7. Comparison of model prediction results with experimental results in 4” horizontal flow loop (C5 crude oil,  $\theta=180^\circ$ ,  $C_H=1$ ,  $C_W=30$ ).

### 7.2.3 Results with corrosion inhibitor

The experimental data for “quat” inhibitor (Chapter 5., Section 5.3.2) at different inhibitor concentrations (1ppm, 5ppm, 20ppm) obtained by Li (2009) in a doughnut cell were used to originally obtain  $C_W$  from Equation (7.14). The experimental data obtained by Li (2009) in the small scale apparatus were scaled up to a 4” horizontal flow loop using the scale-up method described by the author. To simulate those results, the oil-in-water contact angles for LVT200 oil underneath the steel surface pre-wetted with LVT200 oil in 1wt% NaCl with 1ppm, 5ppm and 20ppm “quat” inhibitor shown in Figure 5-34 are  $74^\circ$ ,  $103^\circ$  and  $151^\circ$ , respectively were used. Figure 7-8 shows the comparison of model prediction results with experimental results for 1ppm “quat” inhibitor in a doughnut cell scaled up to a 4” horizontal flow loop. The new model and

old model perform similarly for this case using value of 30 for  $C_w$ . However, for experimental cases of 5ppm and 20ppm inhibitor concentration, it was found that the value of 30 for  $C_w$  made the new model results fit the experimental results much better. *Figure 7-9* and *Figure 7-10* show the comparison of model predictions with experimental results for these two experimental cases. It can be seen that the old model over-predicts the critical entrainment velocity for full water entrainment. The new model prediction results agree well with the empirical results, which is further verified by looking at the test results for 5ppm “quat” performed in the large scale 4” flow loop by using the same value 30 of  $C_w$  as shown in *Figure 7-11*.



*Figure 7-8.* Comparison of model prediction results with experimental results in doughnut cell scaled up to 4” horizontal flow loop (LVT200 oil with 1ppm “quat”,  $\theta = 75^\circ$ ,  $C_H = 1$ ,  $C_w = 30$ ) (Li, 2009).

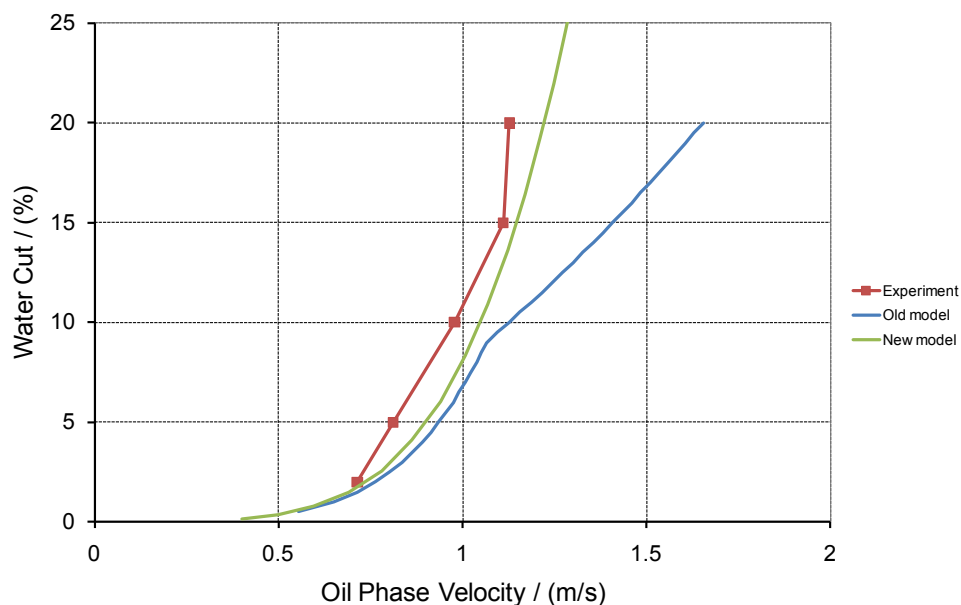


Figure 7-9. Comparison of model prediction results with experimental results in doughnut cell scaled up to 4" horizontal flow loop (LVT200 oil with 5ppm "quat",  $\theta = 103^\circ$ ,  $C_H = 1$ ,  $C_W = 30$ ) (Li, 2009).

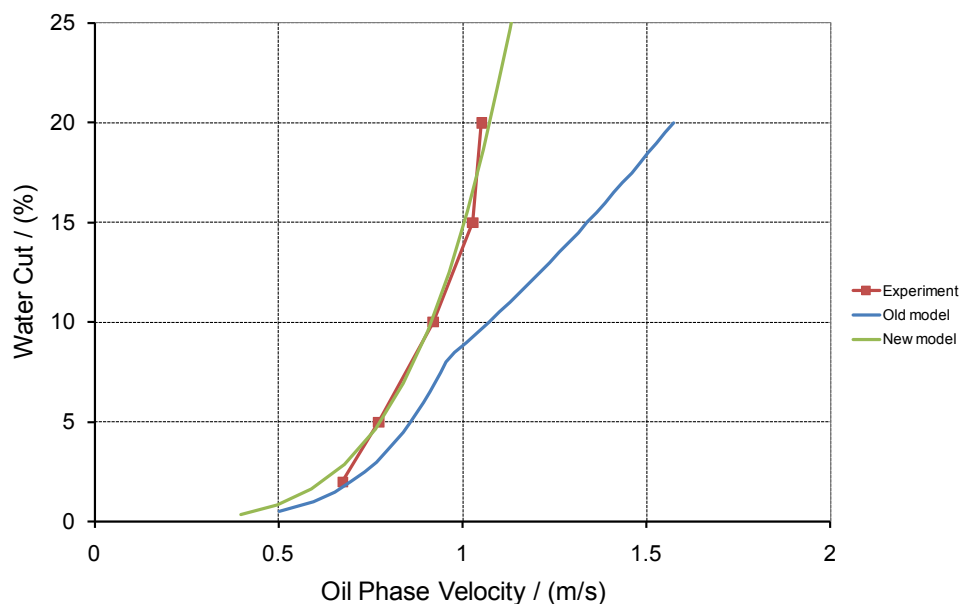


Figure 7-10. Comparison of model prediction results with experimental results in doughnut cell scaled up to 4" horizontal flow loop (LVT200 oil with 20ppm "quat",  $\theta = 143^\circ$ ,  $C_H = 1$ ,  $C_W = 30$ ) (Li, 2009).

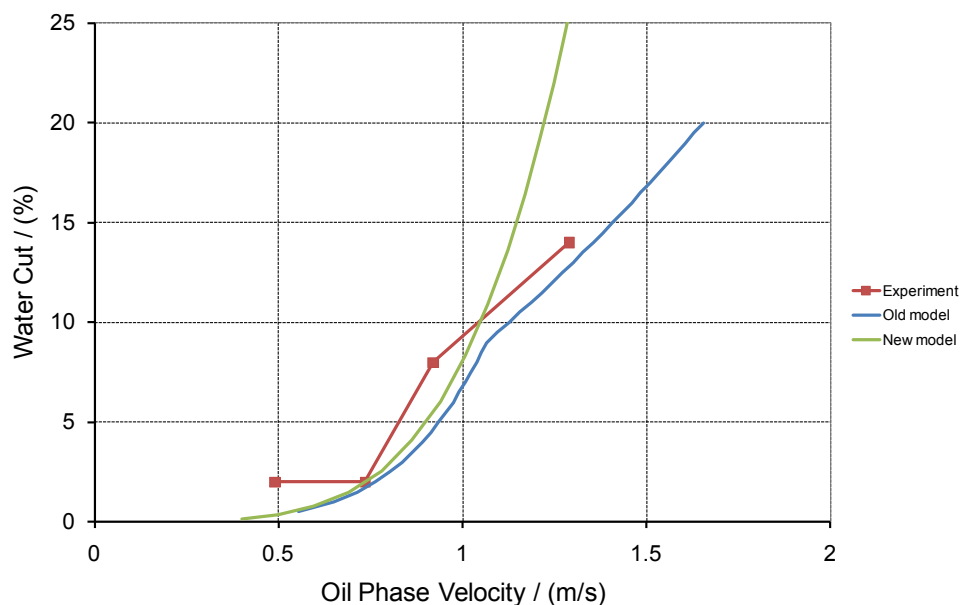
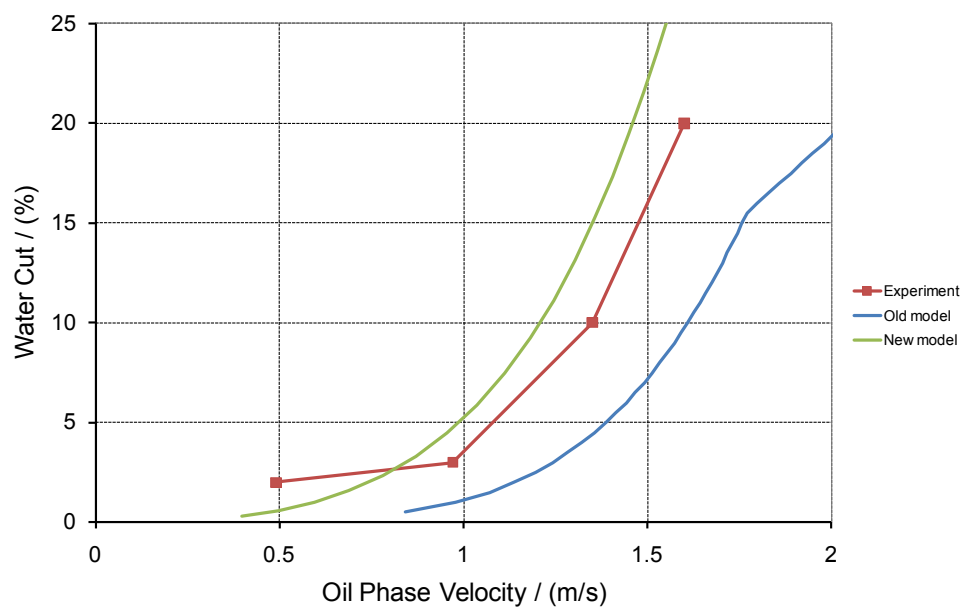


Figure 7-11. Comparison of model prediction results with experimental results in 4” horizontal flow loop (LVT200 oil with 5ppm “quat”,  $\theta=143^\circ$ ,  $C_H=1$ ,  $C_W=30$ ) (Li, 2009).

#### 7.2.4 Results with surface active chemical additive

Figure 7-12 and Figure 7-13 show the comparison of model prediction results with experimental results of LVT200 model oil containing 0.01% and 0.05% myristic acid, respectively, in a 4” horizontal flow loop (Ayello, 2010). The myristic acid is a surface active chemical similar to the ones found in crude oils. It can be seen that the old model drastically over-predicts the critical entrainment velocity for oil wetting, while the new model performs better by using the value 30 for  $C_W$ , especially for the lower concentration of myristic acid. For the unrealistically high concentration of myristic acid, 0.05%, the new model also over-predicts the critical oil phase velocity for full water entrainment. At this concentration there were inconsistencies between the wall

conductance probe results and observed flow pattern in the flow loop, and this result is considered less reliable, so the new model's performance cannot be discounted based on this result alone.



*Figure 7-12.* Comparison of model prediction results with experimental results in 4" horizontal flow loop (LVT200 oil with 0.01% myristic acid,  $\theta=180^\circ$ ,  $C_H=1$ ,  $C_W=30$ ) (Ayello, 2010).

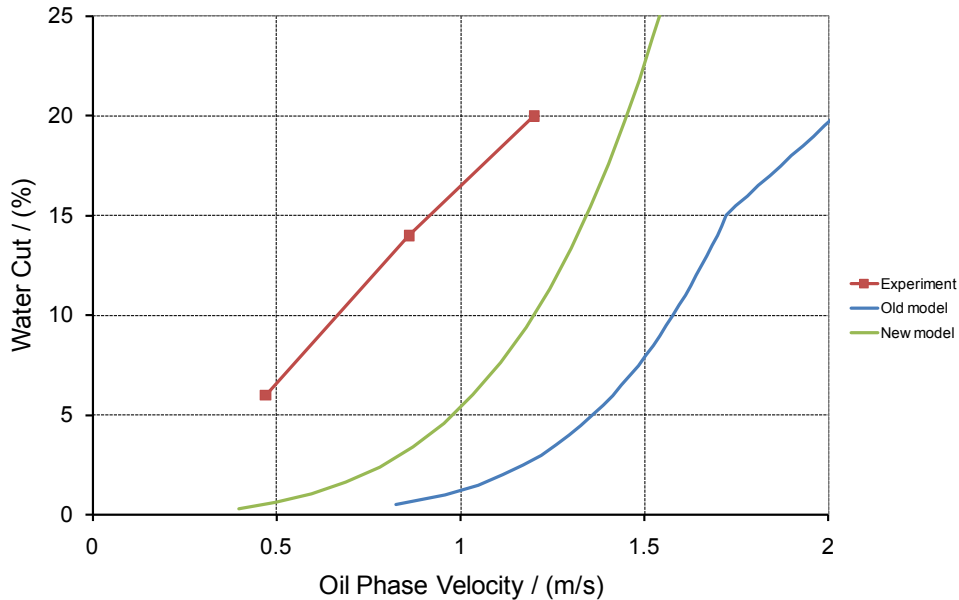


Figure 7-13. Comparison of model prediction results with experimental results in 4" horizontal flow loop (LVT200 oil with 0.05% myristic acid,  $\theta=180^\circ$ ,  $C_H=1$ ,  $C_W=30$ ) (Ayello, 2010).

### 7.3 Summary

A new phase wetting prediction model that considers the effect of surface wettability is proposed, based on the old water wetting model. The new model considers the effect of surface wettability in order to calculate the maximum water droplet size in oil-water flow. In the new model, it is assumed that the kinetic energy of the oil phase is used to create new interfaces, which include oil-water interfaces and oil-steel interfaces. A new constant  $C_W$  is introduced in the new model. It was found that the single value of 30 for  $C_W$  best fits most experimental results. The new model can significantly improve the prediction of the critical oil phase velocity for full water entrainment, which is

verified by the experimental results with different crude oils and model oil containing surface active chemicals.

## CHAPTER 8 : CONCLUSIONS AND RECOMMENDATIONS FOR FUTURE WORK

### 8.1 Conclusions

A comprehensive study was carried out to elucidate surface state effects on water wetting and carbon dioxide corrosion in oil-water two-phase flow. Flow patterns, phase wetting regimes and CO<sub>2</sub> corrosion in large diameter, horizontal and inclined oil-water two-phase flow were experimentally investigated. The effects of surface state were varied: bare steel surfaces with different measures of surface roughness, steel surface with corrosion film, oil or water pre-wetted steel surfaces and the effect on surface wettability was experimentally studied using a novel apparatus, a goniometer contact angle measurement system. In order to validate and complement the results obtained using the goniometer system, the effects of dynamic wetting on wettability and CO<sub>2</sub> corrosion were also studied using a horizontal rotating cylinder (HRC) system. Based on the existing water wetting model (Cai, Netic, & de Waard, 2004) and the experimental results obtained by the present author in collaboration with Li (2009) and Ayello (2010), a new mechanistic model is proposed accounting for the effects of surface wettability for phase wetting prediction in oil-water two-phase flow.

The main findings and achievements of this study are as follows.

1. Three types of phase wetting regimes (stable water wetting, intermittent wetting and stable oil wetting) were identified.
2. Comprehensive phase wetting maps were constructed based on the results obtained using wall conductance probes.

3. Oil type was determined to have a significant effect on the transition from stable oil wetting to intermittent wetting. Much of this influence can be ascribed to the physical properties of the oil: density, viscosity and oil-water interfacial tension.
4. Pipe inclination was found to have a significant effect on the phase wetting transition with an inclination over 45°.
5. It was discovered that the surface roughness or surface state (whether iron carbonate covered the steel surface or not) did not affect a surface's wettability, although for very rough surfaces it was found that a higher water-in-oil contact angle was obtained, which may related to the hysteresis in the measurements caused by the high surface roughness.
6. It was shown that for both water-in-oil and oil-in-water contact angle measurements, increasing the temperature tended to make the steel surface less hydrophilic.
7. The results of contact angle measurements were found to depend heavily on the experimental procedure. It was seen that pre-wetting steel surface with either water or oil can have a great effect on the wettability. Crude oil pre-wetting of the steel surface and the addition of "quat" inhibitor (5 ppm) can both lead the transition of the wettability of steel surface from hydrophilic to hydrophobic.
8. The experimental results for dynamic wetting tests in HRC indicated that for a water/LVT oil system, the steel surface shows preferential water wetting behavior under dynamic conditions, which is in agreement with the static contact angle measurements results obtained in goniometer system.

9. The prediction of the old phase wetting prediction model was found to have very good agreement with experimental results for LVT200 model oil in the large scale 4" diameter flow loop. As for the predictions for crude oil, or LVT200 oil with added corrosion inhibitor and other surface active chemicals, the old model was found to grossly over-predict the critical oil phase velocity for full water entrainment.
10. Building on the old water wetting model, a new mechanistic phase wetting prediction model was proposed, accounting for the effect of surface wettability.
11. The new model was shown to significantly improve the prediction of the critical oil phase velocity for full water entrainment, as verified by the experimental results for different crude oils and models oil with added surface active chemicals.

## **8.2 Recommendations for future work**

Although the present research has fulfilled most of the original objectives, there is still some work to be done in the future. Topics yet to be examined should include:

1. Investigation of surface wettability of steel surface with deposits such as mill scale, iron sulfide, etc.
2. Effect of corrosion inhibitor on surface wettability of steel surface with deposits such as iron carbonate, mill scale, and iron sulfide, etc.
3. Effect of corrosion inhibitor on the dynamic wetting of steel surface in oil-water system in a horizontal rotating cylinder.
4. Validation of the new phase wetting prediction model proposed in this dissertation with more experimental data and field data.

5. Oil-water-gas three-phase flow in the fully inclinable large flow loop.

**REFERENCES**

- Adams, C.D., Garber, J.D., Walters, F.H., & Singh, C. (1993). *Verification of computer modeled tubing life predictions by field data*. Paper presented at the NACE Corrosion/93, paper no. 93082.
- Adamson, A.W., & Gast, A.P. (1997). *Physical Chemistry of Surfaces* (6th ed.). New York: John Wiley & Sons, Inc.
- Al-Wahaibi, T., & Angeli, P. (2009). Predictive model of the entrained fraction in horizontal oil-water flows. [Article]. *Chemical Engineering Science*, 64(12), 2817-2825.
- Al-Wahaibi, T., & Angeli, P. (2007). Transition between stratified and non-stratified horizontal oil-water flows. Part I: Stability analysis. *Chemical Engineering Science*, 62(11), 2915-2928.
- Al-Wahaibi, T., Smith, M., & Angeli, P. (2007). Transition between stratified and non-stratified horizontal oil-water flows. Part II: Mechanism of drop formation. *Chemical Engineering Science*, 62(11), 2929-2940.
- Angeli, P., & Hewitt, G.F. (1998). Pressure gradient in horizontal liquid-liquid flows. *International Journal of Multiphase Flow*, 24(7), 1183-1203.
- Angeli, P., & Hewitt, G.F. (2000a). Flow structure in horizontal oil-water flow. *International Journal of Multiphase Flow*, 26(7), 1117-1140.
- Arirachakaran, S., Oglesby, K.D., Malinowsky, M.S., Shoham, O., & Brill, J.P. (1989). *An analysis of oil/water flow phenomena in horizontal pipes*. Paper presented at the SPE Professional Production Operating Symposium. Paper No.18836.

- Ayello, F. (2010). *Crude Oil Chemistry Effects on Corrosion Inhibition and Phase Wetting in Oil-Water Two-Phase Flow*. Doctoral Dissertation, Ohio University.
- Barnea, D. (1986). Transition from annular flow and from dispersed bubble flow--unified models for the whole range of pipe inclinations. *International Journal of Multiphase Flow*, 12(5), 733-744.
- Barnea, D.. (1987). A unified model for predicting flow-pattern transitions for the whole range of pipe inclinations. *International Journal of Multiphase Flow*, 13, 1-12.
- Barnea, D., Shoham, O., & Taitel, Y. (1982). Flow pattern transition for vertical downward two phase flow. *Chemical Engineering Science*, 37(5), 741-744.
- Batchelor, G.K. (1951). Pressure fluctuations in isotropic turbulence. *Proceedings of the Cambridge Philosophical Society*, 47, 359-374.
- BBC (2006). "Alaska hit by 'massive' oil spill" from <http://news.bbc.co.uk/2/hi/americas/4795866.stm>
- Berg, J.C. (Ed.). (1993). *Wettability*. New York: Marcel Dekker, Inc.
- Blake, T.D. (1988). *Wetting Kinetics-How Do Wetting Lines Move?* Paper presented at the AIChE International Symposium on the Mechanics of Thin Film Coating. New York, NY.
- Blake, T.D., & Ruschak, K.J. (1997). Liquid Film Coating. In S. Kistler, Schwiezer, P. (Ed.). London, U.K.: Chapman & Hall.
- Bockris, J.O.M., Drazic, D., & Despic, A.R. (1961). The electrode kinetics of the deposition and dissolution of iron. *Electrochimica Acta*, 4, 325.

- Bond, W.N., & Newton, D.A. . (1928). Bubbles, drops, and Stokes' law. *Philosophy Magazine*, 5, 794-800.
- Brauner, N. (2001). The prediction of dispersed flows boundaries in liquid-liquid and gas-liquid systems. *International Journal of Multiphase Flow*, 27, 885-910.
- Brauner, N., & Moalem Maron, D. (1992b). Stability analysis of stratified liquid-liquid flow. *International Journal of Multiphase Flow*, 18(1), 103-121.
- Brauner, N., & Moalem Maron, D. (1992a). Flow pattern transitions in two-phase liquid-liquid flow in horizontal tubes. *International Journal of Multiphase Flow*, 18, 123-140.
- Brennen, C.E. (2005). *Fundamentals of Multiphase Flow*. New York, N.Y.: Cambridge University Press.
- Brodkey, R.S. (1967). *The phenomena of fluid motions*. Reading, MA: Addison-Wesley.
- Brondel, D., Edwards, R., Hayman, A., Hill, D., Mehta, S., & Semerad, T. (1994). Corrosion in the oil industry. *Oilfield Review*, 6(2), 4-18.
- Cai, J., Nestic, S., & de Waard, C. (2004). *Modeling of water wetting in oil-water pipe flow*. Paper presented at the NACE Corrosion/04, paper no. 04663.
- Cai, J., Nestic, S., Li, C., Tang, X., Ayello, F., Cruz, C.I.T., *et al.* (2005). *Experimental studies of water wetting in large diameter horizontal oil-water pipe flows*. Paper presented at the SPE Annual Technical Conference and Exhibition, paper no. 95512-MS.

- Charles, M.E., Govier, G.W., & Hodgson, G.W. (1961). The horizontal pipeline flow of equal density oil-water mixtures. *Canadian Journal of Chemical Engineering*, 39, 27-36.
- Charles, M.E., & Lilleleht, L.U. (1966). Correlation of pressure gradient for the stratified laminar-turbulent pipeline flow of two immiscible liquids. *Canadian Journal of Chemical Engineering, liquids.*, 44(1), 47-79.
- Chen, X.T., Cai, X.D., & Brill, J.P. (1997). A general model for transition to dispersed bubble flow. *Chemical Engineering Science*, 52(23), 4373-4380.
- Churchill, S.W. (1973). Empirical expressions for the shear stress in turbulent flow in commercial pipe. *AIChE Journal*, 19(2), 375-376.
- Clay, P.H. (1940). The mechanism of emulsion formation in turbulent flow. *Proceedings of the Section of Sciences*, 43, 852-965.
- Colebrook, C.F. (1939). Turbulent flow in pipes, with particular reference to the transition region between the smooth and rough pipe laws. *Journal of Institution of Civil Engineers*, 11, 133-156.
- Cox, A.L. (1985). *A study of horizontal and downhill two-phase oil-water flow*. Unpublished Master Thesis, University of Texas at Austin, Austin, TX.
- de Gennes, P.-G., Brochard-Wyart, F., & Quéré, D. (2003). *Capillarity and Wetting Phenomena: Drops, Bubbles, Pearls, Waves*. New York: Springer.
- de Waard, C., & Lotz, U. (1993). *Prediction of CO<sub>2</sub> corrosion of carbon steel*. Paper presented at the NACE Corrosion/93, paper no. 93069.

- de Waard, C., & Milliams, D.E. (1975a). *Prediction of carbonic acid corrosion in natural gas pipelines*. Paper presented at the First International Conference on the Internal and External Protection of Pipes, paper no. F1.
- de Waard, C., Smith, L., & Craig, B.D. (2001). *The influence of crude oil on well tubing corrosion rates*. Paper presented at the EUROCORR 2001, The European Corrosion Congress.
- de Waard, C., & Milliams, D.E. (1975b). Carbon acid corrosion of steel. *Corrosion*, 31, 177-181.
- Drelich, J., Fang, C., & White, C.L. (2002). Measurement of Interfacial Tension in Fluid-Fluid System. *Encyclopedia of Surface and Colloid Science*, 3152-3166.
- Eisenberg, M., Tobias, C.W., & Wilke, C.R. (1954). Ionic mass transfer and concentration polarization at rotating electrodes. *Journal of The Electrochemical Society*, 101, 306-319.
- Fairuzov, Y.V., Arenas-Medina, P., Verdejo-Fierro, J., & Gonzalez-Islas, R. (2000). Flow pattern transportation in horizontal pipelines carrying oil-water mixtures: full-scale experiments. *Journal of Energy Resources Technology*, 122, 169-176.
- Fairuzov, Y.V. (2000). Numerical simulation of transient flow of two immiscible liquids in pipeline. *AIChE Journal*, 46(7), 1332-1339.
- Farshad, F., Rieke, H., & Garber, J. (2001). New developments in surface roughness measurements, characterization, and modeling fluid flow in pipe. [Article]. *Journal of Petroleum Science and Engineering*, 29(2), 139-150.

- Gadelmawla, E.S., Koura, M.M., Maksoud, T.M.A., Elewa, I.M., & Soliman, H.H. (2002). Roughness parameters. [Article]. *Journal of Materials Processing Technology*, 123(1), 133-145.
- Gray, L.G.S., Anderson, B.G., Danysh, M.J., & Tremaine, P.G. (1989). *Mechanism of Carbon Steel Corrosion in Brines Containing Dissolved Carbon Dioxide at pH 4*. Paper presented at the NACE Corrosion/89. Paper No.464.
- Haaland, S.E. (1983). Simple and explicit formulas for the friction factor in turbulent pipe flow. *Journal of Fluids Engineering*, 105(1), 89-90.
- Hager, W.H. (2003). Blasius: A life in research and education. *Experiments in Fluids*, 34(5), 566-571.
- Hinze, J.O. (1955). Fundamentals of the hydrodynamic mechanism of splitting in dispersion processes. *AIChE Journal*, 1(3), 289-295.
- Hurlen, T., Gunvaldsen, S., Tunold, R., Blaker, F., & Lunde, P.G. (1984). Effects of carbon dioxide on reactions at iron electrodes in aqueous salt solutions. *Journal of Electroanalytical Chemistry*, 180, 511-526.
- Jones, D.A. (1996). *Principles and Prevention of Corrosion* (2nd ed.). Upper Saddle River, NJ: Prentice Hall.
- Kermani, M.B., & Morshed, A. (2003). Carbon dioxide corrosion in oil and gas production - A compendium. [Review]. *Corrosion*, 59(8), 659-683.
- Koch, G.H., Brongers, M., Thompson, N.G., Virmani, Y.P., & Payer, J.H. (2002). *Corrosion costs and preventive strategies in the United States*.

- Kurban, A.P.A., Angeli, P.A., Mendes-Tatsis, M.A., & Hewitt, G.F. (1995). *Stratified and dispersed oil-water flows in horizontal pipes*. Paper presented at the 7th International Conference on Multiphase Production, 277-291.
- Levich, V.G. (1962). *Physicochemical Hydrodynamics*. Englewood Cliffs, N.J.: Prentice-Hall.
- Li, C. (2009). *Effect of Corrosion Inhibitor on Water Wetting and Carbon Dioxide Corrosion In Oil-Water Two-Phase Flow*. Doctoral Dissertation, Ohio University.
- Mattsson, L. (1997). Surface roughness and microtopography. In D. Brune, Hellborg, R., Whitlow, H. J., Hunderi, O. (Ed.), *Surface Characterization: a user's sourcebook* (pp. 82-100): Scandinavian Science Publisher.
- Miller, C.A., & Neogi, P. (1985). *Interfacial Phenomena: Equilibrium and Dynamic Effects*. New York: Marcel Dekker.
- Moody, L.F. (1947). An approximate formula for pipe friction factors. *Transactions of the ASME*, 69(12), 1005-1006.
- Moody, L.F. (1944). Friction Factors for Pipe Flow. *Transactions of the ASME*, 66(8), 671-684.
- Nesic, S. (2007). Key issues related to modeling of internal corrosion of oil and gas pipelines-A review. *Corrosion Science*, 49, 4308-4338.
- Nesic, S., Cai, J., & Lee, K.J. (2005). *A Multiphase Flow and Internal Corrosion Prediction Model for Mild Steel Pipelines*. Paper presented at the NACE Corrosion/2005, Paper No.05556.

- Nesic, S., & Carroll, F. (2003). Horizontal rotating cylinder - a compact apparatus for studying the effect of water wetting on carbon dioxide corrosion of mild steel. *Corrosion*, 59(12), 1085-1095.
- Nesic, S., & Postlethwaite, J. (1996a). An electrochemical model for prediction of CO<sub>2</sub> corrosion. *Corrosion*, 52, 280-293.
- Nesic, S., Thevenot, N., Crolet, J.L., & Drazic, D.M. (1996b). *Electrochemical properties of iron dissolution in the presence of CO<sub>2</sub>-basics revisited*. Paper presented at the NACE Corrosion/96, Paper no.96003.
- Nesic, S., Wang, S., Cai, J., & Xiao, Y. (2004). *Integrated CO<sub>2</sub> corrosion-multiphase flow model*. Paper presented at the Corrosion/04, paper no.04626.
- Nyborg, R. (2003). Corrosion Control in Oil and Gas Pipelines. *Exploration & Production: The Oil & Gas Review*, 2, 79-82.
- Oddie, G., Shi, H., Durlofsky, L.J., Aziz, K., Pfeffer, B., & Holmes, J.A. (2003). Experimental study of two and three phase flows in large diameter inclined pipes. [Article]. *International Journal of Multiphase Flow*, 29(4), 527-558.
- Oglesby, K.D. (1979). *An experimental study on the effect of oil viscosity, mixture, velocity and water fraction on horizontal oil-water flow*. Unpublished Master Thesis, University of Tulsa, Tulsa, OK.
- Rodriguez, O.M.H., & Oliemans, R.V.A. (2006). Experimental study on oil-water flow in horizontal and slightly inclined pipes. *International Journal of Multiphase Flow*, 32(3), 323-343.

- Russell, T.W.F., Hodgson, G.W., & Govier, G.W. (1959). Horizontal pipeline flow of mixtures of oil and water. *Canadian Journal of Chemical Engineering*, 37, 9-17.
- Schmitt, G., & Stradmann, N. (1998). *Wettability of steel surfaces at CO<sub>2</sub> corrosion conditions-1. effect of surface active compounds in aqueous and hydrocarbon media*. Paper presented at the NACE Corrosion/98, paper no. 98028.
- Shi, H. (2001). A study of oil-water flows in large diameter horizontal pipelines. Unpublished Ph.D. Dissertation. Ohio University.
- Smith, L.M. (1987). *Controlling factors in the rate of CO<sub>2</sub> corrosion* Paper presented at the UK Corrosion '87.
- Taitel, Y., & Dukler, A.E. (1976). A Model for Predicting Flow Regime Transitions in Horizontal and near Horizontal Gas-Liquid Flow. *AIChE Journal*, 22, 47-55.
- Teeters, D., Wilson, J.F., Andersen, M.A., & Thomas, D. C. (1988). A dynamic wilhelmy plate technique used for wettability evaluation of crude oils. *Journal of Colloid and Interface Science*, 126(2), 641-644.
- Thomas, T.R. (1999). *Rough Surfaces* (2nd ed.). London: Imperial College Press.
- Trallero, J.L., Sarica, C., & Brill, J.P. (1997). A study of oil/water flow patterns in horizontal pipes. *SPE Production & Facilities*, 12(3), 165-172.
- Valle, A., & Kvandal, H. (1995). *Pressure drop and dispersion characteristics of separated oil-water flow*. Paper presented at the 1st International Symposium on Two-Phase Modelling and Experimentation, Rome, Italy.
- Vedapuri, D., Bessette, D., & Jepson, W.P. (1997). *A segregated flow model to predict water layer thickness in oil-water flows in horizontal and slightly inclined*

*pipelines*. Paper presented at the the 8th International Conference on Multiphase Production, 75-105.

Whitehouse, D. J. (2003). *Handbook of surface and nanometrology*. London: Institute of Physics Publishing.

Wicks, M., & Fraser, J.P. (1975). Entrainment of water by flowing oil. *Materials Performance*, 14(5), 9-12.

Wu, Y. (1995). Entrainment method enhanced to account for oil's water content. *Oil & Gas Journal* 93(35), 83-86.

Young, T. (1805). An Essay on the Cohesion of Fluids. *Philosophical Transactions of the Royal Society of London*, 95, 65-87.